

DTIC FILE COPY

4

**RADC-TR-89-289**  
**Final Technical Report**  
**December 1989**

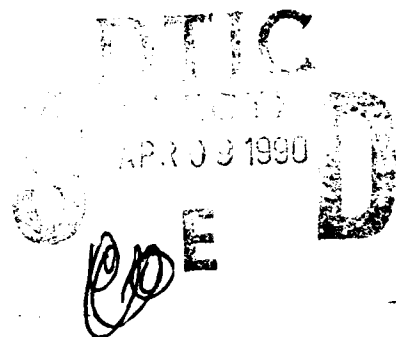


**AD-A220 445**

# **ATMOSPHERIC TURBULENCE MEASUREMENTS IN SUPPORT OF ADAPTIVE OPTICS TECHNOLOGY**

**Airborne Research Associates**

**Sponsored by**  
**Strategic Defense Initiative Office**



*APPROVED FOR PUBLIC RELEASE; DISTRIBUTION UNLIMITED*

The views and conclusions contained in this document are those of the authors and should not be interpreted as necessarily representing the official policies, either expressed or implied, of the Strategic Defense Initiative Office or the U.S. Government.

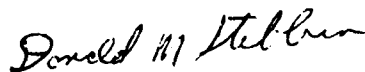
**Rome Air Development Center**  
**Air Force Systems Command**  
**Griffiss Air Force Base, NY 13441-5700**

**90 04 10 122**

This report has been reviewed by the RADC Public Affairs Division (PA) and is releasable to the National Technical Information Services (NTIS) At NTIS it will be releasable to the general public, including foreign nations.

RADC-TR-89-289 has been reviewed and is approved for publication.

APPROVED:



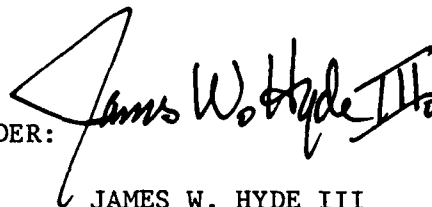
DONALD M. STEBBINS  
Project Engineer

APPROVED:



FRANK J. REHM  
Technical Director  
Directorate of Surveillance

FOR THE COMMANDER:



JAMES W. HYDE III  
Directorate of Plans & Programs

If your address has changed or if you wish to be removed from the RADC mailing list, or if the addressee is no longer employed by your organization, please notify RADC (OCSP ) Griffiss AFB NY 13441-5700. This will assist us in maintaining a current mailing list.

Do not return copies of this report unless contractual obligations or notices on a specific document require that it be returned.

R. M. Markson  
B. W. Anderson  
C. W. Fairall  
D. W. Thomson  
A. B. White  
W. J. Syrett

**Principal Investigator:** Ralph M. Markson  
(617) 899-1834

Approved for public release; distribution unlimited.



Accession For

NTUS GRACE

DTIC TAB

Unannounced

Justification

By

DTIC TAB

DATE

A-1

UNCLASSIFIED

SECURITY CLASSIFICATION OF THIS PAGE

REPORT DOCUMENTATION PAGE				Form Approved OMB No. 0704-0188	
1a. REPORT SECURITY CLASSIFICATION UNCLASSIFIED			1b. RESTRICTIVE MARKINGS N/A		
2a. SECURITY CLASSIFICATION AUTHORITY N/A			3. DISTRIBUTION/AVAILABILITY OF REPORT Approved for public release; distribution unlimited.		
2b. DECLASSIFICATION/DOWNGRADING SCHEDULE N/A					
4. PERFORMING ORGANIZATION REPORT NUMBER(S)  N/A			5. MONITORING ORGANIZATION REPORT NUMBER(S)  RADC-TR-89-289		
6a. NAME OF PERFORMING ORGANIZATION  Airborne Research Associates		6b. OFFICE SYMBOL (If applicable)	7a. NAME OF MONITORING ORGANIZATION  Rome Air Development Center (OCSF)		
6c. ADDRESS (City, State, and ZIP Code)  46 Kendal Common Road Weston MA 02193			7b. ADDRESS (City, State, and ZIP Code)  Griffiss AFB NY 13441-5700		
8a. NAME OF FUNDING/SPONSORING ORGANIZATION Strategic Defense Initiative Office		8b. OFFICE SYMBOL (If applicable) SDIO-T-DE	9. PROCUREMENT INSTRUMENT IDENTIFICATION NUMBER  F30602-86-C-0021		
8c. ADDRESS (City, State, and ZIP Code)  Office of the Secretary of Defense Wash DC 20301-7100			10. SOURCE OF FUNDING NUMBERS		
			PROGRAM ELEMENT NO. 63221C	PROJECT NO. D174	TASK NO. 06
					WORK UNIT ACCESSION NO. 03
11. TITLE (Include Security Classification)  ATMOSPHERIC TURBULENCE MEASUREMENTS IN SUPPORT OF ADAPTIVE OPTICS TECHNOLOGY					
12. PERSONAL AUTHOR(S) R. M. Markson, B. W. Anderson, C. W. Fairall, D. W. Thomson, A. B. White, W. J. Syrett					
13a. TYPE OF REPORT Final		13b. TIME COVERED FROM Dec 85 TO Dec 87		14. DATE OF REPORT (Year, Month, Day) December 1989	
				15. PAGE COUNT 328	
16. SUPPLEMENTARY NOTATION  N/A					
17. COSATI CODES			18. SUBJECT TERMS (Continue on reverse if necessary and identify by block number)		
FIELD	GROUP	SUB-GROUP			
04	01		Optical Turbulence Radar Backscatter		
			Atmosphere Index of Refraction		
20	06		Atmospheric Turbulence (Continued on reverse)		
19. ABSTRACT (Continue on reverse if necessary and identify by block number) This report is concerned with the relation of meteorological conditions to parameters and processes that influence the optical propagation properties of the turbulent atmosphere. The approach is centered around the use of aircraft and surface based remote sensors to investigate the relationship of the refractive index structure function parameter, $C_n^2$ , to various meteorological variables and to generally evaluate the accuracy of measurements of $C_n^2$ by in situ and remote means. The relation of the atmospheric turbulence profile to the synoptic context and the use of physical models to predict the profile using standard meteorological profile data was also investigated. The study features two modes of data acquisition: 1) continuous archiving of 1 hr average wind profiles and turbulence levels with VHF doppler radar profilers, and 2) high time resolution aircraft measurements in association with other measurements (ground based optical scintillometers, thermosondes, radar profilers, and doppler sodar profilers). In one case all of the surface based systems were assembled in an intensive "campaign" given the acronym EWAK. (Continued on reverse)					
20. DISTRIBUTION/AVAILABILITY OF ABSTRACT <input checked="" type="checkbox"/> UNCLASSIFIED/UNLIMITED <input type="checkbox"/> SAME AS RPT. <input type="checkbox"/> DTIC USERS			21. ABSTRACT SECURITY CLASSIFICATION UNCLASSIFIED		
22a. NAME OF RESPONSIBLE INDIVIDUAL Donald M. Stebbins			22b. TELEPHONE (Include Area Code) (315) 330-3055		22c. OFFICE SYMBOL RADC (OCSF)

DD Form 1473, JUN 86

Previous editions are obsolete.

SECURITY CLASSIFICATION OF THIS PAGE

UNCLASSIFIED

ABSTRACT

This project is concerned with the relation of meteorological conditions to parameters and processes that influence the optical propagation properties of the turbulent atmosphere. The approach is centered around the use of aircraft and surface based remote sensors to investigate the relationship of the refractive index structure function parameter,  $C_n^2$ , to various meteorological variables and to generally evaluate the accuracy of measurements of  $C_n^2$  by in situ and remote means. The relationship of the of the atmospheric turbulence profile to the synoptic context and the use of physical models to predict the profile using standard meteorological profile data was also investigated. The study features two modes of data acquisition: (1) continuous archiving of 1 hr average wind profiles and turbulence levels with VHF doppler radar profilers, and (2) high time resolution aircraft measurements in association with other measurements (groundbased optical scintillometers, thermosondes, radar profilers, and doppler sodar profilers). In one case all of the surface based systems were assembled in an intensive 'campaign' given the acronym EWAK.

The atmospheric turbulence profiles and resultant optical propagation parameters have been found to be strongly influenced by synoptic conditions. In particular, the turbulence is substantially affected by to strength and location of the jet stream. A very strong correlation between wind shear (which is maximum above and below the core of the jet) and pilot reports of turbulence was found. Richardson number gave a much weaker indication, possibly because of the poorer quality of the vertical temperature gradient data. A comparison of five different methods (four measurement and one model) of obtaining optical  $C_n^2$  showed average disagreements as large as a factor of three. The planetary boundary layer was found to contribute significantly

to the correlation length,  $r_0$ . A study of the ratio of temperature to velocity microturbulence showed that the assumption of a constant mixing efficiency (used in the Van Zandt model) may not be valid for very weak turbulence. Variations of  $C_n^2$  at fixed altitude were found to be as large as one order of magnitude for one hour time or 50 km space scales. An evaluation of a Xondar III doppler sodar was conducted to assess its utility for quantitative monitoring of  $C_n^2$  in the boundary layer. Profiles of  $C_n^2$  were obtained to a maximum height of 250 to 900 m depending on atmospheric conditions. We believe that the boundary layer performance of this system can be improved significantly with minor modifications to the hardware and software.

# ACKNOWLEDGEMENTS

Some of the Penn State effort was directly supported by the Air Force Office of Scientific Research contract number AFOSR-86-0049; the radar systems were originally obtained on AFOSR-83-0275. Robert Peters and Scott Williams of the Department of Meteorology, PSU, were primarily responsible for the construction and operation of the radars (with external assistance as described in the appendices).

The authors wish to acknowledge Lt. Beth Beecher, Mr. Ted Messier and Capt. Mike Moss for their contributions to and analysis of the EWAK experiment.

CONTENTS

	<u>Page</u>
1. Introduction	6
2. Aircraft measurements of $C_n^2$	11
2.1 Theory	11
2.2 Data processing	11
2.3 $C_n^2$ calibration	13
2.4 Aircraft data	15
3. Sodar Evaluation	19
3.1 Sodar measurements of turbulence	19
3.2 Theory	19
3.3 The Xondar III system	21
3.4 Sodar/aircraft comparison	23
3.5 Other sodar data	34
4. Conclusions	38

APPENDICES

- A. Turbulence and mean meteorological profiles for flights 13-22
- B. "Long Term Studies of Refractive Index Structure Parameter in the Troposphere and Stratosphere"
- C. "Analysis of Temperature and Velocity Microturbulence Parameters from Aircraft Data and Relation to Atmospheric Refractive Index Structure"



## 1. Introduction

### 1.1 Background

This report describes work done in a program of atmospheric measurements and analysis to verify and improve optical measurements and models of atmospheric refractive index structure parameter ( $C_n^2$ ) and other derived atmospheric optical parameters such as the coherence length ( $r_0$ ) and the isoplanatic angle ( $\theta_0$ ). The primary in situ standard for this work was the Airborne Research Associates' (ARA) instrumented aircraft. Two remote sensors were also used, a VHF doppler radar wind profiler and a monostatic doppler sodar wind profiler. The intensity of the backscattered signal measured with these remote sensors is proportional to radar  $C_n^2$  and  $C_T^2$ , respectively.

The basic goals of the study were:

- a. Direct comparison of aircraft and stellar scintillometer measurements of optical  $C_n^2$  vertical profiles from 2-10 km altitude.
- b. Aircraft measurements of  $C_n^2$  below 2 km altitude to assess the relative importance of the boundary layer region on  $r_0$  and  $\theta_0$ .
- c. Constant altitude aircraft measurements of  $C_T^2$  to provide an assessment of the horizontal variability.
- d. An evaluation of the Van Zandt et al. (1981) model for  $C_n^2$ .
- e. A study of the usefulness of third generation acoustic radar (sodar) for continuous groundbased monitoring of  $C_n^2$  profiles (via  $C_T^2$ ) in the boundary layer.

The work described here, which emphasizes atmospheric optical

propagation, was funded by and done in conjunction with the Rome Air Development Center (RADC). An adjunct activity at Penn State University, basic research on the dynamics of free atmospheric turbulence, was carried out with funding from the Air Force Office of Scientific Research (AFOSR). The aircraft measurements were carried out in two modes: (1) A major intensive field experiment involving a variety of groundbased optical measurement systems. (2) More limited studies involving aircraft turbulence profiles with a single groundbased optical system (at Rome, NY) and/or surface based doppler systems (usually at Penn State). A total of 22 flights were made.

The intensive field program (which was given the acronym EWAK) was held at Penn State in early May, 1986. Given the scale of the experiment, optical propagation scientists from several other laboratories were also invited to participate. Four different optical systems plus a balloon born  $C_n^2$  system (thermosonde) were operated in conjunction with the aircraft and doppler systems (see Table 1). All optical equipment was operated between 30 April and 6 May. Fortunately, during this week skies were clear on every night but one. During this period four aircraft flights were made (another four flights were made during the optical setup period) and 35 thermosondes were launched.  $C_n^2$  was also measured on a short tower at the optical/sodar site at Penn State.

Following EWAK, an additional 14 aircraft flights were made over the next year and a half. Since EWAK took place in the spring, the remaining flights were made in summer, fall, and winter. Only the last two flights were not done in conjunction with a groundbased remote turbulence sensing system. A chronology is given in Table 2.

Table 1. Summary of participants and measurements for the EWAK intensive field experiment held at Penn State in May, 1986.

<u>Measurement</u>	<u>Institution</u>	<u>Contact</u>
Surface micrometeorology	PSU	C. Fairall
Sodar	PSU	D. Thomson
Radar (VHF1,VHF2)	PSU	D. Thomson
Thermosonde ( $C_n^2$ )	AFGL	J. Brown
Aircraft	ARA	R. Markson
Optical $C_n^2$ profile#1	RADC	D. Stebbins
Optical $C_n^2$ profile#2	AFGL	E. Murphy
Optical scintillometer ( $r_o$ )	NPS	D. Walter
Optical scintillometer ( $\theta_o$ )	AFWL	J. Davidson

Table 2. Chronology of aircraft flights for the entire program.

<u>Flight#</u>	<u>Site</u>	<u>Date</u>	<u>GMT</u>	<u>Remote Sensors</u>	<u>Comments</u>
1	PSU	4/13/86	1400	***	Test flight
2	PSU	4/14/86	1500	Radar, sodar	
3	PSU	4/18/86	2100	Radar, sodar	
4	PSU	4/19/86	1700	Radar, sodar	
5	PSU	5/3/86	1400		Recording failure
6	PSU	5/4/86	0400	EWAK	
7	PSU	5/4/86	0300	EWAK	
8	PSU	5/6/86	1700	EWAK	
9	RADC	8/11/86	2250	Optical $C_n^2$ , sodar	
10	RADC	8/12/86	1500	Optical $C_n^2$ , sodar	
11	RADC	8/13/86	0200	Optical $C_n^2$ , sodar	
11-b	RADC	8/13/86	1400	Optical $C_n^2$ , sodar	
12	RADC	10/10/86	1700	Optical $C_n^2$	
13	PSU	8/1/87	2100	Radar, sodar	
14	PSU	8/6/87	2100	Radar, sodar	
15	PSU	8/11/87	2100	Radar, sodar	
16	PSU	8/12/87	1700	Radar, sodar	
17	PSU	9/3/87	2100	Radar, sodar	Test flight
18	PSU	9/4/87	1800	Radar, sodar	
19	PSU	10/14/87	2100	Radar, sodar	
20	PSU	10/15/87	1800	Radar, sodar	
21	Boston	12/21/87	1800		Horizontal
22	Boston	12/23/87	1600		Horizontal

## 1.2 Scope of this report

The analysis of the results has been a very large job involving a number of people. As a result, certain components have been completed and written up already. Results for the first four goals outlined above have been described extensively in an MS thesis (Beecher, 1987) and a final technical report to the AFOSR (Fairall et al., 1988). Both of these documents are included as appendices in this report. The main text of this report will be devoted to an evaluation of the sodar (item e above) and a summary of our overall conclusions. A discussion and evaluation of the accuracy of microthermal  $C_n^2$  measurements is also included. In the near future we anticipate completion of the in-depth study of the radar  $C_n^2$  applications in the form of a Ph.D. thesis by Capt. Michael Moss (Florida State University). Most of the analysis of the radar  $C_n^2$  data presented in the appendix has been performed by Capt. Moss as a part of his Ph.D. dissertation research. Capt. Moss, a graduate student at Florida State University, performed most of this thesis research at Penn State as it was the only university in the country to have VHF and UHF profilers available.

## 2. Aircraft measurement of $C_n^2$

### 2.1 Theory

$C_n^2$  can be related to micrometeorological variables by (Wesely, 1976)

$$C_n^2 = A(C_T^2 + 2 B C_{Tq} + B C_q^2) \quad (1)$$

where A and B are functions of temperature (T), pressure and specific humidity (q);  $C_T^2$ ,  $C_q^2$ , and  $C_{Tq}$  are temperature and humidity structure function parameters. The values of A and B are radiation-type and wavelength dependent. For optical wavelengths,  $C_n^2$  is almost always dominated by the temperature structure function parameter in the atmosphere. Therefore, we will focus our attention on  $C_T^2$ .

The temperature structure function parameter can be estimated from the one-dimensional temperature variance spectral density,  $\phi_T(f)$ , which is computed from a time series of temperature fluctuation measurements.

$$C_T^2 = 4 (2\pi/u)^{2/3} f^{5/3} \phi_T(f) \quad (2)$$

where u is the mean speed of the air relative to the sensor (i.e., the aircraft true air speed) and f the frequency. In using (2) we are assuming that the measurements are in a valid region of the inertial subrange of locally isotropic turbulence (Panofsky and Dutton, 1984).

### 2.2 Data Processing

The temperature fluctuations necessary to use (2) are measured using standard microthermal temperature-resistance sensors and very sensitive

resistance bridges. Fluctuations in the bridge output voltage is proportional to atmospheric temperature fluctuations. The spectrum of the bridge voltage fluctuations,  $\phi_v$ , is expected to be

$$\phi_v = (i G G_B R_i \alpha)^2 (\phi_T + N_u + N_T + N_v / (i R_i \alpha)^2) \quad (3)$$

where  $i$  is the current to the sensor with ice point resistance  $R_i$  and temperature-resistance coefficient  $\alpha$ ;  $G_B$  is the bridge gain and  $G$  the combined subsequent signal conditioning and recording gains;  $N_u$  is the velocity sensitivity contamination noise,  $N_T$  is temperature noise detected by the sensors but not due to turbulence, and  $N_v$  is the broadband voltage noise of the detector. This relation and a number of other factors relevant to the measurement problem are discussed in great detail by Fairall and Markson (1984).

The fluctuation data are recorded in flight on FM tape and later processed in the laboratory. The time series can be spectrally analyzed either with a computer based digitizer and FFT processor or with a realtime computer controlled spectral analyzer (Hewlett Packard 3562A). The results given here were all processed with the HP device. Because of the contaminating influence of the various noise sources included in (3), computation of  $C_n^2$  is not straightforward. For reasonably strong turbulence, the real signal ( $\phi_T$ ) overwhelms the noise terms in (3) and there are no problems. However, in weak turbulence ( $C_n^2 < 10^{-17} \text{ m}^{-2/3}$ ) some additional effort is required to extract the signal from of the noise. Beecher (1987) developed a useful algorithm to improve the automated analysis of the data. Use of this algorithm is a process of several steps:

- (i) Noise subtraction. Determine the broadband noise ( $N_v$ ) by looking in the high frequency end of the spectrum (where the real signal is negligible). Then subtract the noise from the spectrum.
- (ii) Defiltering. Remove the effects of the highpass analog filter used in recording. This will restore the low frequency content of the atmospheric spectrum which is most likely to be well above the noise.
- (iii) Slope checking. The slope of the spectrum is computed in  $\log(\phi)$  vs  $\log(f)$  coordinates. According to (2), this slope should be  $-5/3$  in the inertial subrange. The slope was checked in several selected frequency bands.

Initially the slope of the spectrum was checked between 5 and 18 Hz. If the slope was not within 20% of  $-1.667$ , then various steps were taken (noise subtraction, defiltering) and the slope checked again. Spectra that failed to meet this final criterion were simply rejected. Further detail and examples are given in Chapter 6 of Beecher (1987).

### 2.3 $C_n^2$ Calibration

Examination of expressions (2) and (3) suggests that a number of factors are involved in computing  $C_n^2$  and that each represents a potential source of error. During EWAK two coincident aircraft and AFGL thermosonde flights were made and at some altitudes considerable disagreement was observed in  $C_n^2$  values. This disagreement could have been due to sampling error, improper temperature bridge calibration, processing errors, etc. Lacking a suitable standard for high altitude turbulence, we have checked the consistency of the aircraft data by comparison with ground based measurements.

Two comparisons have been examined. First, in order to check the bridge



calibrations and general methodology, an AFGL and a Penn State temperature bridge were run side-by-side on the micromet tower at the site at Rock Springs, PA. Completely independent systems (sensors and bridges) were mounted on the tower at a height of 8 m. A paired sensor, rms processing method was used (Fairall and Markson, 1984). The rms outputs of both bridges were recorded as half-hour averages on the same data acquisition system. About 5 days data were taken. Values of  $C_T^2$  were computed and converted to  $C_n^2$  using (1). The comparison of the two systems is shown in Fig. 1. The average disagreement was 9% with a point to point scatter of about 25%.

Direct comparisons of the aircraft  $C_n^2$  measurements with tower measurements were not feasible at State College because of restrictions on low altitude flights in a nearby populated area. Following EWAK, the aircraft was deployed to an experiment at Hobbs, NM, where a ground station was setup at an abandoned B-17 airbase. There the ground station had measurements of  $C_T^2$  on a tower at a height of 2 m above the surface (which was very flat and smooth). A number of aircraft profiles of  $C_T^2$  were made in the area. Typically the lowest aircraft altitude used was 6 m. A sample aircraft profile of  $C_T^2$  and  $\epsilon$  (rate of dissipation of turbulent kinetic energy) is shown in Fig. 2. The lowest two data points on the graph (E for  $\epsilon$  and C for  $C_T^2$ ) are taken from the ground station. The solid lines depict similarity model fits to the data (Fairall, 1987). Since the aircraft data are not from the same altitude as the tower data, a similarity model has been used to extrapolate the aircraft results to 2 m. In the example shown here, the solid line passes right through the tower values, indicating excellent agreement. Using this approach, we have compared aircraft and tower  $C_n^2$  for 10 flybys of the surface station (Fig. 3). The values of  $C_n^2$  are much larger at Hobbs than at PSU because of the much greater sensible heat fluxes and the

closer proximity to the surface (2 m versus 8 m). The agreement here is quite good, especially when we consider the locally inhomogeneous surface (tarmac and grass).

#### 2.4 Aircraft Data

Some 22 flights were made during this project, three did not yield usable data (see Table 2). The data were analyzed in 100 second blocks which typically yielded a vertical resolution of 300 m for profiles and a horizontal resolution on the order of 5 km. Profiles were usually from 0.1 to 10 km altitude but several times the upper altitude was restricted due to air traffic control. The last two flights were directed towards long horizontal runs. Above the boundary layer, the  $C_n^2$  values were generally between  $10^{-18}$  and  $10^{-16} \text{ m}^{-2/3}$ , although higher values were found in occasional strong CAT regions. Besides the  $C_n^2$ ,  $C_T^2$ , and  $\epsilon$  data, aircraft measurements of mean potential temperature and mean water vapor mixing ratio are available. For the profiles near State College, mean wind and microwave  $C_n^2$  profiles were also available from the Penn State radar. For flights 2-12, all of the available data were summarized in the MS thesis by Beecher. Since this document is included as an appendix, that data has not been reproduced in the body of this report. For flights 13-22, we have included the aircraft turbulence and mean data as Appendix A. Radar data were archived for flights 13-20, but are still being analyzed by Capt. Moss and are not available at this time.

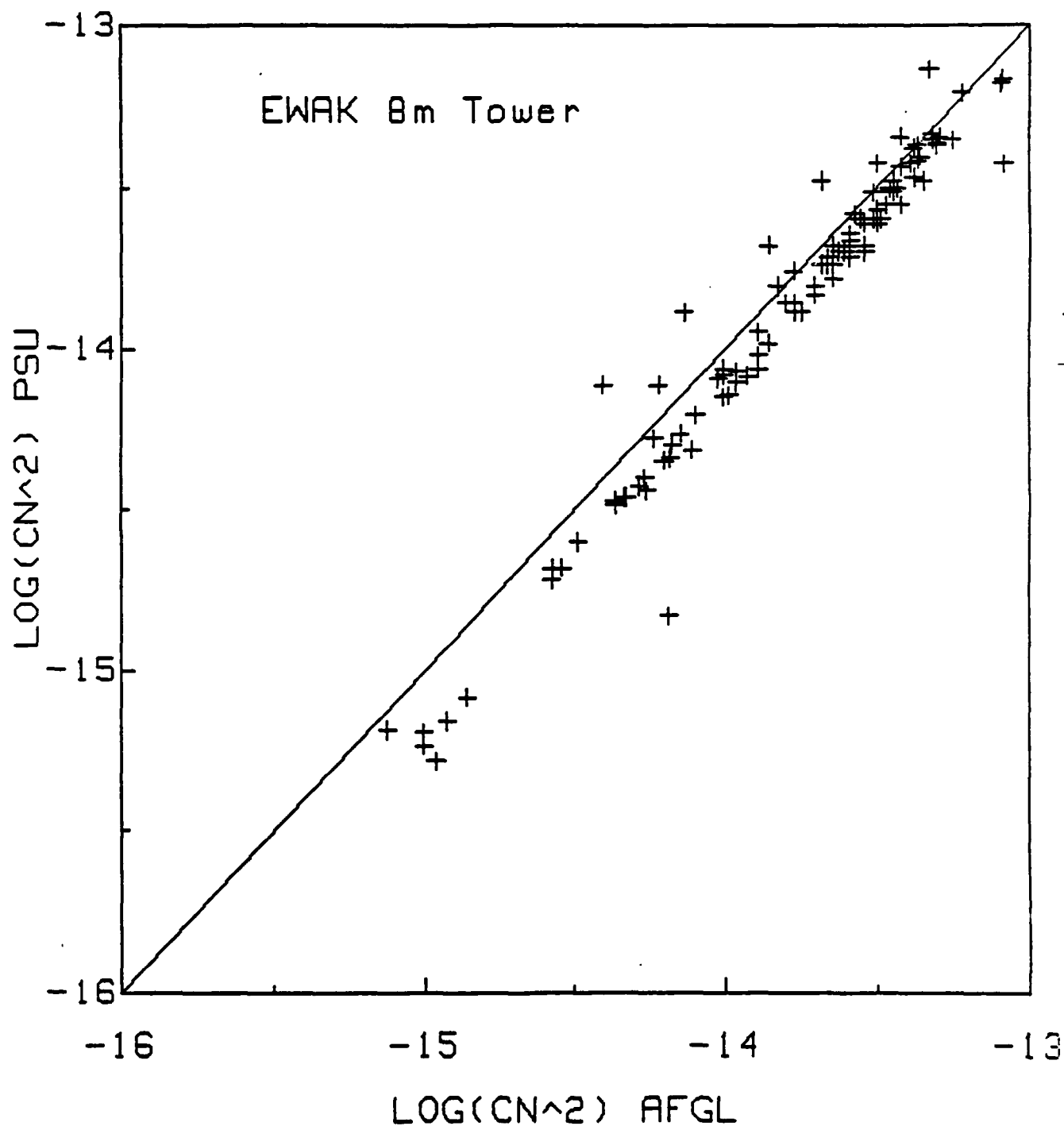


Fig. 1 Comparison of measurements of optical  $C_n^2$  from tower mounted sensors using a Penn State and an AFGL temperature bridge.

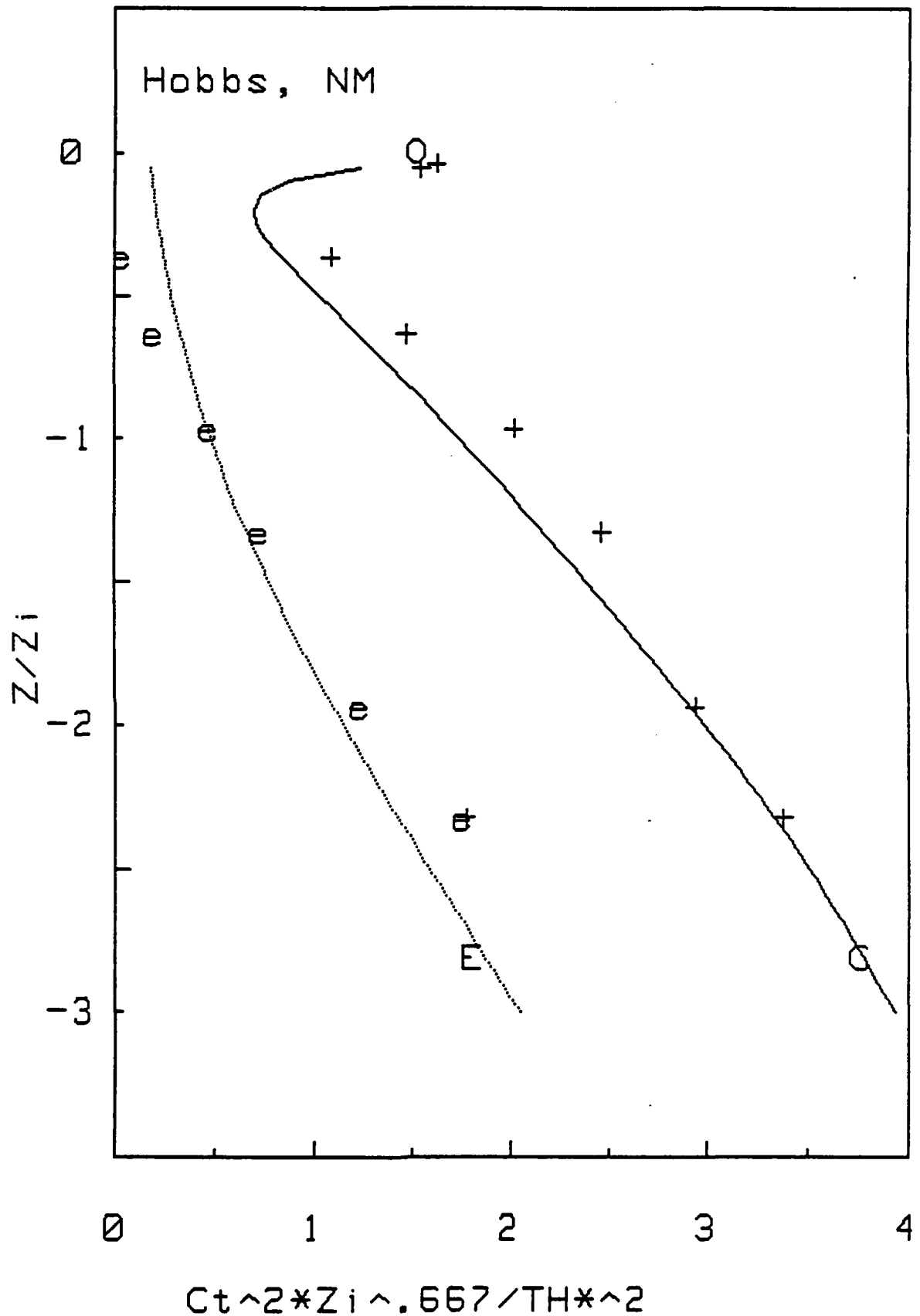


Fig. 2 An example of aircraft measured profiles of  $C_T^2$  (+ symbol) and  $\epsilon$  (e symbol) from Hobbs, NM. The solid curve is the Monin-Obukhov similarity model. The ground stations measurements are designated by E (for  $\epsilon$ ) and C (for  $C_T^2$ ).

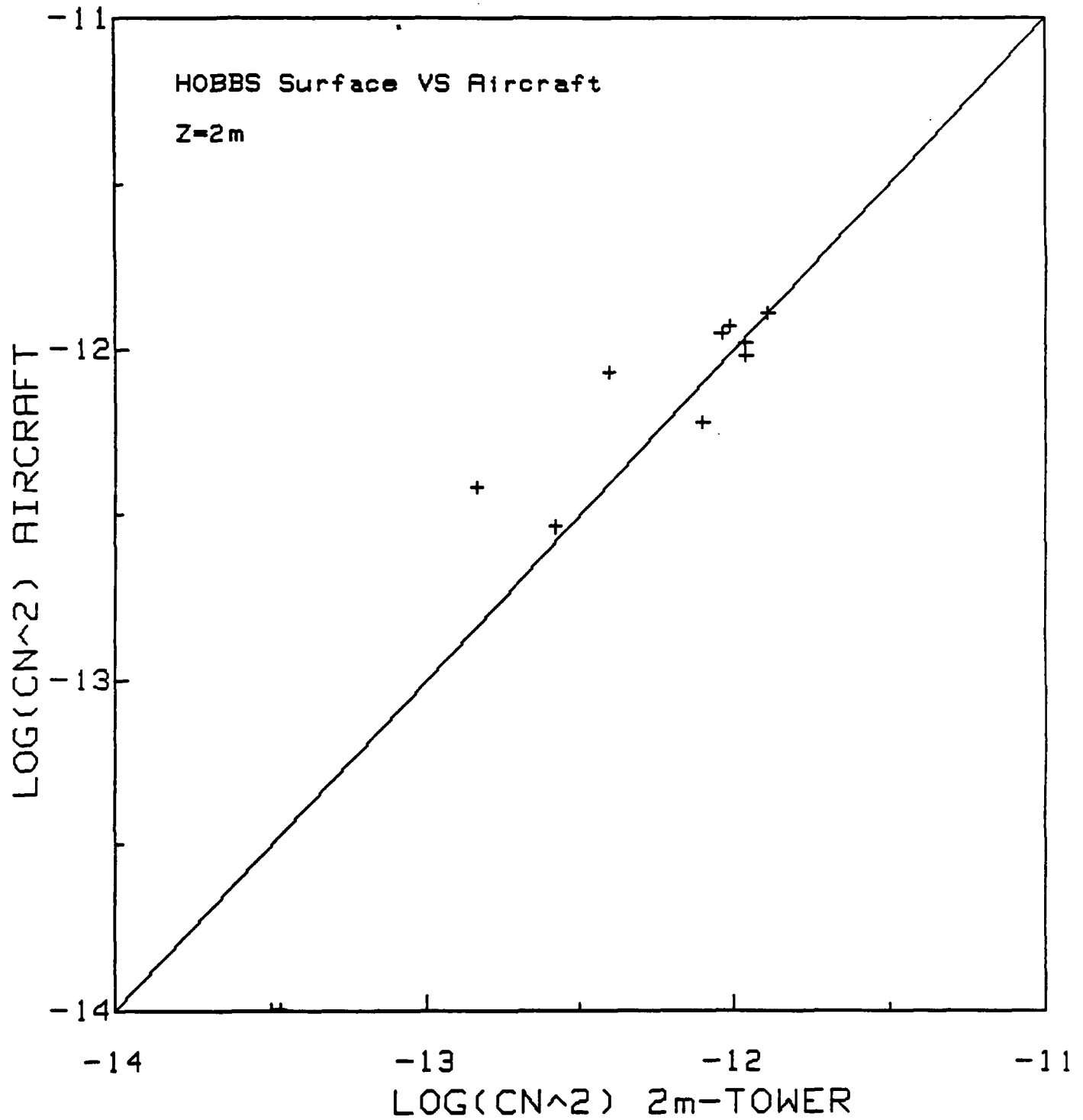


Fig. 3 Direct comparison of aircraft (extrapolated to  $z=2$  m) versus ground station  $C_n^2$  values.

### 3 Sodar Evaluation

#### 3.1 Sodar measurements of turbulence

Acoustic radars (sodar) have been used for quantitative measurements of  $C_T^2$  for some time (e.g., Neff, 1975; Thomson et al., 1978). Doppler acoustic systems are now available that, in principle, should allow measurement of mean velocity profiles and variability. As is the case for clear-air radar, the sodar backscatter intensity is proportional to  $C_n^2$ . For monostatic sodars the operative variable is acoustic  $C_n^2$  which, as in optical  $C_n^2$ , is dominated by the temperature structure function (Wesely, 1976). The largest values of  $C_n^2$  typically occur in the atmospheric boundary layer (ABL) which, in the daytime, has a vertical extent on the order of 1 to 2 km. Thus the low level portion of the  $C_n^2$  profile is often critical in determining integrated optical path variables. In this regard, the optical correlation length,  $r_o$ , is particularly sensitive. Since most remote sensors with high altitude capabilities (e.g., profiling scintillometers or clear-air radar) are unable to provide information about  $C_n^2$  in the ABL, computation of  $r_o$  and  $\theta_o$  usually requires extrapolation of the lowest level of data down to the surface. The final results can be quite sensitive to the extrapolation method, so a low level  $C_n^2$  profiling capability is very desirable. Historically, sodar have not been able to suitably meet this need because of their limited vertical range (about 300 m). However there are now sodars available that can provide doppler wind measurements up to about 1 km altitude. In this section we will examine the use of one such system (Xontech Corporation's model Xondar III) to measure profiles of  $C_n^2$ .

#### 3.2 Theory

The basis for relating the received power for a sodar to the relevant atmospheric turbulence parameter is the monostatic acoustic radar equation (Neff, 1975):

$$P_r = P_t \exp(-2\alpha R) (c\tau/2) [A*G/R^2] \sigma(\pi) \quad (4)$$

where  $P_r$  is the received power,  $P_t$  the transmitted power, and  $R$  the range. The exponential factor describes the round-trip loss of power resulting from attenuation by air where  $\alpha$  is the average absorption coefficient for sound at the frequency of the sodar. The factor  $(c\tau/2)$  is the radial extent of the range gate (at range  $R$ ) which is determined by the speed of propagation,  $c$ , and the acoustic pulse duration,  $\tau$ . The factor in the square brackets  $([])$  is the solid angle subtended by the antenna aperture area,  $A$ , at range  $R$  from the scattering volume, modified by an effective aperture factor,  $G$ , arising from the antenna's directivity. The quantity  $\sigma(\pi)$  is the scattering cross section per unit volume (for scattering  $180^\circ$  from the initial direction of propagation) and is given by

$$\sigma(\pi) = 0.00753 \lambda^{-1/3} C_{Tv}^2 T_v^2 \quad (5)$$

where  $\lambda$  is the acoustic wavelength,  $T_v$  is the virtual temperature, and we have indicated that the sodar is sensitive to the virtual temperature structure function parameter (i.e., fluctuations of atmospheric density). Normally we can assume

$$C_{Tv}^2 = C_T^2 \quad (6)$$

to within about 20% accuracy. Combining (4) and (5) gives us an expression for the temperature structure function parameter

$$C_T^2 = 132.8 T_V^2 \lambda^{1/3} R^2 \exp(2\alpha R) / [P_T AG(cr/2) G_d] P_R \quad (7)$$

Note in (7) we have included an additional factor, the total detector gain,  $G_d$ , to describe various stages of amplification to the signal after it is received by the transducers.

### 3.3 The Xondar III system

The system used for this study was the Xondar III manufactured by Xontech Corporation. This is a monostatic sodar using a phased array antenna with 25 transducers. By changing the phasing of the transducers, three different beam orientations are generated to obtain doppler estimates of the three wind components. All processing and control is done with an IBM PC computer with a special controller board and operating system. Data are archived on 5.25" floppy discs. The system specifications are summarized in Table 3.

The system used in the EWAK study was serial number 001 of this model. In other words, Penn State acquired the first unit the company sold and EWAK was also our first experience with it. Since 1986 we have acquired two additional units. We have operated these units at State College, PA; Huntsville, AL; Savannah River Laboratory, SC; San Nicolas Island, CA; Monterey, CA; and Harrisburg, PA (at the Three Mile Island nuclear power facility). Unit 001 was also operated briefly at Rome Air as a follow-on to EWAK, but because of hardware problems the results were not very useful. As is typical with technically advanced instrumentation, there were many startup problems with the systems and our own learning curve in understanding their

Table 3. Xondar III acoustic radar system specifications.



Wavelength	0.21 m
Transmitted power:	
Electrical	704 W
Acoustical	176 W
Operating frequency	1600 Hz
Pulse duration	200 ms
Pulse half length ( $\tau/2$ )	34 m
Antenna aperture area	$0.5 \text{ m}^2$
Antenna effective aperture factor ( $G^*$ )	0.4
Total detector gain:	
Wind table	78 dB
Sounder output	108 dB

\* See Hall and Wescott, 1974.

behavior and diagnosing hardware/software problems. Xontech has made several improvements to the hardware based on problems that we have uncovered. They are also now offering several different versions of the system software to meet different needs. While this provides greater flexibility, it also has added to our confusion since it seems that almost every experiment for which we have used the sodars has had a different version of the software.

The software used during EWAK provided only the mean received power as part of the wind table at the end of an averaging period (say 10 minutes). Thus the  $C_T^2$  information was available with the same temporal and spatial averaging as was the wind information. A later version of the software provided an additional output of the received power with one minute time resolution and 8.7 m vertical resolution. This is the same information (referred to as 'sounder output') that is used to drive a facsimile printer, but is provided as a serial stream that can be archived digitally on a second computer. This second method, which was first used on the San Nicolas Island deployment, was used for the aircraft comparisons in State College in August and September, 1987. Archiving the received power separately greatly complicates the analysis but it allows a much closer look at atmospheric fine structure (both temporal and spatial). Furthermore, the sounder output has additional electronic stages that increase the total gain by 30 dB.

### 3.4 Sodar/aircraft comparison

Aircraft  $C_n^2$  measurements were taken in the vicinity of the sodar at Rock Springs, PA, during two periods: EWAK in 1986 and August to October, 1987. The comparisons were made in a series of level runs by the aircraft at fixed altitude. Usually, the horizontal runs were 2 minutes in duration (about 6 km) over agricultural land and parallel to Tussey Ridge. The sodar

site was typically located about the middle of the run.

The EWAK period comparisons are shown in Figs. 4a-4d. The solid curves indicate the sodar  $C_T^2$  computed from the average power given in the wind table. The raw powers have had a mean background removed. This background is believed to be the noise level (in some cases greater levels are due to environmental noise and wind noise of the antenna) of the detector. Removing the background value improves the signal to noise significantly at the upper altitudes. Since there is a limit to the accuracy of this noise subtraction process, a residual background noise remains, which is crudely indicated in these figures by the dashed straight line. The aircraft values for the 2 minute level runs are indicated by the circles. The comparison is quite good although there is a clear indication that the sodar overestimates  $C_T^2$  below 100 m. This is probably due to the acoustic energy of local ground reflections.

The 1987 comparisons are shown in Figs. 5a-5e. Remember, these sodar values are computed from the sounder output which is available about once a minute. The curves shown represent 20 minute time averages and 5 point median smoothing in the vertical. The noise level has also been subtracted from this sodar data. The residual noise level is apparent as the smooth line above 200 to 300 m. For these data the ambient  $C_T^2$  values are much lower than during the EWAK period, partly because most of the flights were in the late afternoon and approaching the minimum near sundown. Considerably better altitude coverage is observed at most other times of the day. Again, the profiles indicate that the sodar  $C_T^2$  are not valid below about 100 m. Only on the afternoon of August 12 do we see reasonable  $C_T^2$  values of the 300 m. However, the  $C_n^2$  values for these days appear to be on the order of  $10^{-16}$ , which are quite low for the boundary layer. Notice also that the 'noise curve' gives an indication of the sensitivity of the sodar as a

EWAK UNCORRECTED SODAR PROFILE  
OF  
TEMPERATURE STRUCTURE PARAMETER

4-14-86

10:57

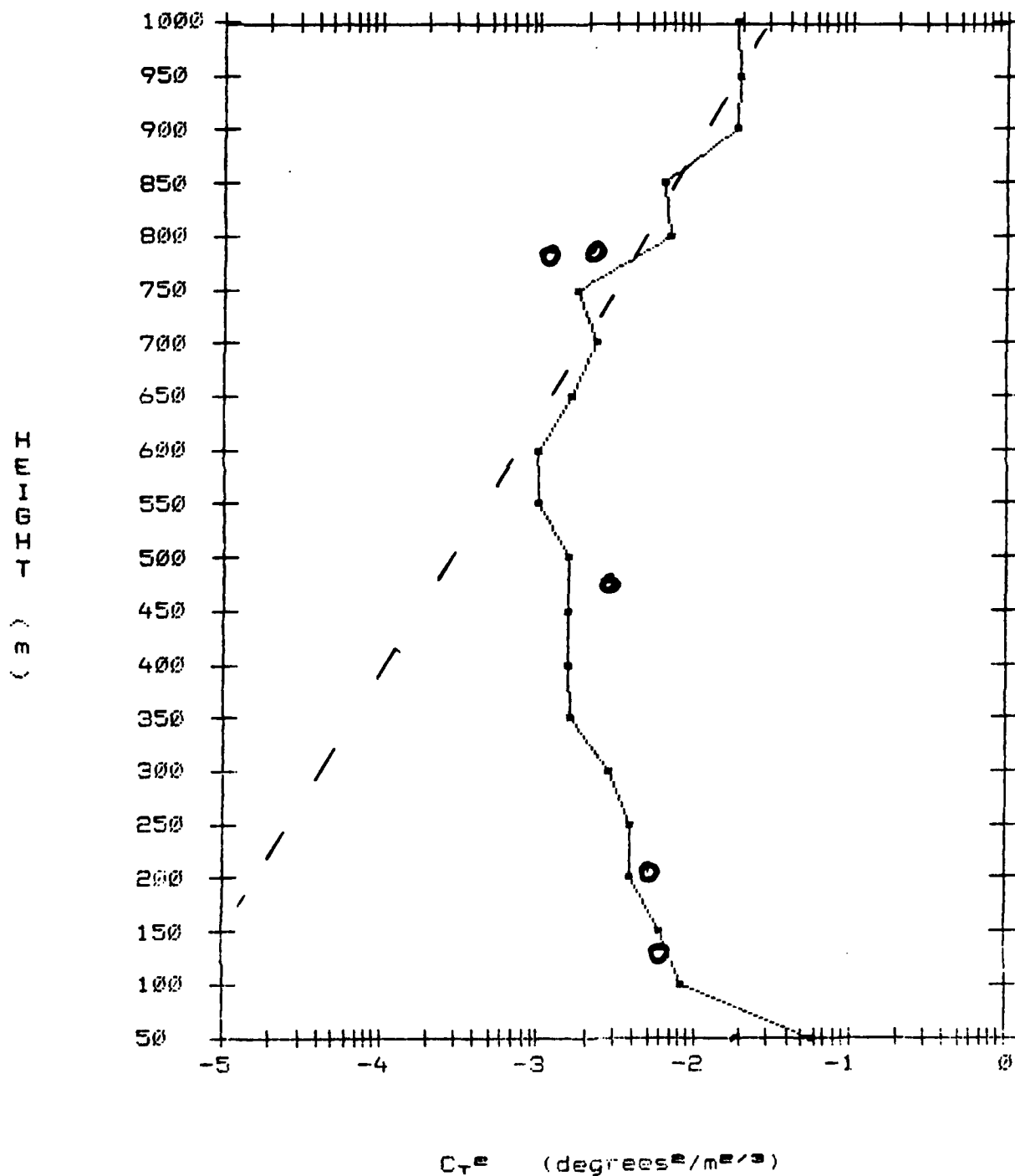


Fig. 4a Profiles of  $C_T^2$  from 4-14, 10:57 EST during EWAK. The solid line denotes a half hour average of sodar data, the circles denote 2-minute level aircraft values.

EWAK UNCORRECTED SODAR PROFILE  
OF  
TEMPERATURE STRUCTURE PARAMETER

4-18-84

16:55

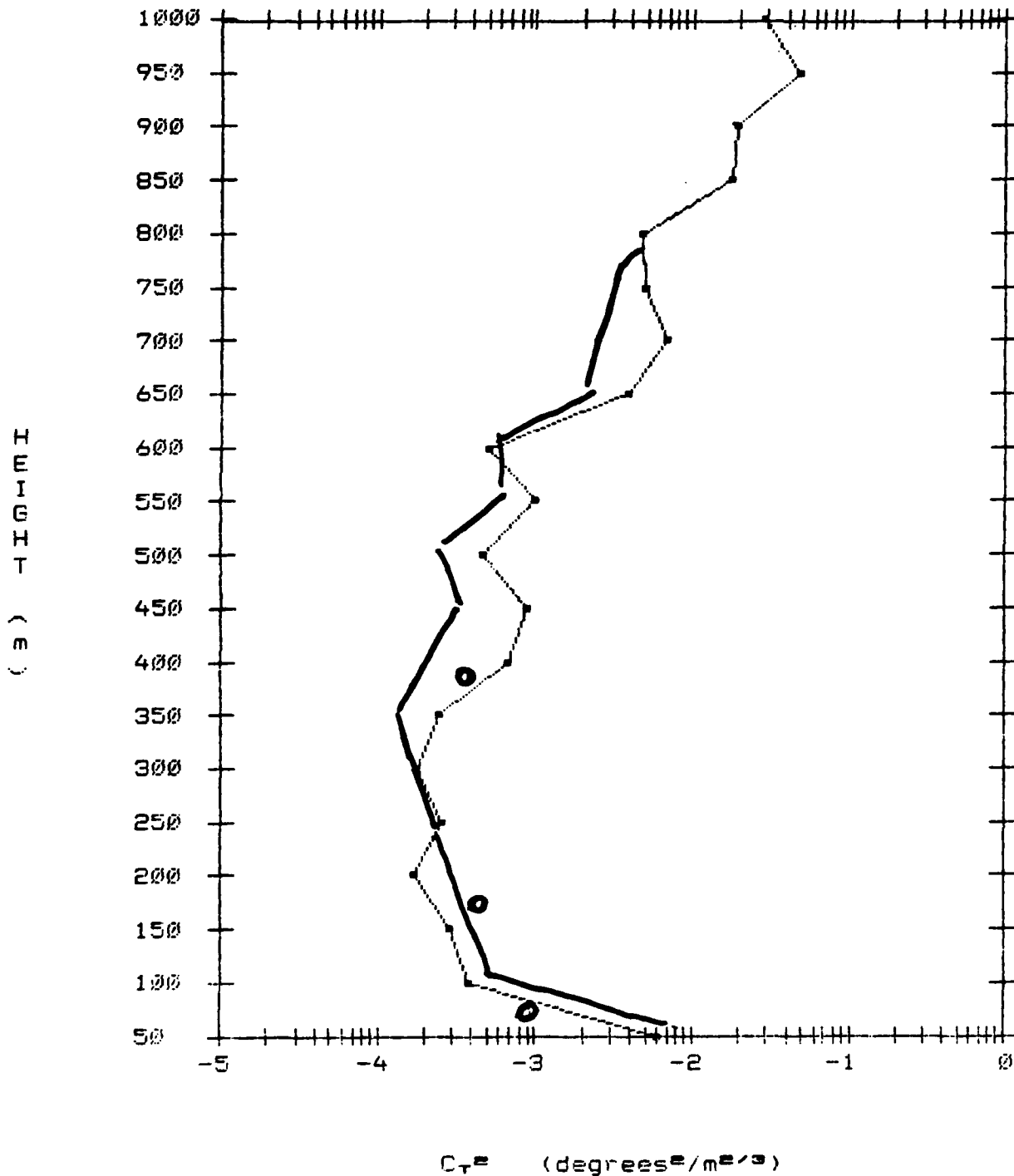


Fig. 4b Profiles of  $C_T^2$  from 4-18, 16:55 EST during EWAK. The solid line denotes a half hour average of sodar data, the circles denote 2-minute level aircraft values.

EWAK UNCORRECTED SODAR PROFILE  
OF  
TEMPERATURE STRUCTURE PARAMETER

4-19-86

12: 1

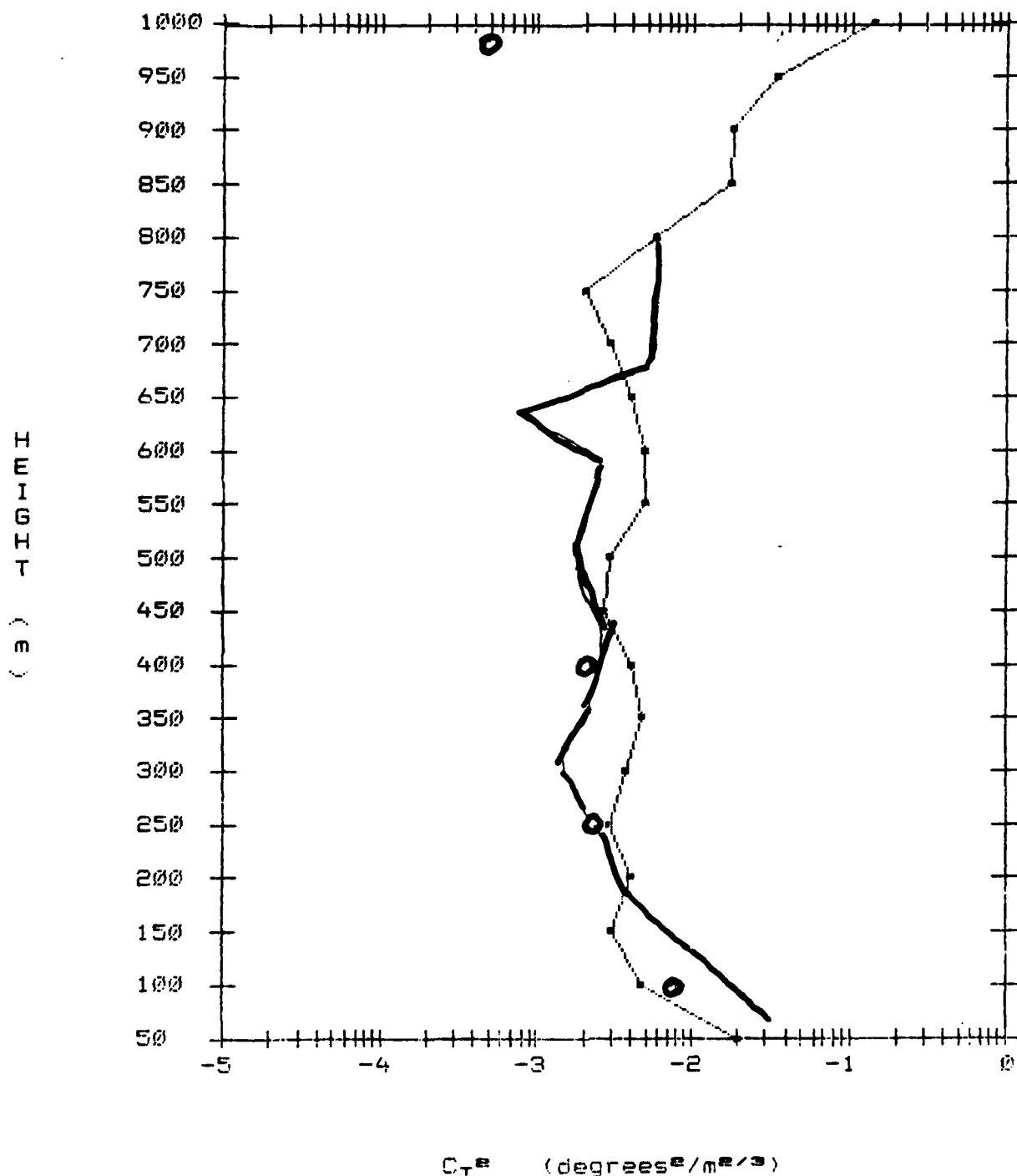


Fig. 4c Profiles of  $C_T^2$  from 4-19, 12:01 EST during EWAK. The solid line denotes a half hour average of sodar data, the circles denote 2-minute level aircraft values.

EWAK UNCORRECTED SODAR PROFILE  
OF  
TEMPERATURE STRUCTURE PARAMETER

5- 4-86

1:26

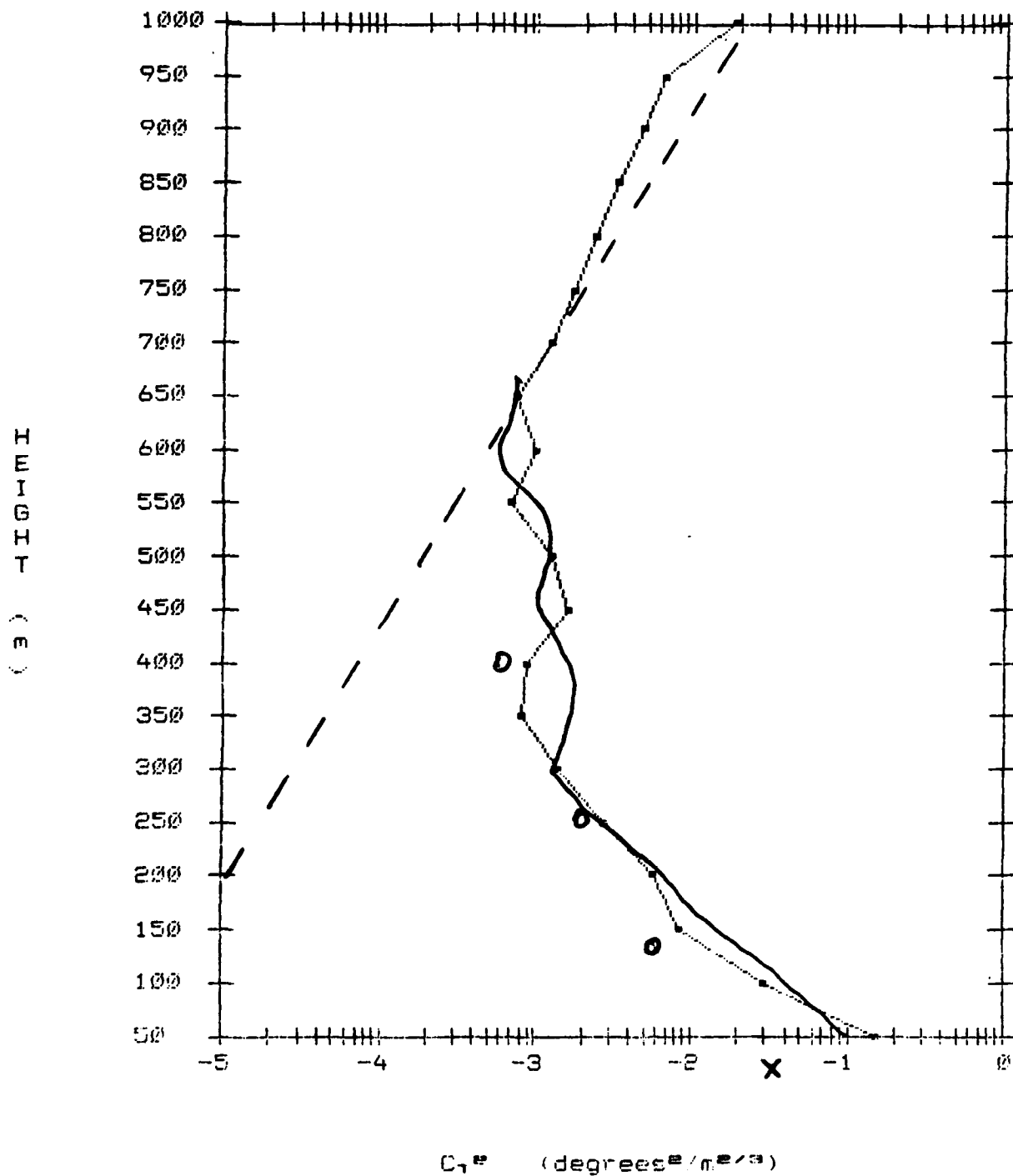


Fig. 4d Profiles of  $C_T^2$  from 5-04, 1:26 EST during EWAK. The solid line denotes a half hour average of sodar data, the circles denote 2-minute level aircraft values.

# EWAK CT<sup>2</sup> DATA COMPARISON

AUGUST 1, 1987 (17:50)

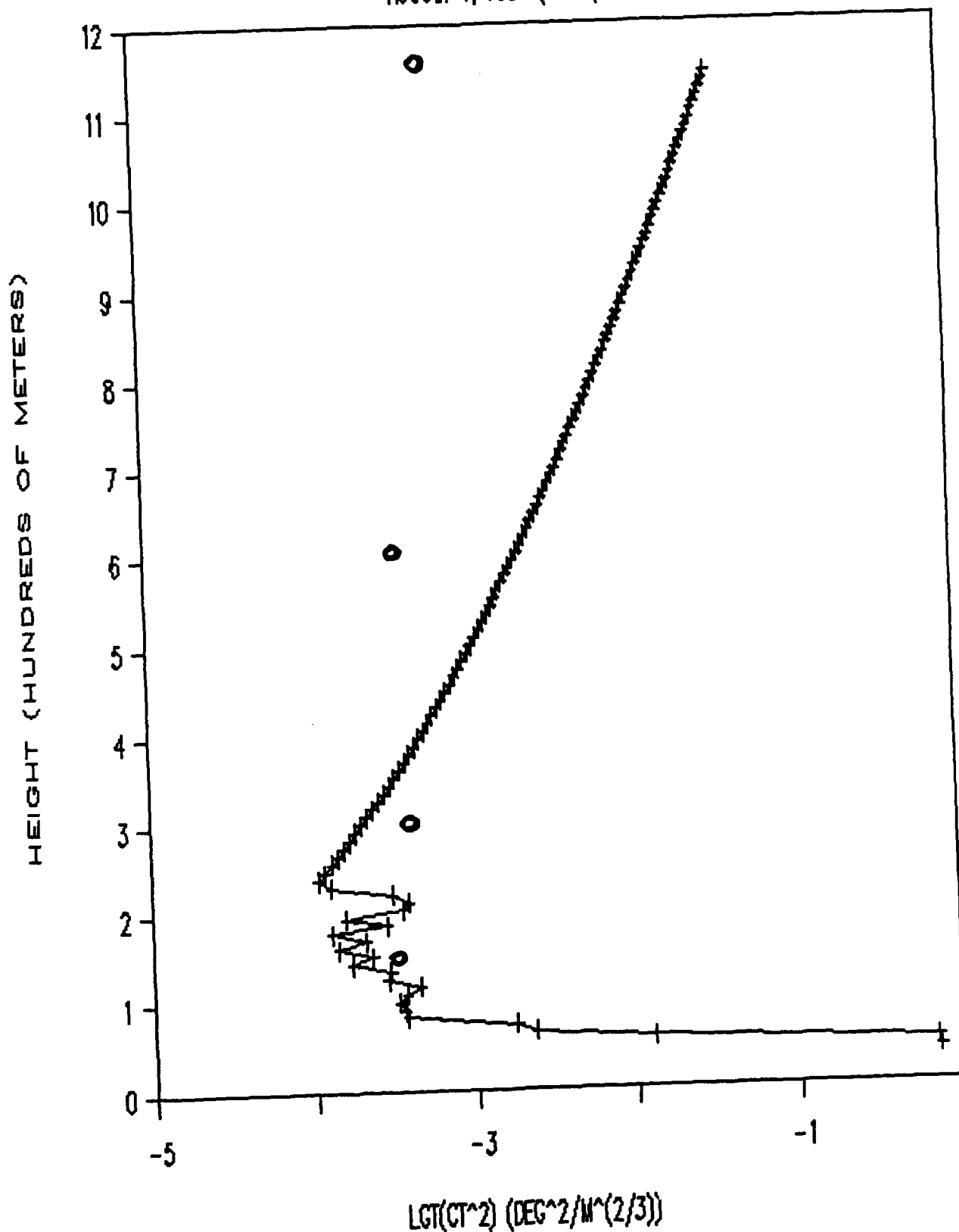


Fig. 5a Profiles of  $C_T^2$  from 8-01, 17:50 EDT one year after EWAK. The solid line denotes a 20 minute median of sodar data, the circles denote 2-minute level aircraft values.



# EWAK CT<sup>2</sup> DATA COMPARISON

AUGUST 6, 1987 (18:45)

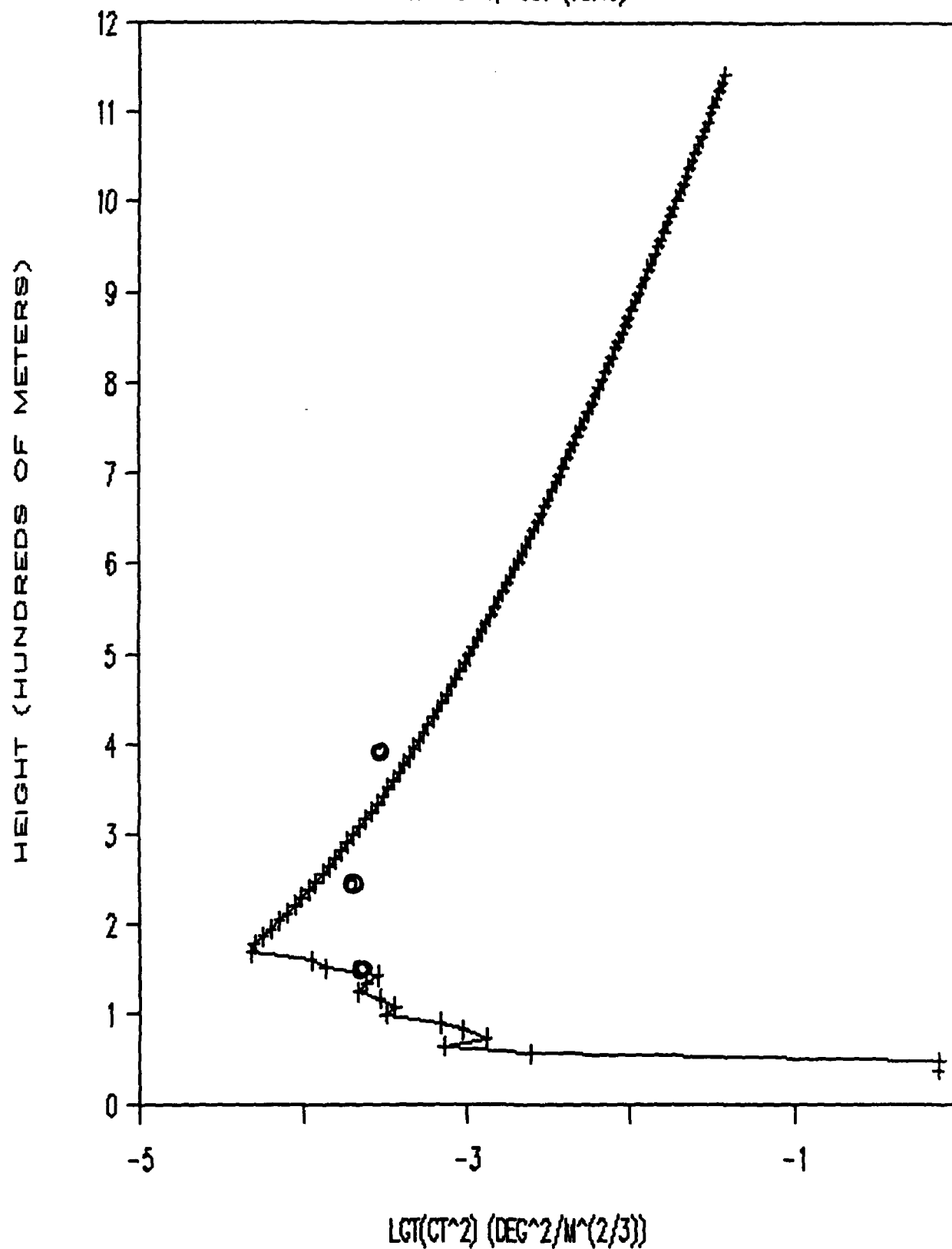


Fig. 5b Profiles of  $C_T^2$  from 8-06, 18:45 EDT one year after EWAK. The solid line denotes a 20 minute median of sodar data, the circles denote 2-minute level aircraft values.

# EWAK CT<sup>2</sup> DATA COMPARISON

AUGUST 11, 1987 (18:00)

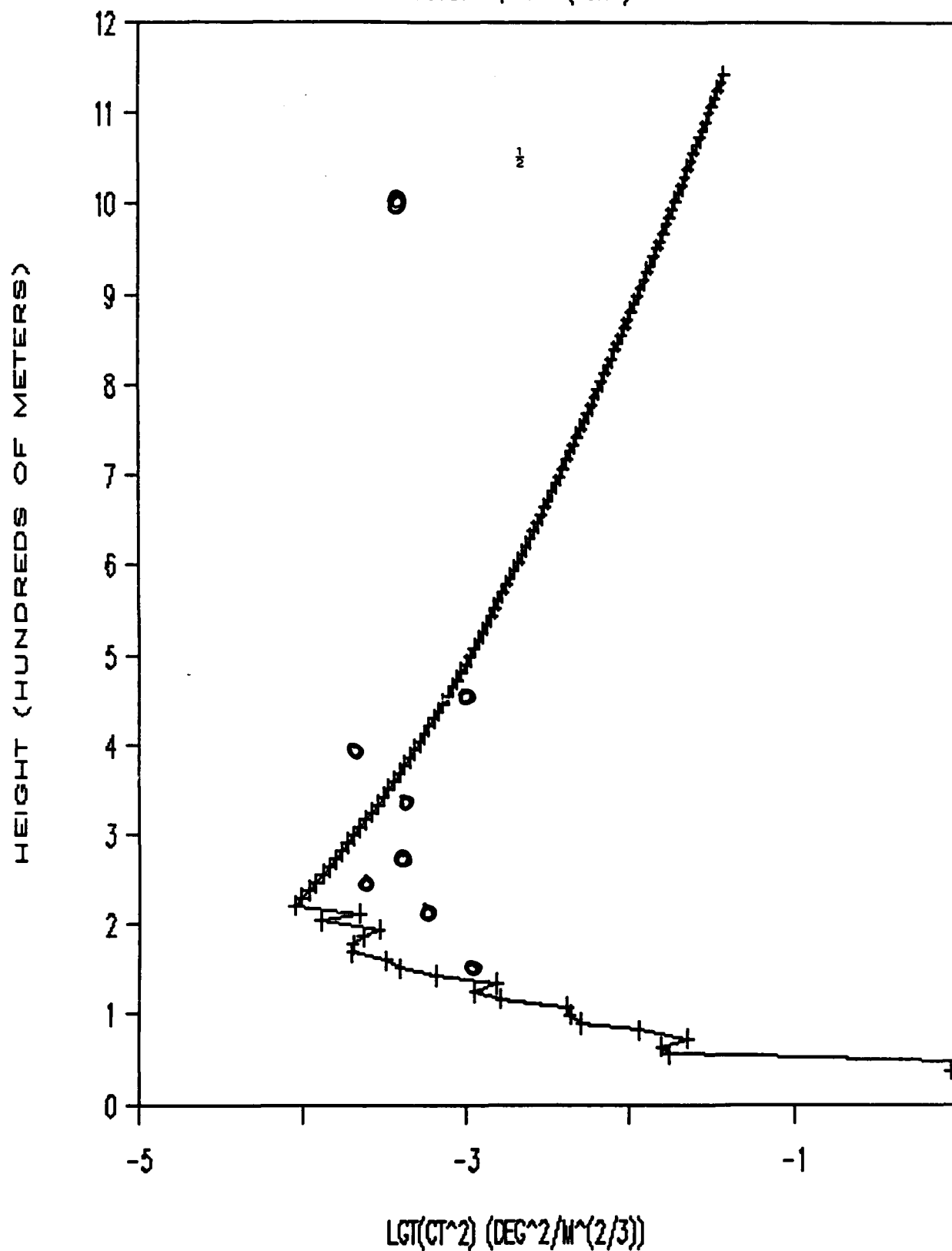


Fig. 5c Profiles of  $C_T^2$  from 8-11, 18:00 EDT one year after EWAK. The solid line denotes a 20 minute median of sodar data, the circles denote 2-minute level aircraft values.

# EWAK CT<sup>2</sup> DATA COMPARISON

AUGUST 12, 1987 (12:15)

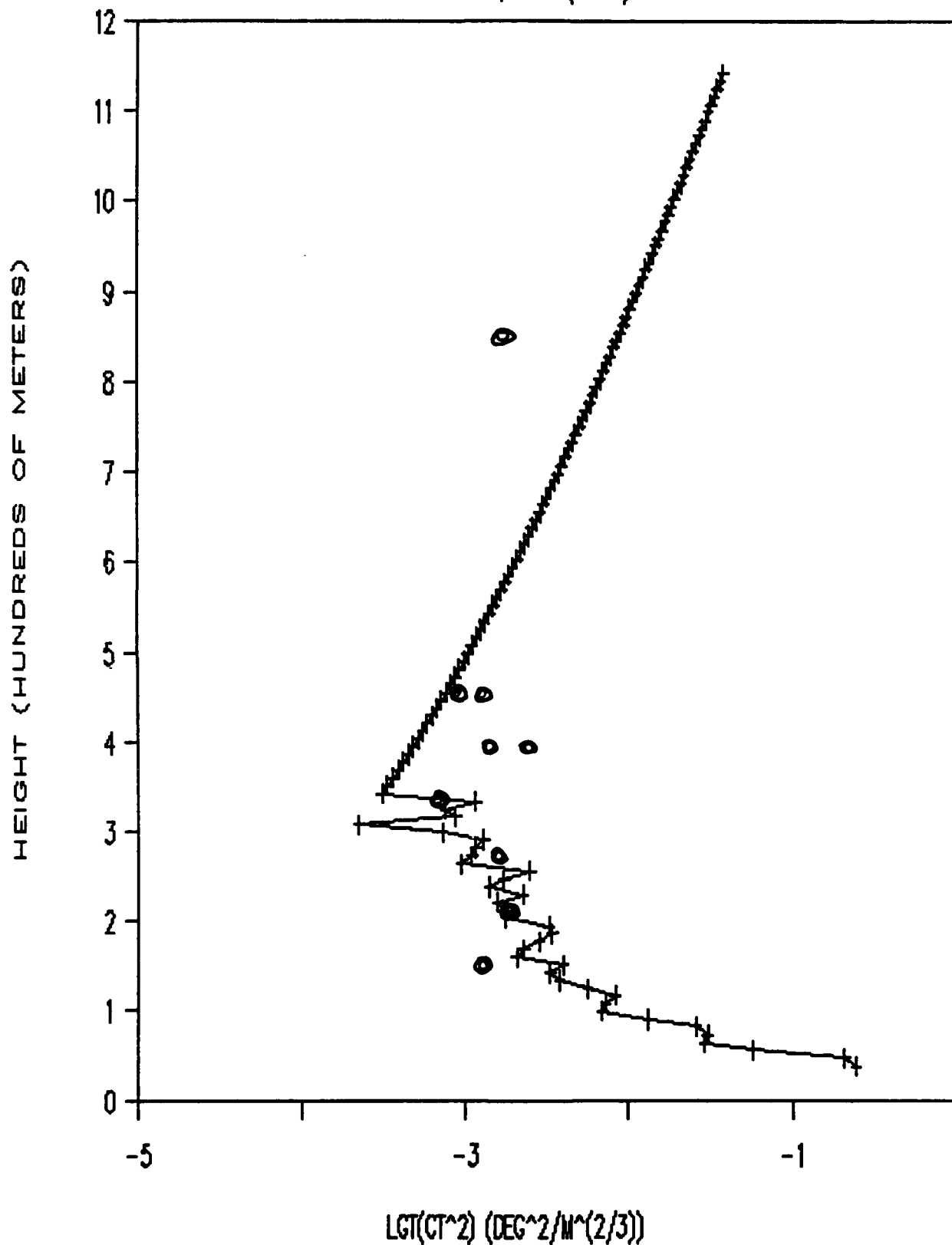


Fig. 5d Profiles of  $C_T^2$  from 8-12, 12:15 EDT one year after EWAK. The solid line denotes a 20 minute median of sodar data, the circles denote 2-minute level aircraft values.

# EWAK CT<sup>2</sup> DATA COMPARISON

AUGUST 12, 1987 (14:28)

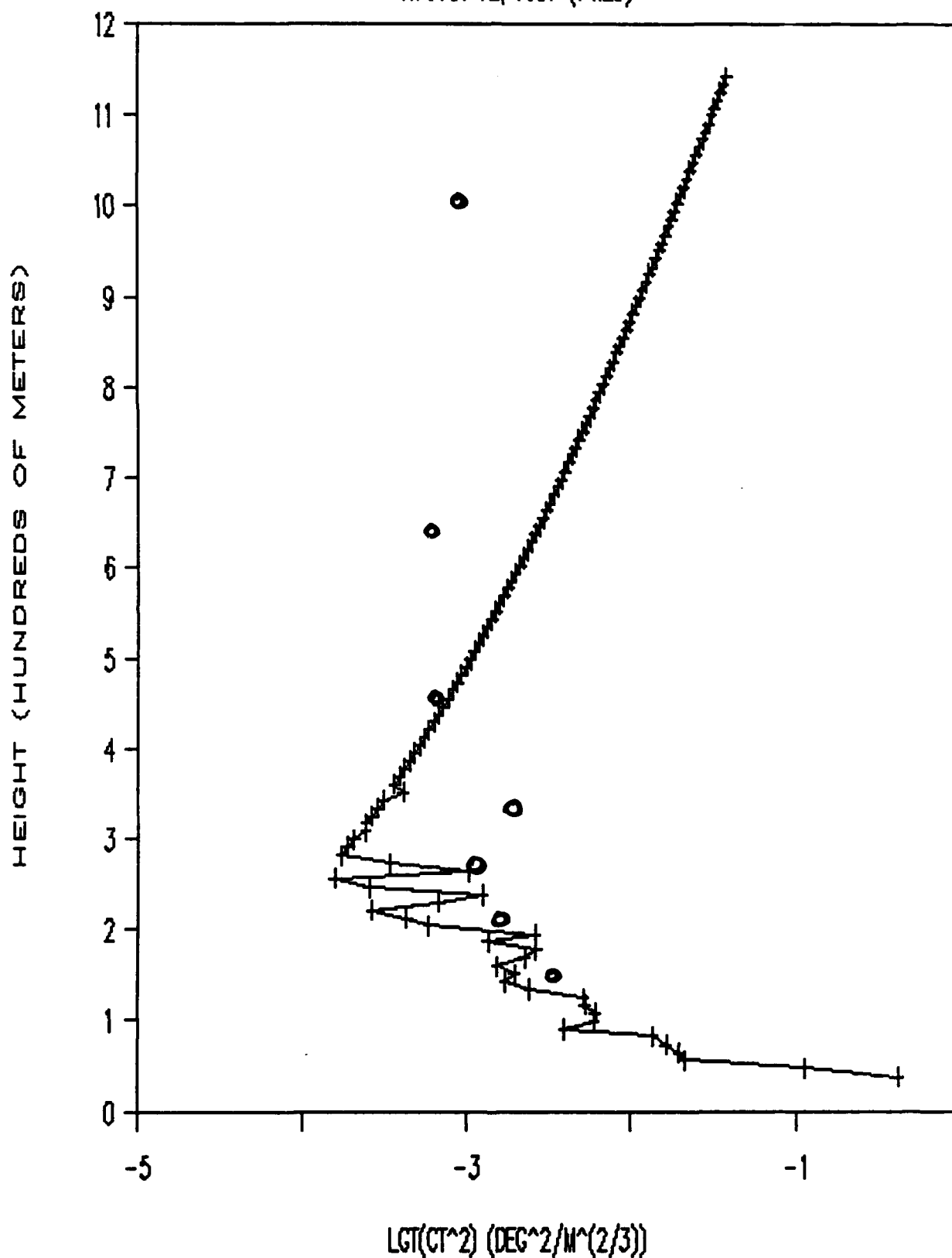


Fig. 5e Profiles of  $C_T^2$  from 8-12, 14:28 EDT one year after EWAK. The solid line denotes a 20 minute median of sodar data, the circles denote 2-minute level aircraft values.

function of altitude. For example, at  $z=1$  km a  $C_n^2$  of  $2 \times 10^{-14}$  (i.e.,  $C_T^2 = 2 \times 10^{-2}$ ) would be just detectable above the noise while at 200 m a value of  $1 \times 10^{-16}$  is detectable. Of course, this height dependence of the detectability is a result of the  $1/r^2$  dependence of the strength of the returned signal.

### 3.5 Other sodar data

In July of 1987 we operated one of our Xondar sodars on San Nicolas Island, located about 60 miles west of Los Angeles. This operation was part of a large field program to study marine stratocumulus clouds. Since the Eastern Pacific is characterized by strong subsidence and weak convection, the boundary layer heights are typically lower than those at inland locations; between 200 and 1000 m. This is well within the range of the sodar. The sodar was operated for three weeks and winds were obtained from 100 m up to the top of the boundary layer continuously during the entire period. Thus, winds and  $C_T^2$  profiles were routinely obtained to heights of 600 and 700 m.

Two sample profiles are shown (Figs. 6a-6b). Fig. 6a shows a case (July 8 about midnight) where the inversion is at an altitude of 400 m. Again, the first 100 m of the profiles are almost certainly not usable. The inversion is clearly visible as a two order of magnitude increase in  $C_T^2$  in less than 100 m. Above the inversion, the  $C_T^2$  decreases rapidly down to the noise level. Note that the noise curve is virtually identical to that obtained in 1987 at Rock Springs. This probably indicates that the source of the noise is internal to the sodar. Much later in the day on July 8 (Fig. 6b) the inversion had moved up to 650 m. Notice that now the noise level above the inversion is not a nice smooth line. This implies that in this case the noise

level was due to external sources associated with the daytime activity at the site (the system was being operated in a Western Sea Gull rookery which, combined with sea lions and surf produced a continuous shoreline cacaphony).

# FIRE/SNI SODAR CT^2

JULY 8, 1987 (00:50)

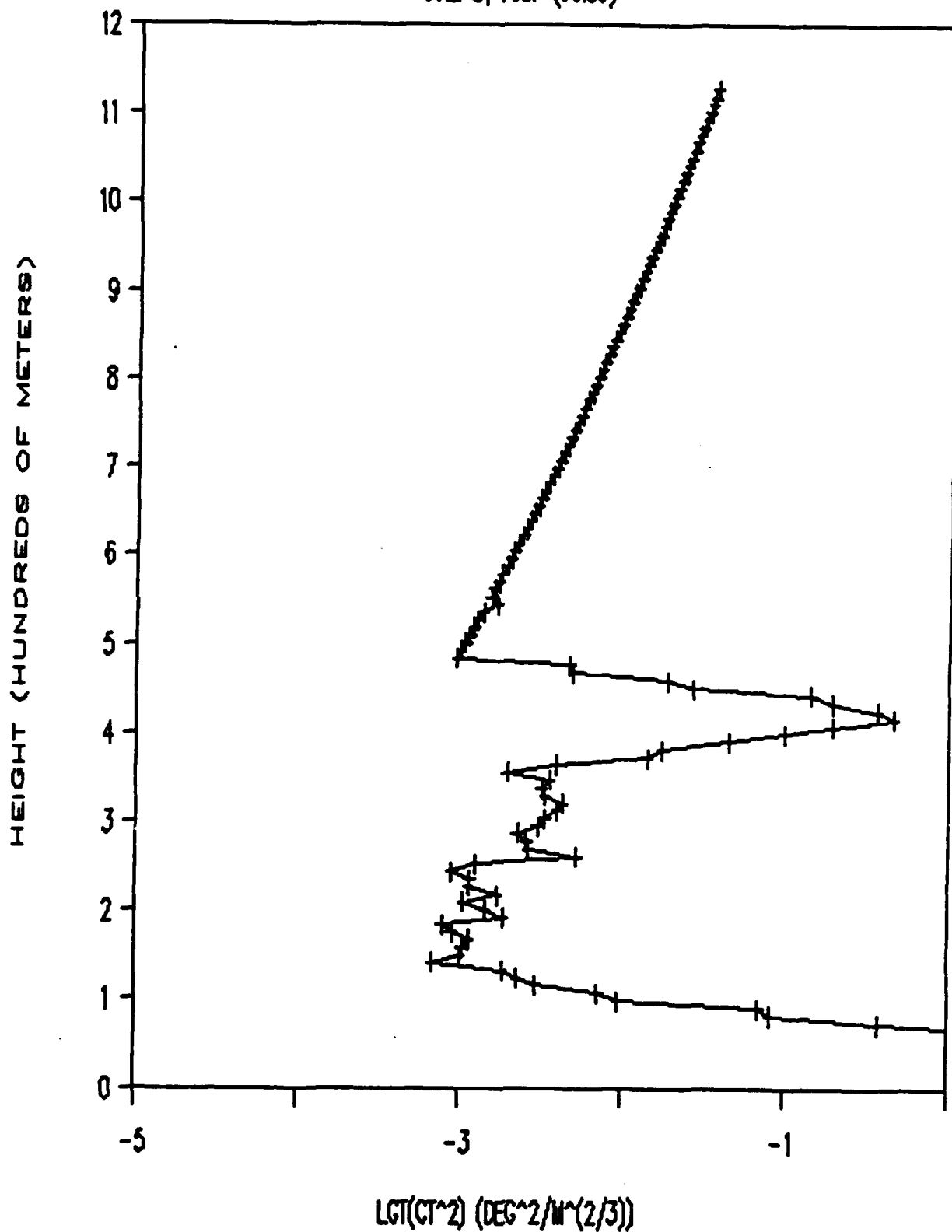


Fig. 6a Profiles of  $C_T^2$  from 8-08, 00:50 GMT from San Nicolas Island. The solid line denotes a 20 minute median of sodar data. The capping inversion is visible as the maximum at 400 m.

# FIRE/SNI SODAR CT<sup>2</sup>

JULY 8, 1987 (10:59)

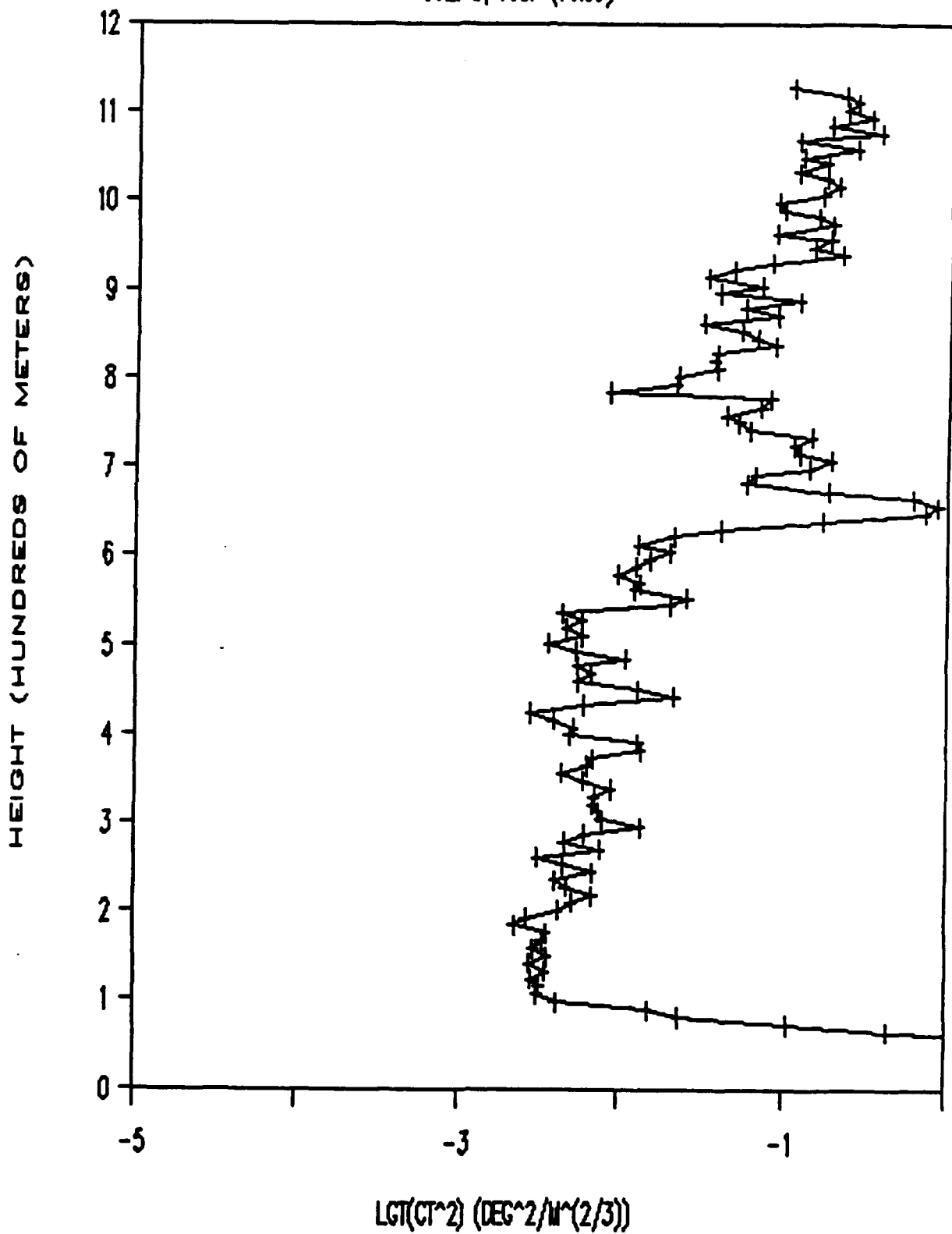


Fig. 6b Profiles of  $C_T^2$  from 8-08, 10:59 GMT from San Nicolas Island. The solid line denotes a 20 minute median of sodar data. The capping inversion is visible as the maximum at 630 m.



#### 4. Conclusions

As we discussed in the introduction, the majority of the work performed on this project has been described in a technical report (Fairall et al., 1988; Appendix B) and an MS thesis (Beecher, 1987; Appendix C). The main body of the present report is intended to deal with the subject of the sodar performance. However, before moving on to that subject, we will state a few conclusions that summarize the results of Appendices B and C.

\* In Fig. 4 in Appendix B a comparison of  $C_n^2$  profiles from five different methods (scintillometer, thermosonde, radar, aircraft, and model) is shown for two cases. The rms disagreement at any altitude is on the order of a factor of three. This is quite large and is still basically unexplained, although it may be primarily due to sampling variability.

\* For the few cases examined (section 7.4 in Appendix C), the boundary layer contribution to  $\theta_0$  was only about 1% but the contribution to  $r_0$  was about 10 to 30 %. These were nighttime cases. The contribution is expected to be higher during the day.

\* The variability of  $C_n^2$  is indicated in the difference between up and down aircraft profiles, level aircraft data (Appendix A), and the temporal variability at fixed location (e.g., from the radar). Order of magnitude variations are observed on one hour time scales with a vertical resolution of 300 to 1000 m. Similar variability is observed for spatial scales on the order of 30 km, but surprisingly it doesn't increase much for much longer scales.

\* The van Zandt (1981) model was found to agree on average with the aircraft data, but with considerable rms disagreement. The thermosonde and scintillometer were about a factor of 2 or 3 lower. An analysis of the ratio of  $C_T^2/C_u^2$  showed that the assumption of constant mixing efficiency

(see Appendix B) may not be valid for weak turbulence. Thus the model will tend to underestimate  $C_n^2$  when it is small.

\* Attempts to use mean meteorological profiles (wind speed and temperature) to compute Richardson numbers in order to predict layers of severe CAT were not successful. A much higher correlation was obtained simply by using the wind shear alone. It is not clear if this implies something significant about the dynamics or if it is simply the result of low quality data or inadequate sampling by rawinsondes. In other words, rawinsonde data do not seem to be adequate to use for computing Richardson number.

Regarding the accuracy of the aircraft  $C_n^2$  measurements, some progress was made. Clearly the basic sensors and bridges used by PSU and AFGL are in close agreement (Fig. 1) when run side by side near the ground. Comparison of aircraft measurements with a small tower in New Mexico also indicated reasonable agreement (Fig. 3). But, since both of these comparisons are for very strong turbulence (compared to the free troposphere), they cannot be considered as definitive verification for high altitude performance.

The evaluation of the sodar turned out to be much more complicated than expected. On balance, we would have to say that it is inconclusive. The comparisons with the aircraft look fairly good but there are some inconsistencies that we cannot explain. Only recently did we find out that the power given in the wind table and the power available at the sounder output do not have the same gains. This was established by comparing the dB given simultaneously from each source. Thus it is difficult to explain the apparent good agreement obtained during EWAK (with the wind table) and the 1987 period (using the sounder output). Furthermore,  $C_T^2$  values computed from the sounder output from the San Nicolas Island measurements are very high (as large as  $3 \times 10^{-1}$ ) at the inversion. While we don't have independent measurements available to us at this time, such values are at about an order

of magnitude greater than those predicted by models. Finally, the behavior of the noise background of the sodar suggests that its sensitivity has not been optimally utilized. Apparently some internal electronic noise (such as the A/D converter) is limiting the performance rather than the environmental acoustic noise. Since the doppler system uses spectral processing, apparently much more sensitive intensity information is potentially available. This is obvious since we often obtain winds when the backscatter intensity indicates nothing but the background noise. In conclusion there is both substantial room for improvement in the hardware and much more work will be required to establish methods for calibrating these systems.

## References

- Beecher, E.A., 1987: Analysis of temperature and velocity microturbulence parameters from aircraft data and relation to atmospheric refraction index structure. M.S. thesis, Pennsylvania State University, ppl65.
- Fairall, C.W. and R. Markson, 1984: Aircraft measurements of temperature and velocity microturbulence in the stably stratified free troposphere. Proc. Seventh Symposium on Turbulence and Diffusion, AMS, Boulder, CO.
- Fairall, C.W., 1987: A top-down and bottom-up diffusion model of  $C_T^2$  and  $C_q^2$  in the entraining convective boundary layer. J. Atmos. Sci., 44, 1009-1017.
- Fairall, C.W., D.W. Thomson, and R. Markson, 1988: An aircraft and radar study of temperature and velocity microturbulence in the stably stratified free troposphere. Proc. Eighth Symposium on Turbulence and Diffusion, AMS, San Diego, CA, 61-65.
- Fairall, C.W., D.W. Thomson, and W.J. Syrett, 1988: Long term studies of the refractive index structure parameter in the troposphere and stratosphere. Technical Report, Pennsylvania State University, University Park, PA, pp67.
- Hall, F.F. Jr., and J.W. Wescott, 1974: Acoustic antennas fro atmospheric echo sounding. J. Acoust. Soc. Am., 56, 1376-1382.
- Neff, W.D., 1975: Quantitative evaluation of acoustic echoes from the planetary boundary layer. Technical Report NOAA TR ERL 322-WPL 38, Wave Propagation Laboratory, Boulder, CO, pp 34.
- Panofsky, H.A. and J.A. Dutton, 1984: Atmospheric Turbulence. Wiley, New York, pp450.
- Thomson, D.W., R.L. Coulter, and Z. Warhaft, 1978: Simultaneous measurements

of turbulence in the lower atmosphere using sodar and aircraft. J. Appl. Meteor., 17, 723-734.

Van Zandt, T.W., K.S. Gage and J.M. Warnock, 1981: An improved model for the calculation of profiles of  $C_n^2$  and  $\epsilon$  in the free atmosphere from background profiles of wind, temperature and humidity. Proc. 20th Conf. on Radar Meteorology, AMS, Boston, MA.

Wesely, M.L., 1976: The combined effect of temperature and humidity fluctuations on refractive index. J. Appl. Meteor., 15, 43-49.

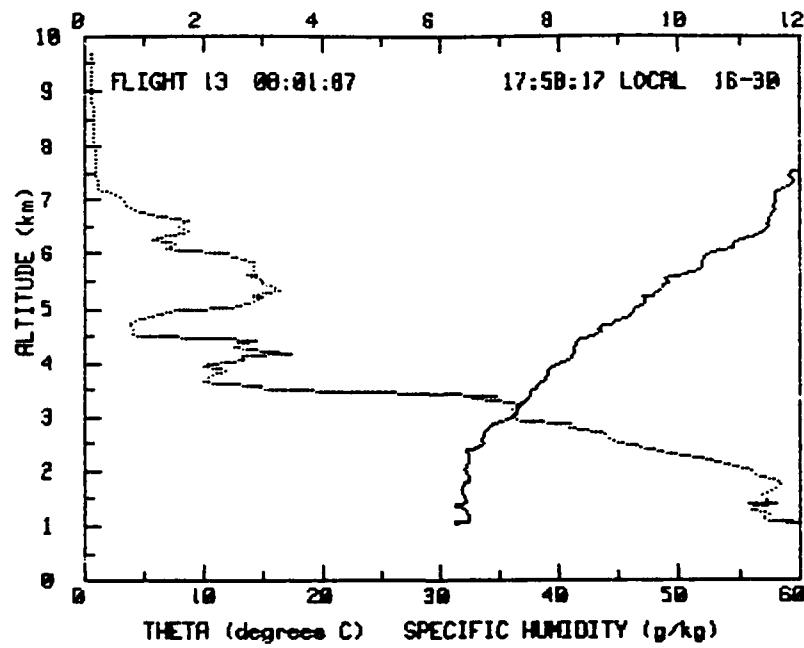
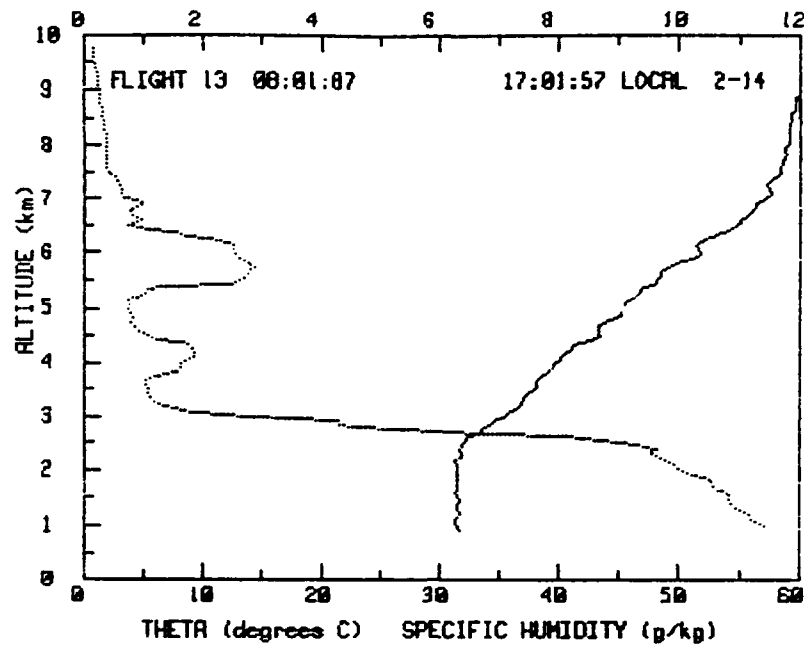
APPENDIX A

Profiles of mean meteorological variables ( $\theta$  and  $q$ ), profiles of turbulence parameters, and level flight turbulence parameters for flights 13 through 22.

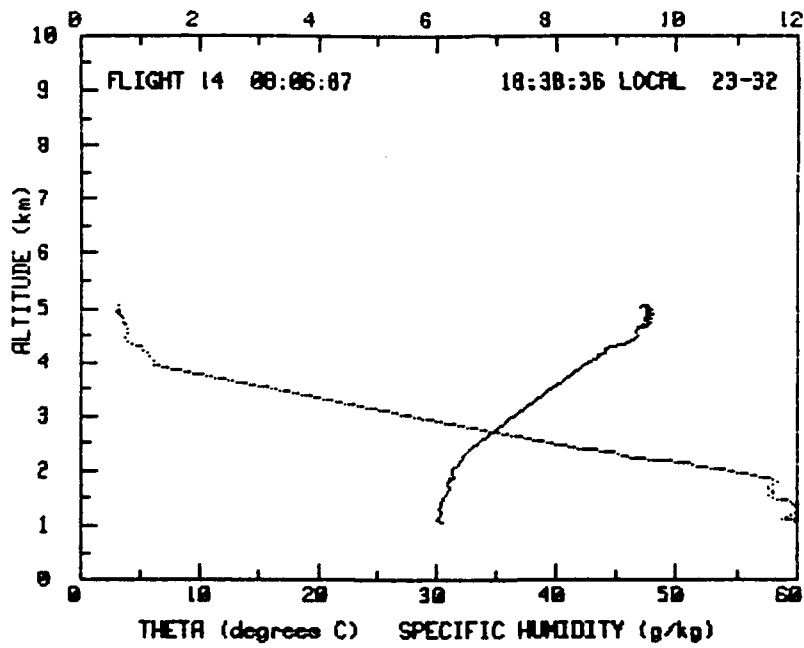
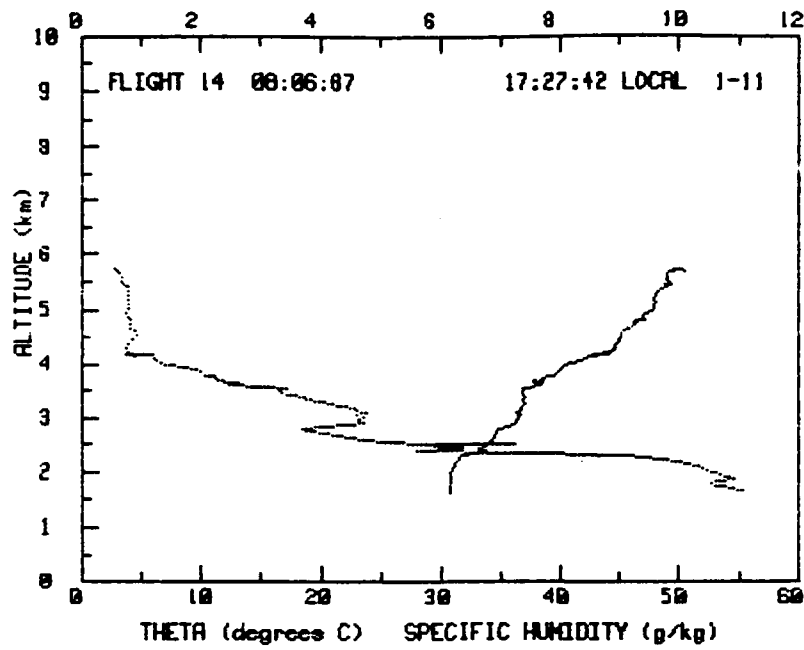
Part AI

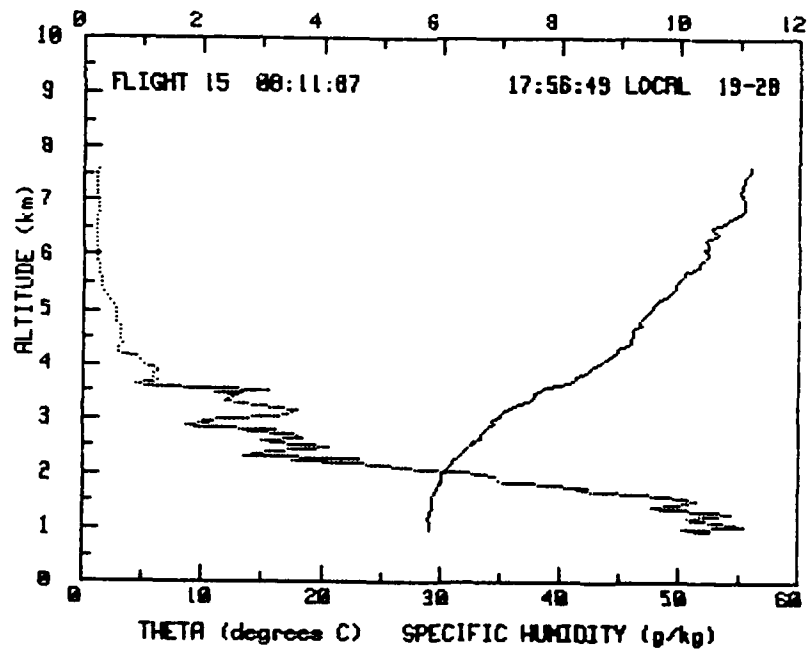
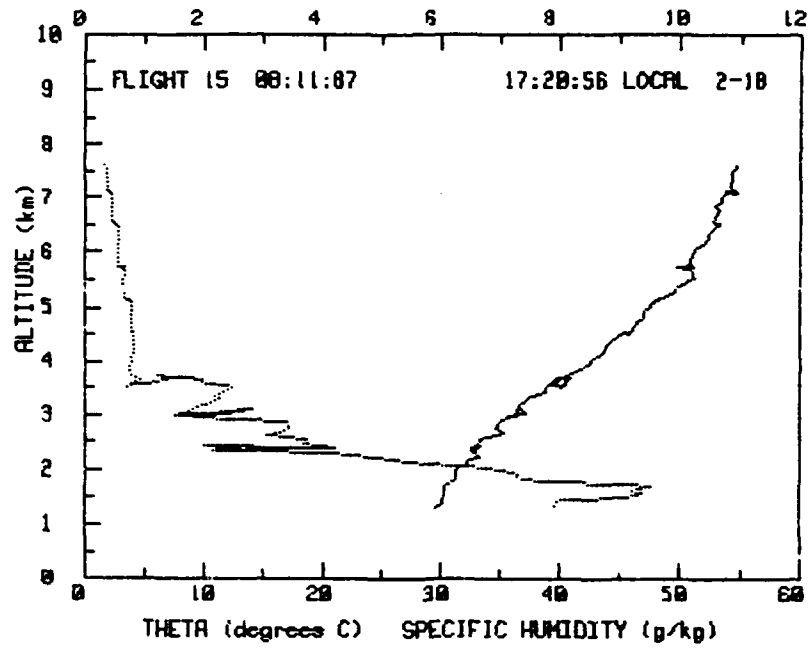
Mean Meteorological Profiles

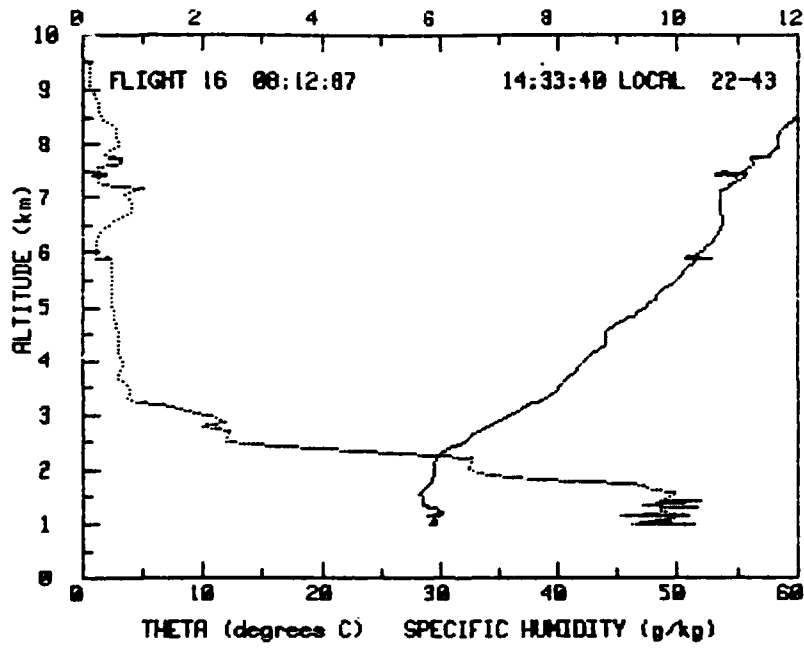
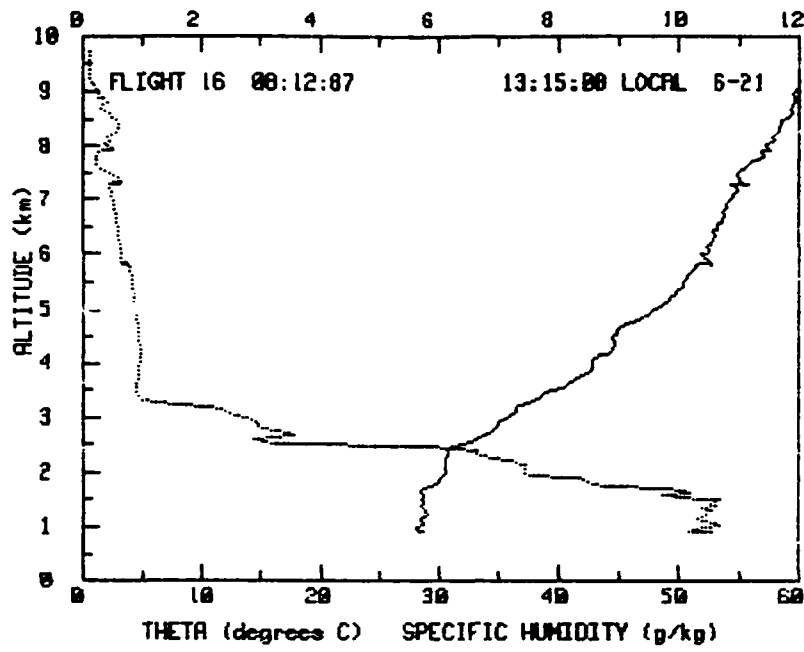
The series of graphs in this section depict the mean profiles of potential temperature ( $\theta$ ) and specific humidity ( $q$ ) on the days and times indicated on the graph.

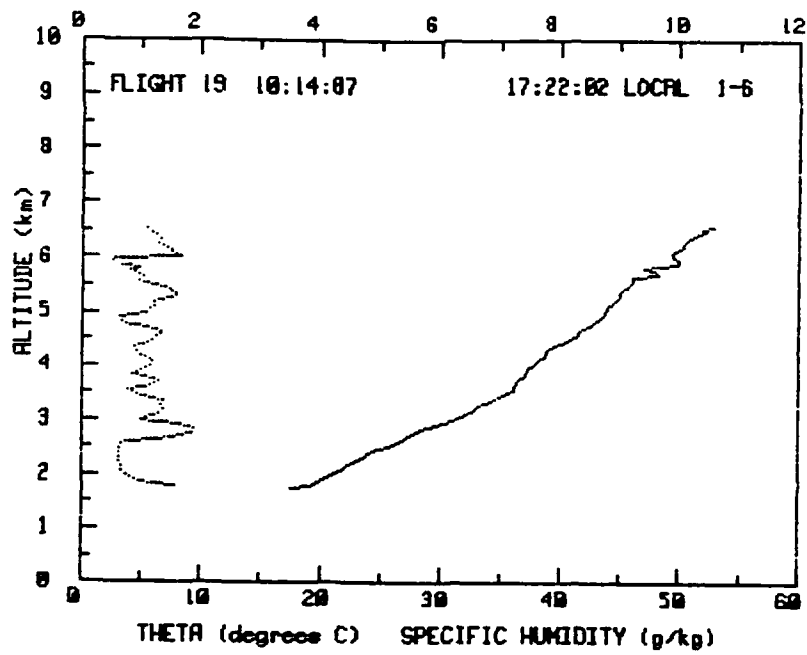
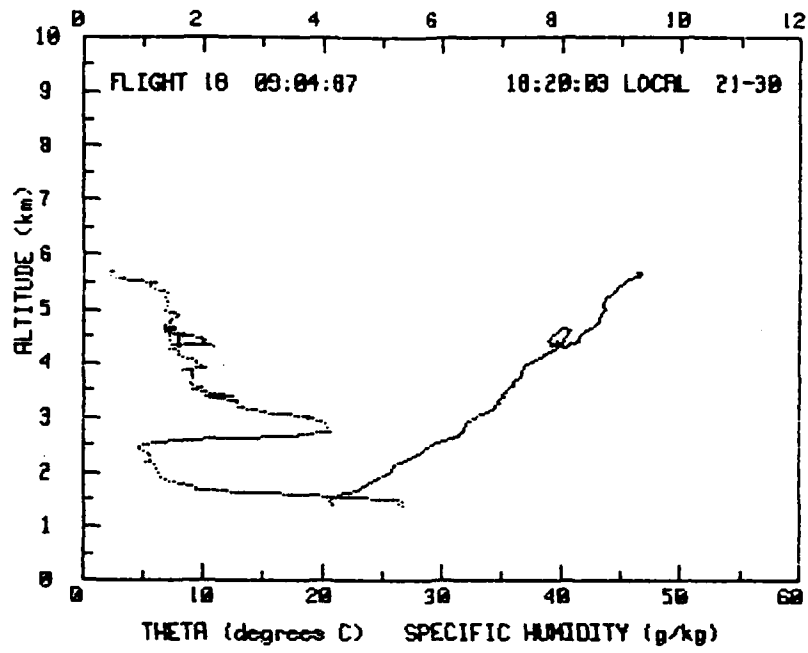


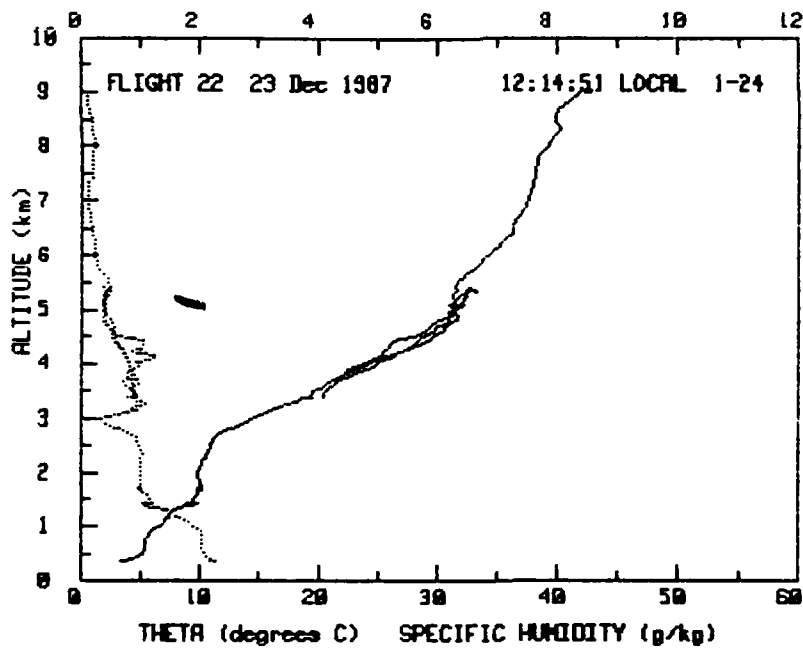
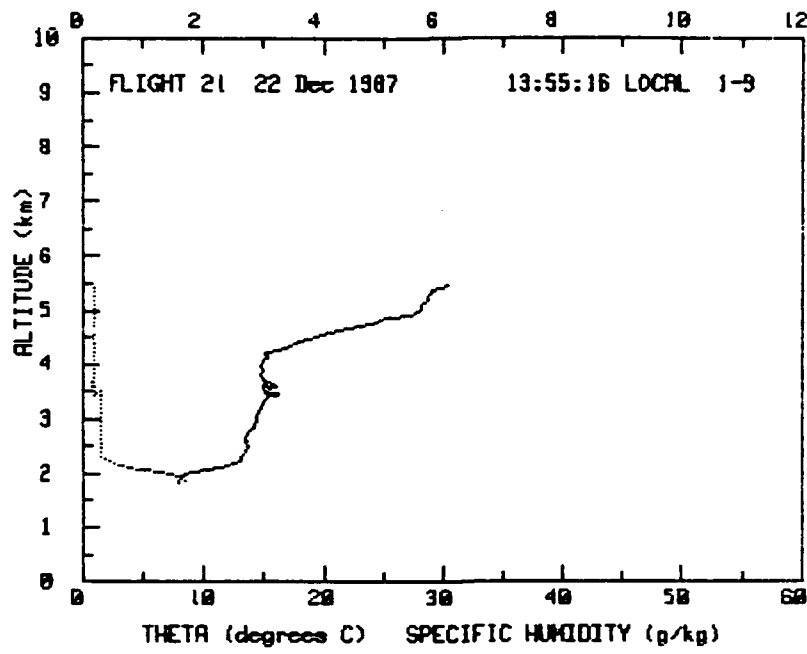








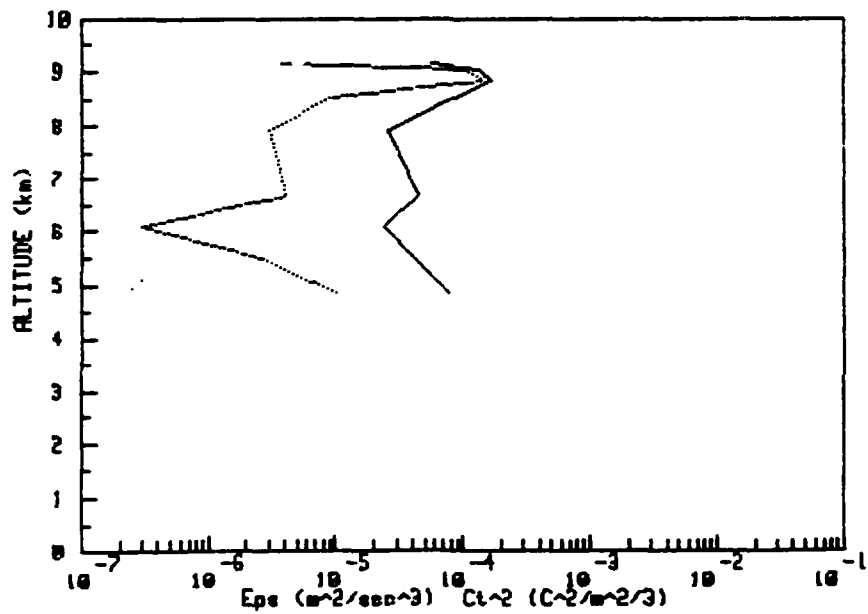
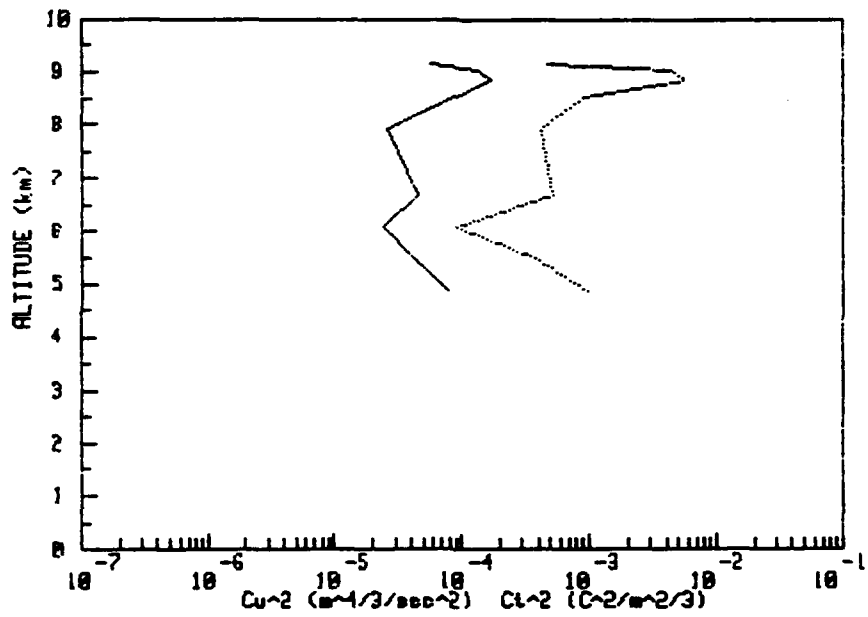
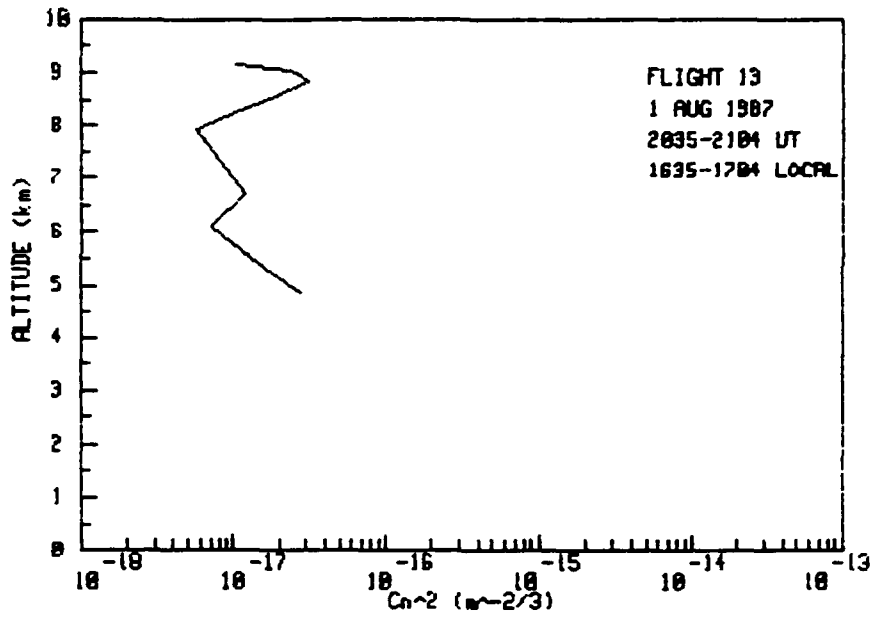


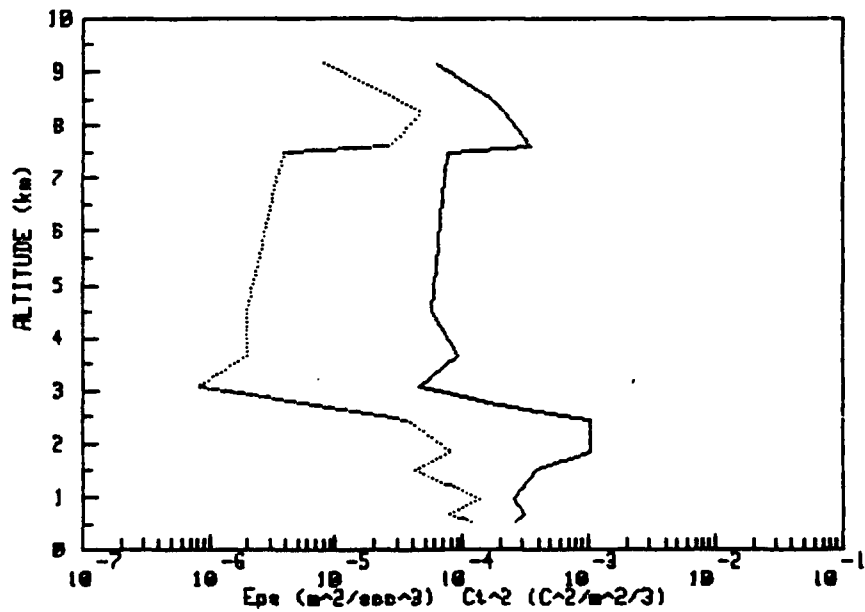
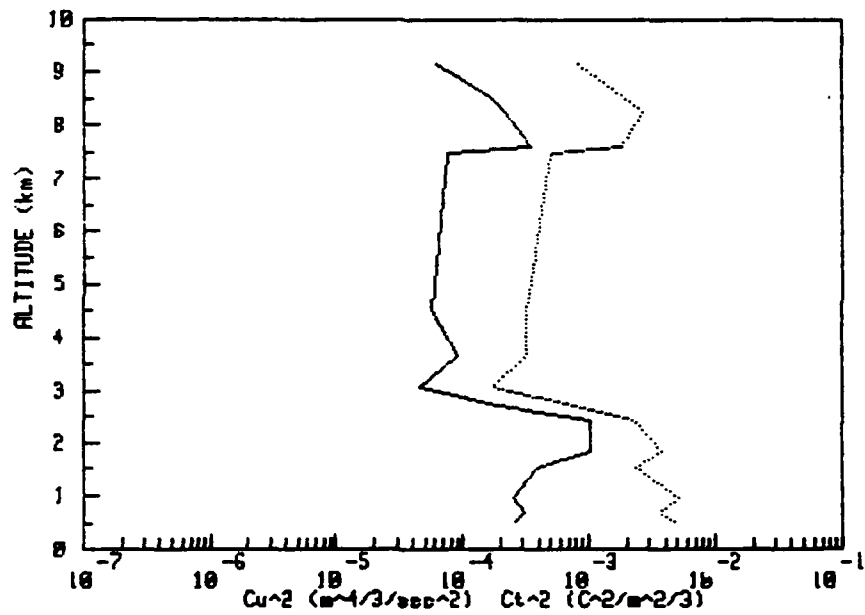
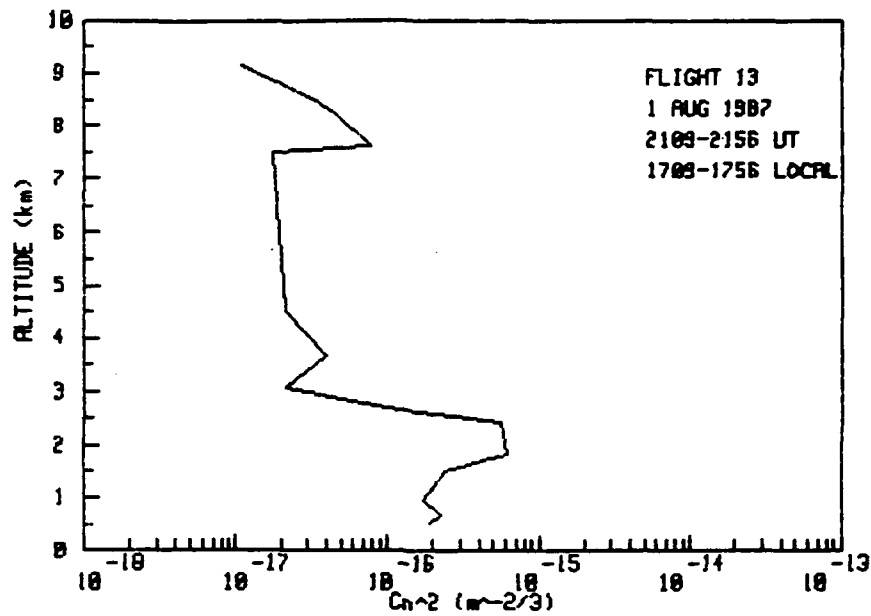


Part AII

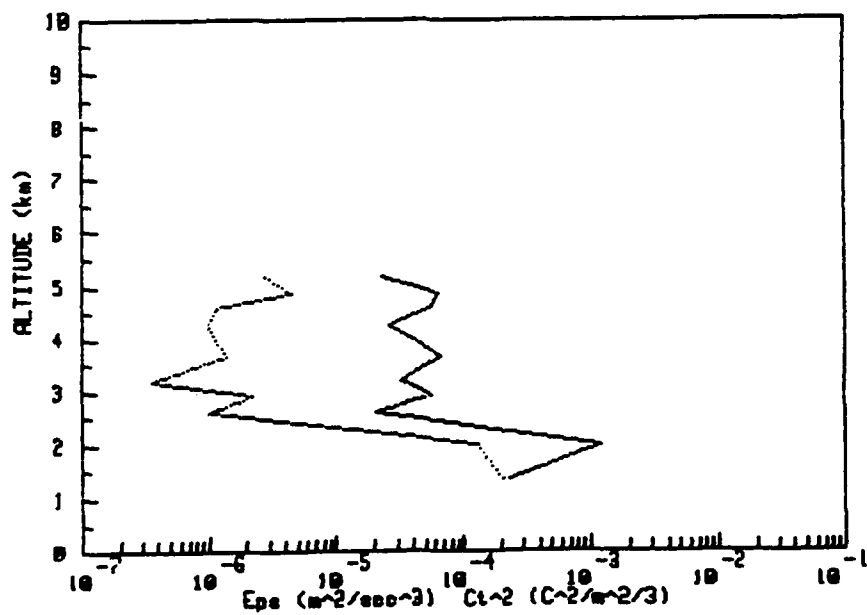
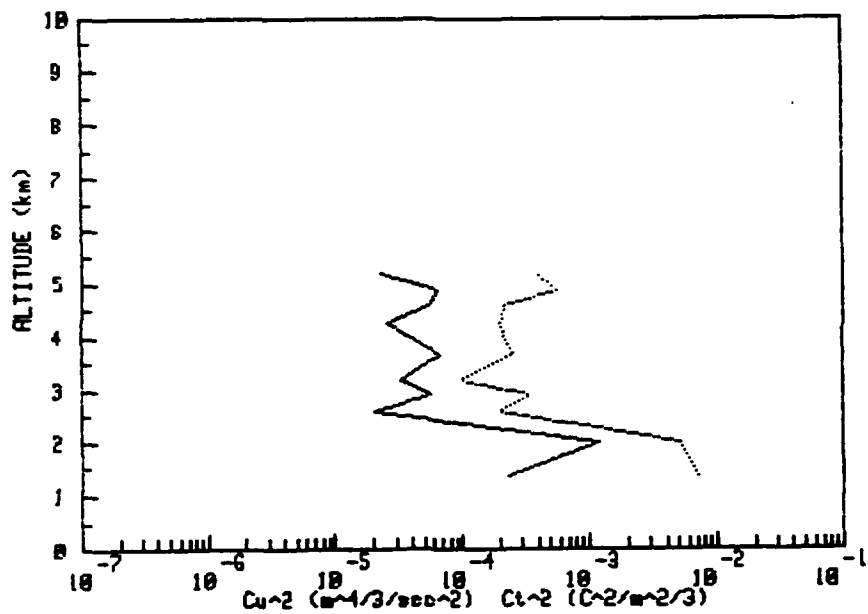
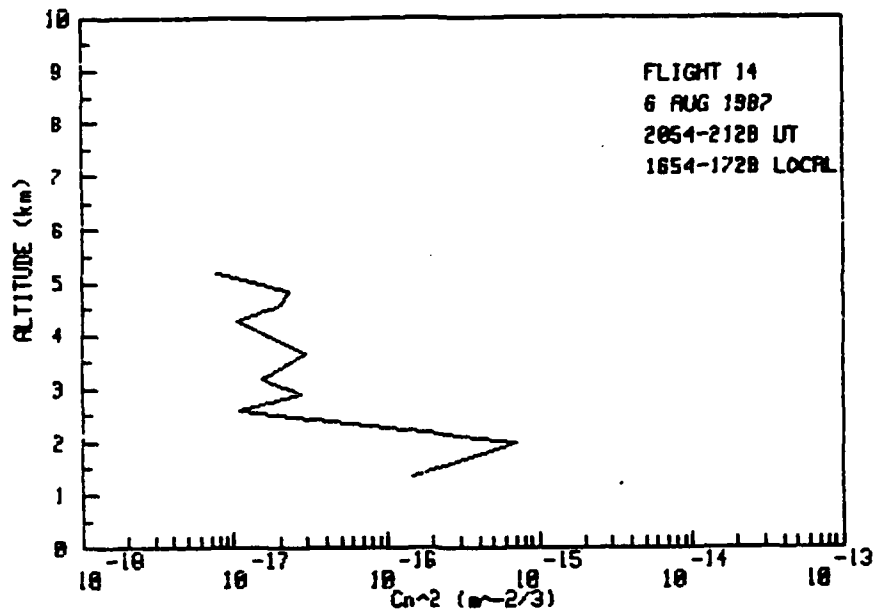
Turbulence Profiles

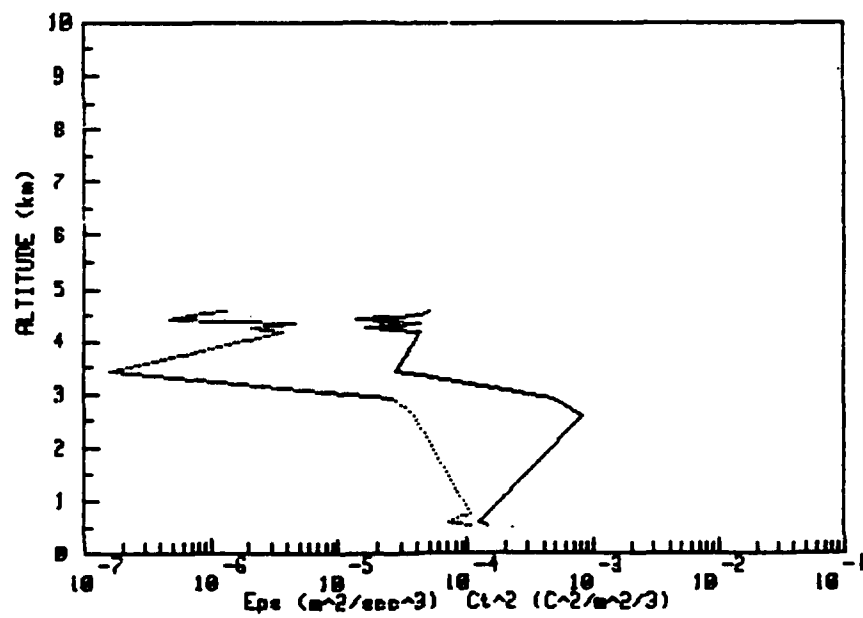
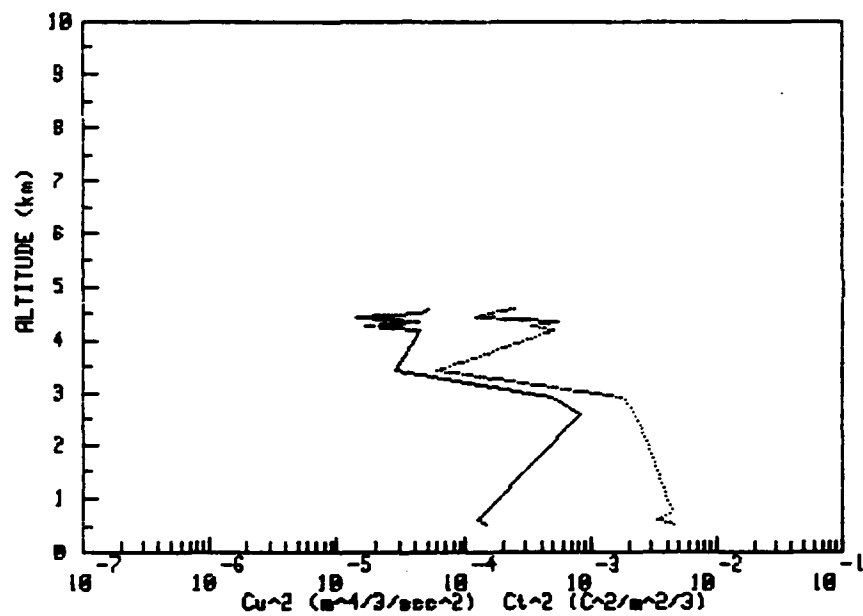
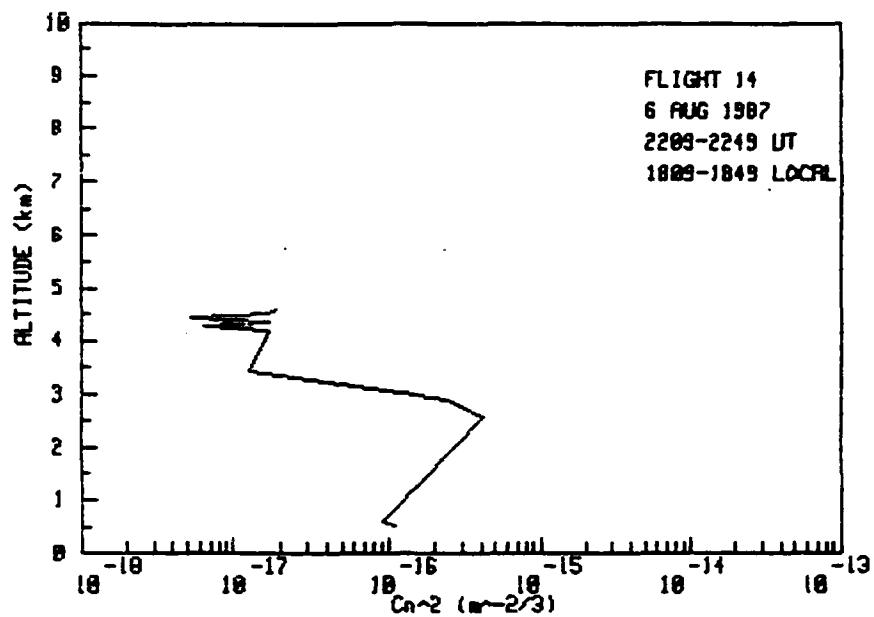
The series of graphs in this section depict the profiles of turbulence quantities. The upper panel is optical  $C_n^2$  computed from microthermal measurements of  $C_T^2$  assuming negligible water vapor contribution. The middle panel depicts the structure function parameters for velocity ( $C_u^2$ , dotted line) and temperature ( $C_T^2$ , solid line). The lower panel shows  $C_T^2$  and the rate of dissipation of turbulent kinetic energy,  $\epsilon$  (dotted line). The flight number, date and time are indicated on the graph.

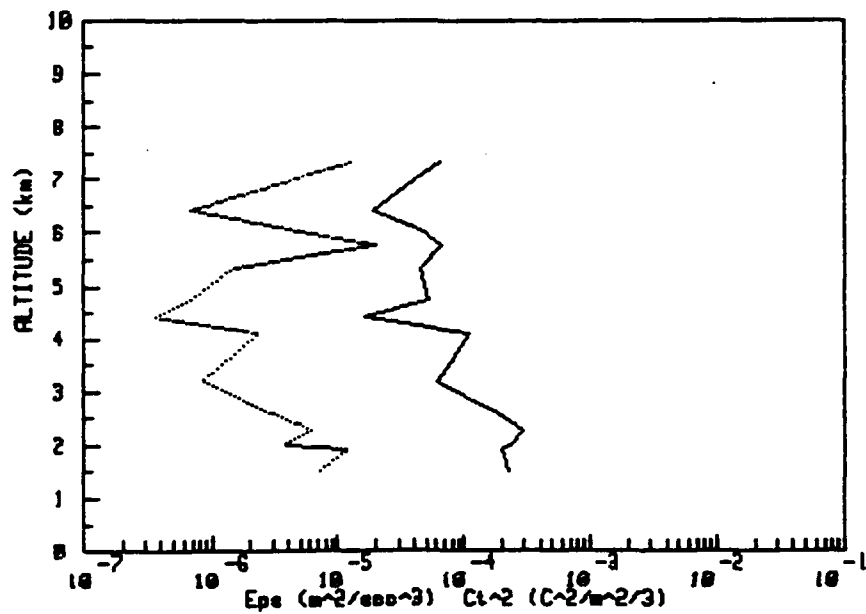
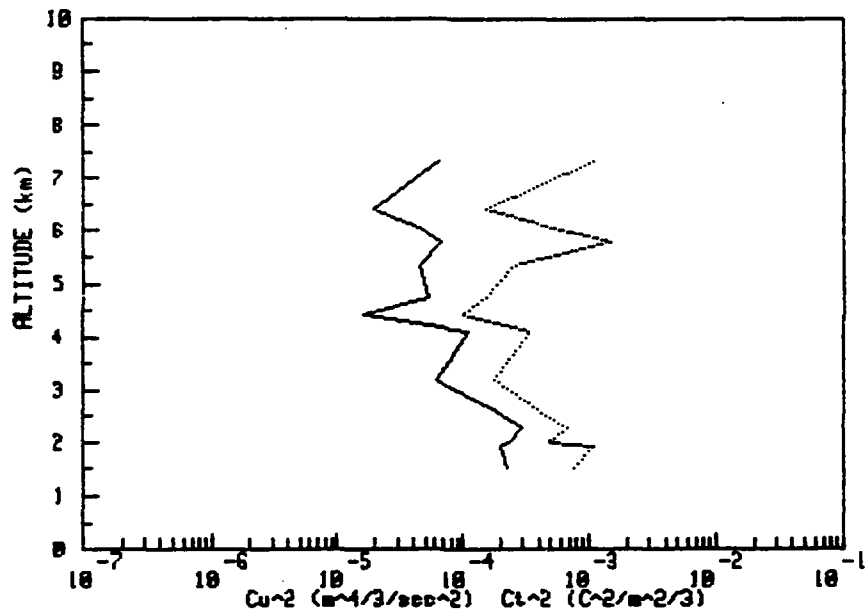
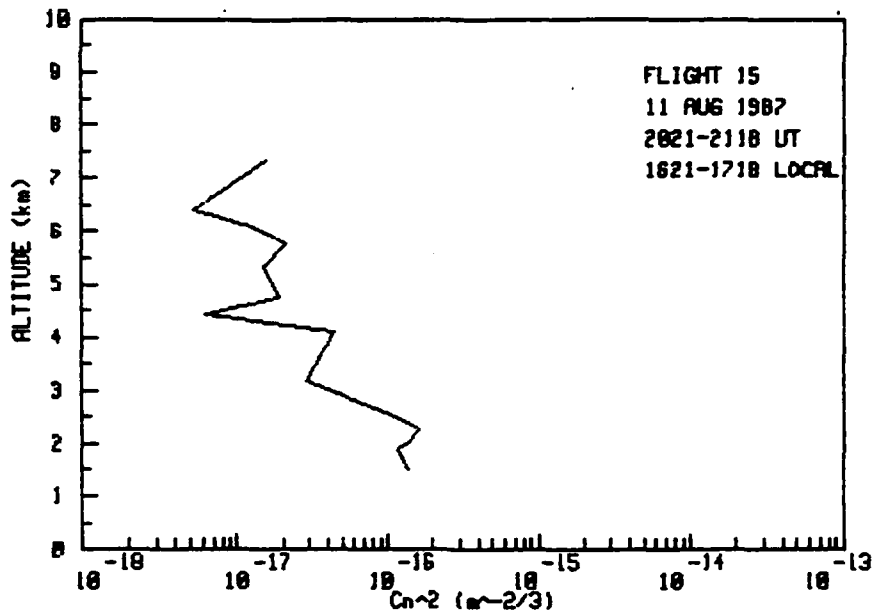


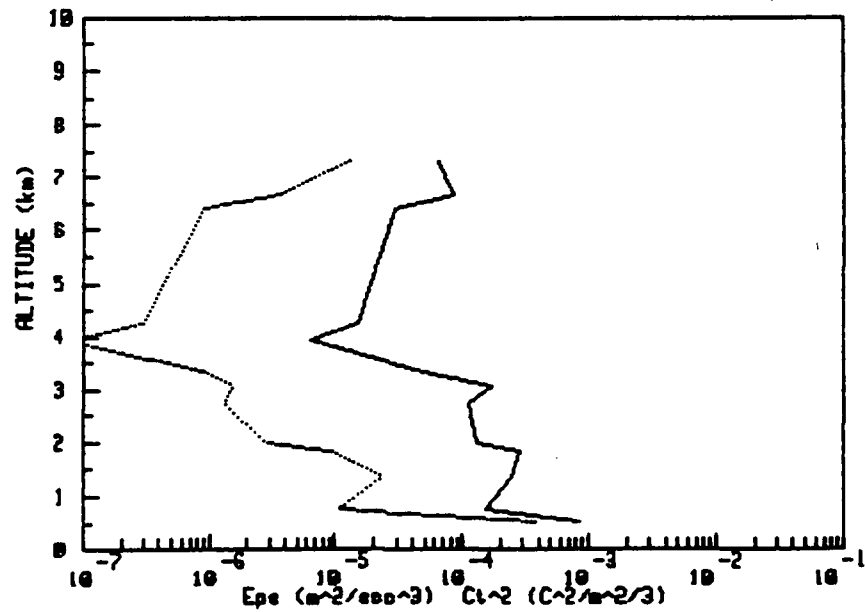
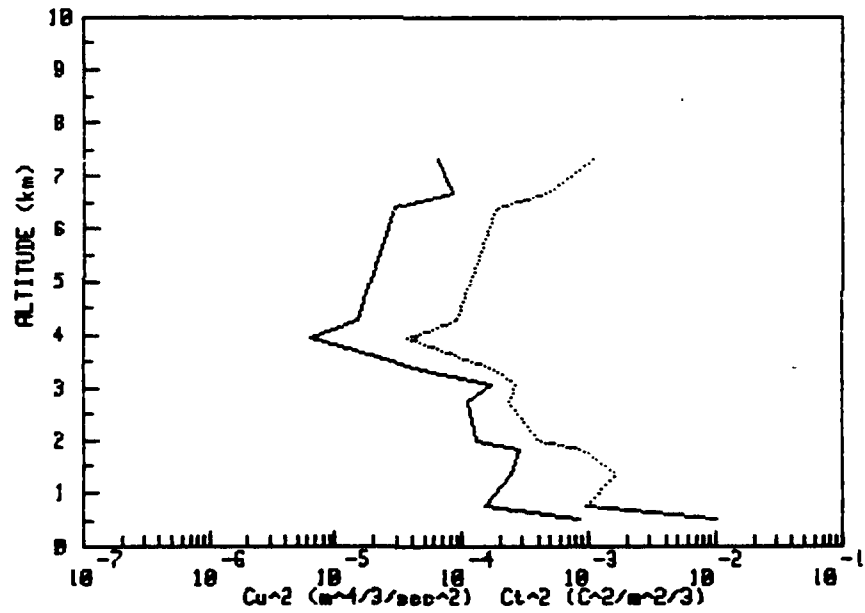
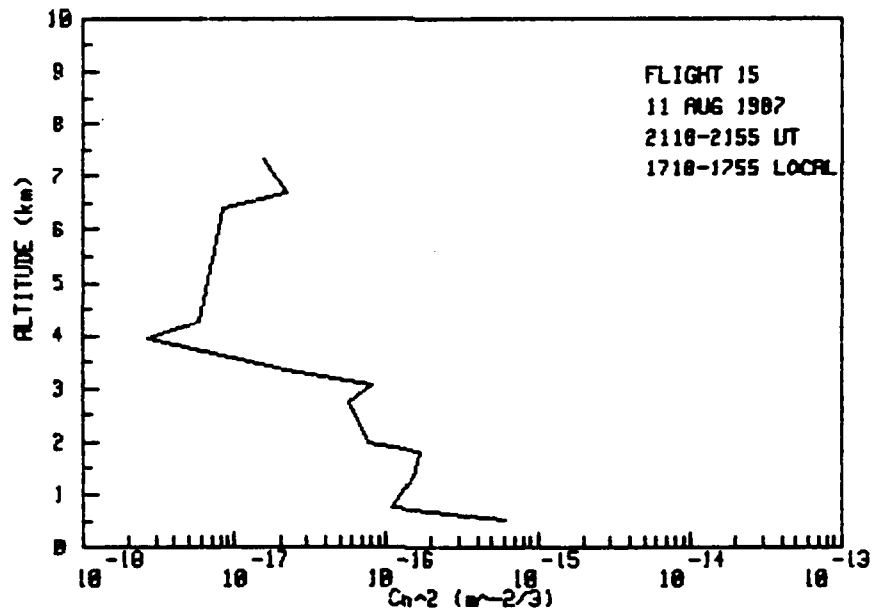


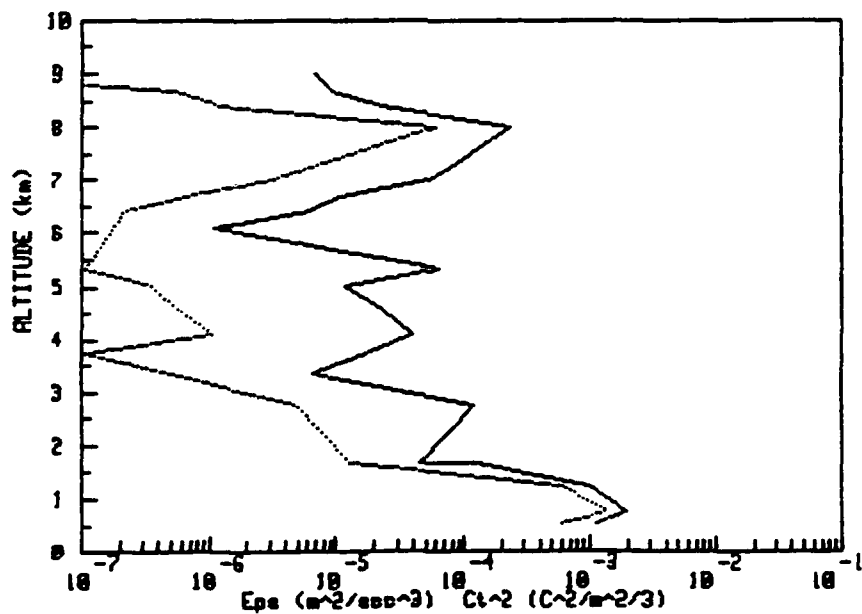
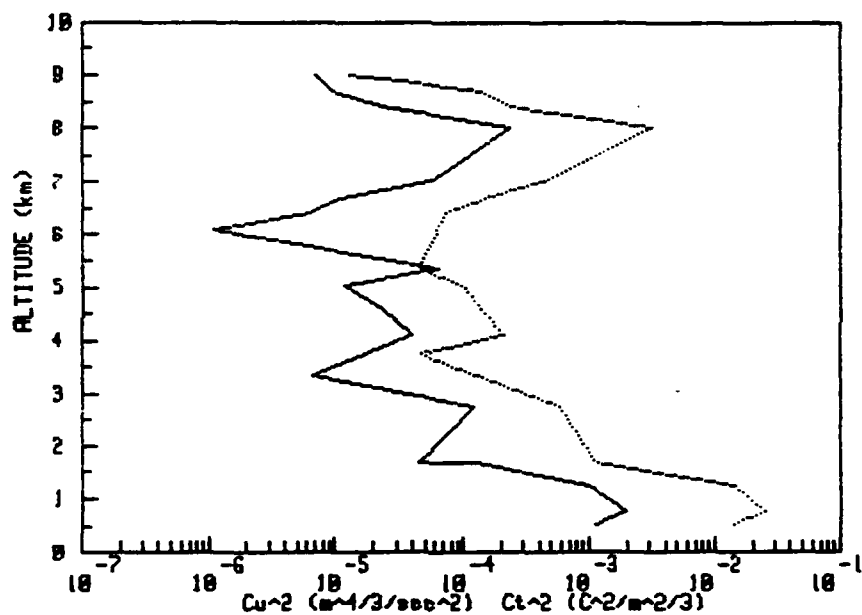
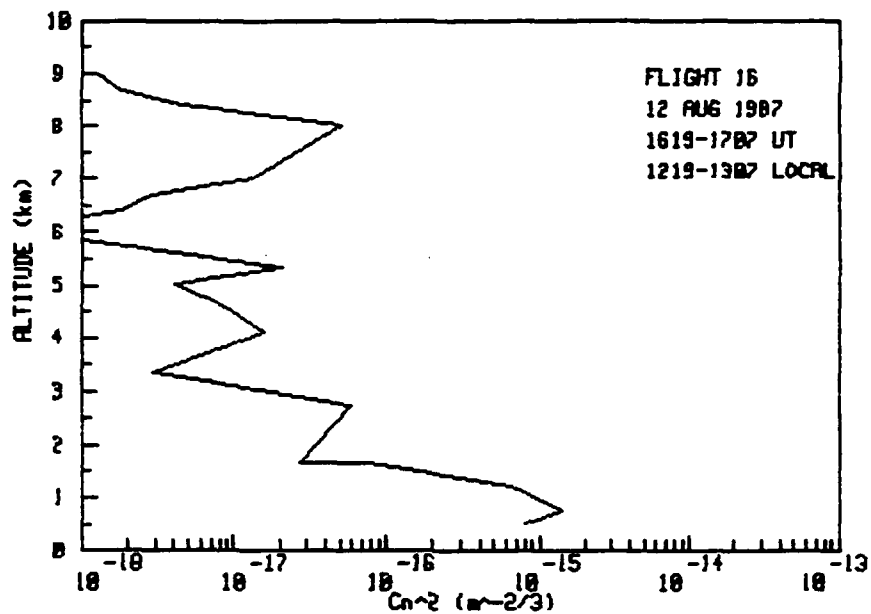


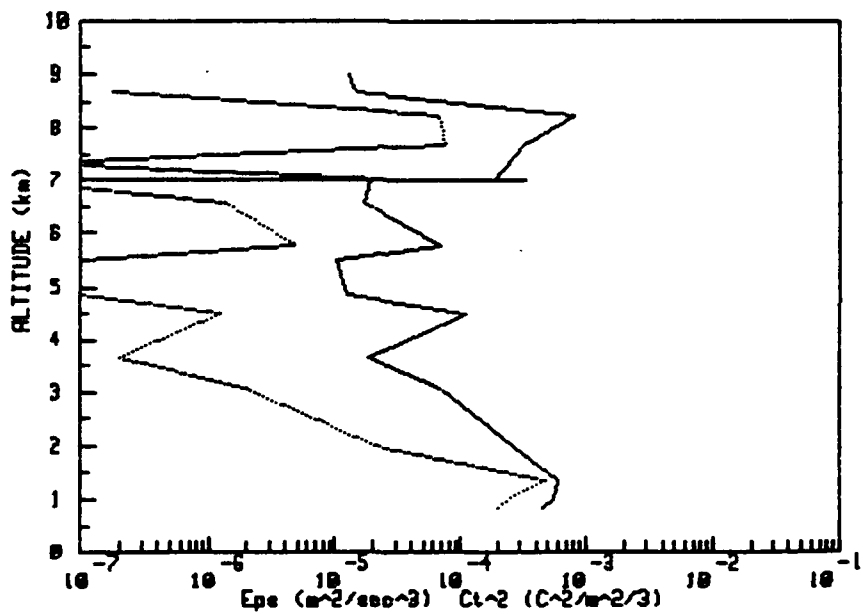
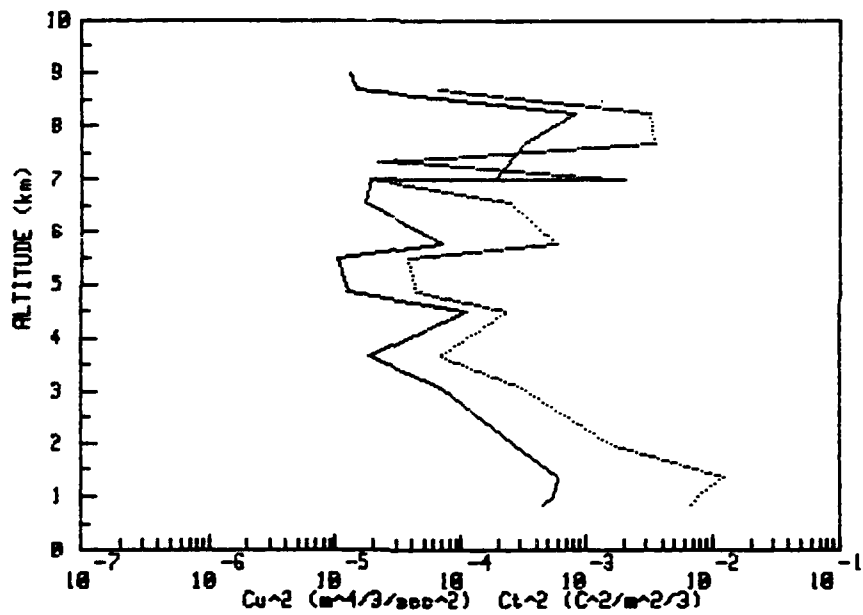
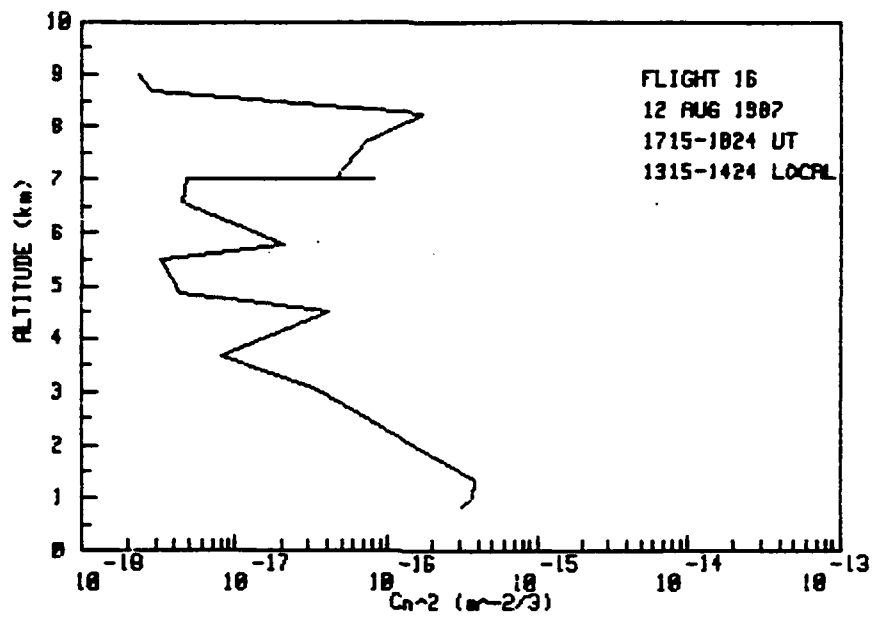


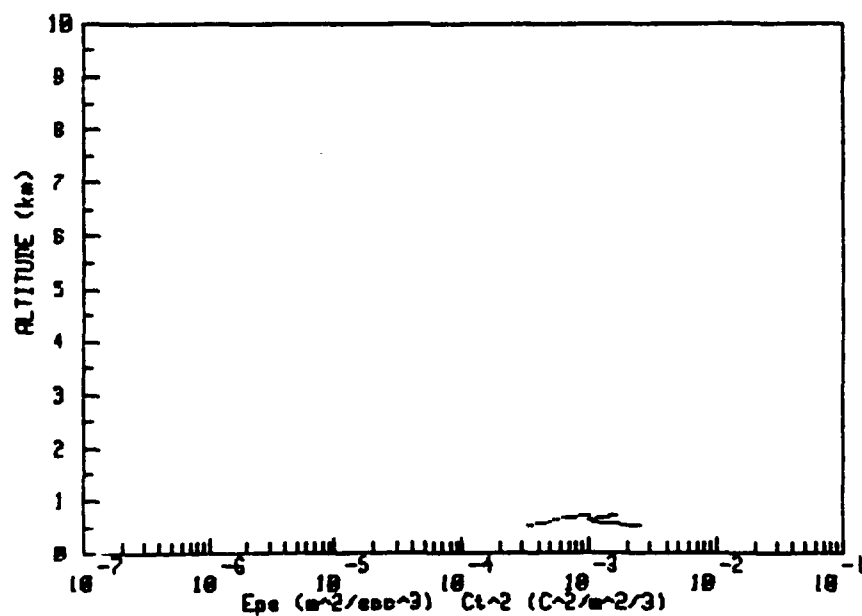
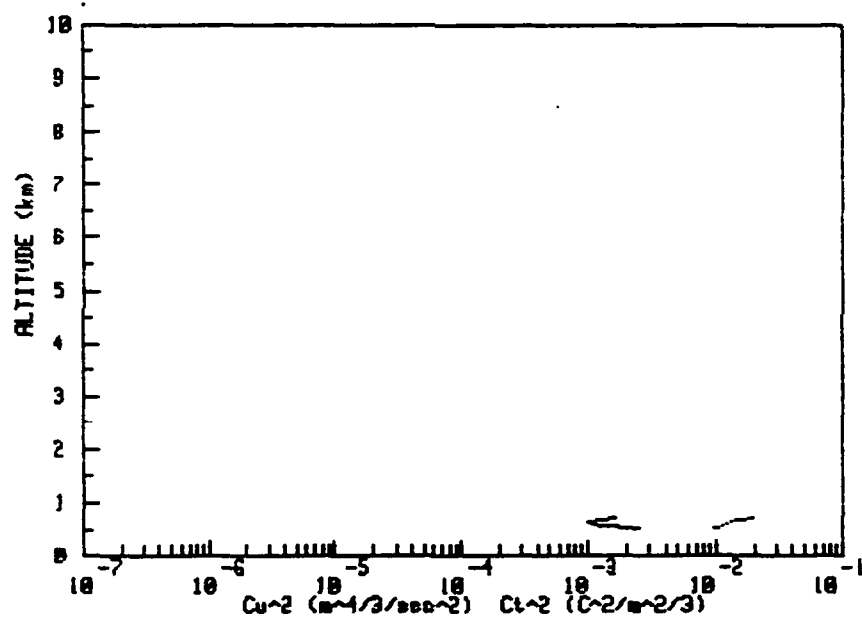
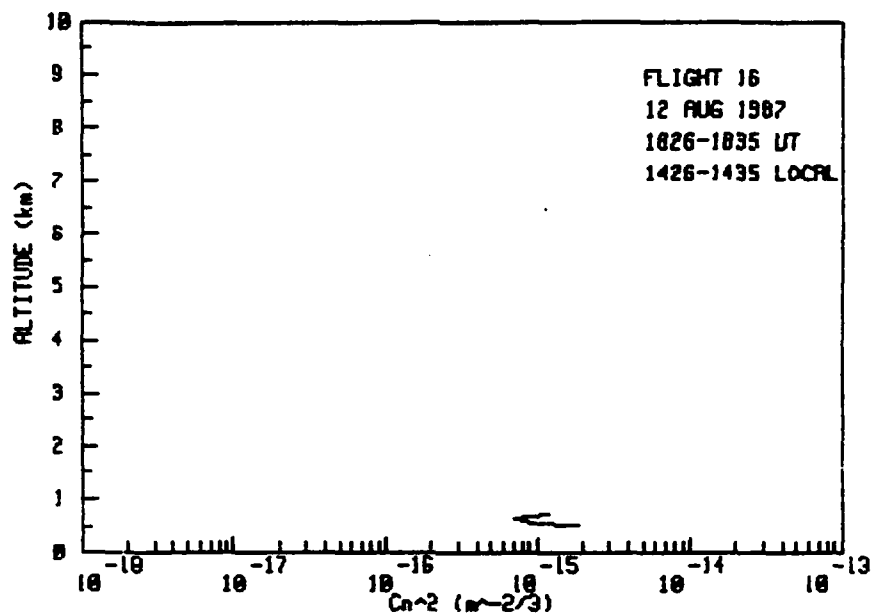


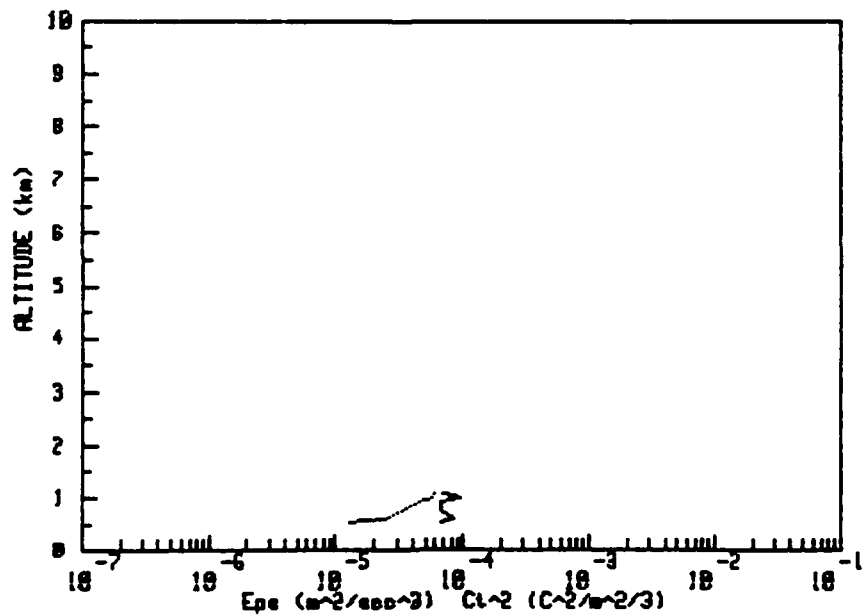
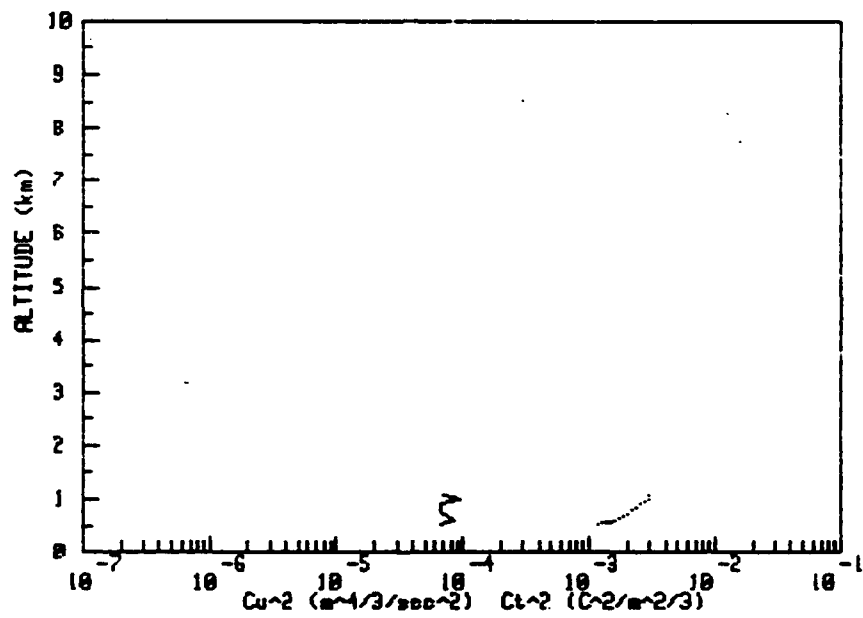
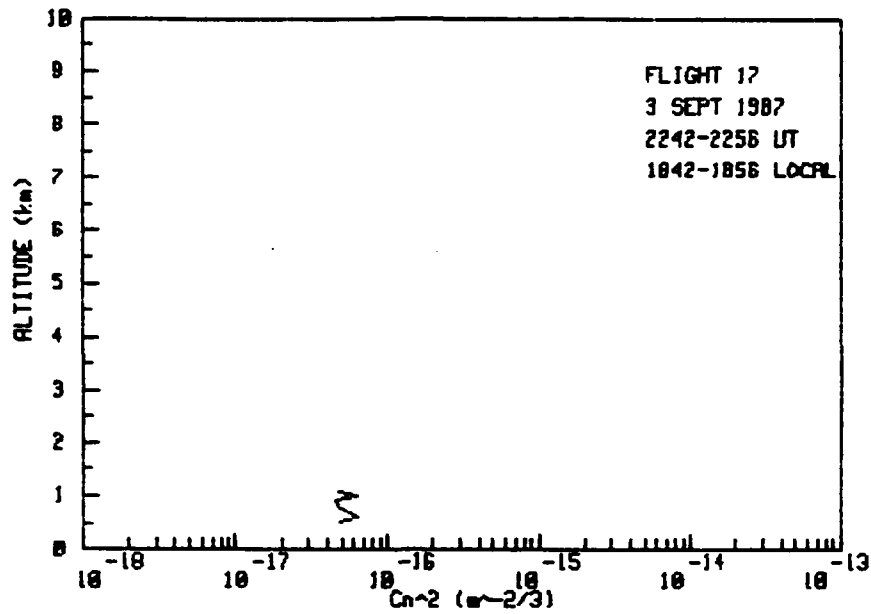




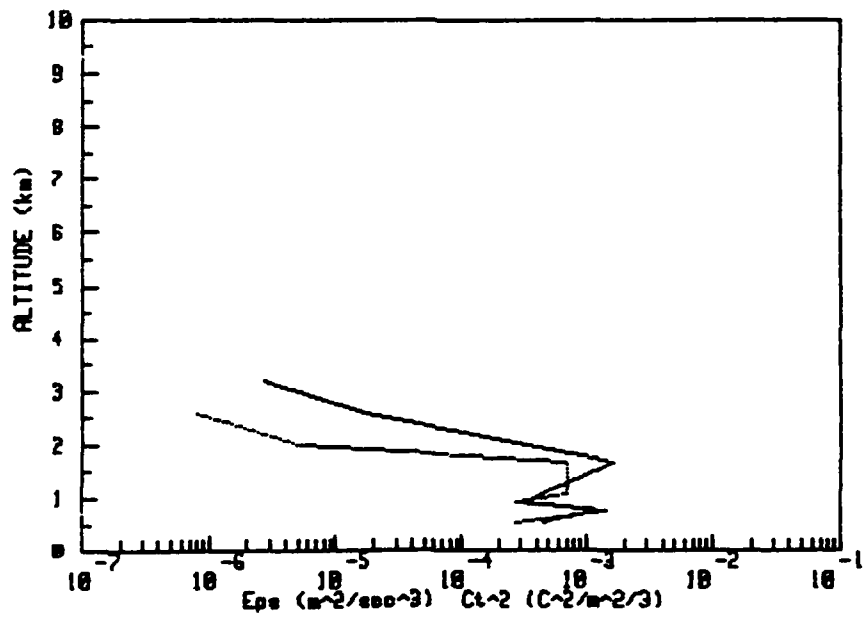
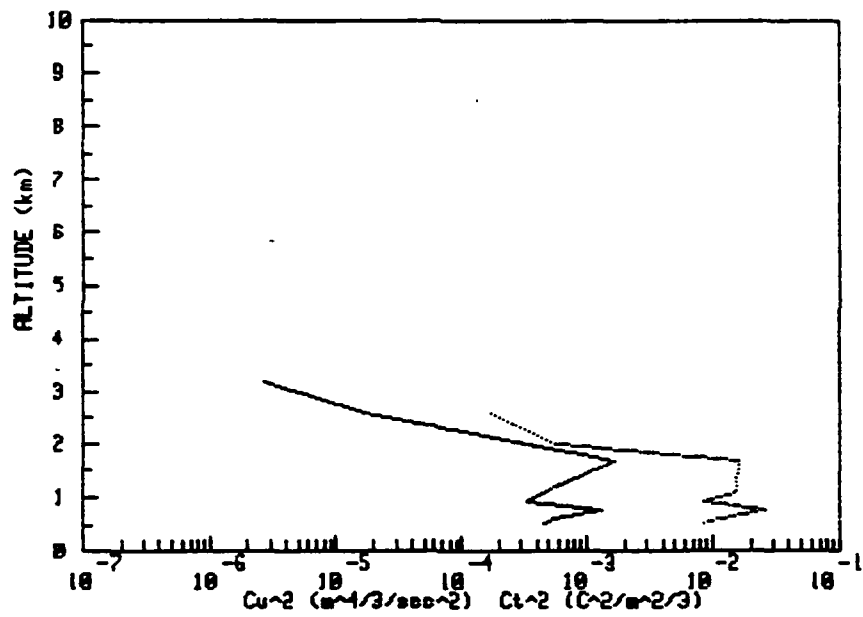
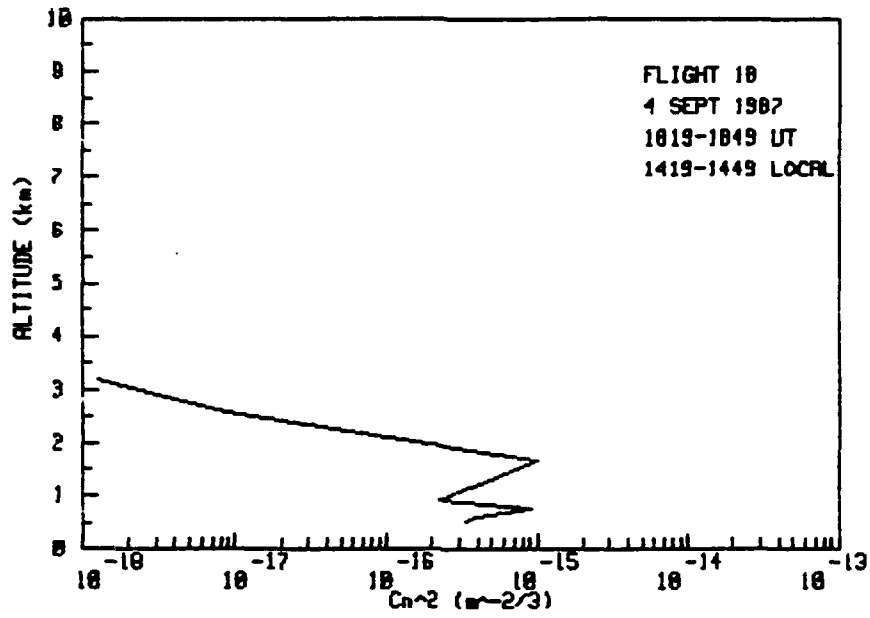


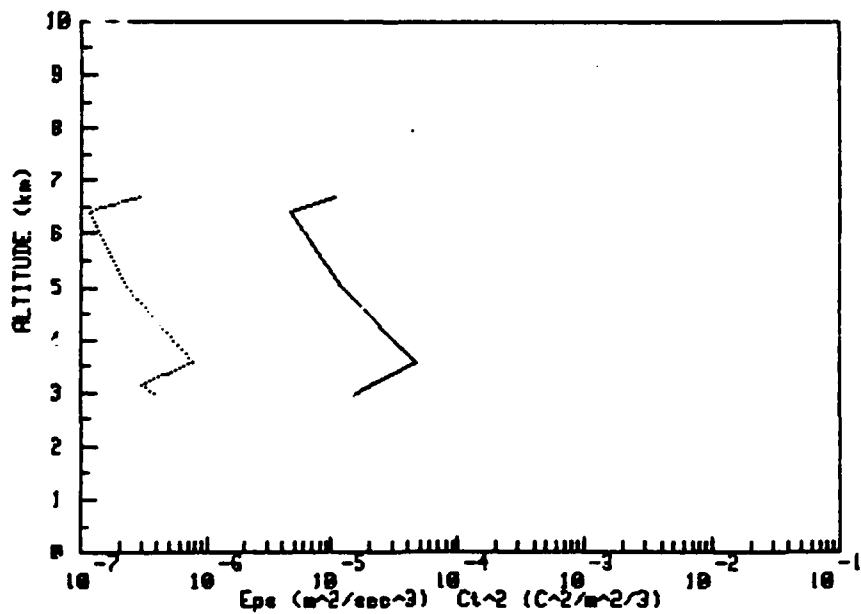
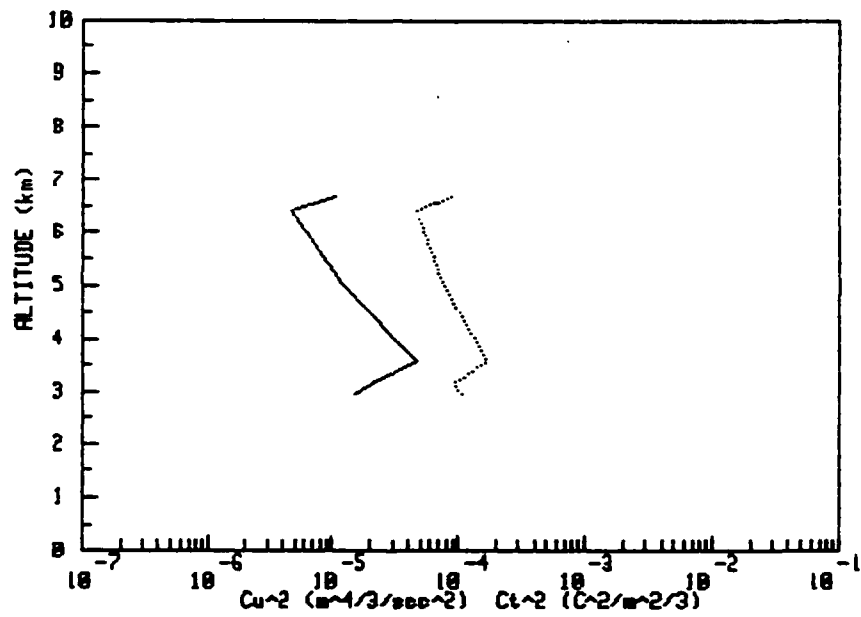
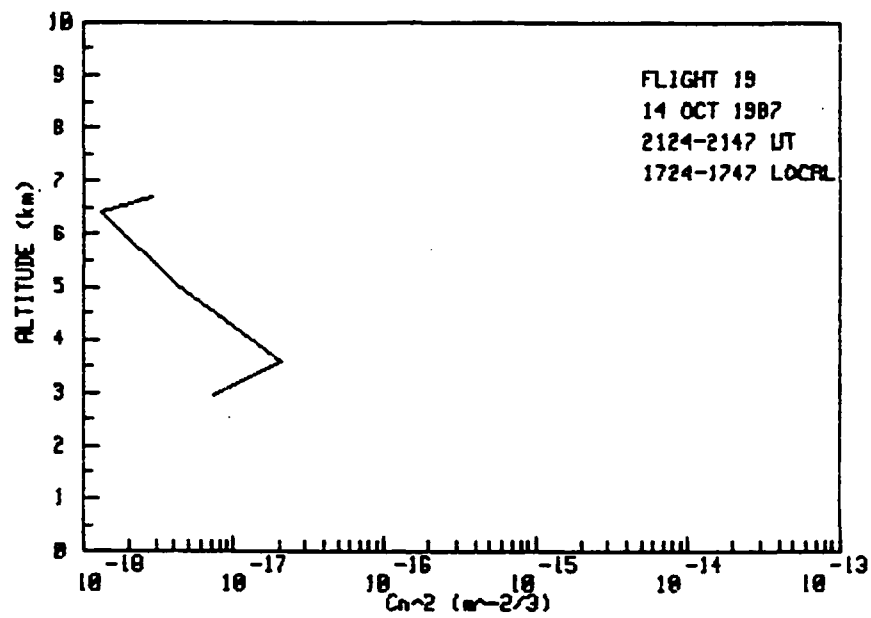


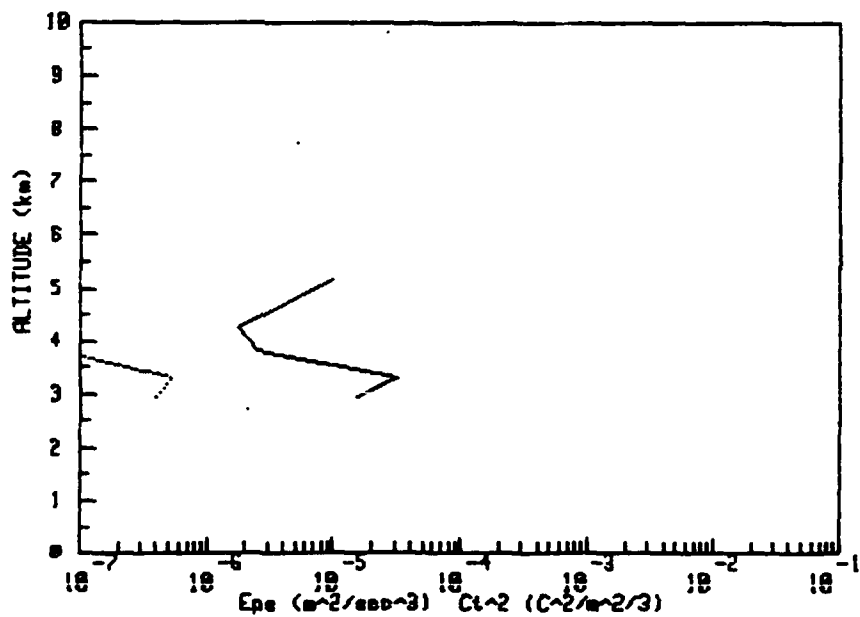
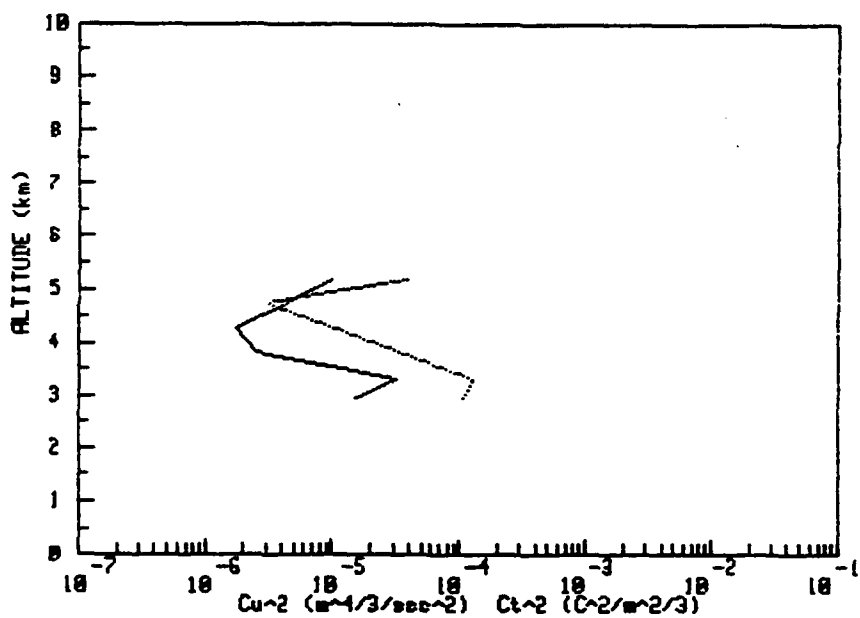
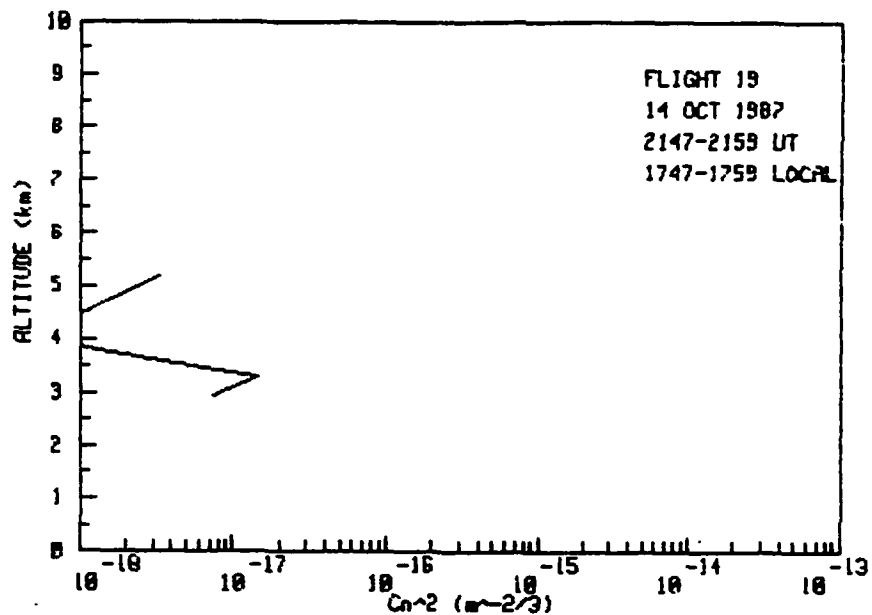


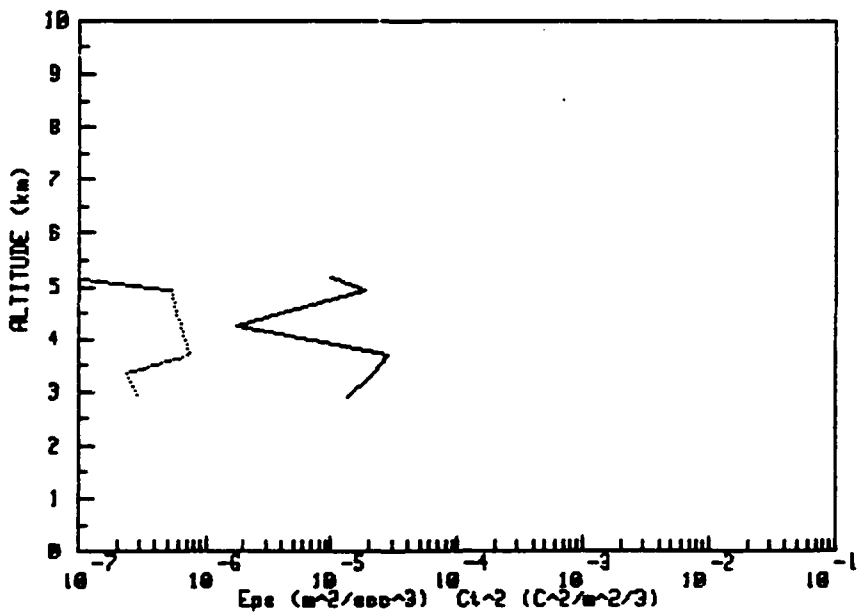
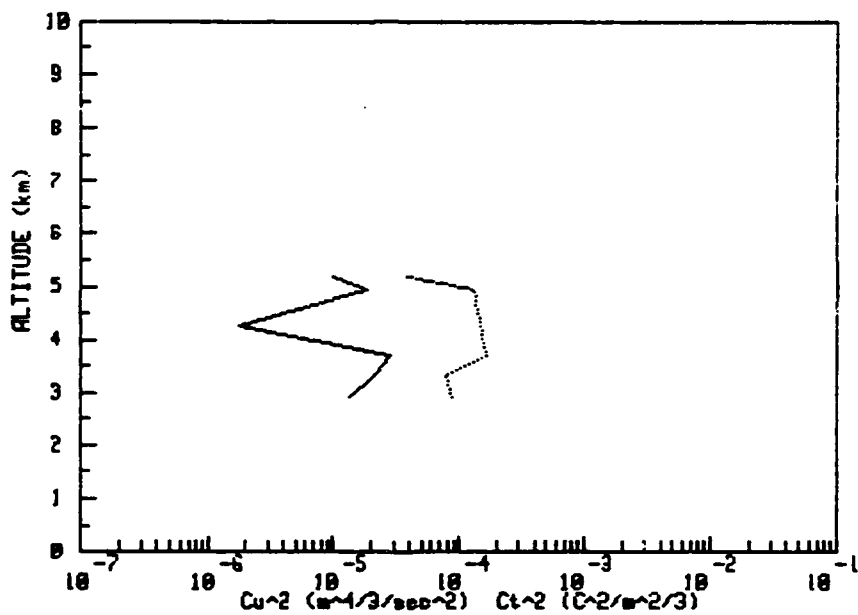
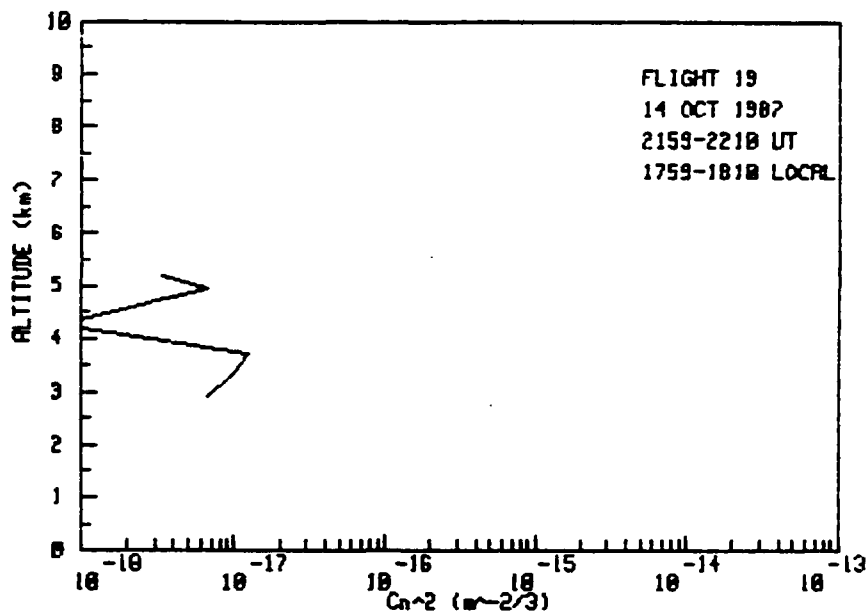


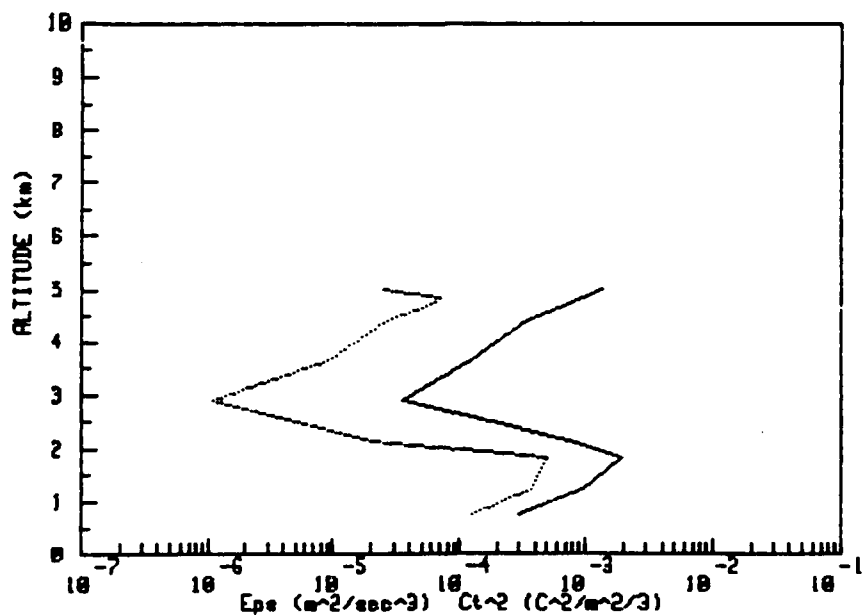
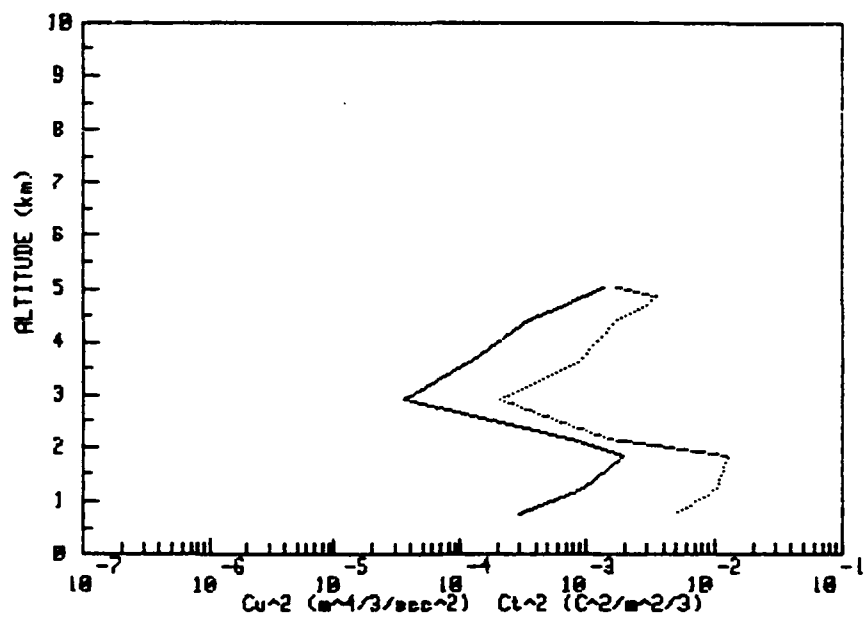
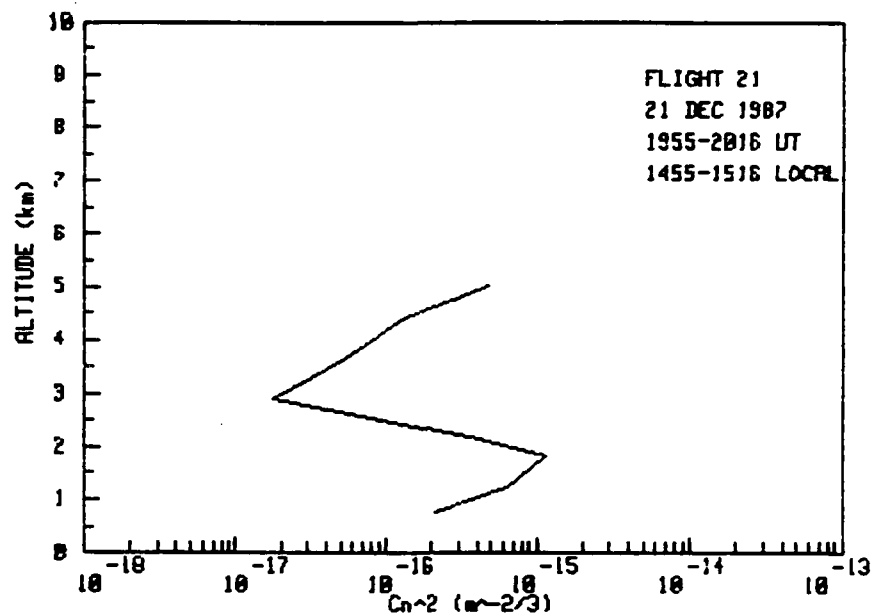


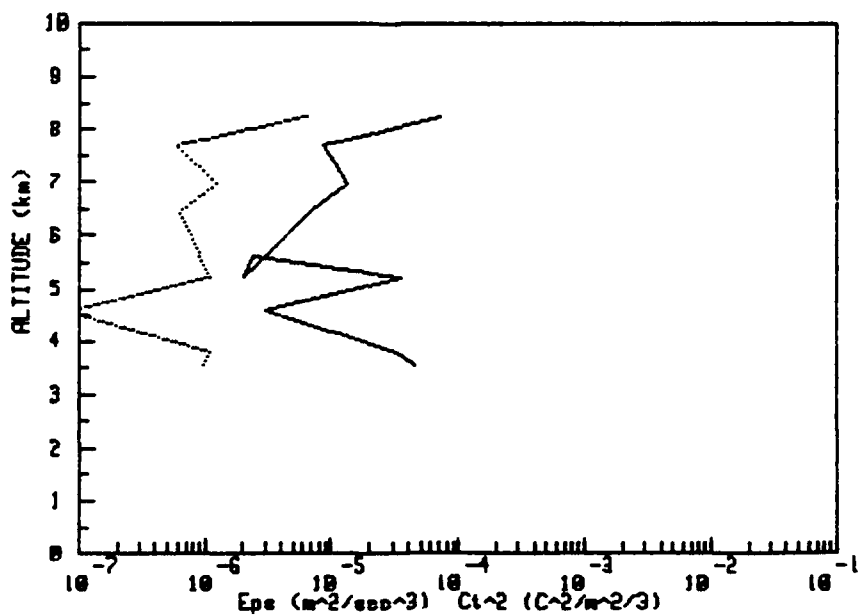
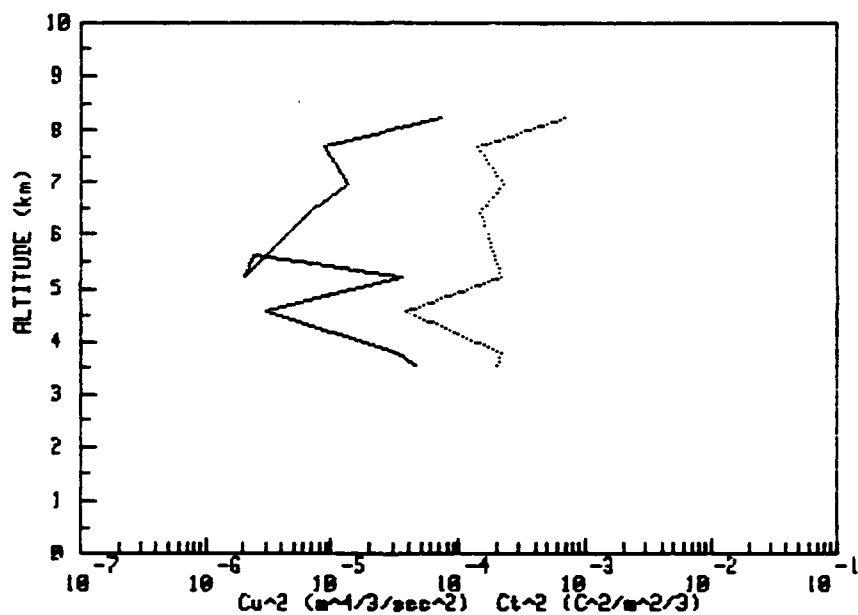
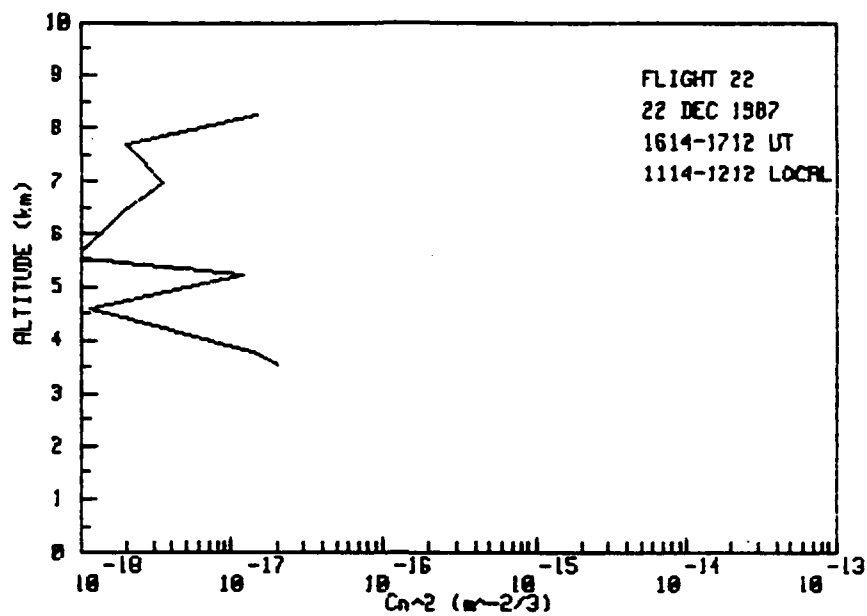


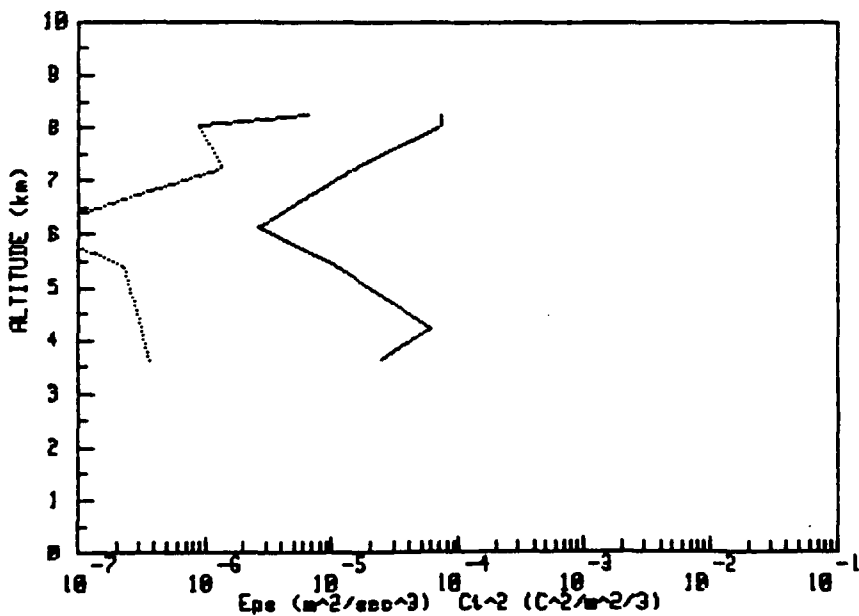
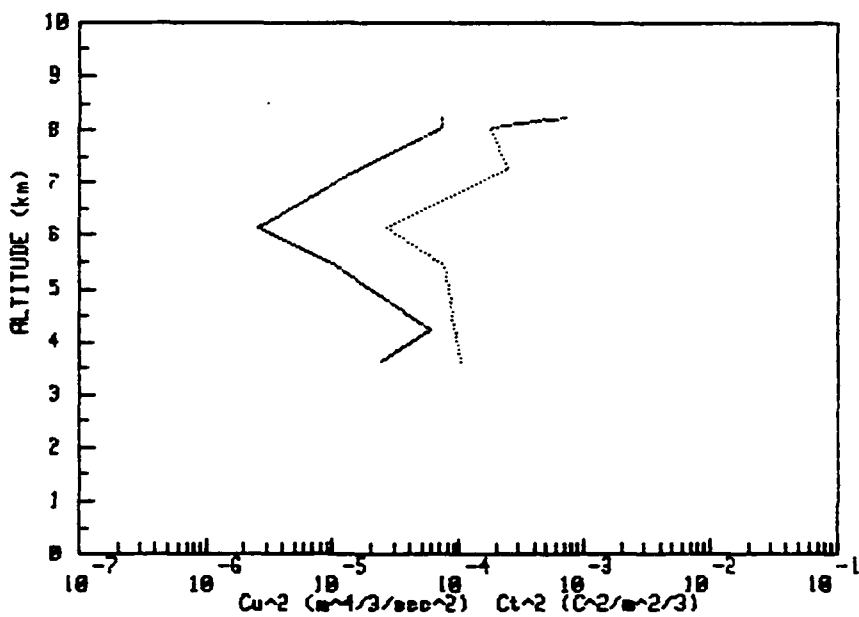
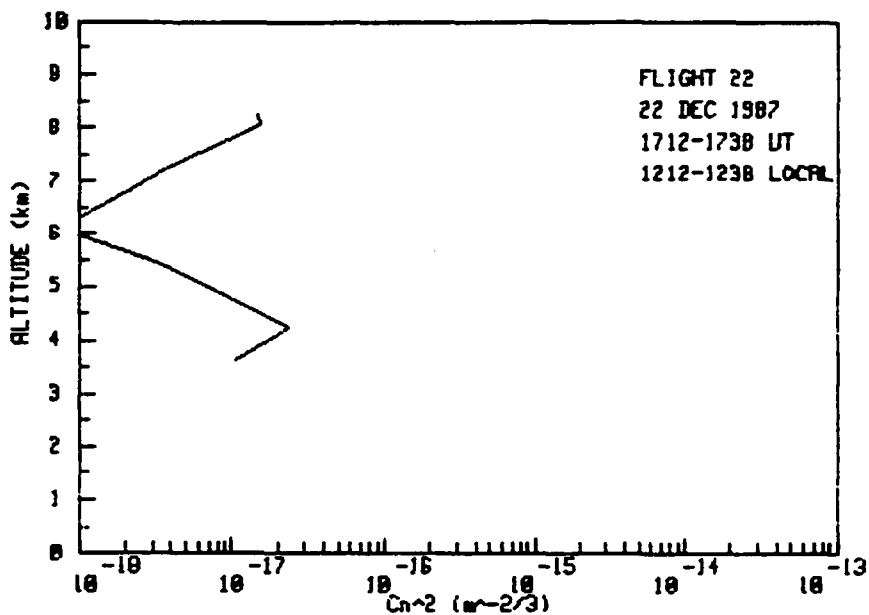


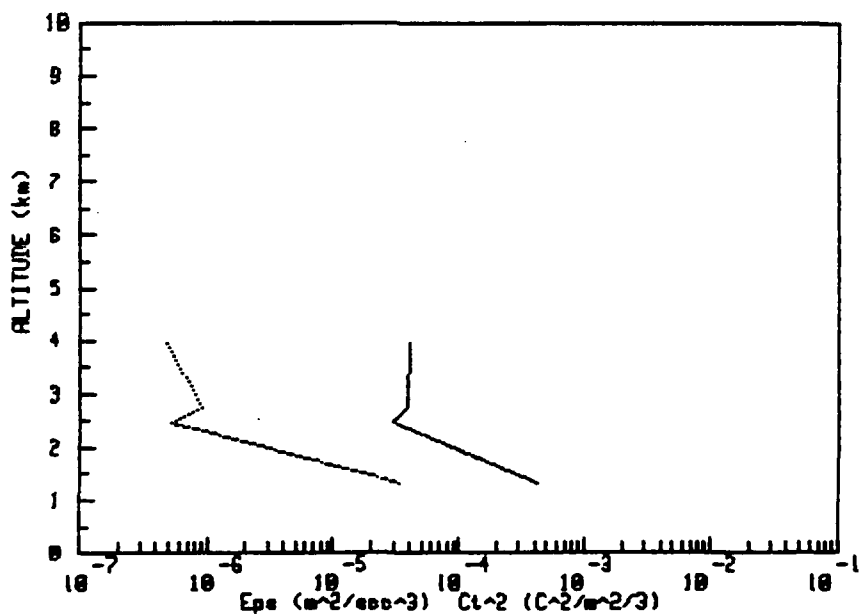
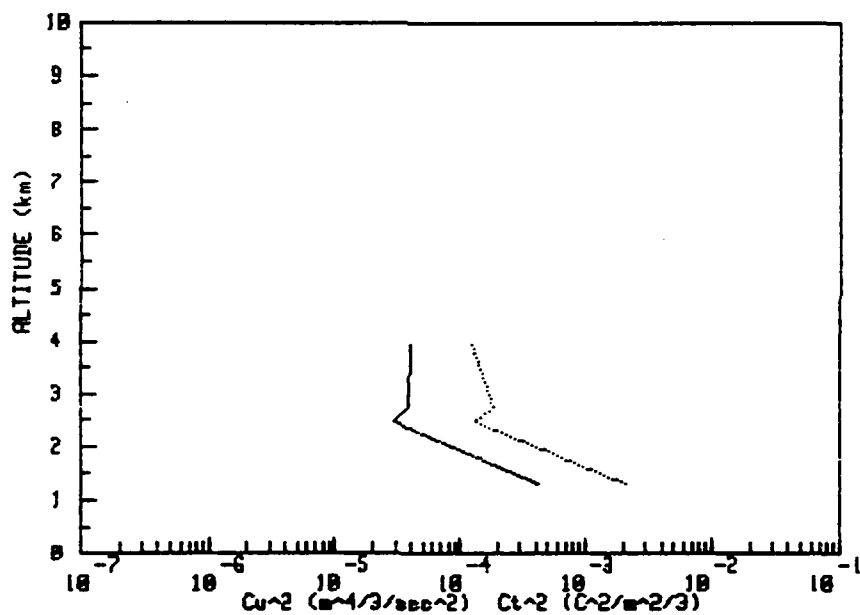
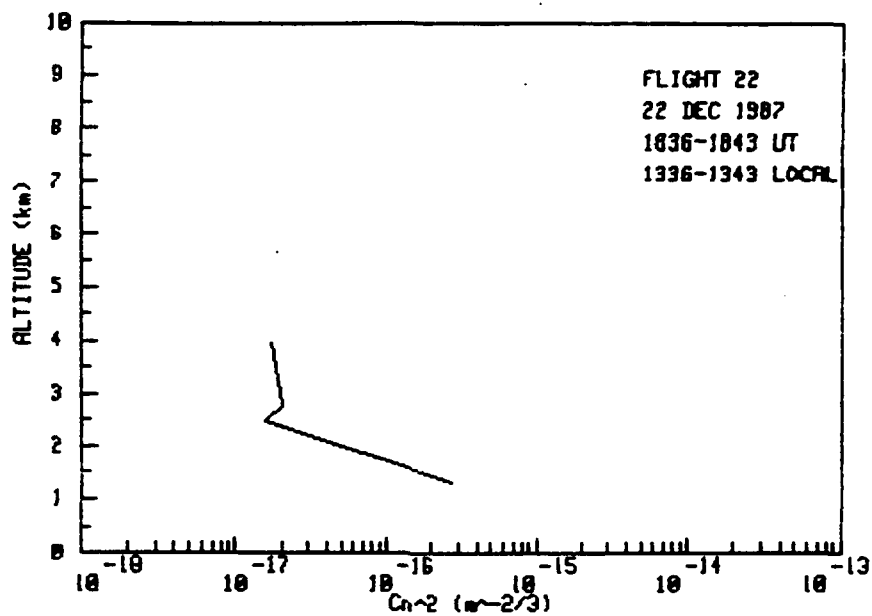










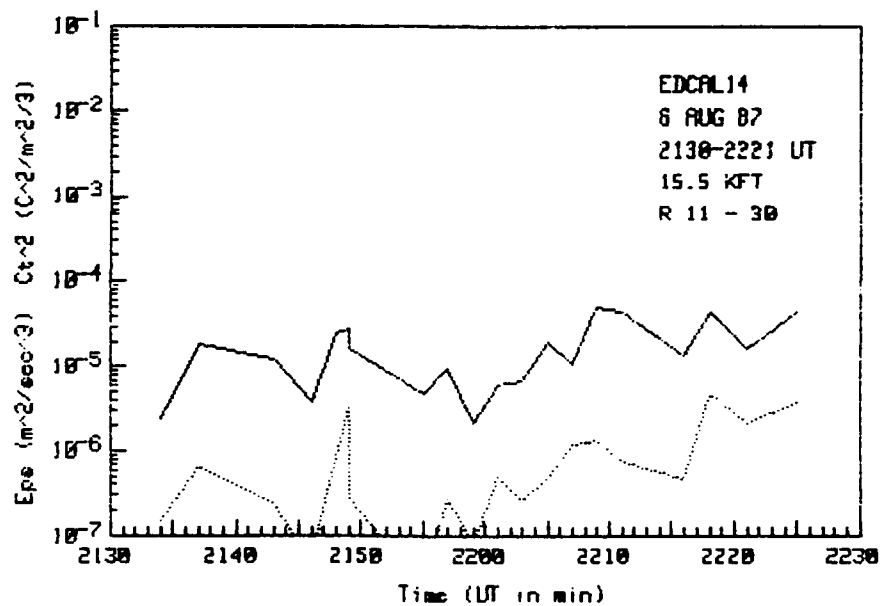
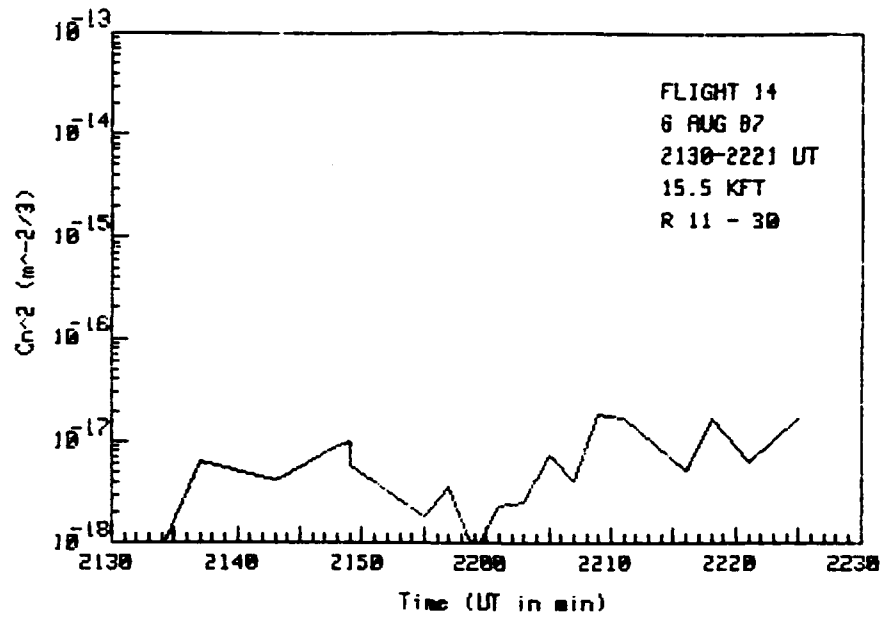


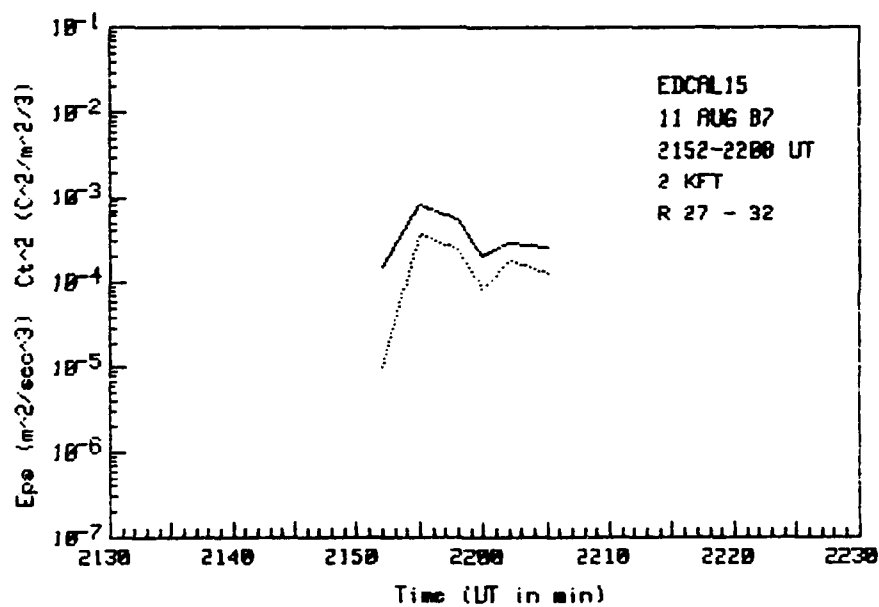
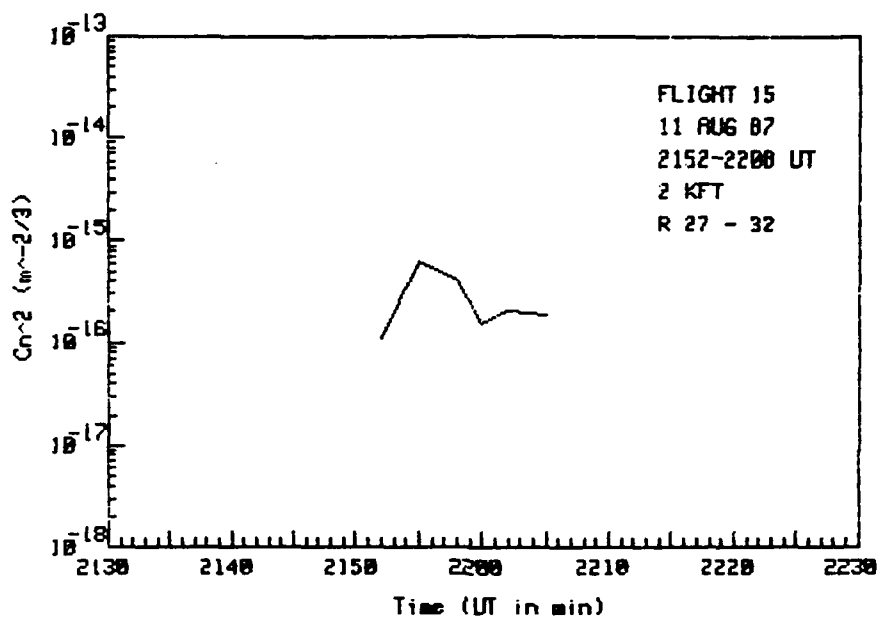


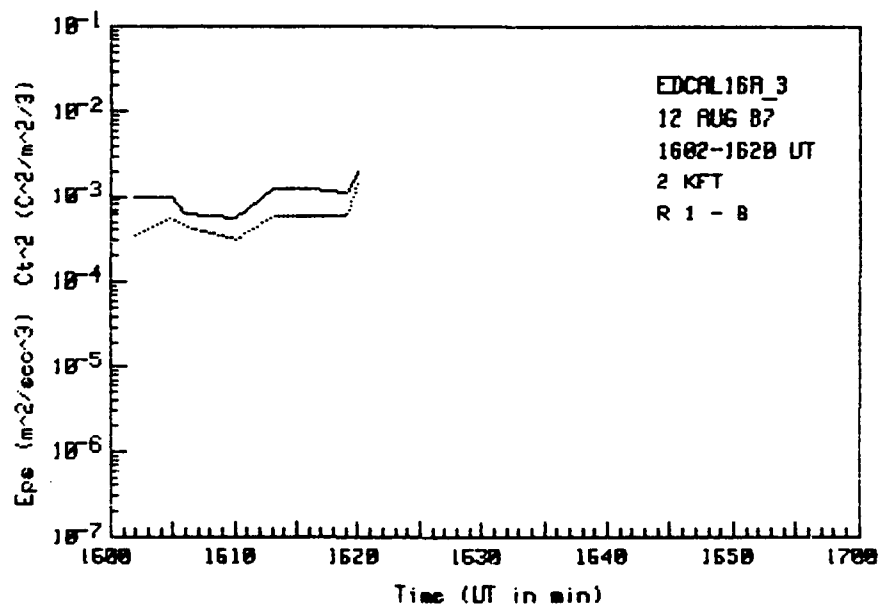
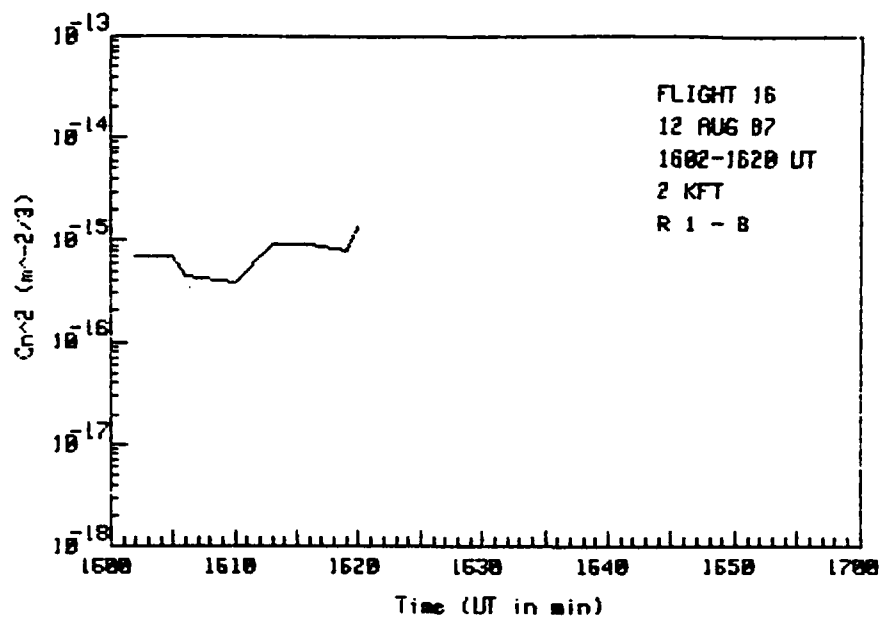
Part AIII

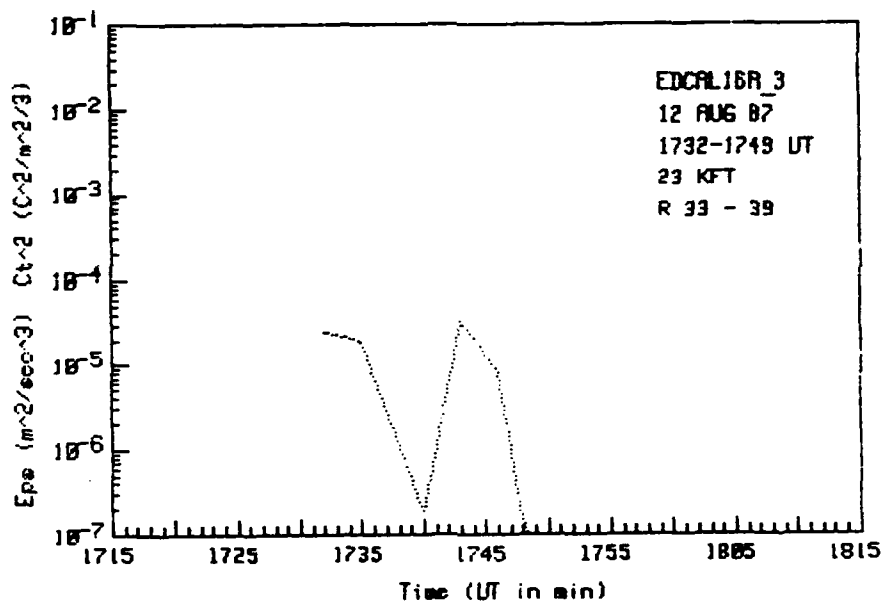
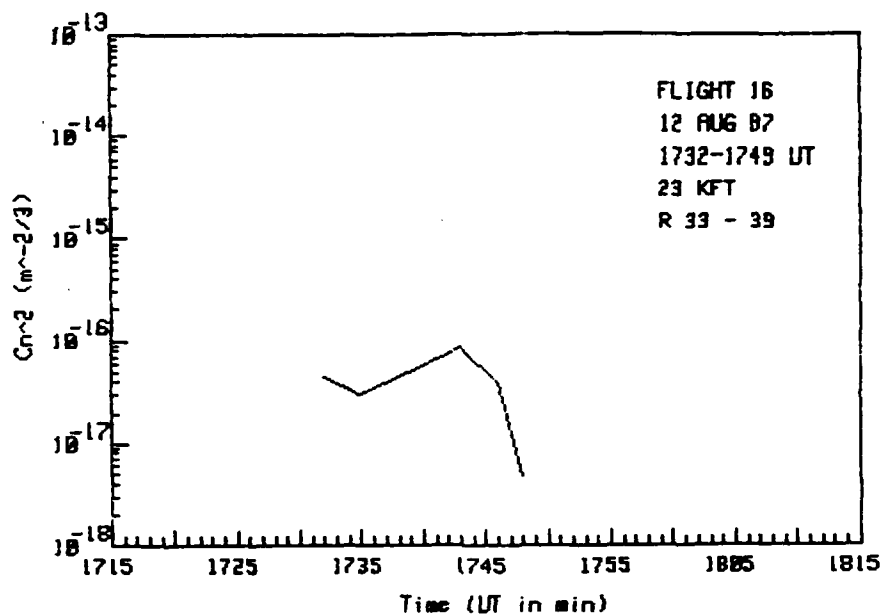
Horizontal variability

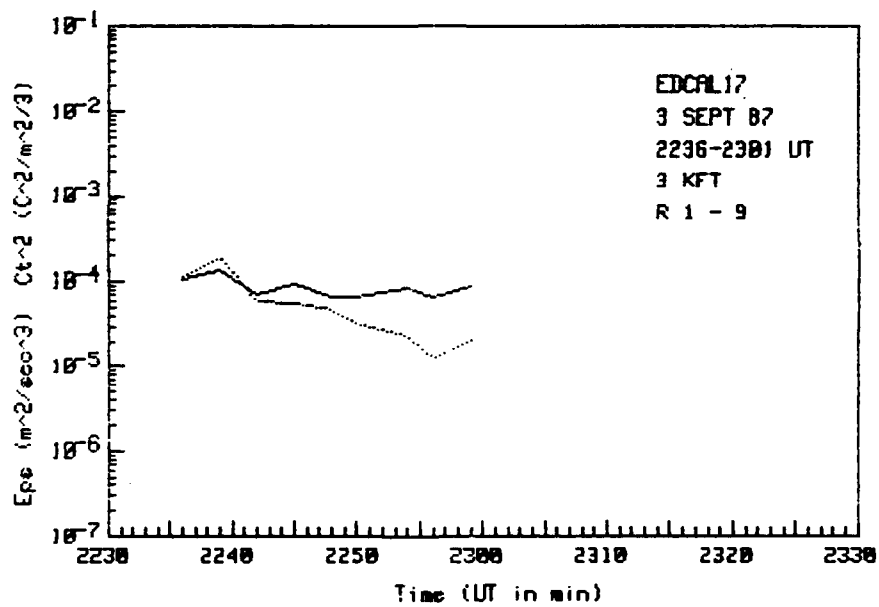
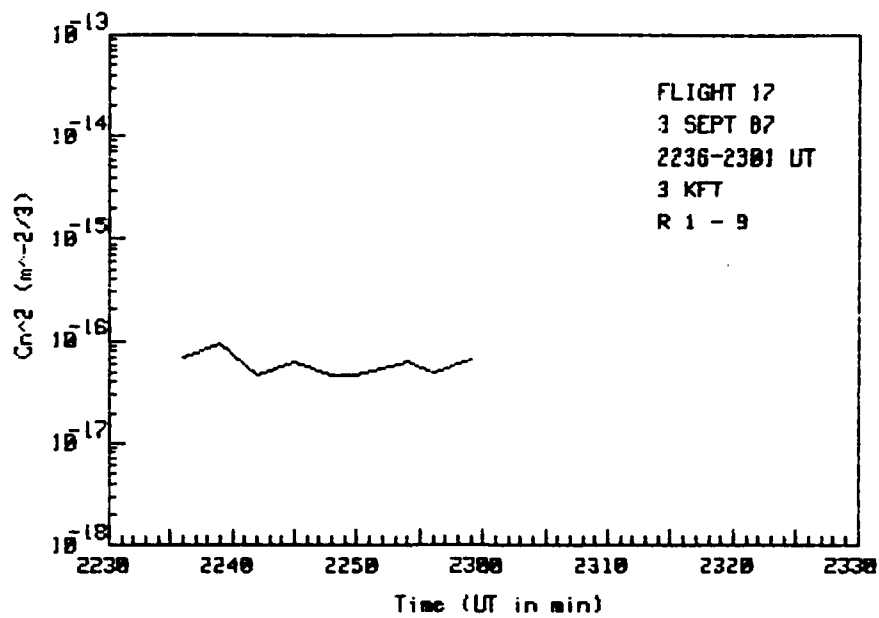
The graphs in this section depict turbulence parameters measured during level flight and are intended to give some indication of the horizontal variability of the parameters. The upper panel is optical  $C_n^2$  and the lower panel shows  $\epsilon$  (dotted line) and  $C_T^2$  (solid line). The flight number, date, GMT, and altitude (in thousands of feet) are indicated on the graph.

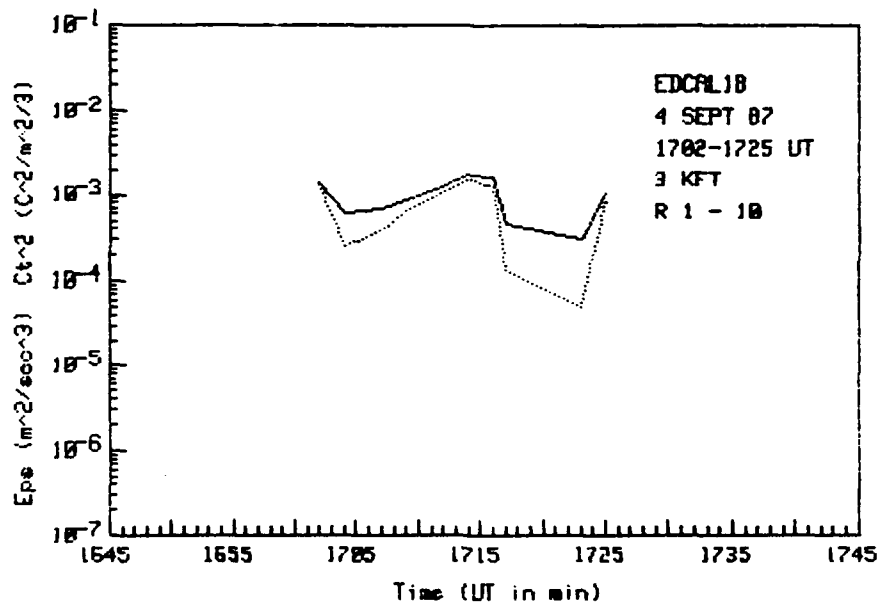
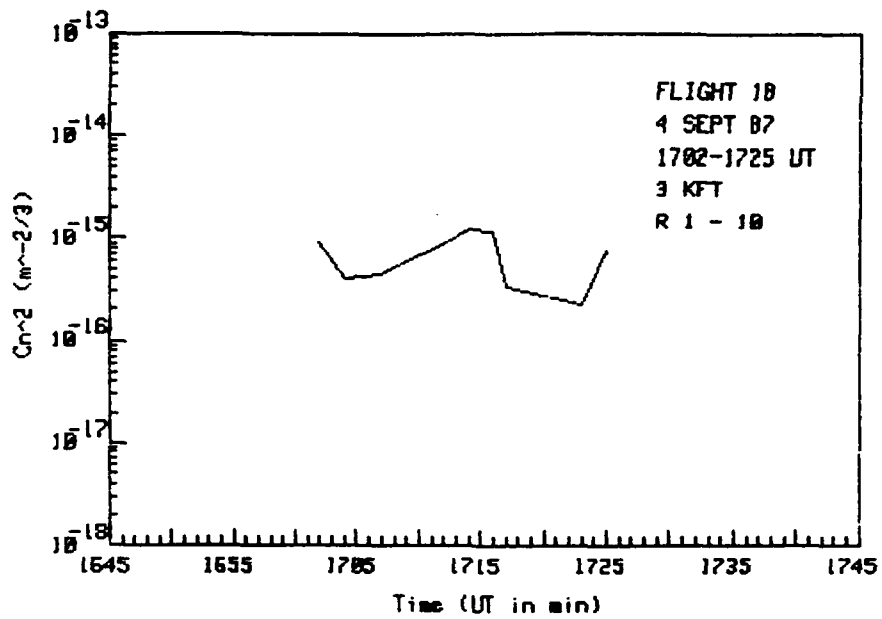


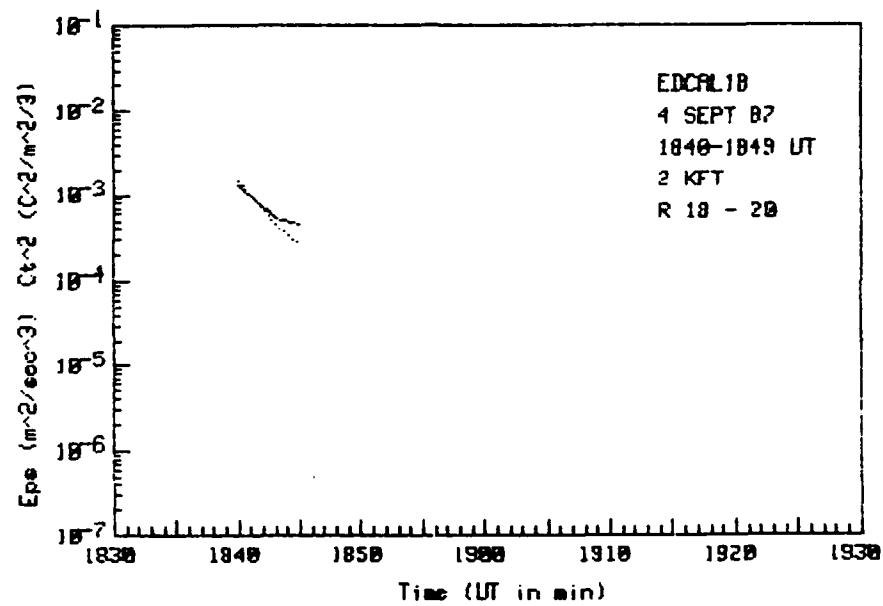
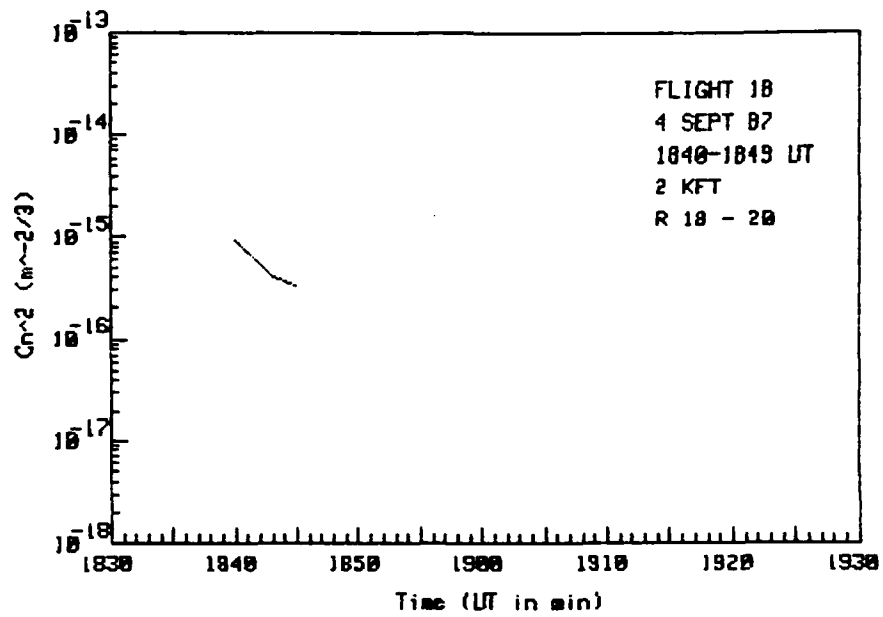




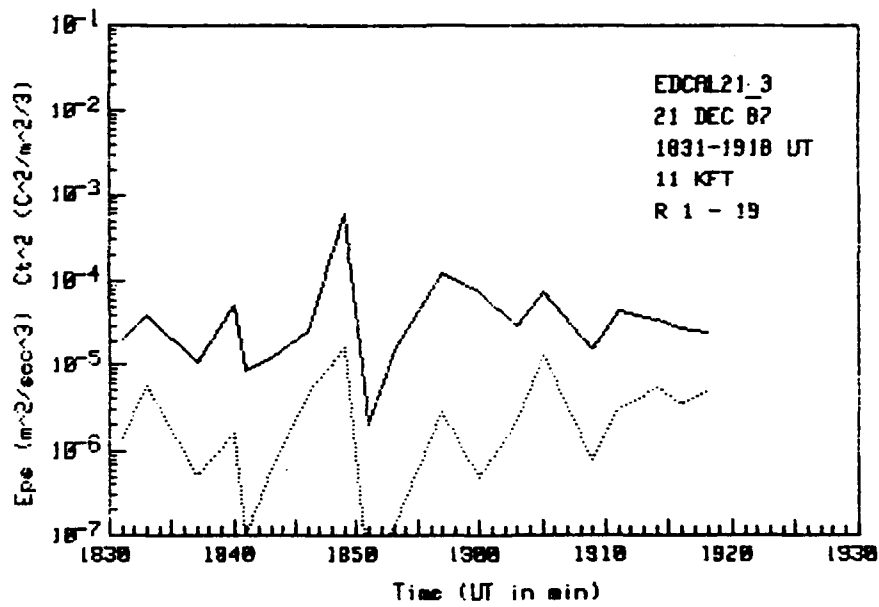
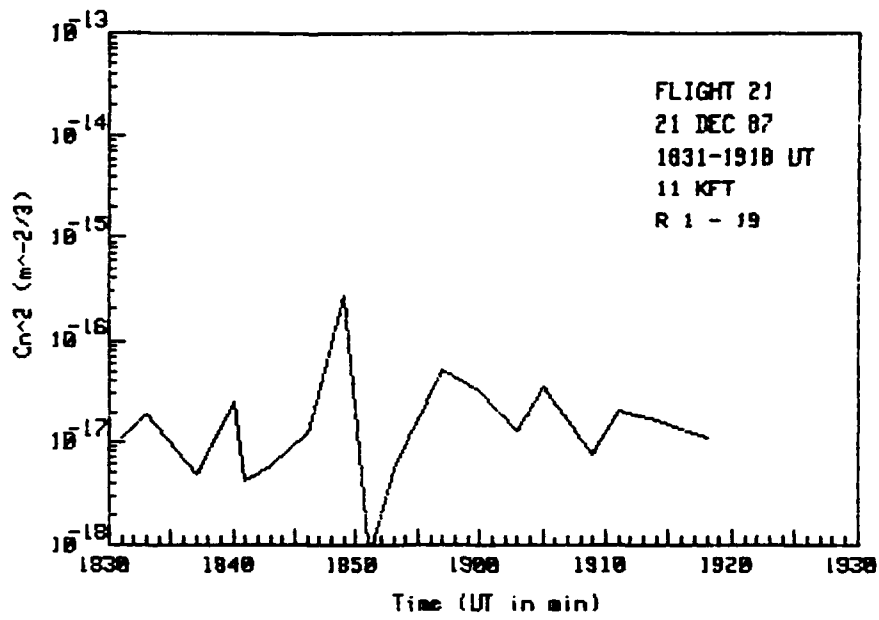


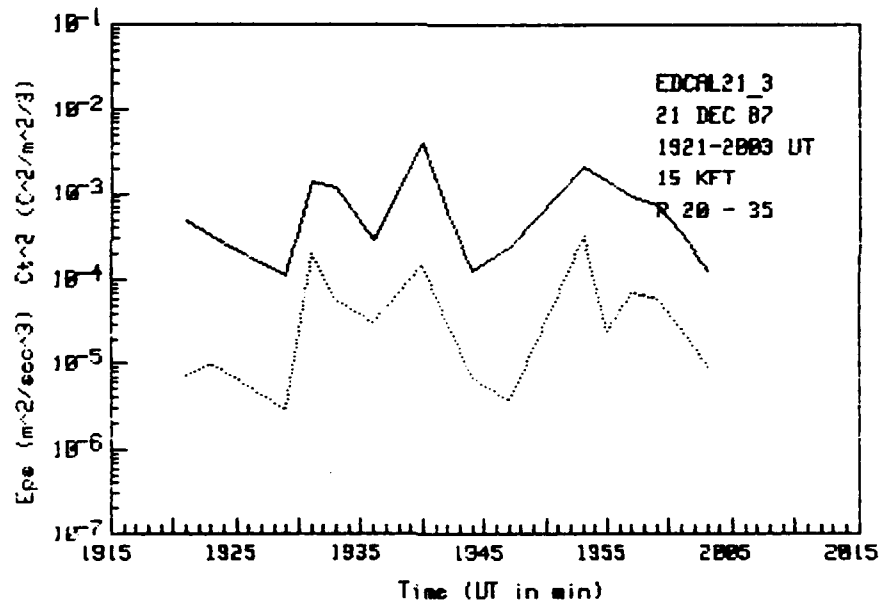
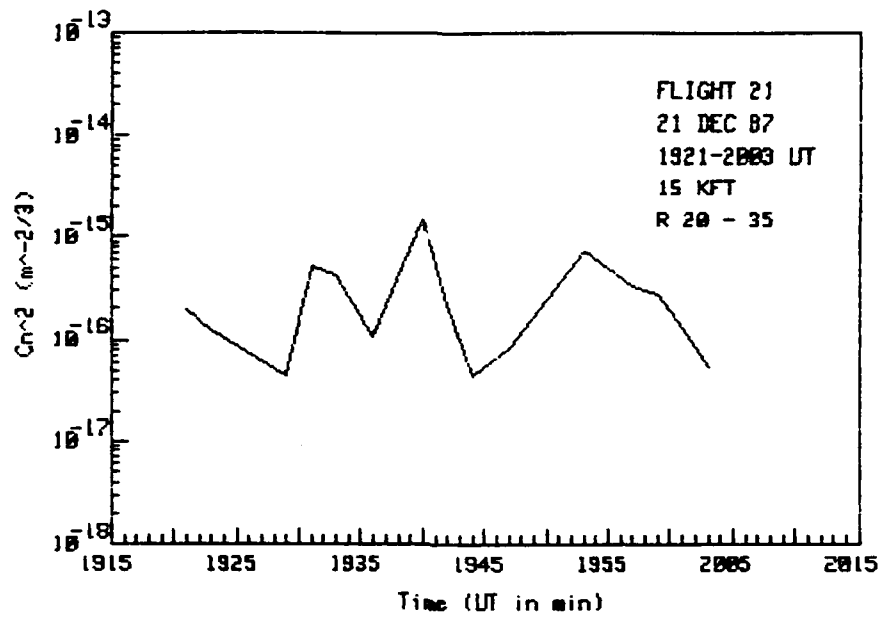


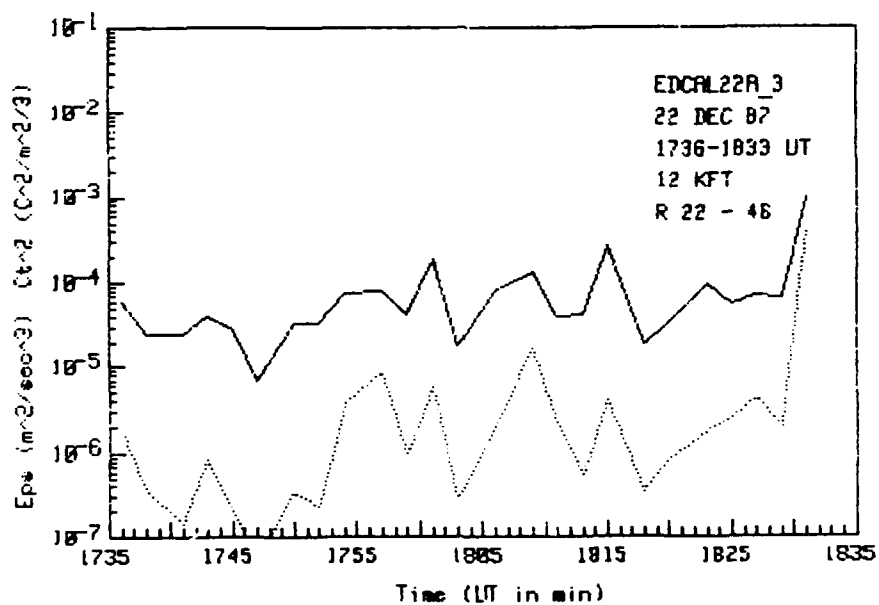
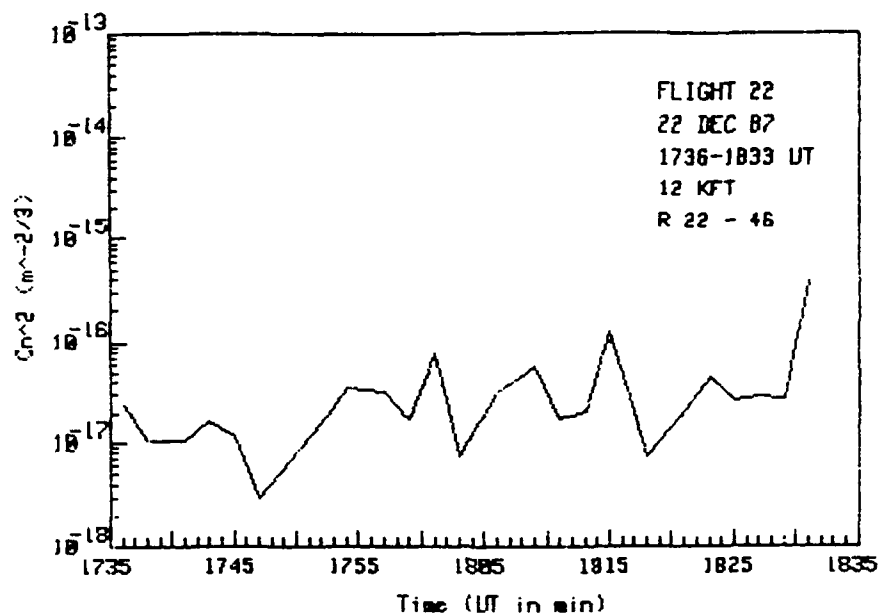












APPENDIX B

Reprint of a final report "Long term studies of the refractive index structure parameter in the troposphere and stratosphere" submitted to the Air Force Office of Scientific Research. Note, this report also contains appendices A and B, so beware of confusion.

Final Report

Contract AFOSR-86-0049

Long Term Studies of the Refractive Index Structure Parameter  
in the Troposphere and Stratosphere

C.W. Fairall, D.W. Thomson, and W.J. Syrett

Department of Meteorology

505 Walker Building

The Pennsylvania State University

University Park, PA 16802

ABSTRACT

This project is concerned with the relation of meteorological conditions to parameters and processes that influence the optical propagation properties of the turbulent atmosphere. The approach is centered around the establishment of a climatology of refractive index structure function parameter as measured with a network of Doppler radars. The relation of the atmospheric turbulence profile to the synoptic context and the use of physical models to predict the profile using standard meteorological profile data is also being investigated. The study features two modes of data archiving: (1) continuous archiving of 1 hr average wind profiles and turbulence levels, and (2) high time resolution measurements in association with other measurements (ground-based optical scintillometers, aircraft or radiosondes) in an intensive 'campaign' given the acronym EWAK.

The atmospheric turbulence profiles and resultant optical propagation parameters have been found to be strongly influenced by synoptic conditions. In particular, the turbulence is substantially affected by to strength and location of the jet stream. A very strong correlation between wind shear (which is maximum above and below the core of the jet) and pilot reports of turbulence was found. Richardson number gave a much weaker indication, possibly because of the poorer quality of the vertical temperature gradient data. A comparison of five different methods (four measurement and one model) of obtaining optical  $C_n^2$  showed average disagreements as large as a factor of three. A study of the ratio of temperature to velocity microturbulence showed that the assumption of a constant mixing efficiency (used in the Van Zandt model) may not be valid for very weak turbulence. The potential for using operational numerical forecast models to compute turbulence estimates from predicted wind and temperature profiles was examined in a preliminary

look at the ability of the NMC Nested Grid Model (NGM) to reproduce the wind speed and direction directly measured by the radars. The standard deviation between the radar and model was on the order of 6 m/s for wind speed and 15 degrees for wind direction at the initial analysis time. The uncertainty in wind direction increased to about 25 to 30 degrees for a 48 hr forecast but the uncertainty in wind speed did not change significantly. A systematic difference of several m/s was found during the winter, probably due to over smoothing of mesoscale features by the model.

ACKNOWLEDGEMENTS

This work was directly supported by the Air Force Office of Scientific Research contract number AFOSR-86-0049; the radar systems were originally obtained on AFOSR-83-0275. Robert Peters and Scott Williams of the Department of Meteorology, PSU, were primarily responsible for the construction and operation of the radars (with external assistance as described in the appendix).

The authors wish to acknowledge Lt. Beth Beecher and Capt. Mike Moss for their contributions to and analysis of the EWAK experiment. Special thanks to Ralph Markson and Bruce Anderson of Airborne Research Associates for their aircraft participation in EWAK and to Don Stebbins of Rome Air for his interest in putting EWAK together.



CONTENTS

- I. Introduction
- II. Refractive Index of Air
- III. Background on Clear Air Turbulence
- IV. Application of VHF and UHF Doppler Radar
- V. Summary of Work Completed
- VI. Suggested Future Research
- VII. References
- VIII. Summary of Publications and Presentations

Figures

Appendix A. Profiler System Description

Appendix B. Notes Concerning the Use of Clear Air Doppler Radars for the  
Measurement of  $C_n^2$

## I. Introduction

The importance of turbulence in the atmospheric boundary layer, which is the basic living environment of humankind, has long been recognized. Only in the last few decades has the importance of free atmospheric (i.e., above the boundary layer) turbulence been recognized. Even in the absence of clouds, stably stratified fluids (e.g., the free troposphere and stratosphere) are observed to experience intermittent transitions to turbulent regimes. Although it is referred to as Clear Air Turbulence (CAT) it does occur in regions of stable clouds such as alto or cirrostratus. The beautiful breaking wave clouds provide visual evidence of CAT. CAT is important in aircraft performance and safety, optical propagation, EM propagation and communications, atmospheric dispersion of pollutants, and as a source of viscous drag in the 'free' atmosphere.

The atmospheric refractive index structure function parameter,  $C_n^2$ , is important in a broad range of optical propagation applications (see Section II). Examples of the consequence of atmospheric microturbulence on optical systems include: reduced intensity (Yura, 1971), beam wander (Fried, 1966), scintillation and coherence (Fried and Schmeltzer, 1967), and anisoplanatism (Fried, 1981). The consequences of spatially and temporally varying  $C_n^2$  can be computed for a specific optical system, at least in principle, by specifying the values of  $C_n^2$  along the optical path. While an extensive base of data and theory is available for planetary boundary layer (PBL) properties of  $C_n^2$  (see Fairall et al., 1982; Fairall, 1987), only a few case studies are available for the free troposphere and the lower stratosphere (Walters and Kunkel, 1981). The ALLCAT (i.e., HICAT, MEDCAT, etc.) program of the late 1960's focused primarily on large scale turbulence severe enough to damage aircraft or discomfit passengers. Now the structure and dynamical

properties of both CAT and  $C_n^2$  in the free troposphere and lower stratosphere are receiving renewed attention. For  $C_n^2$  this is because of the recognition of the importance of the isoplanatic angle in the performance of a variety of ground-to-space systems that utilize adaptive optics. Concurrently development of VHF clear air Doppler radars, the performance of which are directly proportional to  $C_n^2$ , has rekindled the interest of the meteorological community in the climatology and dynamics of CAT. It turns out that this is still poorly understood. For example, a recent long term study of  $C_n^2$  using VHF radar (Nastrom et al., 1981) revealed substantial diurnal and seasonal variations even in the stratosphere. This study suggested that strong tropospheric convection and the jet stream were relevant factors in the intensity of CAT but, at present, this is only conjecture based on physical plausibility.

The investigation of atmospheric turbulence involves the collection of data, the development of theory and the implementation of models. The data tells us what is 'up there' at the time of the measurement, but the theory and models are true indices of our understanding of the phenomena. With models we attempt to predict an important but difficult to measure variable (e.g.,  $C_n^2$ ) from variables that we expect to have at our disposal (e.g., regional scale radiosonde information). Dynamical models of turbulence based on the Navier-Stokes and turbulent kinetic energy (TKE) equations have a rich tradition in PBL research. Both second order closure and large eddy simulations have provided great insights into the structure of PBL turbulence. In contrast, the only model of CAT in use today is purely statistical in nature (Van Zandt et al., 1981; Moss, 1986).

Remote sensors are ideal for the study of climatological properties of turbulence in the free troposphere and stratosphere. In this regard, the VHF

and UHF Doppler radars are particularly well suited because of their all weather and day/night capabilities. The Penn State Department of Meteorology is now completing a mesoscale triangular network of three VHF radars under funding provided by the DoD (AFOSR) University Research Instrumentation Program. DoD (AFOSR and ONR) funding has also been obtained for the construction of a multichannel mm-wave radiometer system for continuous groundbased measurements of temperature profiles and integrated water vapor/liquid. Subsystems of this radiometer are now being tested. It is expected to be online at Penn State in mid 1988. Finally, a fourth Doppler radar has been constructed. It is a UHF system similar in concept to the VHF systems but operating at 0.75 m rather than 6 m wavelength. The UHF system has a smaller, more portable antenna, better vertical resolution (100 m vs. 300 m for the VHF systems) and far superior low altitude capabilities (minimum range of 200 m). The radar systems are capable of producing a wind and turbulence profile with roughly 30 to 90 second time resolution. Thus, they are also ideal for highly detailed studies of turbulence and its relationship to mesoscale phenomena. The combination of the mesoscale triangle of VHF profilers, the UHF profiler and the radiometers constitutes an atmospheric observing system that represents a quantum jump in our ability to study the atmosphere.

This report describes a two year project to use these systems to study the seasonal and diurnal climatology of  $C_n^2$ , the atmospheric dynamical processes responsible for the variability of  $C_n^2$ , and to investigate measurement methods and models of  $C_n^2$ . The results have been published in the open literature (see section VIII) and in a number of graduate assistant M.S. theses [Beecher (1987), Carlson (1987), Knowlton (1987), Neiman (1987), and Syrett (1987)]. The work combined the full power of the department's

observing systems, access to national data networks and weather/satellite information, and cooperation with a number of government research laboratories. During the study an intensive field program was held at Penn State involving in situ measurements with aircraft and thermosonde balloons and a variety of ground based electro-optical systems (e.g., scintillometers). This study was given the acronym EWAK and involved scientists from a number of DoD laboratories (see section IV). The purpose of EWAK was to compare measurement methods and to test/develop models of clear air turbulence. The emphasis on relating turbulence to mesoscale and synoptic scale structures was intended to promote the extension of the results to different climatological regions. A thorough understanding of these relationships should lead to assessment and forecasting of atmospheric turbulence with a combination of satellite informational and numerical global weather models.

## II. Refractive Index of Air

For many purposes the effects of atmospheric gas on propagating electromagnetic and acoustic radiation may be conveniently subdivided into the following subcategories:

- a) mean density gradients result in beam refraction and, consequently, tracking or pointing errors,
- b) density and velocity fluctuation caused by turbulence produce refractive index variations which, in turn, degrade system performance.

Regarding the bulk radar refractive index,  $n$ , of atmospheric gas it is convenient to specify it in terms of the refractivity,  $N = (n-1) \cdot 10^6$ , in which case

$$N = 77.6 (P + 4810 e/T)/T \quad (1)$$

where  $N$ ,  $T$ ,  $P$  and  $e$  are in units of ppm, K, mb (total pressure), and mb (vapor pressure), respectively. The second term including  $e$  specifies the contribution by polar molecules (principally water). It is often negligible at optical frequencies where the humidity coefficient is much smaller.

For specification of the effects of turbulence the relevant atmospheric properties are the refractive index structure function parameter,  $C_n^2$ , (Tatarski, 1961) and the inner scale or Kolmogorov scale of turbulence,  $L_k$  (Livingston, 1972; Hill and Clifford, 1978).  $C_n^2$  can be related to micrometeorological variables by (Wesely, 1976)

$$C_n^2 = A(C_T^2 + 2 B C_{Tq} + B^2 C_q^2) \quad (2)$$

where  $A$  and  $B$  are functions of temperature ( $T$ ), pressure and specific humidity

(q);  $C_T^2$ ,  $C_{Tq}$ , and  $C_q^2$  are the temperature and humidity structure function parameters. The values of A and B are also radiation-type and wavelength dependent.  $L_k$  is related to the viscosity and density of air (both functions of altitude) and the rate of dissipation of turbulent kinetic energy,  $\epsilon$  (Hinze, 1975).

### III. Background on Clear Air Turbulence

#### A. Microturbulence

In general, atmospheric turbulence is anisotropic. However, it is known that at small size scales (large values of wavenumber,  $k$ ), the eddies become increasingly isotropic. In the isotropic limit it can be shown that (Hinze, 1975) the structure function parameter,  $C_x^2$ , for the unspecified variable,  $X$ , ( $X$  could be  $u$ ,  $T$ ,  $q$ , or  $n$ )

$$C_x^2 = \langle (X(r) - X(r+d))^2 \rangle / d^{2/3} \quad (3)$$

is independent of the spacing,  $d$ . In this equation  $X(r)$  denotes the value of  $X$  at position  $r$  while  $X(r+d)$  denotes the value at a position a distance  $d$  from  $r$ ; the brackets denote an average. Using dimensional arguments, Kolmogorov showed that in the isotropic limit the one-dimensional variance spectrum obeys a  $k^{-5/3}$  wavenumber dependence

$$\varphi_x(k) = \beta_x \chi_x \epsilon^{-1/3} k^{-5/3} \quad (4)$$

where  $\chi_x$  is the rate of dissipation of one half of the variance of  $X$  and  $\beta_x$  is an empirical constant (on the order of 0.5 for velocity and 0.8 for scalars). It can similarly be shown that

$$\varphi_x(k) = 0.25 C_x^2 k^{-5/3} \quad (5)$$

where the factor 0.25 represents several mathematical constants. Note that (4) and (5) imply the Corrsin relation



$$C_x^2 = 4 \beta_x x_x \epsilon^{-1/3} \quad (6)$$

Velocity is a special case (since  $x_u = \epsilon$ ) so that

$$C_u^2 = 2.0 \epsilon^{2/3} \quad (7)$$

#### B. TKE and Variance Budget Equations

The simplified, horizontally homogeneous budget equations for TKE (symbol E) and scalar variance (symbol  $\langle x^2 \rangle$ ), are

$$DE/Dt = -\langle uw \rangle \partial U / \partial z + (g/\theta) \partial \theta / \partial z - \epsilon + \text{transport} \quad (8a)$$

$$D(\langle x^2 \rangle / 2) / Dt = -\langle xw \rangle \partial X / \partial z - x_x + \text{transport} \quad (8b)$$

where the small symbols denote turbulent fluctuations and the capital symbols denote average values, U is the streamwise velocity, W the vertical velocity, g the acceleration of gravity,  $\theta$  the potential temperature and z the altitude. Assuming a state of dynamic equilibrium, neglecting transport, and using an eddy diffusion coefficient, K, to express the covariance term

$$\langle uw \rangle = -K_m \partial U / \partial z \quad (9a)$$

$$\langle xw \rangle = -K_x \partial X / \partial z \quad (9b)$$

we can use (8) to express the dissipations

$$\epsilon = K_m (\partial U / \partial z)^2 [1 - Ri / Pr] \quad (10a)$$

$$\chi_x = K_x (\partial X / \partial z)^2 \quad (10b)$$

where  $Pr = K_m / K_H$  is the turbulent Prandtl number and  $Ri$  is the gradient Richardson number

$$Ri = N^2 / S \quad (11)$$

The factor  $S$  is the square of the vertical gradient of the vector mean wind and  $N$  is the Brunt-Vaisala frequency, which in the atmosphere is approximately given by

$$N^2 = (g/\theta) \partial \theta / \partial z \quad (12)$$

Using (10) we can obtain the ratio of the scalar dissipation to the TKE dissipation

$$\chi_x / \epsilon = (\beta_u / \beta_x) C_x^2 / C_u^2 = [(\partial X / \partial z)^2 / N^2] Ri / (Pr - Ri) \quad (13)$$

In the oceanographic literature (Gregg, 1987), this is expressed in terms of the mixing coefficient,  $\gamma$ ,

$$\gamma_x = \chi_x N^2 / [(\partial X / \partial z)^2 \epsilon] \quad (14)$$

In actively turbulent layers with  $Pr=1$  and  $Ri=0.25$ , (13) implies  $\gamma=Ri/(Pr-Ri)=1/3$ . Gossard and Frisch (1987) have used the shear budget

equations to show that  $\beta_x \gamma / \beta_u \approx 3/2$  while Gage and Nastrom (1986) have shown that equipartition of two-dimensional TKE and potential energy due to gravity wave displacements in a stratified fluid implies  $\beta_x \gamma_\theta / \beta_u = 2$  for large scale (anisotropic) turbulence. As we shall discuss later, relations derived from (13) have been used to compute  $\epsilon$  and  $K_m$  from clear air radar data.

### C. Clear Air Turbulence Length Scales

The field of turbulence contains a bewildering variety of length scales which we will not attempt to discuss here. For our purposes, we focus on the smallest scales present, the Kolmogorov microscale  $L_k$ , and the scale of the dominant vertical motions (eddy overturning scale)  $L_o$ , which is related to the integral scale calculated from the vertical velocity autocorrelation function. At the Kolmogorov scale, viscosity is rapidly destroying the turbulent fluctuations; the spectrum begins to deviate from the -5/3 behavior at sizes an order of magnitude larger than this (Hill and Clifford, 1978). In stratified turbulence, the overturning scale is proportional to the buoyancy length scale,  $L_b$  (Gregg, 1987), also referred to as the Ozmidov scale. In terms of the turbulent parameters, these scales are

$$L_k = (\nu/\epsilon^3)^{1/4} \quad (15a)$$

$$L_b = (\epsilon/N^3)^{1/2} \quad (15b)$$

The inertial subrange occurs for those size scales smaller than  $L_b$  and greater than  $L_k$ . If  $L_b = L_k$ , then the energy containing vertical motions are rapidly destroyed by viscosity; if  $L_b = 10L_k$ , then no inertial subrange is anticipated.

The ratio of the length scales forms a natural activity parameter to

classify the turbulent state (Gibson, 1987)

$$A = (L_b/L_k)^{4/3} = \epsilon / (\nu N^2) \quad (16)$$

Gregg (1987) suggests the following empirical classifications

<u>Value of A</u>	<u>Turbulent State</u>
A < 15	Decaying turbulence, $\langle wu \rangle \langle w\theta \rangle \approx 0$
A > 200	Isotropic
A > 10000	Fully developed

The physical interpretation of the mixing coefficient and the activity parameter can be illustrated by noting that the turbulent diffusivity can be expressed as  $K_x = A_t \gamma_x \nu$ . Thus, when the product of the activity parameter and the mixing coefficient exceeds one, then the turbulent mixing processes are more efficient than molecular diffusivity.

The concept of length scales is also used to eliminate the eddy diffusion coefficients from (10) by invoking mixing length theory (Hinze, 1975)

$$K = c_1 E^{1/2} L_o \quad (17)$$

where  $c_1$  is an empirical constant and the square root of  $E$  represents a velocity scale. The dissipation is also related to these quantities

$$\epsilon = c_2 E^{3/2} / L_o \quad (18)$$

These relations can be used in (10) to yield

$$C_u^2 = 2 \epsilon^{2/3} = 2 (c_1/c_2^{1/3}) (\partial U/\partial z)^2 L_o^{4/3} \quad (19a)$$

$$C_x^2 = 2 (\beta_x/\beta_u) (c_1/c_2^{1/3}) / (Pr-Ri) (\partial X/\partial z)^2 L_o^{4/3} \quad (19b)$$

Notice that (19a) can be manipulated to give

$$\epsilon/N^3 = (c_1^{3/2}/c_2^{1/2})/Ri^{3/2} L_o^2 = L_b^2 \quad (20)$$

The most common convention is to fix the ratio  $c_1/c_2^{1/3}=1$  and to assume that in actively turbulent layers  $Ri=0.25$ . This implies that  $L_o=0.35 L_b$  (Hocking, 1982). Because the constants are chosen arbitrarily, there is no physical significance to this particular ratio of  $L_o$  to  $L_b$ . Since  $L_b$  is considered to be the outer limit of the validity of the inertial subrange, it makes sense that the true integral scale and the energy containing scale are larger than  $L_b$ . It is also clear that application of these expressions is likely to be confused by our inability to be sure of the values of  $Pr$  and  $Ri$  and by the fact that the assumptions of stationarity and negligible transport will not be valid in all conditions.

#### D. Statistical Models of $C_n^2$

Van Zandt et al. (1978,1981) have developed a model of  $C_n^2$  based on a statistical integration of simplified forms of (19). In this approach, a smooth mean profile with a vertical resolution roughly equivalent to a rawinsonde is the input. Velocity and temperature (and, therefore, shear and temperature gradient) fluctuations are allowed (relative to the mean profile) with probability distributions obtained from a mix of empirical analysis and theory about gravity wave effects. Active turbulent regions are assumed to

exist when the fluctuations produce  $Ri < 0.25$ . By integrating the joint probability distribution over shear, temperature gradient, and size scale space, an average value,  $\langle C_n^2 \rangle$ , is computed.

The value of  $\langle C_n^2 \rangle$  obtained in this manner is the expected value at some altitude; as such, it does not actually contain any information about the vertical distribution. We can see that, at any specific time, quite different results for  $C_n^2$  can be obtained from measurements depending on the vertical resolution. Suppose that the vertical resolution (e.g., a radar range gate of several hundred meters) is much greater than the turbulent patch thickness,  $H$ . In this case, we would expect that the radar produces sufficient averaging to be consistent with model assumptions. A high resolution radar, or a high vertical resolution in situ measurement (e.g., an aircraft flying at constant altitude) is likely to produce a measurement that is either in an inactive region or in an active region. Thus a high resolution measurement at a particular altitude may require averaging over a long period of time to be consistent with the model. The time required would be many times longer than the typical lifetime of an actively turbulent layer, which appears to be on the order of a few hours (Syrett, 1987; also, see the discussion in Section III-F).

In an earlier paper Van Zandt et al. (1978) examined this issue with their statistical model by computing the probability of turbulence occurring at a fixed altitude,  $F$ . This has been interpreted by some (e.g., Weinstock, 1981) as the expected fraction of a range gate of thickness,  $2\Delta$ , that is occupied by turbulence of average scale,  $L_b = L_0$ , i.e.,  $F = L_b / (2\Delta)$ . Obviously, this assumes that the patch thickness is much less than the range gate thickness and that only one layer is likely to occur per range gate. Thus, average measurements produced in this fashion are interpreted as

$$\langle \epsilon \rangle = F \epsilon \quad (21a)$$

$$\langle C_x^2 \rangle = F C_x^2 \quad (21b)$$

where the values on the right hand side represent data within the active layers where  $Ri=0.25$ . While the value of  $F$  depends on the mean conditions, Gage et al. (1980) use the model to show that  $F^{1/3} N^2$  is approximately constant and has the value of  $4 \cdot 10^{-5}$  in the troposphere and  $8 \cdot 10^{-5}$  in the stratosphere.

The Van Zandt model has never been tested in detail. It has been evaluated by comparing radar measured  $C_n^2$  with predictions from rawinsondes. In a few cases, optical and in situ data have also been used. On average, the model does quite well for  $C_n^2$ ; this is not shocking because the model originally contained one unspecified constant which was selected to fit radar data. The internal details of the model, such as the probability distributions for shear,  $N$ , and  $F$ , have not been evaluated. Also, the model appears to overpredict  $\epsilon$  by two orders of magnitude (Fairall and Markson, 1984). Even the model predictions of  $C_n^2$  have never been examined for a large data set. Furthermore, the model is incomplete in that it provides information about the probability of observing turbulence ( $F$ ) and, perhaps, the typical size scale of the turbulence ( $\langle L_0 \rangle$ ), but it tells us nothing about the vertical distribution of turbulent regions nor does it guarantee that the patch size ( $H$ ) is the same as  $L_0$ . Observations in the ocean (Gregg, private communication) and in the atmosphere (Barat and Bertin, 1984) show that  $H \gg L_0$ .

#### E. Inactive Regions

The Van Zandt model partitions the atmosphere vertically into regions with active turbulence ( $Ri < 0.25$ ) and regions that are considered to be nonturbulent (or the turbulence makes a negligible contribution to the average of  $C_n^2$ ). By inactive, we mean that there is no production of TKE or variance which implies that the covariance terms in (9) must be zero. This condition is met when the activity parameter is less than 15. Thus, we can define a threshold value (Gibson, 1987) for the dissipation rate,  $\epsilon_t$ , such that values of  $\epsilon$  less than  $\epsilon_t$  imply decaying turbulence,

$$A_t = \epsilon_t / (\nu N^2) = 15 \quad (22)$$

A typical value in the free troposphere is  $\epsilon_t \approx 5 \times 10^{-8} \text{ m}^2 \text{ s}^{-3}$ . Even if  $A > 15$  the turbulence may be decaying if the destruction terms exceed the production terms. Sometimes the term 'fossil' turbulence is used to describe this state although that term is also applied to residual temperature structure that remains after the velocity turbulence has been consumed.

Decaying turbulence has been extensively studied in the laboratory using flow through grids (e.g., Itsweire et al., 1986). Atmospheric studies are quite rare, although Nieuwstadt and Brost (1986) performed a large eddy simulation model study of the decay of convective turbulence. We can use the TKE budget equation to analyze decaying turbulence, where we drop the production terms

$$\partial E / \partial t = -\epsilon \quad (23)$$

However, if we eliminate  $E$  with (18), then we obtain a differential equation for  $\epsilon$



$$d\epsilon/\epsilon^{4/3} = -(3/2) (c_2/L_o)^{2/3} dt \quad (24)$$

If we assume that the size scale remains constant throughout the decay process then (24) has the solution

$$\epsilon = \epsilon_o (1 + t/t_o)^{-3} \quad (25)$$

where  $\epsilon_o$  is the value of  $\epsilon$  at the beginning of the decay process and  $t_o$  is

$$t_o = 2 [L_o^2/(c_2^2 \epsilon_o)]^{1/3} = c_2^{-2/3} N^{-1} \quad (26)$$

Measurements in the ocean (Dillon, 1982) suggest  $t_o N = 0.3$ , which implies that an inactive region has a turbulent lifetime that is only on the order of a Brunt-Vaisala period. However, this is the value of Brunt-Vaisala period within the turbulent layer itself, which may be much longer (because of mixing) than the value associated with the mean background temperature profile (about two minutes in the atmosphere).

#### F. Active Regions

The dynamics and time scales of regions of active turbulence are fairly complicated and very little complete data is available to aid in the analysis. It is generally conceded that the turbulence is initiated by Kelvin-Helmholtz instability when the Richardson number decreases to a value near 0.25. Several physical processes are able to cause this decrease. Nonturbulent portions of the atmosphere are subjected to fluctuations in shear and/or potential temperature gradient caused by gravity wave disturbances. These fluctuations may cause turbulence as described in the section on statistical

models of CAT. Synoptic and mesoscale dynamical processes also cause evolutions in the shear and lapse rates which can cause turbulence. A classic example of this is the persistent regions of CAT found above and below well developed jet streams. If we take the vertical derivatives of the standard budget equations for the mean wind and potential temperature, then we can create budget equations for the evolution of mean shear and mean lapse rate. These can, in principle, be combined to yield a budget equation for the Richardson number- a 'Richardsonnumberogenesis' process, to paraphrase meteorological jargon.

Once a layer of thickness,  $H$ , becomes turbulent, it is of interest to ponder the temporal duration of the turbulent event. If the turbulence is caused by a gravity wave fluctuation, then we do not expect the event to last more than a fraction of an inertial period (say, a few hours). If the breakdown is due to synoptic processes, then in principle the turbulence can endure as long as the 'Richardsonnumberogenesis' can maintain the instability against turbulent mixing. Once a layer is turbulent, the mixing process tends to cause  $Ri$  to increase. This is because  $\partial U/\partial z$  and  $\partial \theta/\partial z$  are both reduced by mixing, but  $\partial U/\partial z$  occurs as the inverse square in  $Ri$ . Thus, we anticipate that the mixing caused by the turbulence forces  $Ri$  to increase until  $Ri=1$ . At this point, shear production of TKE is roughly canceled by buoyant destruction and the turbulence begins to decay due to dissipation. This process occurs long before we reach  $\epsilon_c$ . In other words, shear production is still active, the fluxes are still nonzero, but buoyant destruction and dissipation exceed production. The layer is decaying but it is still active.

This suggests that we must consider two more time scales: the time scale for the mixing process to occur,  $\tau_m$ , and the time scale for the active region to decay to  $\epsilon_c$ . We assume that the mixing process must transform

kinetic energy into potential energy by destroying the ambient potential temperature gradient for a layer of thickness. Gregg (1987) has shown that this requires an amount of energy equal to  $(1/12)N^2H^2$ , where  $N$  is computed from the background lapse rate when turbulent breakdown occurs. Suppose we let  $P$  be the shear production of TKE and  $B$  the buoyant destruction integrated of the entire thickness of the layer (thus, transport terms become zero); then in a state of slowly evolving equilibrium, the TKE budget equation implies the balance

$$P = B + \epsilon \quad (27)$$

If we substitute the flux Richardson number,  $Rf=P/B$ , we get a relation for the mixing time constant

$$\epsilon \tau_m = (1/Rf-1)B\tau_m = (1/Rf-1)N^2H^2/12 = [(Pr-Rf)/Rf] N^2H^2/12 \quad (28)$$

Therefore, we can write  $\tau_m$  as

$$\tau_m = N^2H^2/(12 \epsilon \gamma) \quad (29)$$

Aircraft measurements of the covariance and gradient terms (Kennedy and Shapiro; 1975, 1980) in the vicinity of the jet stream give an average value of  $\gamma=0.40$ . Representative values in (29) give  $\tau_m$  on the order of 1 hour for a 100 m thick layer with  $\epsilon=1 \times 10^{-4} \text{ m}^2 \text{ s}^{-3}$ . Notice that (29) implies that thicker layers and weaker layers ( $\epsilon$  smaller) will persist much longer.

Once the layer has been mixed as discussed above, then the turbulence begins to decay with the time constant  $t_0$  described in III-D. According to

(25), even if  $t_0$  is relatively short (a few tens of minutes), it will still take hours for  $\epsilon$  to decay from  $10^{-4}$  to the transition level of  $5 \cdot 10^{-8}$ .

#### IV. Applications of VHF and UHF Radar

The use of radar data in optical propagation and CAT studies requires consideration of several factors: radar resolution, range and measured variables, the relationship of radar and optical parameters, and the types of studies that are appropriate for these systems. Details are provided in the literature (e.g., Hocking, 1982) and in our previous proposal, but a brief summary of the main points will be presented here.

The 50 MHz radars have vertical range gate resolution of 300 m up to 8 km and 900 m resolution up to 18 km. The high resolution mode requires 90 s to obtain one profile, the low resolution 3 minutes. In normal operations, a pair of resolution profiles is obtained in 5 minutes. The UHF radar has 100 m resolution to 2.6 km, 300 m resolution to 8 km, and 900 m resolution to 12 km. Both systems have two horizontal and one vertical beam.

The basic raw data produced by the radar is the mean Doppler shift (which is used to compute the mean wind vector), the width of the Doppler spectrum (which is related to the turbulence associated with the wind variance or the mean shear and can be used to estimate  $\epsilon$ ), and the backscatter intensity of the signal (which is related to the radar cross section and is used to calculate radar  $C_n^2$ ). Details concerning the computation of  $C_n^2$  from the radar signal are discussed in Appendix B. Thus the radar provides quantitative measurements of the profiles of  $U$ ,  $\partial U/\partial z$ ,  $\sigma_u$ ,  $\sigma_w$ , and  $C_n^2$ . Models can be applied to this data to estimate  $\epsilon$  (e.g., equation 13),  $K$  (e.g., equation 10), and even  $\partial\theta/\partial z$ .

The radars normally operate continuously and archive data in one hour average blocks. For intensive experiments, we archive the high resolution (temporally and spatially) data, including the raw Doppler spectra and all moment tables. An example of a time series of  $C_n^2$  from two range gates of

a VHF system is shown in Fig. 1. A few examples of studies ideally suited to these systems are: vertical distribution of  $C_n^2$  'hot spots', comparison of daytime versus nighttime  $C_n^2$  at different times of the year, coincidence of high turbulence levels and wind shear/jet stream regions, and correlation with synoptic regimes.

V. Summary of Work Performed

A. Background

This project is concerned with the relationship of meteorological conditions to parameters and processes that influence the optical propagation properties of the turbulent atmosphere. The approach is centered around the establishment of a climatology of refractive index structure function parameter as measured with a network of Doppler radars. The relation of the atmospheric turbulence profile to the synoptic context and a model to predict the profile using standard meteorological profile data is also being investigated. The study features two modes of data archiving: (1) continuous archiving of 1 hr average wind profiles and turbulence levels, and (2) high time resolution measurements in association with other measurements (ground-based optical scintillometers, aircraft or radiosondes) in an intensive 'campaign' given the acronym EWAK.

This project funded one graduate assistant (Syrett) who studied the correlation of turbulence with synoptic context (in relation to jet streams). Two Air Force graduate students have also been working on the project. Capt. Michael Moss is completing a Ph.D. dissertation involving radar data and the Van Zandt model and 2nd Lieut. Elizabeth Beecher has completed a comparison (M.S. thesis) of meteorological and optical microstructure from radar and in situ (particularly aircraft) measurements.

B. The EWAK Experiment

A major optical/meteorological experiment (acronamed EWAK) was held at Penn State from 15 April to 15 May, 1986. Rome Air Development Center (RADC) was planning a combined aircraft/optical experiment for the spring and we convinced them to hold the field program at PSU in order to take advantage of the radar data. Given the scale of this experiment, optical propagation

scientists from several other laboratories were also invited to participate. The enclosed table is a brief summary of the measurements and participants. All optical equipment was operated during an intensive period from 30 April to 6 May when the skies were clear on every night but one. Four aircraft flights were made (another four flights had been made earlier to calibrate the radar) and approximately 35 thermosondes were launched during this period. High time resolution data were logged on the VHF radar and the sodar was operated continuously during the optical measurements. Synoptic meteorological information was carefully analyzed and archived. A meeting was held at AFGL in early September to discuss the preliminary results. One of the PI's (CWF) and three graduate students attended and made presentations.

The standard radar equation is used to calculate  $C_n^2$  from the received power. The calibration factor for the radar is a combination of a number of system constants: antenna gain, line loss, receiver noise, etc. However, the antenna gain for the colinear-coaxial phased arrays used with the Doppler radars has never been rigorously measured. Thus, even the most careful determination of the other calibration factors cannot eliminate all of the uncertainty. Because of this, since the Penn State radars are modeled after the NOAA/WPL systems, we initially decided to use the system constants from the NOAA radars. The analysis of the EWAK data is still ongoing, but it has revealed that the radar calibration is quite good; the values of  $C_n^2$  need to be increased by about a factor of two to agree with the thermosonde balloon measurements. A sample comparison of the uncorrected radar, thermosonde and aircraft profiles of optical  $C_n^2$  is shown in Fig. 2.



Summary of measurements for the EWAK experiment.

<u>Measurement</u>	<u>Institution</u>	<u>Contact</u>
Surface micromet	PSU	C.Fairall
Sodar	PSU.	D.Thomson
VHF1,VHF2	PSU	D.Thomson
Thermosonde ( $C_n^2$ )	AFGL	J.Brown
Aircraft	ARA	R.Markson
Optical $C_n^2$ profile#1	RADC	D.Stebbins
Optical $C_n^2$ profile#2	AFGL	E.Murphy
Optical scintillometer( $r_0$ )	NPS	D.Walters
Optical isoplanometer	AFWL	J.Davidson

Analysis of the aircraft data has been completed and published initially in December (Beecher, 1987) in the form of an M.S. thesis. An initial scientific publication has also been completed (Fairall et al., 1988). We will present a few examples from this work. Fig. 3 shows a sample aircraft profile of microturbulence data from one of the eight flights made during EWAK. Fig. 4 shows two comparisons of optical  $C_n^2$  obtained from the aircraft, the thermosonde, the radar, the Van Zandt model and optical scintillometer data. The optical data is highly variable over the one hour period but is in agreement with the thermosonde and clearly lower than the other two independent methods. Finally, a conglomerate analysis of the small scale turbulence from all flights is shown in Fig. 5. Here the relation of thermal and velocity microstructure (as in equation 13) is examined. Notice that for the special case of temperature

$$(\partial X / \partial z)^2 / N^2 = (T/g) \partial \theta / \partial z \quad (30)$$

By plotting  $C_T^2$  versus  $(T/g) \partial \theta / \partial z C_u^2$  in log-log format, we expect the points to define the dependence of  $\beta_\theta \gamma_\theta / \beta_u$ . If  $\gamma_\theta$  is constant, then we expect a straight line with a slope of one. Clearly this is not what we observed. For strong turbulence (clearly active and nondecaying regions with  $\epsilon > 10^{-4}$ ), the data gives a value of  $\gamma_\theta$  of about 0.5, which is consistent with the jet stream value 0.4 of Kennedy and Shapiro (1980) and the oceanic value 0.3 of Gregg (1987). For the weaker turbulence cases, this value increases by about a factor of 10. The significance of this is not clear. Presently we are not sure of the effects of the vertical averaging necessary to produce the 300 m resolution which is required in order for the data to be compatible with that from the radar.

The second part of the EWAK study is an in depth investigation of the radar  $C_n^2$  and wind data for the EWAK period by Mike Moss, an Air Force graduate student enrolled at Florida State University. This work involves the Van Zandt model, the thermosondes, and the optical data. Since this is a Ph.D. thesis project (which requires three or four years of work), we do not anticipate final results until next year. A preliminary description of the work in progress has been prepared (Moss, 1986).

### C. Climatological/Synoptic Studies

The initial steps in the climatological study of the synoptic context of  $C_n^2$  have been completed. We have been routinely archiving winds and power at one hour intervals. During a one year period, each hour was assigned a synoptic classification based on the weather charts. A grand ensemble analysis of this data base has not been started. For the purposes of this project, we have completed a detailed analysis of one selected synoptic

feature that is of particular interest: the jet stream and the wind shear in its vicinity. This work has now been published initially in the form of an M.S. thesis (Syrett, 1987). A scientific publication is now in preparation (Syrett and Thomson, 1988). Another phase of this work involves comparison of the radar measured winds with both analyzed and predicted winds for the NWS Nested Grid Model (NGM). A paper on this topic has been presented (Thomson et al., 1988). This work is relevant to the numerical prediction of  $C_n^2$  from NGM products.

Hourly measurements of wind speed and direction were examined for two prolonged jet stream occurrences over western Pennsylvania. Data from two of the Penn State radars (McElevys Fort and Crown) were stratified into categories based on location of the jet axis relative to the site. Low resolution data from the Crown radar were also compared to the Pittsburgh rawinsonde. Potential temperature profiles were obtained using isentropically interpolated T and  $T_d$  soundings. The combination of measured wind and interpolated temperature profiles allowed low resolution Ri profiles to be generated for the profiler sounding volume. Both Ri and wind shear statistics were examined along with pilot reports of turbulence in the vicinity of the profiler.

Two cases were examined. Case 1 lasted from 7 November to 14 November 1986. Jet stream case 2 lasted from January 15 to January 23, 1987. A sample time-height cross section of wind speed (Fig. 6) illustrates the structure and variability of the jet stream at the Crown site (just north of Cook Forest in western Pennsylvania). The data were separated into five position categories. The average wind speed and Ri profiles for case 2 are shown in Fig. 7. The vertical resolution of the profiler data is slightly less than 1 km, but was interpolated to 250 m resolution for the analysis. The potential temperature

profiles also have low horizontal resolution because they are extracted from smoothed fields from the NWS observing network. Notice the minima in  $Ri$  in the regions of maximum shear above and below the peak of the jet. Pilot reports of the altitude and severity of turbulence for the western Pennsylvania region were compiled for the period of the event (Fig. 8). The PIREPS were most closely correlated with the magnitude of the shear observed by the radar, rather than the occurrences of low values of  $Ri$  (Fig. 9). This figure unequivocally shows that regions of strong shear are almost sure to have severe turbulence. This is consistent with (19a) which implies the strongest turbulence in the thickest layers (largest  $L_0$ ) and the regions of greatest wind shear ( $\partial U / \partial z$ ). Also, recall that (29) implies that the thickest layers are also the longest lived and, therefore, the most likely to be encountered by aircraft. This result suggests that, as far as severe turbulence is concerned, it is probably a mistake to attempt to derive the Richardson number from low resolution sources, partly because regions of strong shear are likely to have small  $Ri$  anyway.

Preliminary results from the comparisons of the profiler winds with the NGM winds have been surprising. The profiler winds have been compared with analyzed (0 hour 'forecast') and predicted (48 hour forecast) NGM winds. The NGM data is interpolated to the profiler location (both Crown and McElevys Fort sites were used). The profiler data has been examined with several time resolutions: the basic one hour average at the time of the NGM data, a seven hour average (plus and minus three hours about the time of the observation), and a thirteen hour average. The comparison is best for the longer time average, indicating the amount of spatial averaging inherent in the regional scale model or smoothing of extreme observations in the radar data. A sample comparison for the 500 mb wind speed and direction for May, 1987, is shown for

the analysis (Fig. 10) and the 48 hour forecast (Fig. 11). The initial analysis is typically 2.5 m/s different from the radar data and there appears to be no significant systematic bias in the wind direction. It is believed that the NGM underestimates the winds compared to the radar because of smoothing of the fields in the analysis procedure. The 48 hour forecast is noticeably more inaccurate than the analysis, but the deterioration is surprisingly small.

## VI. Suggested Future Research

The general goal of this research is to investigate the fundamental relationships between mean atmospheric structure and microturbulence parameters such as  $C_n^2$ . We wish to study the processes that lead to temporal/horizontal variability and vertical distribution of  $C_n^2$ . The next obvious step in this investigation is to acquire and analyze data from three primary sources:

- (1) Existing data. Radar data from VHF1 and VHF2 archived over the past two years will be available for completion of a climatological analysis. Raw aircraft turbulence data, which is archived on FM tapes, and raw aircraft mean profile data, which is archived on digital tapes with 2 second resolution, from the EWAK experiment could be reanalyzed with finer resolution.
- (2) New Profiler data. We will continue to archive one hour average radar data from VHF1, VHF2, and VHF3 (which is to be in operation in September, 1988). We will also archive one hour average data from the UHF radar, which is to begin regular operation at State College in July, 1988. Also, we hope to begin operation of the mm-wave radiometer system in State College about July of 1988. This system will archive two minute time resolution measurements of integrated water vapor/liquid and temperature profiles. The mesoscale triangle (about 140 km sides) of VHF radar combined with the UHF and thermodynamic sounders will provide an unprecedented look at atmospheric turbulence and dynamical processes.
- (3) Intensive Turbulence and Optical Propagation Experiment (EWAK II). Sometime in the near future it makes sense to have another field program similar to EWAK. We would try to work with the same

institutions as before for the optical measurements. We could also try to interest and invite NASA and NOAA groups with relevant measurement systems (e.g., Melfi's raman lidar).

The variety of scientific issues of interest were discussed in section III. We can divide the issues into four general categories: spatial structure, turbulence dynamics, climatology/synoptic correlations, and comparisons of optical, radar and in situ measurements.

#### A. Spatial Structure

The vertical distribution of the active turbulence areas can be studied with combined aircraft and radar data. We are interested in the probability distributions of patch size, patch lifetime, turbulence scales, and the autocorrelation functions of patch distribution. We can also use aircraft measurements to examine the probability distributions of lapse rate and shear (basic parameterizations in the Van Zandt model). The horizontal and temporal persistence of individual turbulent layers can be studied by cross correlation the  $C_n^2$  data from the three VHF radars and by examining level flight aircraft data.

#### B. Turbulence Dynamics

Here the emphasis is on the microturbulence scaling relations (e.g., the ratio  $C_T^2/C_u^2$ ), the generation and decay process, and the turbulence size scales ( $L_b$  and  $L_o$ ). Aircraft, radar and thermosonde data can all be used. We suggest investigating the use of the radar to measure  $\epsilon$  from the width of the Doppler spectrum. Furthermore, we can compare  $\epsilon$  derived from the width of, for example, a 300 m range resolution spectrum with that from the mean shear derived from overlapping 100 m range resolution data. Thus, we can examine simultaneous measurements of  $C_T^2$  and  $C_u^2$ . The size scales of turbulence can be investigated in several ways. The operation of colocated

VHF and UHF radar will also provide information about the relative intensity of turbulence size scales since they scatter from different atmospheric scales ( $\lambda/2=3$  m and 0.3 m respectively). Profiles of mean temperature from aircraft, rawinsonde, thermosonde, and radiometers would give an indication of  $N$  which, combined with  $\epsilon$ , gives  $L_b$ . The vertical velocity spectrum from the radar can also give an indication of size scales. In active turbulent layers it should reveal  $L_0$ ; in more quiescent layers it should indicate  $N$ . In the intensive experiment, a great deal of effort could be devoted to examining these issues.

#### C. Climatology/Synoptic

The mesoscale triangle of VHF radar will provide high quality dynamical variables usually not available (e.g, divergence and vorticity) that will be extremely useful in interpreting variability in  $C_n^2$ . For example, the jet stream study referred to in section IV would have greatly benefited from a more quantitative classification of conditions than the crude 'distance from the jet axis' categories used. The temperature/humidity radiometers also provide very accurate estimates of dynamic height (e.g., 500 mb) to augment the radar information. We presently plan to continue the large scale synoptic classifications for the gross climatological analysis. We will also continue the studies of the comparisons of radar data and NGM analyzed and forecast fields.

#### D. Comparison of Optical and Meteorological Sensors

We strongly recommend that another joint meteorological and optical experiment be held at Penn State. EWAK I revealed that there are still substantial differences between the various observing systems (often an order of magnitude). Some of this is due to differences in temporal and spatial averaging techniques but a great deal of the disagreement must be due to



undiagnosed problems with the sensors and data processing. A new intensive program would also provide us with other sources of data (e.g., thermosondes and aircraft) and much better spatial and temporal resolution of the important variables. This is necessary, in particular, to determine the importance of the averaging process on the interpretation of measurements and models.

## VII. References

- Barat, J. and F. Bertin, 1984: Simultaneous measurements of temperature and velocity fluctuations within clear air turbulence layers: Analysis of the estimate of dissipation rate by remote sensing techniques. J. Atmos. Sci., 41, 1613-1619.
- Beecher, E.A., 1987: Analysis of temperature and velocity microturbulence parameters from aircraft data and relation to atmospheric refraction index structure. M.S. thesis, Pennsylvania State University, ppl65.
- Carlson, C.A., 1987: Kinematic quantities derived from a triangle of VHF Doppler wind profilers. M.S. thesis, Pennsylvania State University.
- Dillon, T.M., 1982: Vertical overturns: A comparison of Thorpe and Ozmidov length scales. J. Geophys. Res., 87, 9601-9613.
- Fairall, C.W., K.L. Davidson and G.E. Schacher, 1982: Meteorological models for optical properties in the marine atmospheric boundary layer. Opt. Engineer., 21, 847-857.
- Fairall, C.W. and R. Markson, 1984: Aircraft measurements of temperature and velocity microturbulence in the stably stratified free troposphere. Proc. Seventh Symposium on Turbulence and Diffusion, AMS, Boulder, CO.
- Fairall, C.W., 1987: A top-down and bottom-up diffusion model of  $C_T^2$  and  $C_q^2$  in the entraining convective boundary layer. J. Atmos. Sci., 44, 1009-1017.
- Fairall, C.W., D.W. Thomson, and R. Markson, 1988: An aircraft and radar study of temperature and velocity microturbulence in the stably stratified free troposphere. Proc. Eighth Symposium on Turbulence and Diffusion, AMS, San Diego, CA, 61-65.
- Fried, D.L., 1966: Optical resolution through a randomly inhomogeneous medium for very long and very short exposures. J. Opt. Soc. Am., 56, 1372-1380.

- Kennedy, P.J. and M.A. Shapiro, 1975: The energy budget in a clear air turbulence zone as observed by aircraft. Mon. Wea. Rev., 103, 650-654.
- Kennedy, P.J. and M.A. Shapiro, 1980: further encounters with clear air turbulence in research aircraft. J. Atmos. Sci., 37, 986-993.
- Knowlton, L.W., 1987: Kinematic diagnoses of frontal structure and circulations derived from two and three-station VHF Doppler wind profilers networks. M.S. thesis, Pennsylvania State University.
- Livingston, P.M., 1972: A study of target edge response viewed through atmospheric turbulence over water. Appl. Opt., 11, 2352-2357.
- Moss, M.T., 1986: Measurement and modeling of tropospheric/stratospheric refractive index structure parameter. PhD thesis prospectus, Florida State University.
- Nastrom, G.D., B.B. Balsley, and K.S. gage, 1981: Change with season of  $C_n^2$  at Poker Flat, Alaska, from MST Doppler radar observations. Proc. 20th Conf. on Radar Meteorology, AMS, Boston, MA.
- Neiman, P.J., 1987: Wind profiler derived temperature gradients and advections, M.S. thesis, Pennsylvania State University.
- Nieuwstadt, F.T.M., and R.A. Brost, 1986: The decay of convective turbulence. J. Atmos. Sci., 43, 532-546.
- Syrett, W.J., 1987: Some applications of 50 MHz wind profiler data: detailed observations of the jet stream. M.S. thesis, Pennsylvania State University, ppl35.
- Syrett, W.J. and D.W. Thomson, 1988: Detailed observations of the jet stream with the Penn State VHF Doppler radar. J. Clim. Appl. Met., in preparation.
- Tatarski, V.I., 1961: Wave Propagation in a Turbulent Medium. McGraw-Hill, New York, Chapter 7.

- Thomson, D.W., W.J. Syrett, T.T. Warner, and N.L. Seaman, 1988: Comparisons of wind Profiler measurements with NMC NGM analyses and predictions. Proc. 8th Conf. on Numerical Weather Prediction, AMS, Feb. 22-25, Baltimore, MD, pp6.
- Van Zandt, T.W., J.L. Green, K.S. Gage, and W.L. Clark, 1978: Vertical profiles of refractivity turbulence structure constant: comparison of observations by the sunset radar with a new model. Radio Sci., 5, 819-829.
- Van Zandt, T.W., K.S. Gage and J.M. Warnock, 1981: An improved model for the calculation of profiles of  $C_n^2$  and  $\epsilon$  in the free atmosphere from background profiles of wind, temperature and humidity. Proc. 20th Conf. on Radar Meteorology, AMS, Boston, MA.
- Wesely, M.L., 1976: The combined effect of temperature and humidity fluctuations on refractive index. J. Appl. Meteor., 15, 43-49.

#### VIII. Summary of Publications and Presentations

The following is a list of publications and presentations at least partially funded by or directly concerned with this research project.

##### A. Publications

- Williams, S.R. and D.W. Thomson, 1986: An evaluation of errors observed in the measurement of low wind velocities. Handbook for MAP, Vol. 20, SCOSTEP secretariat, Dep. Elec. Comp. Eng., Univ. IL., 256-262.
- Williams, S.R., and R. Peters, 1986: The Penn State Doppler network progress report. Handbook for MAP, Vol. 20, SCOSTEP secretariat, Dep. Elec. Comp. Eng., Univ., IL., 339-341.
- Moss, M.T., 1986: Measurement and modeling of tropospheric/stratospheric refractive index structure parameter. PhD thesis prospectus, Florida State University.
- Beecher, E.A., 1987: Analysis of temperature and velocity microturbulence parameters from aircraft data and relation to atmospheric refraction index structure. M.S. Thesis, Pennsylvania State University, pp165.
- Syrett, W.J., 1987: Some applications of 50 MHz wind profiler data: detailed observations of the jet stream. M.S. thesis, Pennsylvania State University, pp135.
- Fairall, C.W., 1987: A top-down and bottom-up diffusion model of  $C_T^2$  and  $C_q^2$  in the entraining convective boundary layer. J. Atmos. Sci., 44, 1009-1017.
- Thomson, D.W., W.J. Syrett, T.T. Warner, and N.L. Seaman, 1988: Proc. 8th Conf. on Numerical Weather Prediction, AMS, Feb. 22-25, Baltimore, MD, pp6.
- Fairall, C.W., D.W. Thomson and R. Markson, 1988: An aircraft and radar study

of temperature and velocity microturbulence in the stably stratified free troposphere. Proc. 8th Symposium on Turbulence and Diffusion, AMS, April 24-29, San Diego, CA, 61-65.

Williams, S.A. and D.W. Thomson, 1988: Comparisons between Wind Profiler and conventional Loran/Omega based rawinsonde wind measurements. In preparation.

#### B. Oral presentations

"Clear air Doppler radar", C.W. Fairall, RISO National Laboratory (Denmark), Aug. 6, 1986.

"Turbulence measurements with Doppler profilers", D.W. Thomson, Naval Environmental Research and Prediction Facility, June 15, 1986.

"Wind and turbulence measurements with a clear air Doppler radar", C.W. Fairall, Florida State University, Aug. 28, 1986.

"An analysis of synoptic conditions during EWAK", W. Syrett, AFGL, Sept. 4, 1986.

"Radar measurements of  $C_n^2$  during EWAK", M. Moss, AFGL, Sept. 4, 1986.

"Sodar measurements of  $C_n^2$  during EWAK", T. Messier, AFGL, Sept. 4, 1986.

"Aircraft measurements of microturbulence during EWAK", C. Fairall, AFGL, Sept. 4, 1986.

"Wind Profilers", D.W. Thomson, a series of three lectures, Dept. of Meteorology, Naval Postgraduate School, Monterey, CA., Jan., 1987.

"Toward a physical model of  $C_n^2$ ", C. Fairall, Workshop on the Physics of Directed Energy Propagation in the Atmosphere, Las Cruces, NM, March 29, 1988.

"Atmospheric radar or seeing with thick air", C. Fairall, Dept. of Physics, Naval Postgraduate School, Monterey, CA, April 20, 1988.

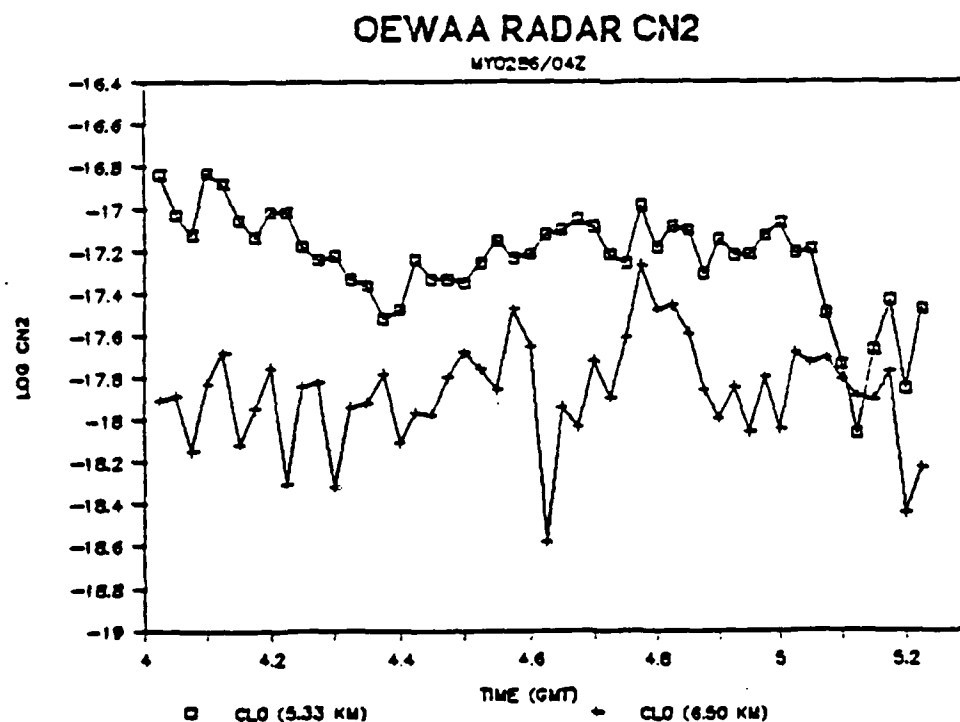
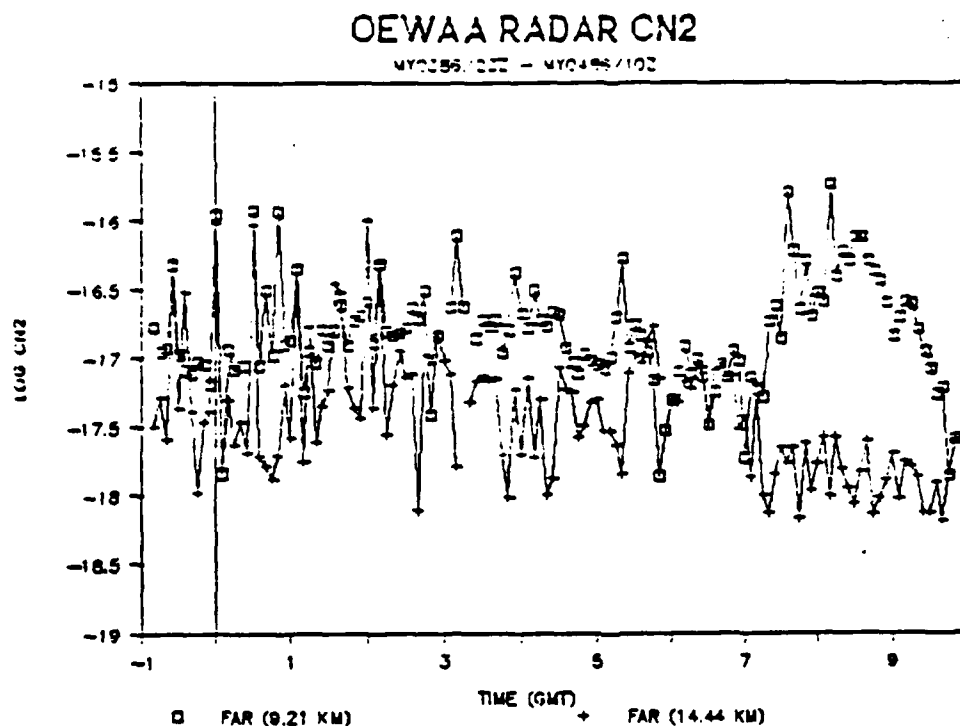


Figure 1. Sample high resolution time series of  $C_n^2$  at two different range resolutions. The upper panel is with 0.9 km vertical resolution and 3 minute time resolution; the lower panel is with 0.3 km vertical resolution and 90 second time resolution. Each panel gives a time series for two different altitudes.

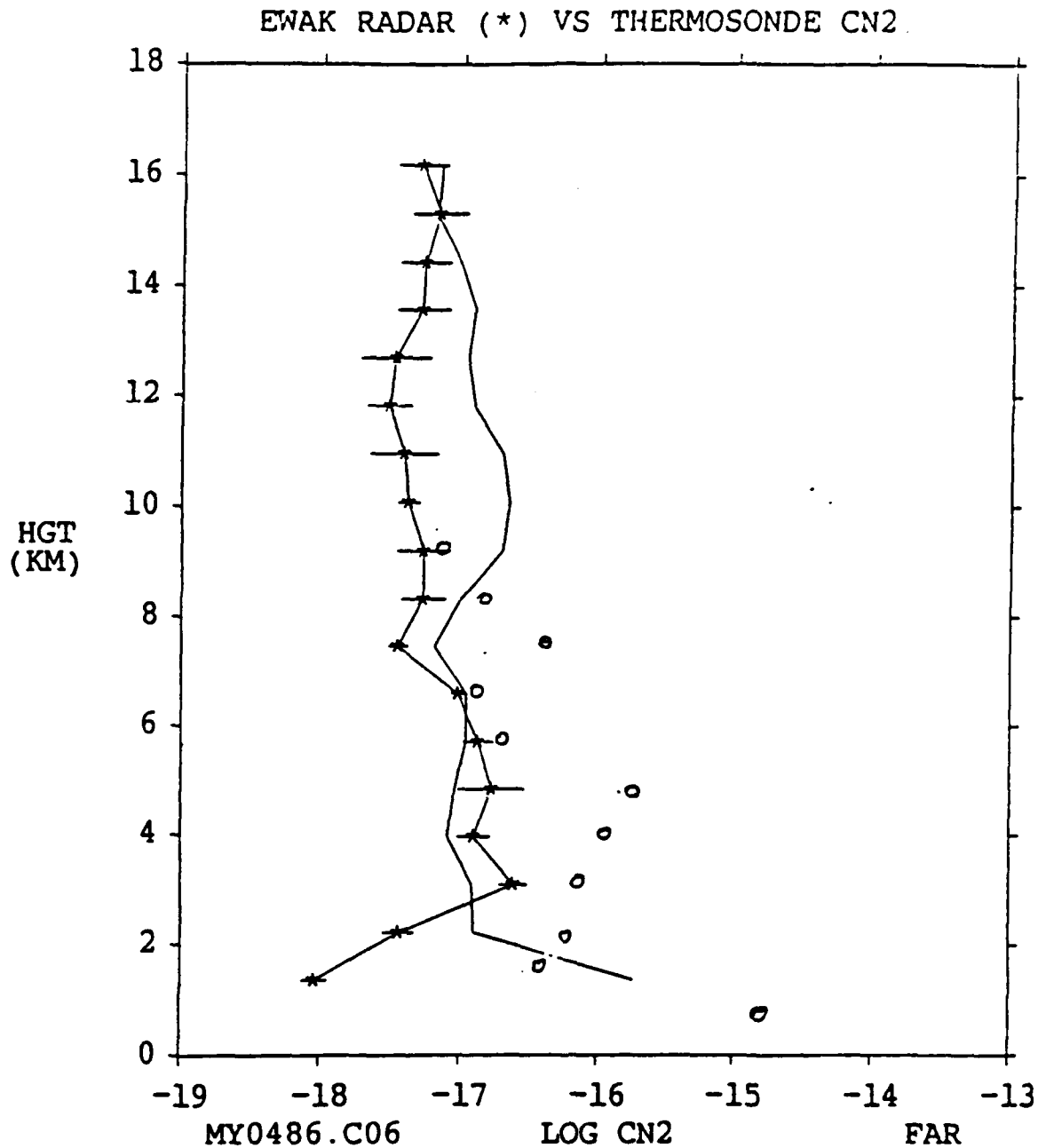


Figure 2. Sample profile of optical  $C_n^2$  from the EWAK experiment. The \* symbol denotes the radar estimate (corrected for moisture effects) with horizontal bars to indicate the standard deviation over an hour. We now believe the radar data should be increased by at least a factor of two from the values indicated in this graph. The solid line is AFGL thermosonde data degraded to the radar resolution by linear averaging. The open circles are from the aircraft measurements using the spectral method. The designator in the lower left corner indicates the profile is for May 4, 1986 at 0600 GMT.



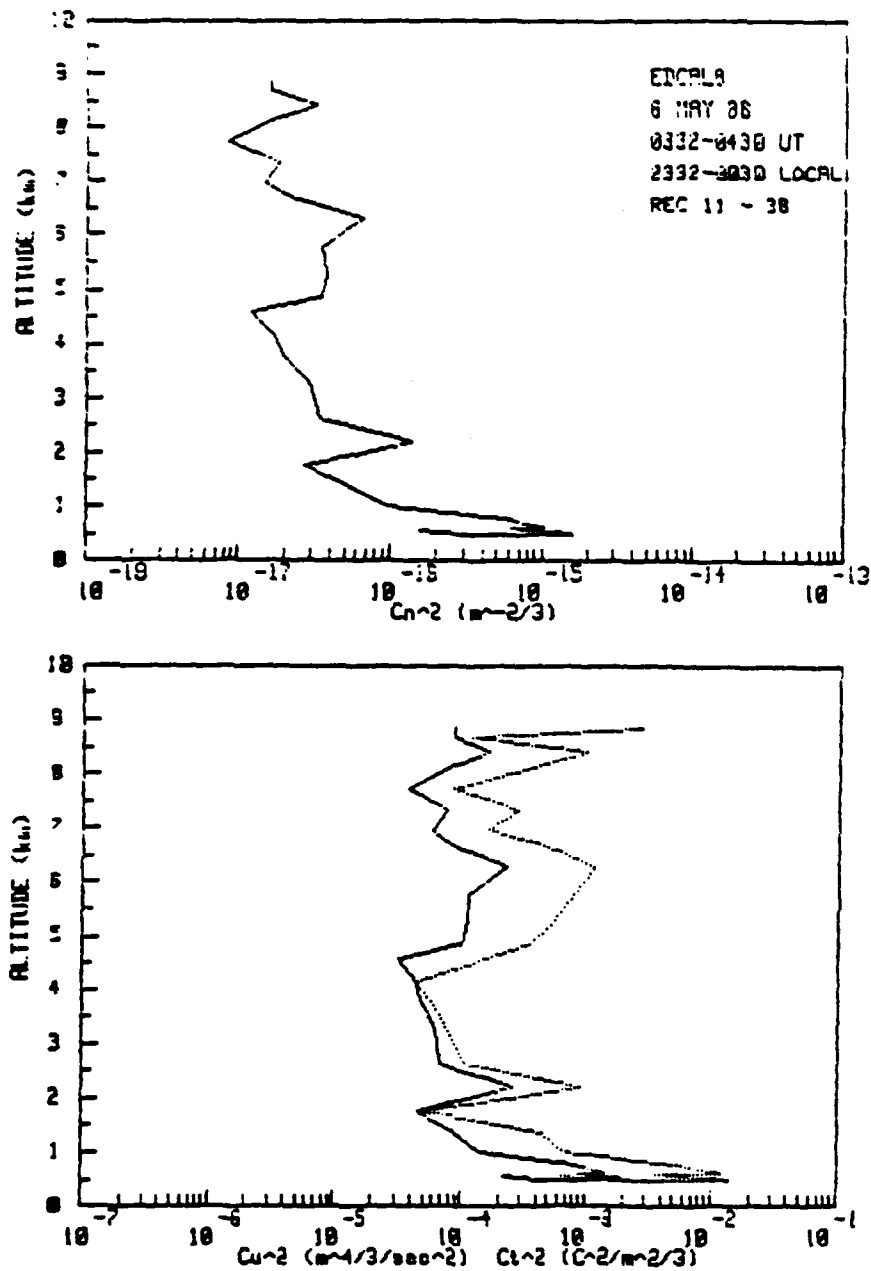


Figure 3. Sample aircraft microturbulence profile. The upper panel is optical  $C_n^2$  vs. altitude; the lower panel is  $C_t^2$  and  $C_u^2$  vs. altitude.

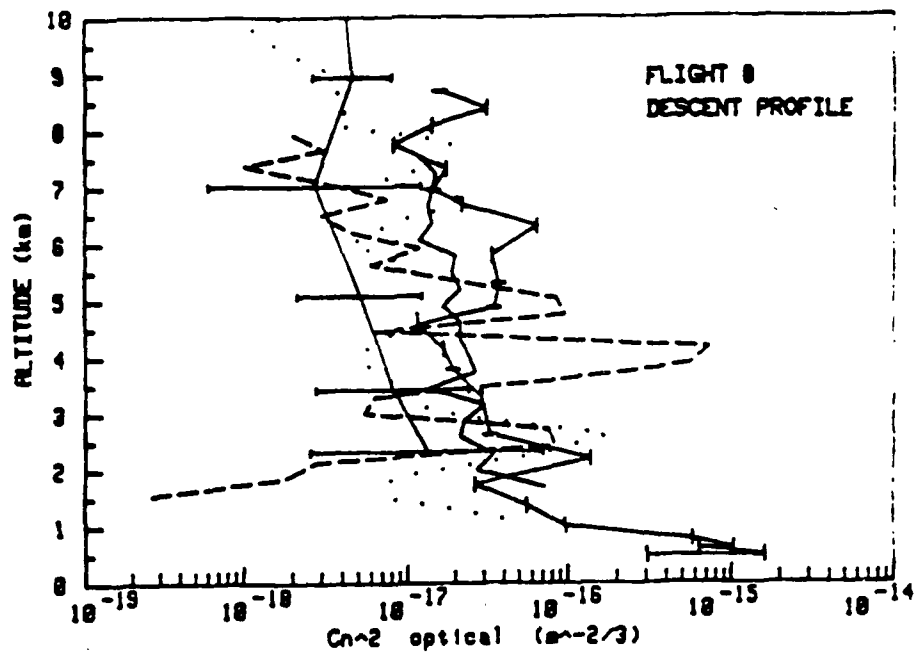
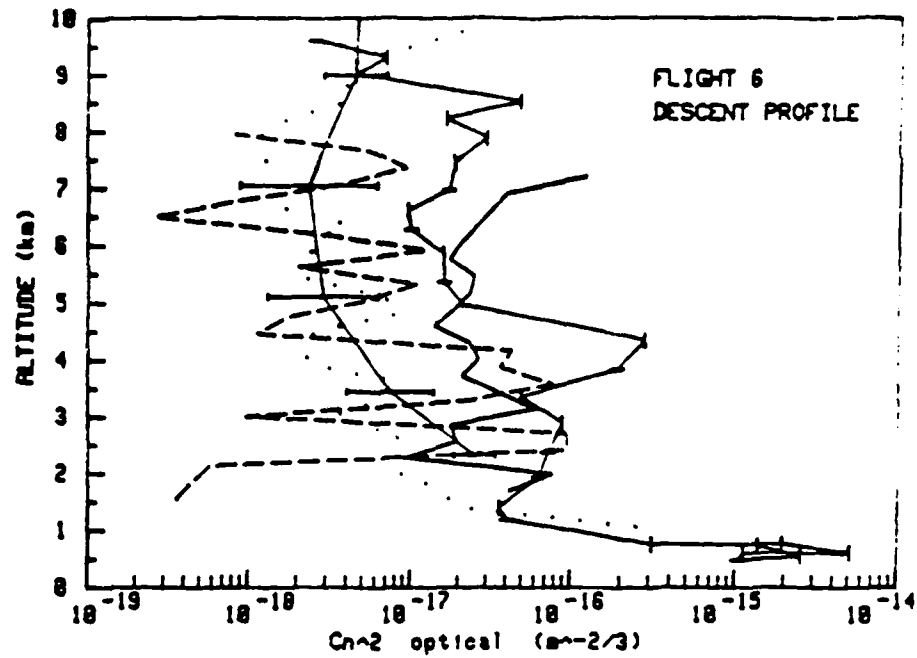


Figure 4. Comparison of various measurements of optical  $C_n^2$  profiles from EWAK. The solid line is the Van Zandt model, the dashed line is the radar, the solid line with horizontal bars is the averaged scintillometer, the solid line with tic marks is the aircraft, and the dotted line is the thermosonde. The upper panel is at about 0000 local time on 4 May 1986; the lower panel is about 2300 local time on 5 May 1986.

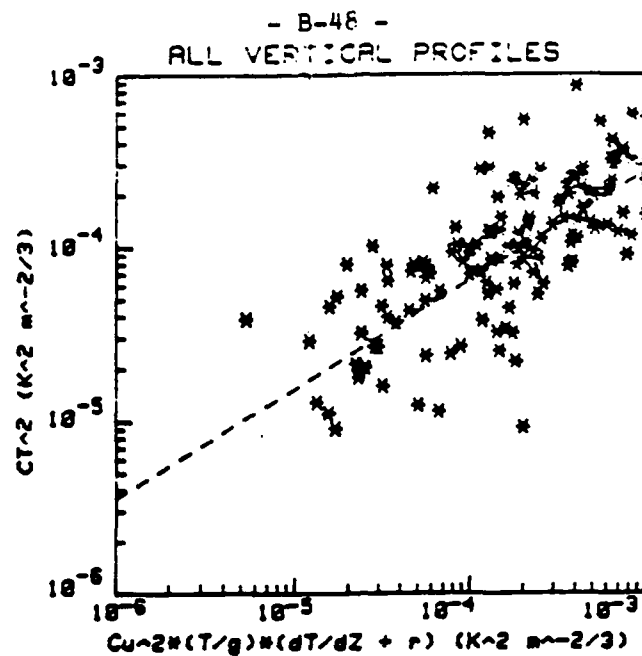


Figure 5a. A comparison of simultaneous values of temperature and velocity microturbulence when normalized using equation 13. A slope of 1 would indicate that  $\gamma_\theta$  was a constant.

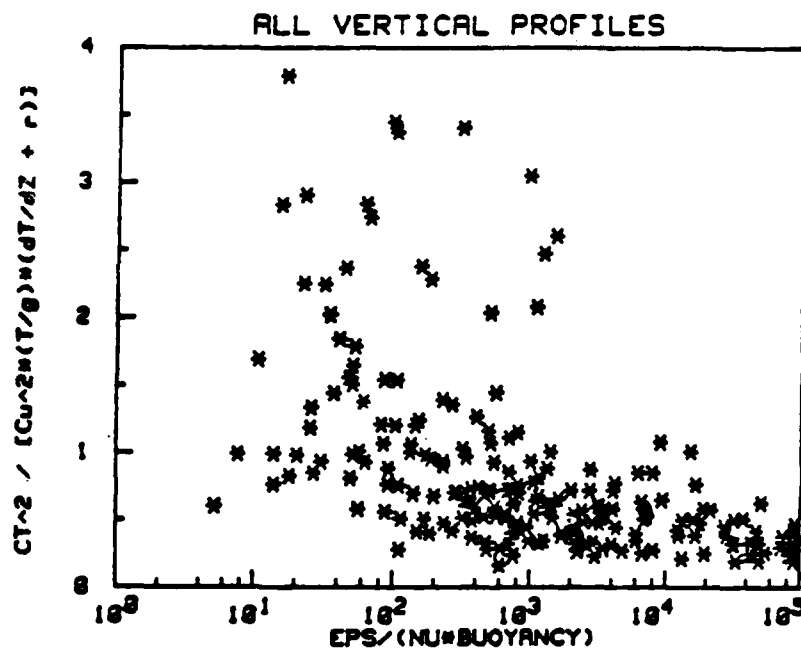


Figure 5b. A composite comparison of  $C_T^2$  normalized by  $C_u^2$  and potential temperature gradient (as in Eqs. 13 and 30) as a function of the activity parameter, A. A constant value would indicate that  $\gamma_\theta$  was a constant.

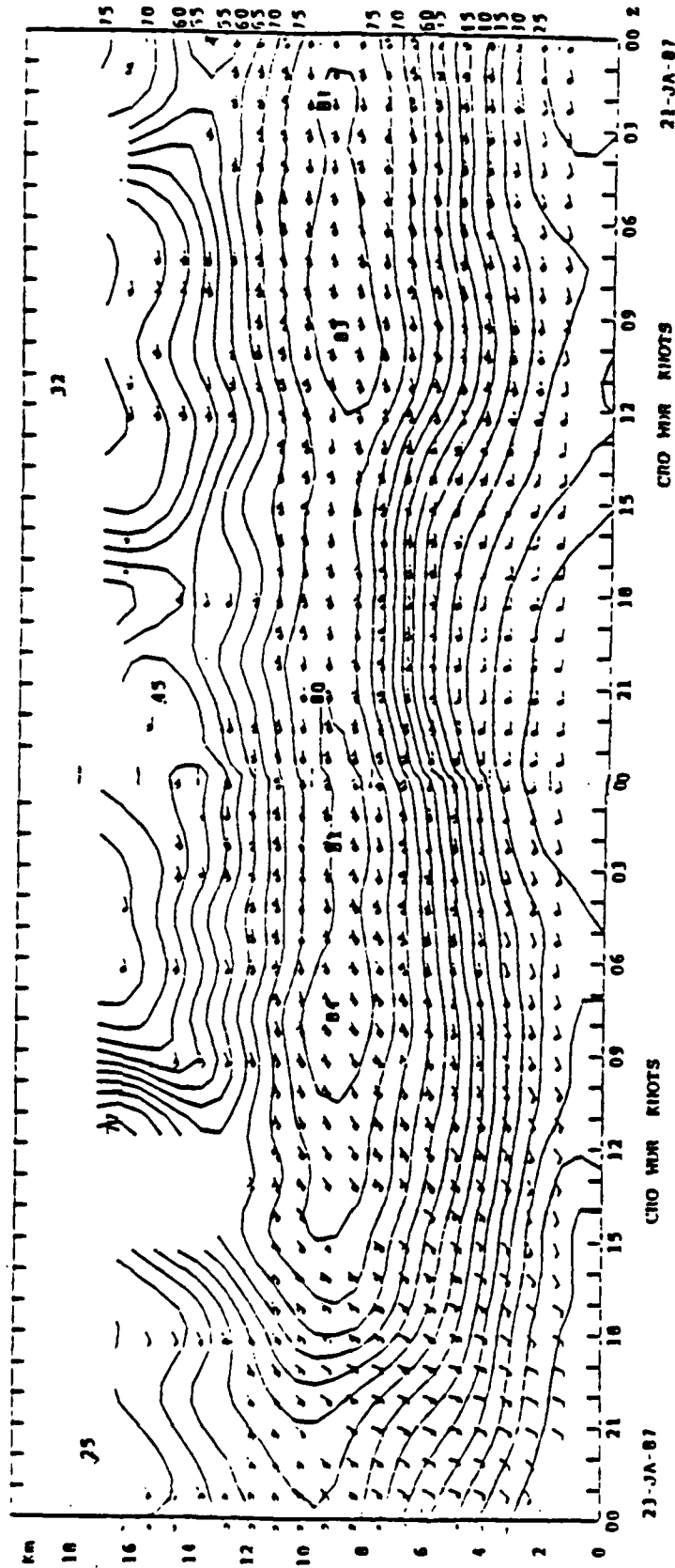
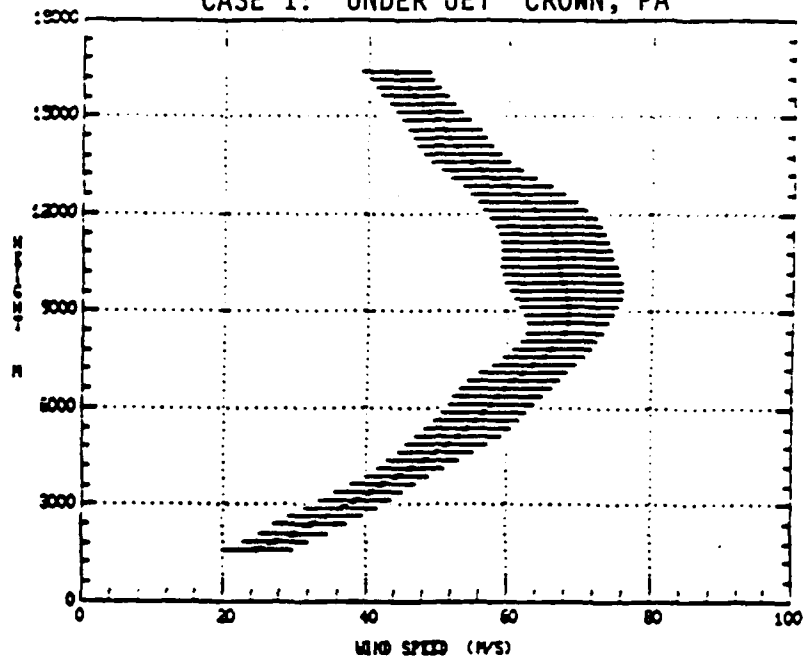


Figure 6. Time-height cross sections of radar winds and directions for a two day period (January 21, 22, 1987) from Case 2 of the study by Syrett (1987). The jet stream is apparent as the wind speed maximum at about 10 km height.

- B-50 -

WIND SPEED: MEAN, STANDARD DEVIATION  
CASE 1: UNDER JET CROWN, PA



WIND SPEED: MEAN, STANDARD DEVIATION  
CASE 2: UNDER JET CROWN, PA

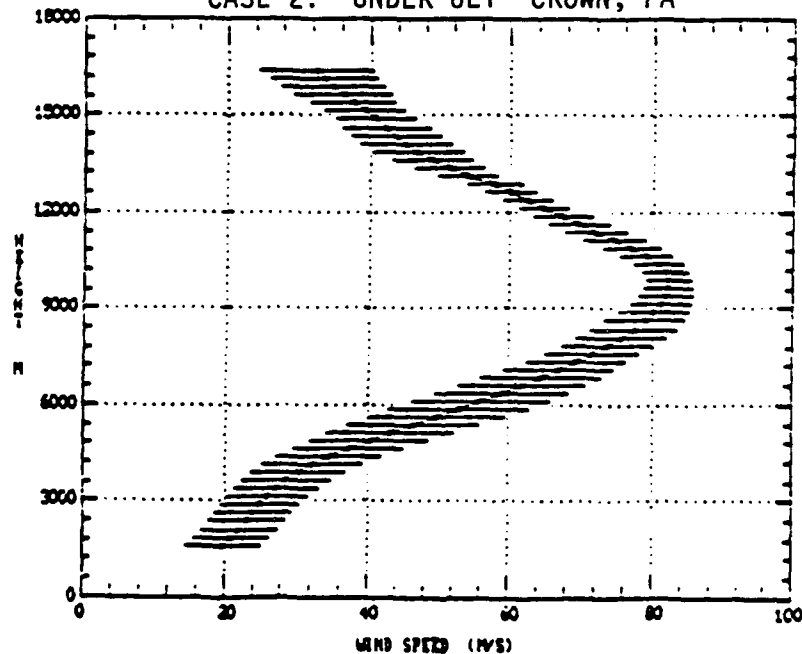


Figure 7a. Average wind speed profiles with the measurement site within 100 km of the jet axis. The horizontal bars indicate the standard deviation for the period. The upper panel is case 1; the lower panel is case 2.

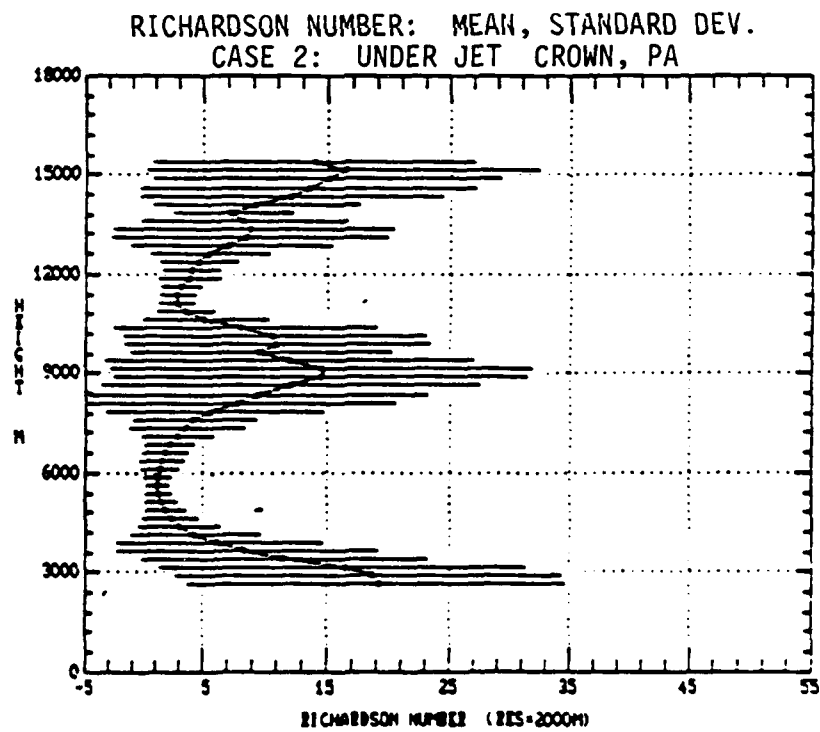
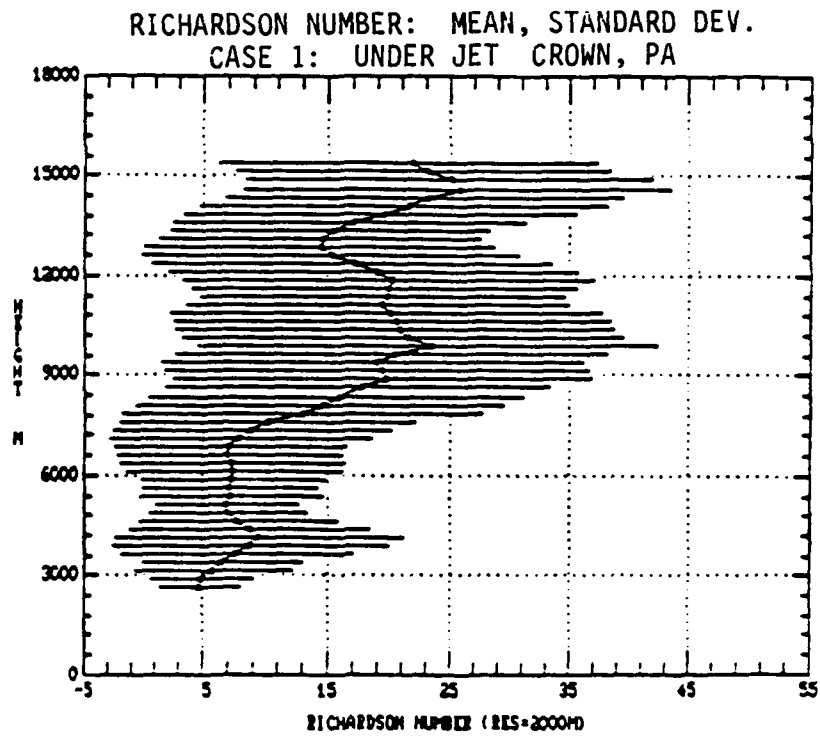


Figure 7b. As in Fig. 7a, but for the Richardson Number derived from the radar winds and interpolated rawinsonde thermodynamic data.

- B-52 -

CASE 2 PILOT REPORTS OF TURBULENCE 3X7 DEGREE BOX

(X:100) TURBULENCE RANGE: 1=LIGHT-MODERATE 2=MODERATE 4=SEVERE 5=EXTREME

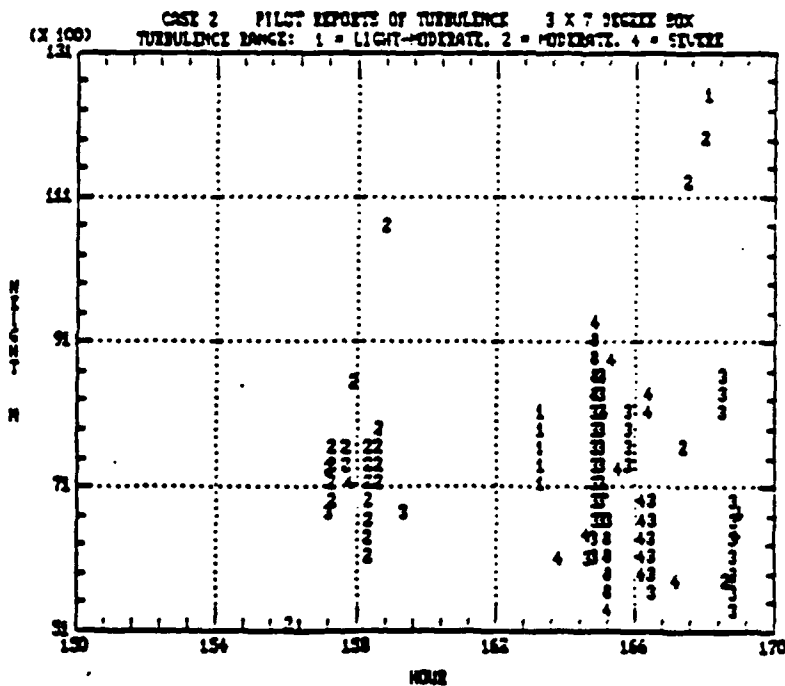
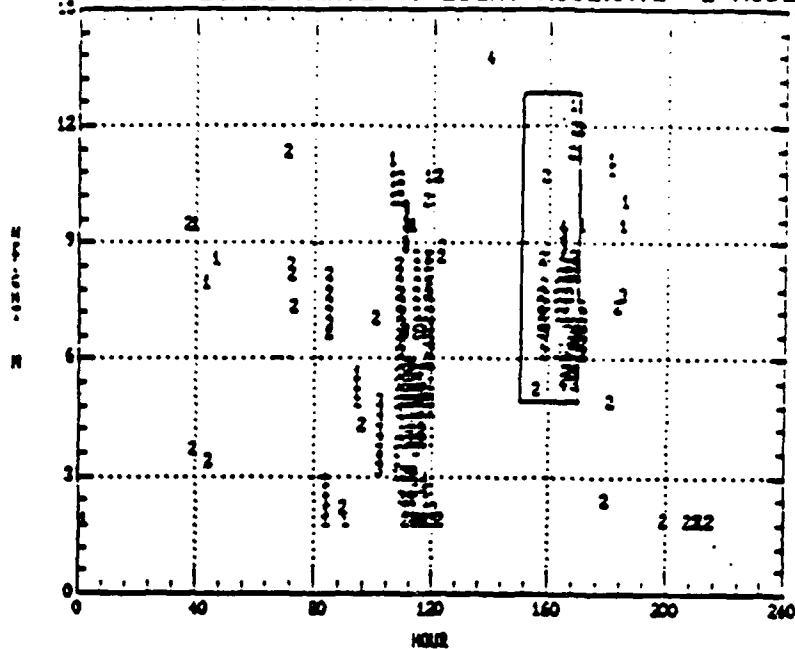


Figure 8. Pilot reports of turbulence in the vicinity of the radar during case 2. The bottom panel is a blowup of the boxed area of the top plot.

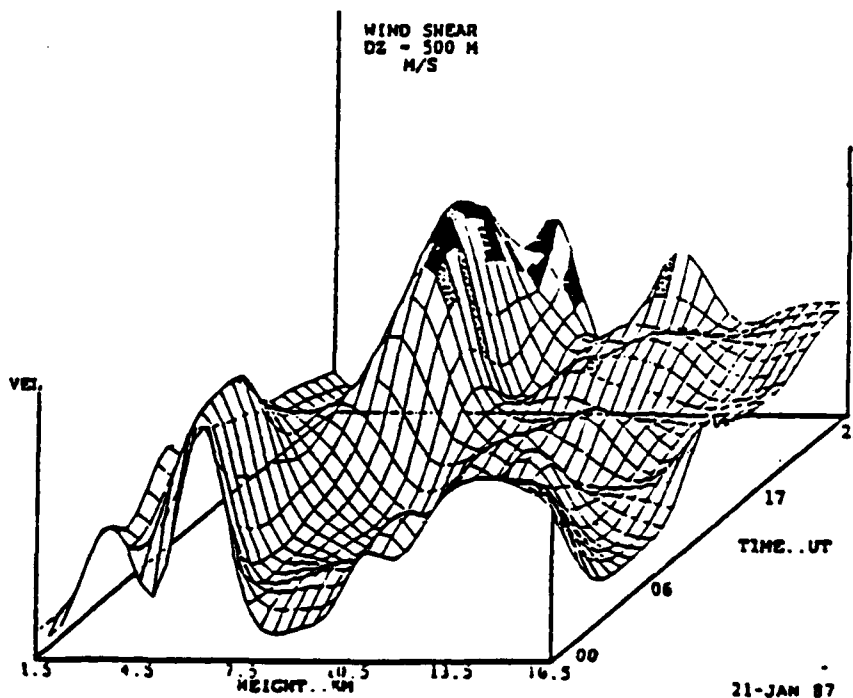
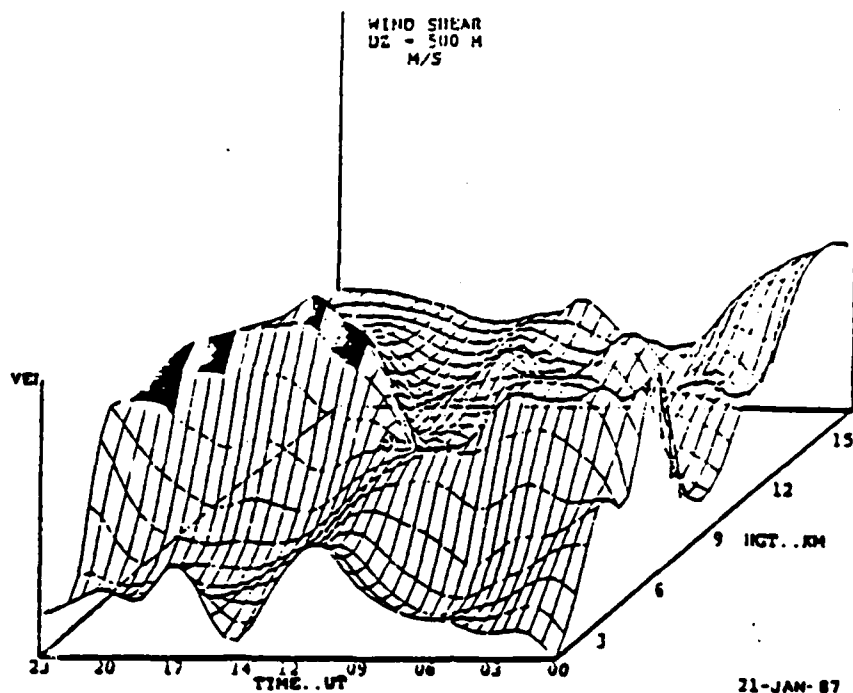
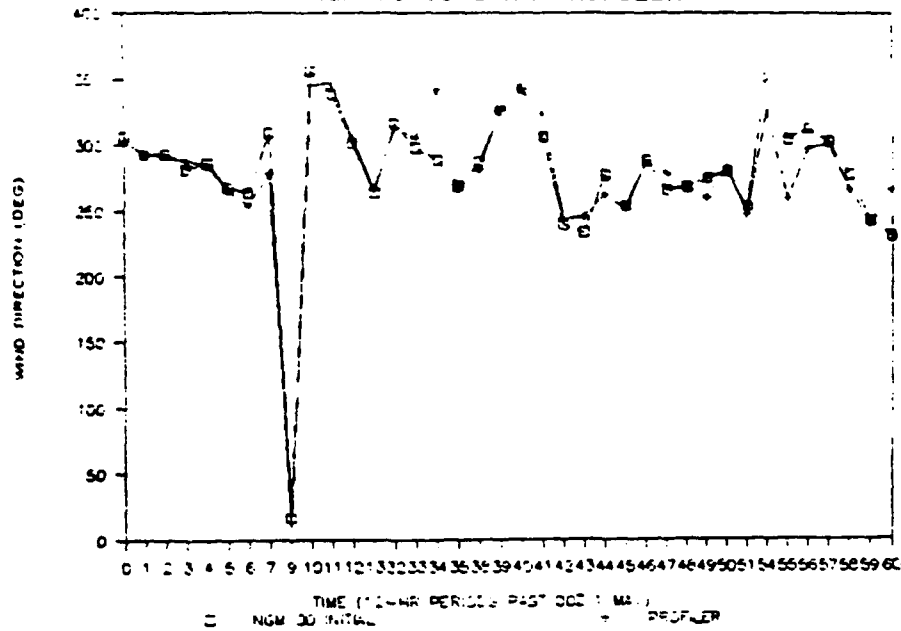


Figure 9. Surface plots of wind shear above the Crown radar during 21 January 1987. The surface defines the time, altitude and magnitude of the wind shear. The shaded areas indicate the pilot reports of turbulence: dark implies severe and dotted implies moderate. The bottom panel is a 90-degree rotation of the upper panel to provide a different view. Note that all pilot reports of severe turbulence occurred during periods of maximum wind shear.



CROWN 500mb WIND DIRECTION, MAY 1987  
NGM-00 vs 1-HR PROFILER



CROWN 500mb WIND SPEED, MAY 1987  
NGM-00 vs 1-HR PROFILER

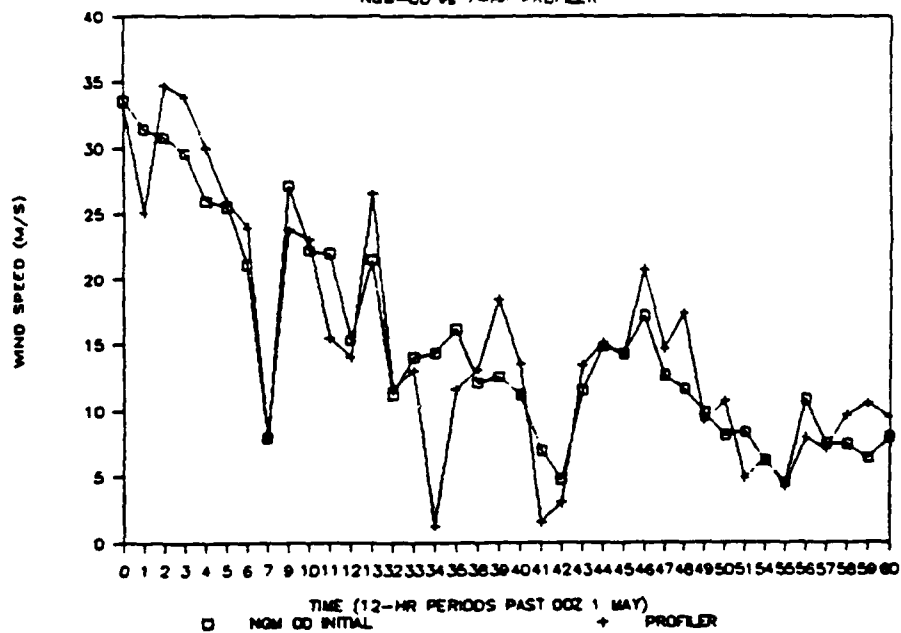


Figure 10. A comparison of the NGM interpolated and radar derived 500 mb wind direction (upper panel) and wind speed (lower panel) for the month of May, 1987. The NGM data represents the smoothed analysis field used to initialize the model (0 forecast).

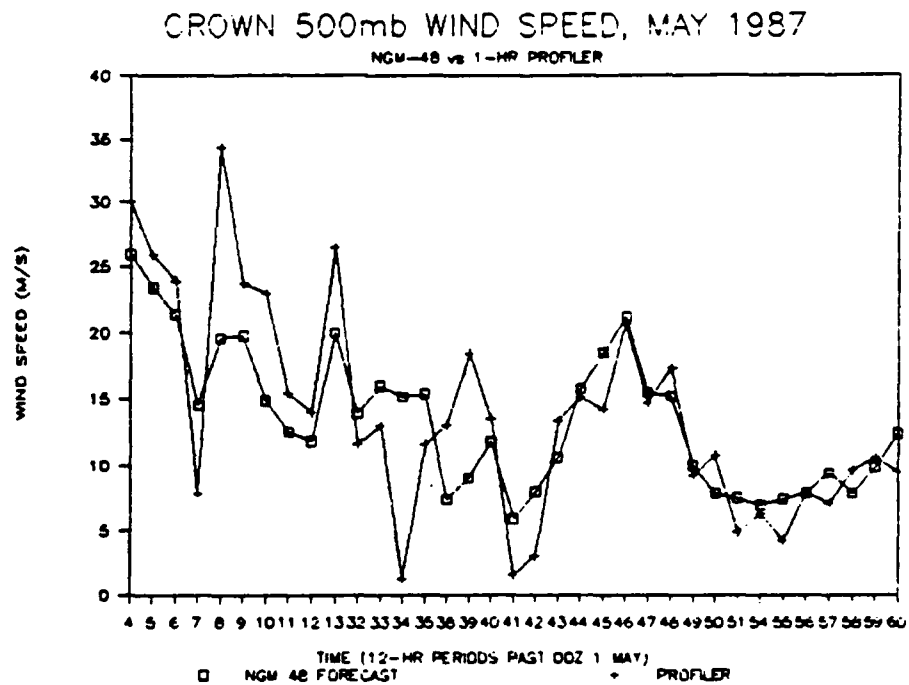
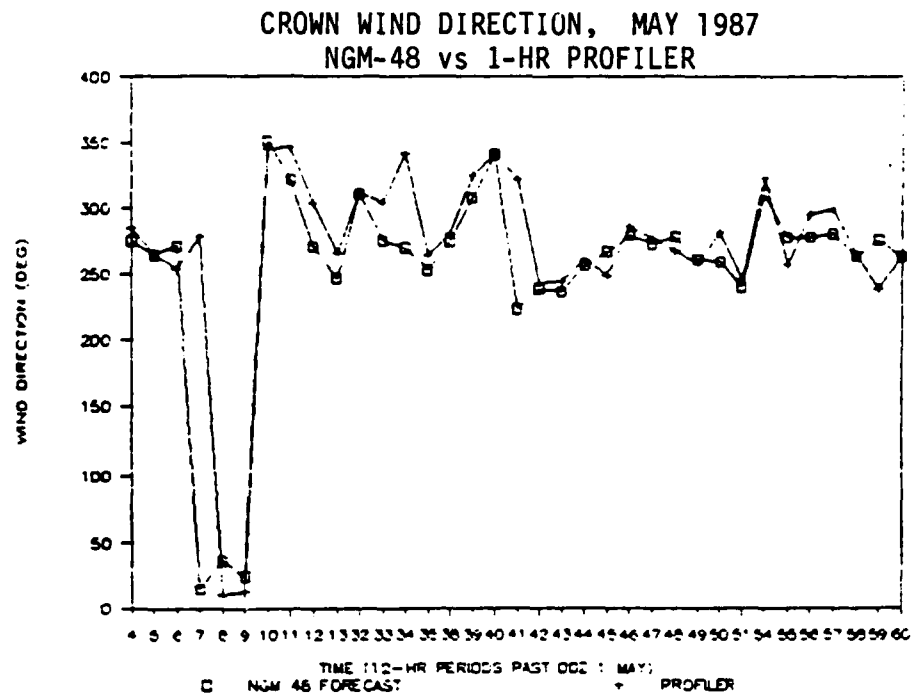


Figure 11. As in figure 10 but for the 48 hour NGM forecast.

## APPENDIX A

### Profiler System Description

Mesoscale meteorological measurements, analysis and prediction are some of the principal areas of research in the Department of Meteorology at Penn State. For more than a decade those members of the faculty concerned with mesoscale analysis, numerical modeling and forecasting have been frustrated by the spatial and temporal inadequacy of conventional network observations for both research and operational applications. For more than five years the Department had sought the substantial financial resources required to deploy a network of VHF Doppler (ST) radars and millimeter wave radiometers for "operational" test and evaluation for wind and thermodynamic profiling. Construction of the ST radar network began in fall of 1983 using funding provided by the Air Force Office of Scientific Research (through the DoD University Research Instrumentation Program) and the University. In 1986 a second AFOSR URIP grant was obtained to fund the acquisition of temperature (50-60 GHz) and humidity (20-30 GHz) profiling radiometers. This document will only discuss the radar systems.

For the foreseeable future the Penn State ST radar program will be focused on applications rather than systems development research. Deployment of the systems would not have been possible without the outstanding cooperation provided by C.G. Little and R. Strauch and their colleagues at the Wave Propagation Laboratory, and also J. Brosnahan of Tycho Technology from whom we bought all of the receivers, transmitters and antennas. With regard to the other major systems components, we have assembled in-house, from WPL documentation, the time-domain-integrator and computer interfaces and have purchased WPL software-compatible Data General Corp. Eclipse computers for each system.

The Penn State network consists of three 6 m wavelength(VHF) and one 0.7 m wavelength(UHF) radars. Fig. 1 indicates the approximate location of a mesoscale triangle formed by the three VHF radar sites within the routine rawinsonde network. In Table 1, a short summary of the specifications for the four radars is given. Experiences, plans and improvements for the PSU network are summarized below.

A. VHF1 50-MHz radar located 15 km south of State College, PA.

1. This system became fully operation June 27, 1985. The primary reason for system failures since the onset has been AC outages which are prevelant in this area. Battery back-up and computer-controlled autorestart of the transmitters has circumvented this problem.

2. Initial performance statistics done by Frisch et al., WPL on August 1985 data , indicate very good performance by VHF1. On Beam #1 the next to last range gate (16.8 km MSL) was able to make a wind measurement 99% of the time, while Beam #2 was able to measure the wind at this height 85% of the time. The difference between the beams is probably due to better pickup by beam #2 of computer/electronic noise from the building. Samples of data from the low altitude range of VHF1 are shown in Figs. 2 and 3.

3. A vertical beam was added in March, 1987, and the latest NOAA/WPL software was installed.

B. VHF2 50-MHz radar located in NW Pennsylvania near Crown, PA.

1. This system was installed May 1, 1986 and has operated since. Performance is often slightly better than VHF1 but a source of interference (radiotelephones from a local trucking company) leads to periods of reduced

data quality.

2. A vertical beam was added in January, 1987, and the latest NOAA/WPL software was installed.

C. VHF3 50-MHz radar located in SW Pennsylvania near Somerset, PA.

1. All hardware is ready for installation pending selection and preparation of a site.

2. A three beam system similar to VHF1 and VHF2 will be used. Some of the hardware from Tycho Technology has been slightly updated.

D. UHF1 portable 405-MHz radar to be semi-permanently based at the PSU Circleville Farm in downtown State College, PA.

1. This system has been used on three major field deployments: the SPACE/MIST-COHMEX experiment in Alabama (June-July, 1986), the FIRE stratocumulus IFO on San Nicolas Island, CA (July, 1987), and the Arizona monsoon experiment (August, 1987).

2. Preparations for basing at Circleville Farm are to be completed in July, 1988.

Table 1: Specifications for the Penn State ST Radars

<u>Item</u>	<u>VHF1.VHF2.VHF3</u>	<u>UHF1</u>
Type	Pulsed Doppler, 3 beam	Pulsed Doppler, 3 beam
Location	1: S. State College 2: Crown, PA 3: Somerset, PA	In State College, trans- portable
Frequency (nom.)	49.9 MHz	404 MHz
Bandwidth	300, 100 KHz	1, 0.3, 0.07 MHz
Peak Power	30 KW	30 KW
Pulsewidth	3.67, 9.67 $\mu$ sec	1, 4, 16 $\mu$ sec
Antenna:		
Type	Phased array CoCo	Phased array CoCo
Dimensions	50 m X 50 m	9 m X 9 m
Zenith angles	90°(vert), 75°	90°(vert), 75°
One site computer	Data Gen. Eclipse	Data Gen. Eclipse
On site processing* at PW- :	3.67 $\mu$ s    9.67 $\mu$ s	1 $\mu$ s    4 $\mu$ s    16 $\mu$ s
Time domain ave	400            125	112        70        35
Spectral ave	8              16	16        32        64
Height spacing (m)	290            870	100       300       800
Spec. resolut.(m/s)	0.49           0.31	0.29    0.29    0.29
Maximum absolute rad. velocity (m/s)	15.7           19.6	18.25   18.25   18.25

\*Software controllable

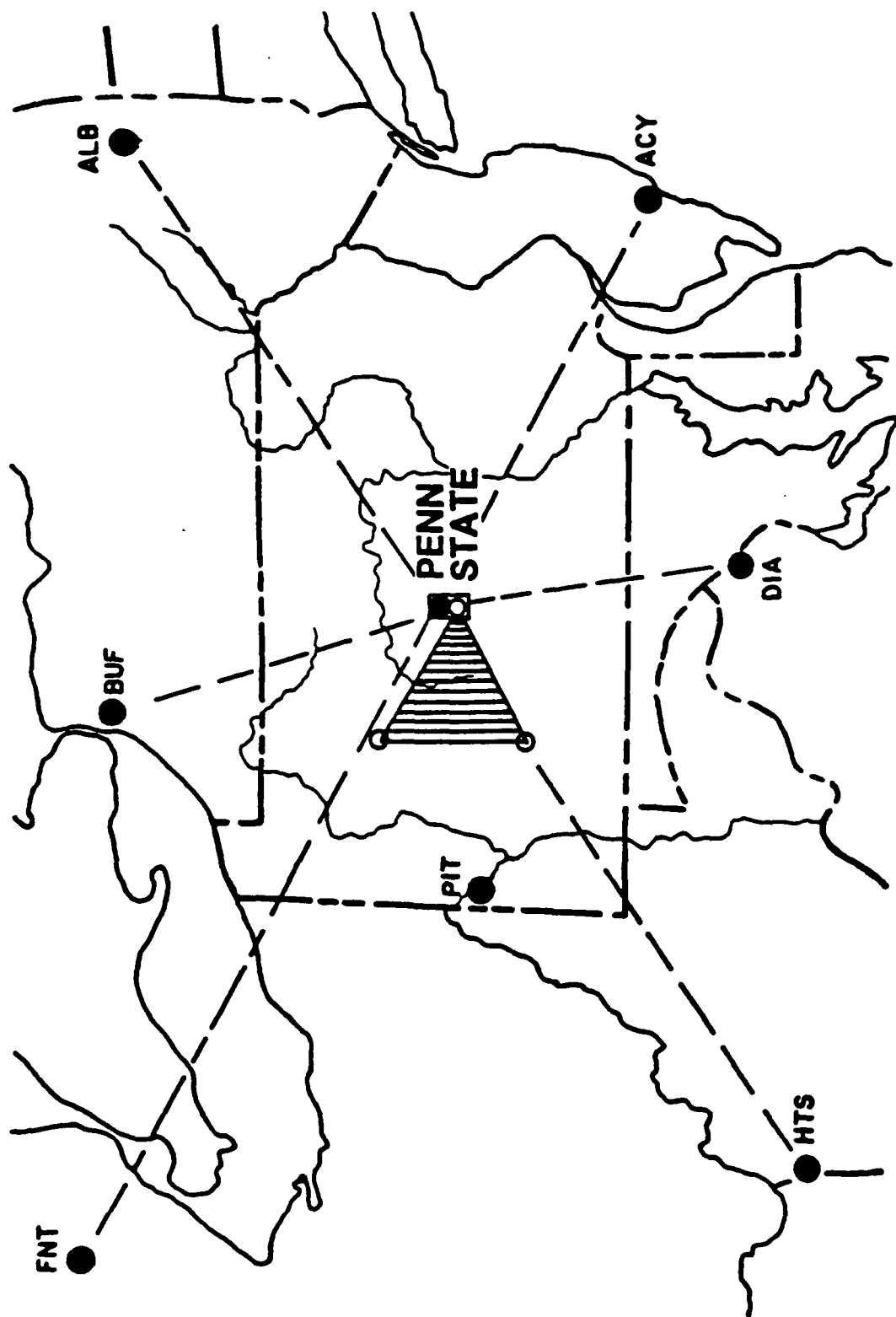


Figure 1 Locations of Penn State radar sites (open circles) and standard rawinsonde sites (solid circles).

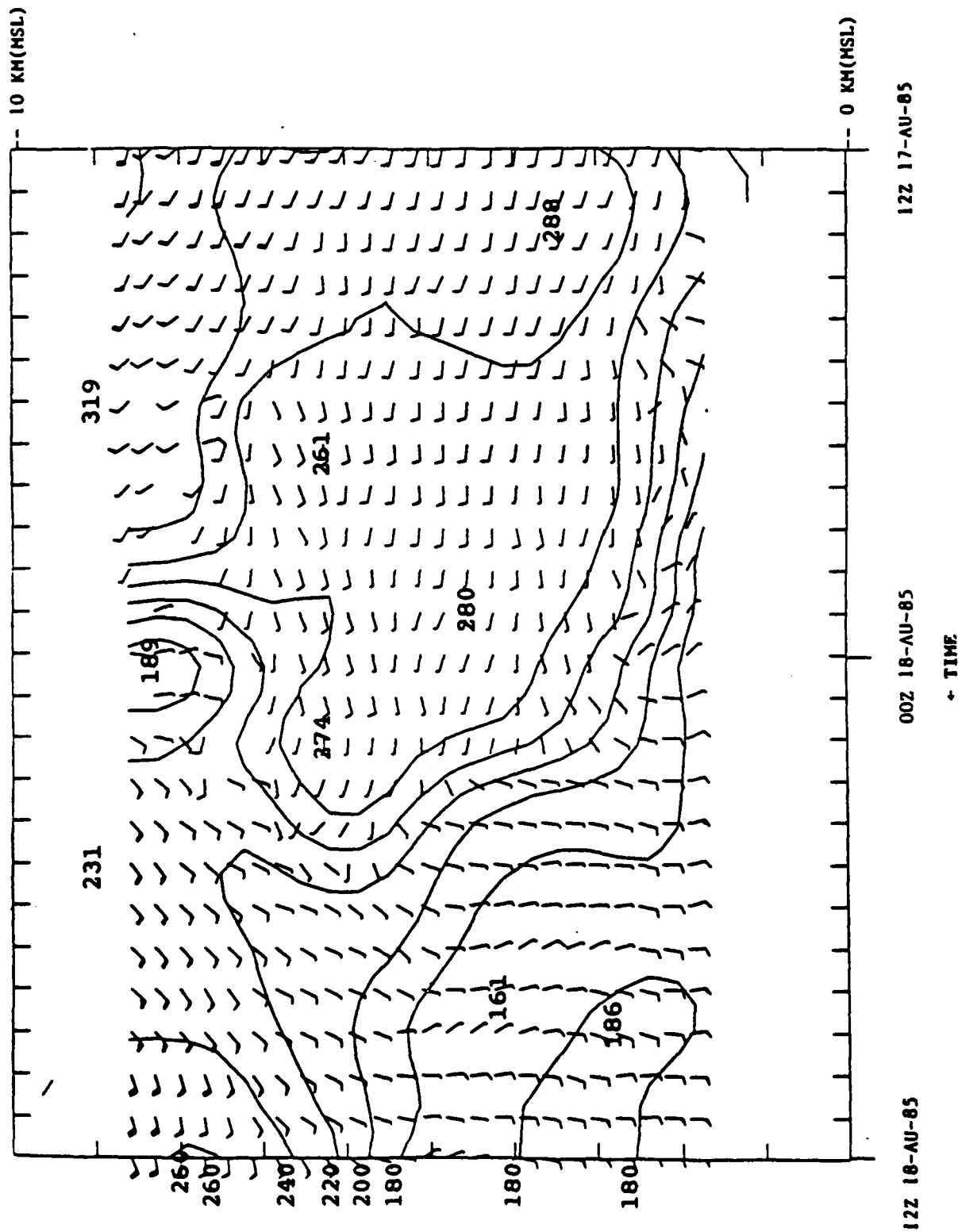


Figure 2 Time/height cross section from VHF 1 (near State College) for a 25 hour period beginning at 12Z on August 17, 1985. The arrows are standard meteorological wind barbs and the solid lines are isolines of wind direction (degrees).



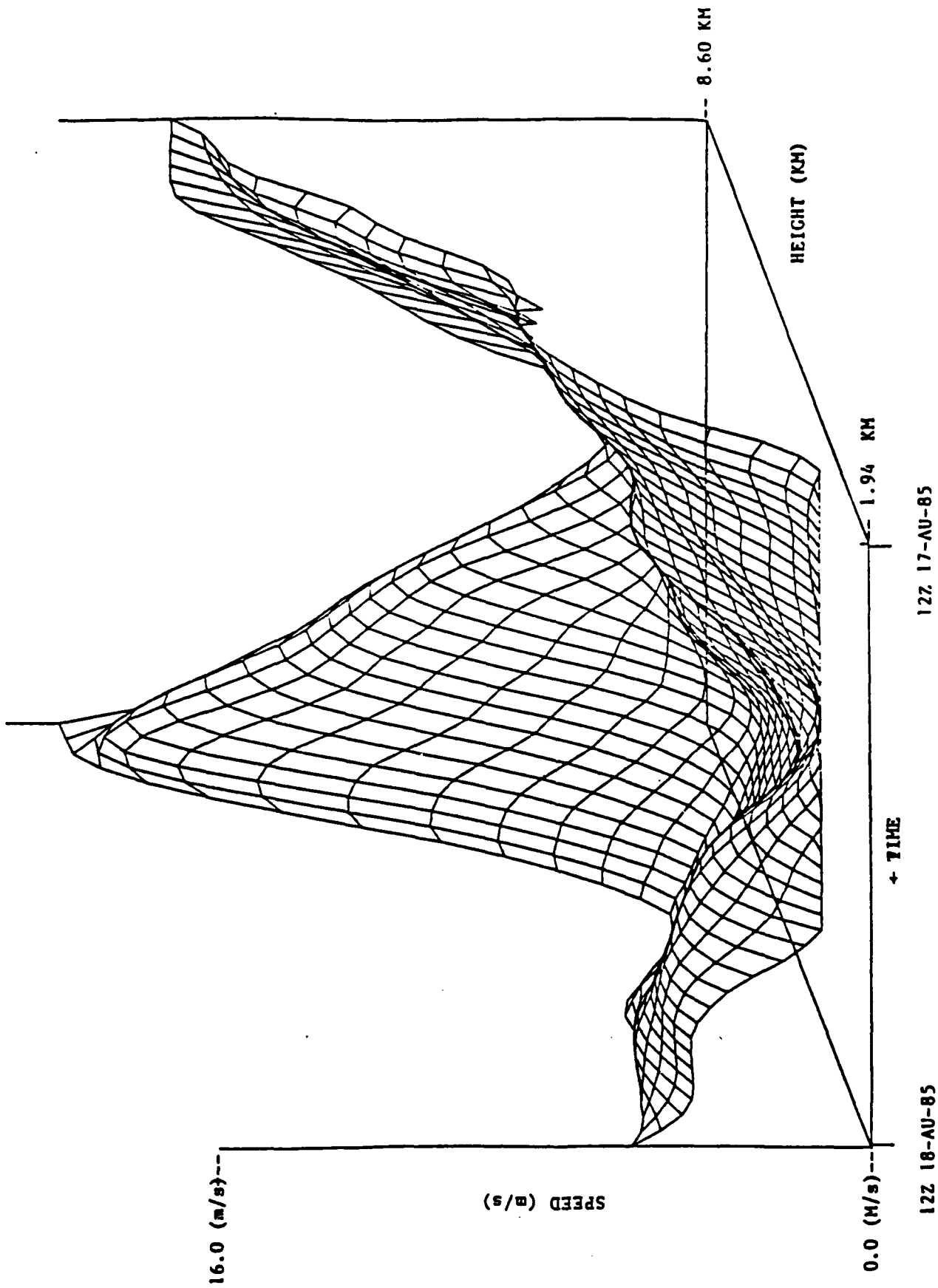


Figure 3 Two dimension plot of wind speed versus time and altitude for the same period as Fig. 2.

APPENDIX B

NOTES CONCERNING THE USE OF CLEAR AIR DOPPLER RADARS  
FOR THE MEASUREMENT OF  $C_n^2$

Robert M. Peters

Department of Meteorology  
The Pennsylvania State University  
University Park, PA 16802

Recently the Penn State clear air radar network has been increasingly utilized not only for wind profiling, but also for the measurement of the refractive structure coefficient associated with isotropic turbulence,  $C_n^2$ . This coefficient is related to received power amplitude of active indirect sensing systems when signal backscatter is caused solely by refractive index variations due to isotropic turbulence. The physical mechanisms associated with this backscatter in the atmosphere are described in detail by WESELY (1976).

The present Penn State clear air radar network consists of two VHF (6M wavelength) Doppler radars and a transportable UHF (75 CM wavelength) Doppler radar. The systems are designed primarily for wind profiling of the troposphere and stratosphere. The Penn State network is described by THOMSON et al. (1984) and is based upon the concepts, signal processing hardware designs and software provided by

the NOAA/ERL Wave Propagation Lab (STRAUCH et al., 1984). An ongoing experimental research effort at Penn State pertains to measurements of turbulent backscatter from radars, optical systems, acoustic systems and direct measurements of turbulence via aircraft and thermosondes. During a recent experiment, one VHF radar was used for this purpose and measurements of the VHF structure coefficient were obtained (MOSS, 1986). It has become evident that the quantitative measurement of radar system power parameters that are required for the determination of  $C_s^2$  are prone to errors that are frequently not addressed in designs that are optimized for Doppler measurements.

In order for backscattered power to be related to isotropic turbulence, it must be known that the received signal amplitude is not modified by other backscatter sources, reflections or interference from other emitters. Continuous interference is usually man made from sources such as arcing power lines, radio transmissions or broadband noise from the digital systems of the radar. Good site selection and radar system engineering practices will prevent interference from these types of emission. Hard targets will cause undesired reflections. Reflections due to ground clutter may be partially eliminated in spectral processing but are best avoided by choosing radar sites that have no large targets visible at distances comparable to the radar's range response. Hard reflections from aircraft will override the atmospheric backscattered signal. The consensus algorithm used for averaging in the Penn State radar software (STRAUCH et al., 1984) will eliminate the short term occurrence of aircraft reflections from an averaged data set. However, the location of major airways should be a factor during radar site selection. Enhanced signal returns from the atmosphere from other natural sources of

anisotropic irregularities will occur with a zenith pointing beam as described by DOVIAK and ZRNIC' (1983). As shown by DOVIAK and ZRNIC' (1983), the response of VHF radars to anisotropic irregularities will be insignificant at a 15 degree off zenith pointing angle, assuming that the layered structure causing the signal enhancement is horizontal. At Penn State, one of the 15 degree off-axis beams of the VHF radar antenna is used for the measurement of  $C_n^2$  as well as for one wind velocity component. Antenna beam side lobe response to enhanced signal returns from the vertical are further reduced by having a zenith null designed into the antenna pattern.

In order to make quantitative measurements of received signal amplitudes, the radar systems's hardware must be calibrated or its calibration inferred from other sources. System hardware for calibration purposes are the antenna system, transmitters, receivers and analog to digital converters used for parameter measurements.

The antenna patterns of large upward pointing VHF phased arrays, such as those used at Penn State, are difficult to measure in their far fields. Computer antenna pattern models are quite accurate with regard to antenna pattern shape. Experience has shown that an antenna will usually have a gain within a few decibels (dB) of that predicted by a validated antenna model, if the antenna is well engineered and installed. Pattern altering metallic objects should not be placed in or near the antenna field if reliance is placed upon previously determined antenna gain figures that are to be used in the measurement of structure parameters. Astronomical noise sources have been used to confirm antenna pointing maxima. Galactic sources are useful in the northern hemisphere (MOSS, 1986) and the sun can be used

in equatorial regions (RIDDLE, 1985). Precise patterns and gains have been determined for the Mu radar facility in Japan by integrating direct satellite measurements as described by SATO et al (1985). The phase and power distribution provided to the elements of the VHF phased array may be directly measured to provide a more accurate input to modeled antenna patterns. The performance of an uncalibrated antenna system may be statistically compared with other systems of known performance and its gain inferred (MOSS, 1986), as long as other system components are calibrated. Computer estimation of  $C_n^2$  may be derived from atmospheric soundings and used to estimate system calibration. A field tested computer model developed by VANZANDT et al. (1981) could possibly be used for this purpose.

Transmitter parameters such as power and pulse width must be known. The Penn State network incorporates transmitters which have internal microprocessor control and monitoring systems. The radar system executive control computer at each site provides a means to remotely monitor and control each radar transmitter in the network. Transmitter power may be monitored via this arrangement, however, this indirect method of measurement is prone to error if the associated electronic circuits are not calibrated. With Penn State systems, the transmitted power level is derived from an adjustable RF voltage monitoring circuit with its output supplied to the analog to digital converter of each transmitter's processor. Each transmitter includes an integral directional coupler. To ensure the accuracy of the transmitter power monitor, the coupling coefficient of each directional coupler should be calibrated and power measurements taken to check and calibrate the microprocessor based power monitoring system.

The receiver system includes not only the radar receivers and preamplifiers, but also the analog to digital converters. For structure parameter measurements, the receiving system gain must be calibrated. For relative power measurements of received signal amplitude, the calibration must be done with test instrumentation. Any changes to the receiving system, such as replacement of a receiver preamplifier, would require recalibration. For radar systems such as the Penn State UHF Doppler radar, this is the most practical method of calibration since the UHF system utilizes one receiver time shared among several antenna pointing angles. The minimum discernable received signal power of the UHF system is limited by the 100 K noise temperature (approximate) of the receiver preamplifier. This type of calibration is unnecessary for the VHF Doppler radars. For these systems, the minimum signal detectability is limited by a galactic noise temperature background in the order of several thousand Kelvins (KO, 1958). For this reason, the galactic noise level is used as an automatic calibration for all receivers at Penn State VHF radar sites. This is accomplished by archiving a spectrally derived estimate of consensus averaged signal to noise ratio (most systems presently archive relative power on a routine basis). Structure parameter errors at close ranges using VHF radar have been observed during recent experiments (MOSS, 1986). The cause for this class of error has not been studied but appears either to be due to a near field antenna response error or receiver dynamic range limiting.

Less than ideal receiver low pass filter stability, calibration and adjustment has been the most significant cause of error of spectrally derived structure parameters from the VHF radars.

Specifically, the presence of DC offsets and gain imbalance between real and quadrature channels will produce a host of errors in spectral signal processing. Each received signal spectrum is actually the result of several averaged spectra, each of which is derived from a time series of coherently integrated received signal amplitudes at each radar altitude. Each signal spectrum is derived from the complex Fast Fourier Transform of the receiver's range gated real and quadrature outputs. Peaks that may occur in each spectrum about the zero frequency line at an equal amplitude at all range gates are usually the result of the presence of a mean or trend in the complex signal data set that is not completely removable by the signal processing software. Image peaks that may occur opposite the spectral peak associated with the clear air signal return usually are a result of dynamic range limiting of the receiving system. A consistent image peak in all range gates is usually associated with a gain or quadrature imbalance between the I and Q channels of the receiving system. Note that the receiving system also includes the analog to digital converters of the signal processing system. Imbalances between the I and Q analog to digital converters will produce the same errors. Errors produced by means, trends and imbalances produce errors in structure parameter data that are not as easily removed as compared to Doppler velocity measurements. The amplitude of a spectral image will always be lower than the true signal so that Doppler peak detecting algorithms will never choose the image peak for Doppler processing. Any means or trends will have an effect in Doppler velocity processing only if the zero amplitude peak is greater than the clear air peak. If the zero peak is larger, then the artificially constant velocity produced in the beam component (which is frequently blamed on ground clutter) can be easily removed from



wind velocity data sets by computer post processing. The effect of these types of spectral errors in obtaining received signal power or signal to noise ratio are not as obvious. The spectral processing algorithm will include ground clutter peaks as part of the returned backscattered signal at low radial wind velocities. Any image peaks that occur will also bias the estimates of received signal power and possibly produce a velocity bias to the estimate. The presence of spectral images will contribute to the estimated noise level thereby producing errors in the signal to noise ratio.

To reduce the errors associated with the receiver system for all types of measurements, the receivers must be carefully adjusted in the lab for gain balance and zero offsets after a period of stabilization. Software solutions can contribute to the reduction of error. The present software used at Penn State (STRAUCH et al., 1984) removes the mean from the received signal data set. Trend removal is more difficult for the real time nature of our signal processing system however improvements have been suggested by STRAUCH (1986). The ultimate solution is to treat the disease, not the symptoms. The filter and output stages of VHF and UHF Doppler receivers should be designed for maximum amplitude stability as well as frequency stability. The manufacturer of the radio frequency subsystems of the Penn State Doppler radars are now providing improved receivers for new systems and retrofits for present systems to reduce the possibility of these types of problems. The Penn State UHF system will have a programmable attenuator added to the receiver system. This will allow the receiver's gain to be fixed at an ideal level depending upon operating requirements. This feature, along with improved on-line spectral display software, will allow field optimization of radar

parameters to reduce the sources of error described herein. An improved method of spectral signal detection has also been developed (PETERS and WILLIAMS, 1988). The new method provides a better signal peak selection mode in the presence of ground clutter or in low signal to noise conditions. Careful attention to clear air radar system performance will result in better estimates of all measurable clear air parameters.

#### REFERENCES

Doviak, R. J. and D. S. Zrnic' (1983), Fresnel zone considerations for reflection and scatter from refractive index irregularities, *Handbook for MAP, Vol. 9*, SCOSTEP Secretariat, Dept. of Electrical Engineering, University of Illinois, 83-97.

KO, H. C. (1958), The distribution of cosmic radio background radiation, *Proc. IRE*, Vol. 46, 208-215.

Moss, M. (1986), Thesis Prospectus, Dept. of Meteorology, Florida State University.

Peters, R. M. and S. Williams (1988), An improved method of clear air signal detection for Doppler wind profiling radars, (in process), Dept. of Meteorology, Penn State University.

Riddle, A. C. (1985), Use of the sun to determine pointing of ST radar beams, *Handbook for MAP, Vol. 20*, SCOSTEP Secretariat, Dept. of

Electrical Engineering, University of Illinois, 410-413.

Sato, T., Y. Inooka, S. Fukao, and S. Kato (1985), Monitoring of the MU radar antenna pattern by satellite OHZORA (EXOS-C), *Handbook for MAP, Vol. 20*, SCOSTEP Secretariat, Dept. of Electrical Engineering, University of Illinois, 414-418.

Strauch, R. G., D. A. Merritt, K. P. Moran, K. B. Earnshaw, and D. Van de Kamp (1984), The Colorado wind-profiling network, *Journal of Atmospheric and Oceanic Technology, Vol.1*, 37-49.

Strauch, R. G. (1986), Changes to data processing, (Memoranda to users of WPL designed systems, March 27, 1986), Wave Propagation Lab, NOAA/ERL, Boulder, CO.

Thomson, D. W., C. W. Fairall, and R. M. Peters (1984), Network ST radar and related measurements at Penn State University: a progress report, *Handbook for MAP, Vol. 14*, SCOSTEP Secretariat, Dept. of Electrical Engineering, University of Illinois, 350-355.

VanZandt, T. E., K. S. Gage, and J. M. Warnock (1981), An improved model for the calculation of profiles of  $C_n^2$  in the free atmosphere, *20th Conf. on Radar Meteorology*, Boston, MA, 129-135.

Wesely, M. (1976), The combined effect of temperature and humidity fluctuations on refractive index, *Journal of Applied Meteorology, Vol. 15*, 43-49.

APPENDIX C

Reprint of an MS thesis titled "Analysis of temperature and velocity microturbulence parameters from aircraft data and relation to atmospheric refraction index structure" by E.A. Beecher.

The Pennsylvania State University

The Graduate School

Department of Meteorology

Analysis of Temperature and Velocity Microturbulence Parameters  
from Aircraft Data  
and Relationship to Atmospheric Refractive Index Structure

A Thesis in

Meteorology

by

Elizabeth A. Beecher

Submitted in Partial Fulfillment  
of the Requirements  
for the Degree of

Master of Science

May 1988

I grant The Pennsylvania State University the nonexclusive right to use this work for the University's own purposes and to make single copies of the work available to the public on a not-for-profit basis if copies are not otherwise available.

---

Elizabeth A. Beecher

We approve the thesis of Elizabeth A. Beecher.

Date of Signature:

12/11/87

C. W. Fairall

Christopher W. Fairall, Associate Professor  
of Meteorology, Thesis Advisor

11. 12. 87

Dennis W. Thomson

Dennis W. Thomson, Professor of Meteorology

11 Dec 87

William M. Frank

William M. Frank, Associate Professor of  
Meteorology, Head of the Department of  
Meteorology

# ABSTRACT

Due to its inherently turbulent nature, the atmosphere has a temporally and spatially variable refractive index, which degrades propagating electromagnetic radiation. The refractive index turbulent structure constant,  $C_n^2$ , is a key parameter for describing refractive variations.  $C_n^2$  can be inferred from optical turbulence (scintillometer), temperature turbulence (aircraft instrumentation or thermosonde) or radar backscatter (profiler) measurements. Vertical integrals of  $C_n^2$  give transverse coherence length,  $r_0$ , and isoplanatic angle,  $\theta_0$ . These can also be measured remotely by an  $r_0$  scintillometer and isoplanometer, respectively.

During an atmospheric optics/meteorology experiment (acronym EWAK) conducted at Penn State University primarily during April and May of 1986, data was collected by all of the aforementioned instruments. An instrumented research aircraft was used to measure vertical profiles of temperature and velocity turbulence ( $C_T^2$  and  $C_u^2$ ) and other meteorological variables. The turbulence instrumentation aboard the aircraft consisted of cold-wire and hot-wire sensors and FM recording apparatus. The taped data was processed via FFT to produce one-dimensional variance spectra (wavenumber range  $0.01$  to  $10 \text{ m}^{-1}$ ). Flights usually produced a 10 km vertical profile; the data was processed to give roughly 0.5 km vertical resolution (similar to that of the radar wind profiler).

Editing was based on percent error between a regression analysis and theoretical  $-5/3$  frequency dependence of the spectra. A majority of spectra showed good evidence of the classic inertial subrange with

-5/3 slope.  $C_T^2$  and  $C_u^2$  were calculated from the regression fit to the inertial subrange power spectral density. The rate of dissipation of turbulent kinetic energy,  $\epsilon$ , was calculated using the so-called Corrsin relation for velocity turbulence. Optical  $C_n^2$  was calculated from  $C_T^2$ .

Considerable interest has developed in models that relate microturbulence parameters to the mean gradients. One such model, proposed by VanZandt et al. (1978; 1981), has as a key variable the gradient Richardson number,  $R_i$ . In actively turbulent regions,  $R_i$  can be related to  $C_T^2$  and  $C_u^2$  as follows:

$$C_T^2 / C_u^2 = 1.6 R_i / (P_r - R_i) (\theta/g) (\partial\theta/\partial z)$$

A scatter plot of  $C_T^2$  versus  $(\theta/g \partial\theta/\partial z) C_u^2$  in the free troposphere showed a range of values from 0.3 to 10 for high and low values of  $C_T^2$ , respectively. Scatter plots of  $C_T^2$  versus  $C_u^2$  showed high correlation of these two parameters, with  $\log C_u^2 = 1.7 \log C_T^2$ .  $R_i = N/S$  and plots of  $N$  versus  $S$  roughly corresponded to the curve depicted by Fairall and Markson (1985).

Plots of  $C_T^2 / C_u^2 (\theta/g \partial\theta/\partial z)$  versus a turbulent activity parameter (Gregg 1987) clearly showed agreement with the suggested activity levels and associated values. At high activity levels, the ordinate value approached 0.4 (equivalent to  $1.6 R_i$  when approximating  $P_r$  as 1 and  $R_i$  as 0.25).

Values of  $N$  and  $S$  were used to obtain values of  $C_n^2$  and  $\epsilon$  with the model of VanZandt et al. Comparisons of  $C_n^2$  profiles measured by the various instruments showed good agreement between scintillometer and thermosonde, and between the VanZandt et al. model



and the aircraft data. The profiler (converted optical values) had some agreement with the thermosonde. Average ratios of each profile to the thermosonde profile were: aircraft 8, model 6.8, profiler 8.1. and the scintillometer 1.1.

Numerical integration of  $C_n^2$  gave estimates of  $r_0$  and  $\theta_0$ . Values from scintillometer, thermosonde and aircraft did not show clear agreement. Based on the aircraft values, the scintillometer and thermosonde  $\theta_0$  values differed by an average of 17%. The thermosonde  $r_0$  values differed by an average of 35%.

Despite good agreement on  $C_n^2$ , the aircraft data and the VanZandt et al. model output clearly disagreed on vertical profiles of  $\epsilon$ , in some cases by several orders of magnitude.

Overall, EWAK provided a chance to compare methods of measuring  $C_n^2$ , as well as an opportunity to obtain microturbulence data for examining relations to the mean gradient structure.

TABLE OF CONTENTS

Chapter

1	INTRODUCTION.....
2	BACKGROUND ON ATMOSPHERIC PROPAGATION.....
2.1	Refractive Index.....
2.2	Propagation Effects.....
2.3	Propagation Parameters and $C_n^2$ Measurements.....
3	MICROTURBULENCE THEORY.....
3.1	The Refractive Index Structure Function...
3.2	$C_n^2$ From Radar Measurements.....
3.3	$C_T^2$ and $C_u^2$ Relationships.....
3.4	The Turbulent Kinetic Energy Dissipation Rate.....
3.5	Turbulence Size Scales.....
4	THE EWAK EXPERIMENT.....
4.1	Overview.....
4.2	Aircraft Instrumentation.....
4.3	Additional Instrumentation.....
5	DATA PROCESSING.....

TABLE OF CONTENTS  
(continued)

Chapter

6	ANALYSIS METHODS.....
6.1	Aircraft Turbulence Data Analysis.....
6.2	Mean Aircraft Meteorological Profiles.....
6.3	Other Data Sources.....
7	RESULTS AND DISCUSSION.....
7.1	Analysis of $C_T^2/C_u^2$ .....
7.2	Mean Gradients and Richardson Number.....
7.3	Profiles of $C_n^2$ .....
7.4	Propagation Parameters.....
7.5	VanZandt et al. Model for $\epsilon$ .....
8	SUMMARY AND CONCLUSIONS.....
	REFERENCES.....

LIST OF TABLES

Table

- 1 Aircraft flight logistics and corresponding data from other instruments during EWAK.....
- 2 Representative editing results for each flight and in total.....
- 3 Estimates of the height of the PBL based on the strength of the signal-to-noise ratio exhibited in the spectra.....
- 4 Calculated vertical profiles of Richardson number based on  $R_i = N/S$  and using N and S values shown in Figure 17.....
- 5 The arithmetically averaged Richardson number at each height for all vertical flights.....
- 6  $X^2$  vertical profiles for each flight during which the profiler operated, calculated at each aircraft observation level in MSL altitude with aircraft-measured temperature and specific humidity profiles.....
- 7  $X^2$  vertical profiles for each flight during which the profiler operated, calculated at each profiler observation level in MSL altitude with aircraft-measured temperature and specific humidity profiles.....
- 8 Arithmetically averaged  $X^2$  vertical profiles from the Table 7 profiles.....
- 9 AFGL-calculated optical parameters from thermosonde data.....
- 10 Average of AFGL-calculated optical parameters from scintillometer data.....
- 11 Optical parameters from aircraft data calculated with the Murphy and Battles assumptions.....

LIST OF FIGURES

Figure

- 1 Voltage variance spectra from first FFT program (128 points).....
- 2 Voltage variance spectra produced by the signal analyzer's 1600 point FFT.....
- 3a The measured 2 Hz high pass temperature turbulence channel filter.....
- 3b The measured 5 Hz high pass velocity turbulence channel filter.....
- 4a The derived atmospheric 2 Hz high pass temperature turbulence channel filter.....
- 4b The derived atmospheric 5 Hz high pass velocity turbulence channel filter.....
- 5a Voltage variance spectra showing editing procedure.
- 5b Voltage variance spectra showing editing procedure.
- 5c Voltage variance spectra showing editing procedure.
- 6 Potential temperature ( $\theta$ ) vertical profiles as measured by aircraft instrumentation.....
- 7 Specific humidity vertical profiles as measured by aircraft instrumentation.....
- 8 Mean wind speed (solid line) and direction (broken line) as measured by the profiler.....
- 9 AFGL thermosonde-measured potential temperature vertical profiles correlating to aircraft flights..
- 10 AFGL thermosonde-measured specific humidity vertical profiles correlating to aircraft flights..
- 11 AFGL thermosonde-measured vertical profiles of mean wind speed (solid line) and direction (broken line).....
- 12 AFGL thermosonde-calculated vertical  $C_n^2$  profiles of raw  $C_n^2$ -optical based on measured  $C_T$  .....

LIST OF FIGURES  
(continued)

Figure

- 13 AFGL scintillometer-measured vertical profiles of  $C_n^2$ -optical taken during the aircraft flight time period.....
- 14 RADC scintillometer-measured vertical profiles of  $C_n^2$ -optical taken during the aircraft flight time period.....
- 15 Vertical profiles of  $C_n^2$ ,  $C_T^2$ , and  $C_u^2$ .....
- 16 A comparison for each vertical flight of  $C_T^2$  versus  $C_u^2$  for spectra above the PBL.....
- 17 A comparison for each level flight of  $C_T^2$  versus  $C_u^2$  for spectra above the PBL.....
- 18 A composite comparison of  $C_T^2$  versus  $C_u^2$  for all vertical profiles.....
- 19 A composite comparison of  $C_T^2$  versus  $C_u^2$  for all level profiles .....
- 20 A composite comparison of  $C_T^2$  versus  $C_u^2$  normalized by the expression  $[T/g (\partial T/\partial z + \Gamma)]$ .....
- 21 Comparison for each vertical profile of  $C_T^2$  divided by  $C_u^2$  normalized as in Figure 20 versus a turbulent activity parameter,  $\epsilon/(\nu N)$ .....
- 22 A composite comparison of  $C_T^2$  divided by  $C_u^2$  normalized as in Figure 20 versus a turbulent activity parameter  $\epsilon/(\nu N)$  for all vertical profiles.....
- 23 Comparisons of the VanZandt et al. parameters  $N$ , the Brunt-Vaisala frequency squared, and  $S$ , the shear squared.....
- 24 A composite comparison of  $N$  versus  $S$  for all flights shown in Figure 23.....
- 25 Comparison of the VanZandt et al. model vertical profile prediction of  $C_n^2$ -optical (solid line) and the aircraft  $C_T^2$ -derived vertical profile of  $C_n^2$ -optical (broken line).....

LIST OF FIGURES  
(continued)

Figure

- 26 A comparison of  $C_n^2$ -radar as derived from profiler (solid line) and from aircraft  $C_n^2$ -optical, multiplied by the conversion factor  $X^2$  to give  $C_n^2$ -radar (broken line).....
- 27 Comparison of vertical profiles of  $C_n^2$ -optical.....
- 28 Comparison of vertical profiles of  $C_n^2$ -optical.....
- 29 Comparison of vertical profiles of epsilon ( $\epsilon$ ), the turbulent kinetic energy dissipation rate, predicted by the VanZandt et al. model (solid line) and measured by the aircraft (broken line)...
- 30 Average vertical profile of eta ( $\eta$ ), the turbulence inner size scale, from aircraft-measured epsilon profiles.....

#### ACKNOWLEDGEMENTS

First and foremost, I would like to express my sincerest gratitude to my thesis advisor, Dr. Christopher W. Fairall. Without his gentle guidance and patient corrections, this work could not have been completed. I also acknowledge Dr. Dennis W. Thomson for his helpful suggestions concerning my work. A special thanks to my fellow graduate students, Mark Miller and James Edson, and their computer expertise that they so willingly shared.

With regard to my program coursework, I thank Dr. Craig F. Bohren and his humor for putting a smile on my face whenever I needed one and for always reminding me of the sheer joy of studying a physical science.

Thanks also to all those involved in EWAK who provided their time, expertise, instruments, and data, and who answered my multitudinous questions: Dr. Ralph Markson (ARA), Capt Mike Moss (Florida State University), Mr. Donald Stebbins (RADC), Mr. Paul Cook (RADC), Mr. James Brown (AFGL), Mr. Robert Beland (AFGL), Mr. Edmund Murphy (AFGL), Dr. Donald Walters (NPS) and Capt Jack Davidson (AFWL).

Finally, I would like to thank my loving husband, Jeff Beecher, for providing "R and R" when needed, as well as always willingly acting as my sounding board for ideas and my source of practical mechanical knowledge.

This research was sponsored in part by the U. S. Air Force under contract #AFOSR-86-0049.



## CHAPTER 1

### INTRODUCTION

For many reasons, there is considerable interest in the vertical profile of the refractive index structure parameter,  $C_n^2$ . This parameter quantifies effects of refractive index fluctuations important for electromagnetic radiation systems whose signals propagate through the turbulent atmosphere. Examples of such systems are satellite communications, remote sensing such as clear air radars, astronomical observation, and certain weapons. In situ measurements are a necessary first step to set up a database for verifying physical and numerical models. Both are required to facilitate the interpretation of remote sensing measurements and to achieve the goal of prediction based on readily available atmospheric data and models.

This project was an analysis of the first segment of the EWAK (E xperiment W ithout A K ronym) electro-optical/meteorological experiment at Penn State University. The purpose of EWAK, conducted principally in April and May of 1986, was to simultaneously operate at the same location several different instruments to measure the refractive index structure parameter, both in situ and remotely, throughout different synoptic and diurnal conditions.

Specifically, this thesis describes a detailed analysis of research aircraft measurements of temperature and velocity turbulence taken with the instrumented Beechcraft Baron of the Airborne Research Associates of Weston, Massachusetts. From these two measurements can be derived the temperature and velocity structure parameters,  $C_T^2$  and  $C_u^2$ . Optical  $C_n^2$  is a function of  $C_T^2$ . The turbulent

kinetic energy dissipation rate,  $\epsilon$ , is related to  $C_u^2$ . Another important relationship examined was that between  $C_T^2$  and  $C_u^2$ .

## CHAPTER 2

### BACKGROUND ON ATMOSPHERIC PROPAGATION

#### 2.1 Refractive Index

A turbulent fluid creates three general effects: it imposes varying forces on any objects embedded in the fluid or in the fluid path, it generates fluxes of fluid properties (e.g., temperature or momentum), and it creates (by density fluxes) variations in the refractive index of the fluid (Panofsky and Dutton 1984). These refractive index variations will affect electromagnetic (EM) and sonic radiation propagating through the fluid. The atmosphere, being a turbulent fluid, has a temporally and spatially variable refractive index structure. The atmosphere's turbulent refractive index fluctuations have plagued astronomers since some of the earliest recorded observations. The twinkling of stars is one of the most obvious visible manifestations. Today, our atmospheric uses of EM radiation are far more diverse than merely receiving visible starlight with our eyes or at a telescopic aperture. Hence, the need exists to characterize and predict the refractive index and its variations over arbitrary pathlengths and view angles.

Henceforth, in this thesis, unless it is specifically otherwise stated, the discussion will be concerned with propagating electromagnetic radiation. Refraction can be considered as a type of scattering (i.e., deviation from the forward direction). Turbulent, non-homogeneous variations of the atmospheric refractive index are on the order of one part in  $10^6$ . This results in very small scattering angles, for which depolarization and intensity attenuation generally

can be neglected (Strohbehn 1978). The real part of the complex refractive index,  $n$ , of a medium can be thought of as a measure of the medium's effect on wave propagation as compared to propagation in a vacuum:  $n(\text{medium}) = c(\text{vacuum})/c(\text{medium})$ , where  $c$  is the phase velocity of the wave. Refractivity, usually denoted by  $N$ , is  $(n-1) \times 10^6$ . The phase speed of the wave is altered (slowed in air compared to vacuum, thus  $n > 1$ ), but the energy  $E$  and frequency  $\nu$  remain the same,  $E = h\nu$  (Hecht 1986). Using geometric optics theory, this can be shown to result in a deviation of the beam's path which is referred to as the phenomenon of refraction (in molecular dipole theory, it is referred to as a scattering event).

Two factors determine the phase speed (and thus refractive index) in a medium: density (number of atoms, molecules or particles per unit volume) and, since each molecule has a wavelength dependent polarizability, molecular composition (Hecht 1986). At optical or shorter wavelengths, temperature variations effectively dominate refractivity changes since atmospheric molecules have low rotational polarizability at these wavelengths (Balsley and Gage 1980). However, at longer wavelengths, specifically microwave radar wavelengths, both temperature and the relative concentration of various molecular species with permanent dipole moments determine the refractive index gradients affecting radiation transmittance (Wesely 1976; Balsley and Gage 1980). In the boundary layer, water vapor content is often highly variable, and thus, may dominate refractivity changes (Balsley and Gage 1980).

If temperature and molecular composition varied negligibly from the standard atmosphere, then the refractive index profile could

easily be calculated. The importance of turbulence is its resultant mixing (Strohbehn 1978). Mixing due to turbulence causes the variations in space and time of the refractive index profile. It is the random nature of turbulence that introduces chaos into the density profile.

## 2.2 Propagation Effects

Variations in refractive index can cause at least six types of EM propagation degradation: beam steering, image dancing, beam spread, spatial coherence degradation, temporal coherence degradation, and scintillation (Dewan 1980).

Beam steering is deviation from the line-of-sight (i.e., the most direct path from source to receiver). The transverse deviation of a narrow beam increases with subsequent distance from the deviating medium. If a turbulent eddy is larger than the width of the beam, it may act as a "prism." This effect can be quite significant for earth-to-space uplinks, because the planetary boundary layer (PBL) is highly turbulent (Dewan 1980).

Image dancing is the modulation of the arrival angle of the whole beam wavefront. It can cause the focal plane for the beam to be angled to a receiver normal to the beam, causing photographic blurring or necessitating larger apertures with lower signal-to-noise ratios (Dewan 1980).

Beam spreading is caused by scattering at small angles near the edge of the beam. This occurs when the beamwidth is greater than the turbulent eddies. This phenomenon occurs most on the space-to-earth downlink (Dewan 1980).

At large distances, a spherical wave from a point source can be approximated as a plane wave. According to Huygen's model, a single wavefront can be thought to consist of an infinite number of points each emitting a "wavelet." The wavelets add together to give the total wave. If the wavelets have a constant phase relation, the wavefront is said to be coherent. When phase difference randomly and continuously changes, the wavefront becomes incoherent (Hecht 1986). When a pathlength difference is introduced across a coherent wavefront (e.g., refraction), a Fraunhofer diffraction pattern may be seen in which maxima/minima occur where the amplitudes of wavelets constructively/destructively interfere. Thus diffraction is one method of testing coherence (Hecht 1986).

A coherent source can be viewed as emitting "pulses," or wave packets (this model combines wave and particle concepts). No source is perfectly monochromatic, thus each wave pulse has a frequency bandwidth. The inverse of the pulse frequency band is the "period" band or coherence period (Hecht 1986). Temporal (or longitudinal) coherence occurs within the coherence period. Spatial (or horizontal) coherence occurs across a wave pulse emitted from a coherent source. Spatial degradation is loss of phase coherence across a wavefront, causing spot blurring on photographic images. It also distorts photomixing processes which rely on mixing of an incoming to a local signal to form a "beat." Temporal degradation is a loss of phase coherence during the coherence period, thus distorting amplitude modulated signals (Dewan 1980).

Scintillation is a coherence effect describing amplitude changes at a focal plane (interference patterns). Spatial scintillation being

fluctuations across a beamwidth (or wavefront), temporal scintillation being fluctuations in time of the total beam amplitude (signal fading) (Dewan 1980).

### 2.3 Propagation Parameters and $C_n^2$ Measurements

A variety of theories have been developed for these degradation effects. In general, an atmospheric turbulence parameter, the refractive index structure constant,  $C_n^2$ , must be specified along the propagation path. By measuring some relevant propagation parameter (e.g., scintillation) the theory can be "inverted" to determine  $C_n^2$ .

One such instrument, the NOAA (National Oceanic and Atmospheric Administration) scintillometer, measures  $C_n^2$ -optically remotely, based on starlight amplitude fluctuations. As one of the six distortions described previously, scintillation has been quantified using an integral of  $C_n^2(z)$ , where  $z$  is the altitude. Tatarskii has shown for temporal scintillations, time averaged amplitude fluctuations (Dewan 1980), that

$$\langle [\ln(A/A_0)]^2 \rangle = 0.56 \ k^{7/6} \int_0^z C_n^2(z) \ z^{5/6} dz \quad (2.1)$$

where  $A$  is the signal amplitude,  $A_0$  is the mean amplitude,  $k$  is the optical wave number, and the angle brackets denote a time average. A stellar scintillometer measures  $\sigma_I^2(d_i)$ , the normalized variance of the spatially filtered signal irradiance for 3 spatial wavelengths,  $d_i$ . Then a profile of  $C_n^2$  is calculated for seven predetermined levels, based on seven weighting functions (only four of which are independent)

$$C_n^2 = B \sum_{i=1}^3 R_i K_i^{8/3} \sigma_I^2(d_i) \quad (2.2)$$

where  $R_i$  weight is given to the  $i$ th spatial wavenumber  $K_i$  ( $K_i = 2\pi/d_i$ ) and

$$B = 1.87 \times 10^{-13} \left[ \int_0^\infty W_c(z) dz \right]^{-1} \quad (2.3)$$

where  $W_c(z)$  is a composite path weighting function (Ochs et al. 1976). The seven predetermined levels are line-of-sight distance from the instrument, so that actual height above ground depends on the zenith angle of the observed star. Some improvements to the NOAA scintillometer were made by AFGL (Air Force Geophysical Lab) to their instrument. They are described in more detail by Murphy and Battles (1986).

An NPS (Naval Postgraduate School)  $r_o$  scintillometer optically measures the transverse coherence length,  $r_o$ , of the image in the focal plane (Donald Walters, telephone conversation, October 1987).  $r_o$  is a scalar measure (in units of aperture size) of spatial wavefront coherence. Crudely stated, the resolution of an image cannot be improved by increasing a single aperture beyond  $r_o$  (Dewan 1980). This helps delineate the aperture size for adaptive optics elements. It has been shown that

$$r_o = 18.5 \lambda^{1.2} \left( \int_0^\infty C_n^2(z) dz \right)^{-3/5} \quad (2.4)$$

with  $r_o$  in cm, wavelength ( $\lambda$ ) in m,  $C_n^2$  in  $m^{-2/3}$ , and altitude in m. Using this integral,  $r_o$  can also be calculated from profiles of  $C_n^2$  (Fried and Mevers 1974).



An AFWL (Air Force Weapons Lab) isoplanometer optically measures  $\theta_o$ , the isoplanatic angle.  $\theta_o$  is a measure of angular coherence for an object with angular size (vs. a point source) that delineates the region through which the object can be viewed coherently without adaptive optics (Loos and Hogge 1979; Murphy and Battles 1986).  $\theta_o$  can also be calculated from a vertical profile of  $C_n^2$  (Murphy and Battles 1986)

$$\theta_o = 58000 \lambda^{1.2} \left[ \int_0^\infty z^{5/3} C_n^2(z) dz \right]^{-3/5} \quad (2.5)$$

with  $\theta_o$  in  $\mu\text{rad}$ , and  $\lambda$ ,  $z$  and  $C_n^2$  in the same units as for  $r_o$ .

Notice that the three parameters discussed here have different propagation path weighting functions ( $\sigma_I^2$  as  $z^{5/6}$ ,  $r_o$  as 1.0,  $\theta_o$  as  $z^{5/3}$ ). Thus, for ground-to-space optical paths,  $r_o$  tends to be dominated by the boundary layer,  $\theta_o$  by the stratosphere, and  $\sigma_I^2$  is somewhere in between.

### CHAPTER 3

#### MICROTURBULENCE THEORY

##### 3.1 The Refractive Index Structure Function

The atmosphere is predominantly hydrostatically stable above the planetary boundary layer (PBL). Nevertheless, observations, such as contrails and rocket trails, have clearly shown that discrete turbulent layers exist (VanZandt et al. 1981). Although turbulence and byproducts of turbulence (fossil eddies) are undoubtedly present, they exist only on an intermittent basis.

While atmospheric turbulence is inherently anisotropic, at small size scales, where viscous dissipation occurs, turbulence can be considered isotropic. For isotropic and homogeneous turbulence, the structure function,  $D$ , depends on spatial scalar distance,  $\xi$ , and is defined as the mean squared difference of the measured passive parameter (e.g., temperature) at two points in space (Hinze 1975).

$$D_T(\xi) = \langle (T(r) - T(r+\xi))^2 \rangle \quad (3.1)$$

where the angle brackets indicate an averaged quantity. In anisotropic turbulence,  $D$  also depends on the orientation of the separation (Hinze 1975).

The autocorrelation  $R$  is defined as the average of the product of deviations from the mean (e.g.,  $T'$ ) at two points in space.

$$R_T(\xi) = \langle T'(r) T'(r+\xi) \rangle \quad (3.2)$$

In the limit, as  $\xi$  approaches infinity, the structure function approaches twice the variance. Variance is equal to the

autocorrelation function at  $\xi=0$  (Tatarskii 1971). Thus,

$$\frac{1}{2} D_T(\xi) = R_T(0) - R_T(\xi) \quad (3.3)$$

In the inertial subrange, it can be shown that the structure function has a power law relation to separation with a constant designated  $C_x^2$  (e.g.,  $C_T^2$ ) (Hinze 1975).

$$D_T(\xi) = C_T^2 \xi^{2/3} \quad (3.4)$$

Similarly, we can define for refractive index,

$$D_n(\xi) = C_n^2 \xi^{2/3} \quad (3.5)$$

The structure constant is only a "constant" in that it is independent of the separation distance; it is still variable over time and space [e.g.,  $C_T^2(x,y,z,t)$ ]. The optical refractive index structure constant can be related to the temperature and humidity structure constants (Nastrom et al. 1981).

$$C_n^2 = f_1^2 C_q^2 + 2 f_1 f_2 C_{qT}^2 + f_2^2 C_T^2 \quad (3.6)$$

where  $f_1 = 0.60 P/T^2$ , and

$$f_2 = -1.2 P q / T^2 \theta - 77.6E-6 P / T \theta \quad (3.7)$$

with pressure in mb, and where  $q$  is specific humidity. Neglecting the effects of humidity, this reduces to (Tatarskii 1971)

$$C_n^2 (\text{optical}) = (79 \times 10^{-6} (P/T^2))^2 C_T^2 \quad (3.8)$$

During the EWAK experiment, the aircraft-measured  $C_T^2$  allowed computation of "dry"  $C_n^2$ -optical. A Lyman-alpha detector on the

aircraft was intended to measure  $C_q^2$  but the threshold sensitivity was too high for the vapor concentrations at the altitudes of interest.

### 3.2 $C_n^2$ From Radar Measurements

Data from a clear-air radar (often referred to as a profiler) can be used to calculate  $C_n^2$ -radar based on radar reflectivity. The backscatter cross section from received power,  $\sigma$ , at the wavelength,  $\lambda$ , can be characterized by  $C_n^2$  (VanZandt et al. 1977) as

$$\sigma = 0.38 C_n^2 \lambda^{-1/3} \quad (3.9)$$

Tatarskii (1971) derives a dimensional relation for  $C_n^2$  based on a refractivity gradient across a turbulent layer

$$C_n^2 = a M^2 L^{4/3} \quad (3.10)$$

where  $a$  is an empirical constant,  $L$  is the layer thickness and

$$M^2 = -77.6 \times 10^{-6} (P/T) [ N/g(1 + 15500q/T) - 7750 q'/T ] \quad (3.11)$$

where  $P$  is pressure in mb,  $T$  is absolute temperature,  $q$  is specific humidity in kg/kg,  $q'$  is  $\partial q / \partial z$ ,  $g$  is acceleration due to gravity, and  $N$  is the Brunt-Vaisala frequency squared. For  $C_n^2$ -optical,  $q$  and  $q'$  are set equal to zero in  $M^2$  (Dewan 1980), which gives the resulting ratio relating optical and radar values

$$(C_n^2\text{- radar}) / (C_n^2\text{- optical}) = X^2 \quad (3.12)$$

with (Fairall and Thomson 1985)

$$X^2 = [1 - 7750 q' (q/T)(g/N) + 15500 q/T]^2 \quad (3.13)$$

### 3.3 $C_T^2$ and $C_u^2$ Relationships

Dimensional analysis shows that in the inertial subrange of isotropic turbulence, the variance spectral density obeys a  $k^{-5/3}$  wavenumber dependence.

$$\phi_T(k_1) = \beta_T \chi_T \epsilon^{-1/3} k_1^{-5/3} \quad (3.14)$$

where  $\beta_T$  is an empirical constant,  $\chi_T$  is the rate of dissipation of one half the temperature variance,  $\epsilon$  is the dissipation rate of the turbulent kinetic energy, and  $k_1$  is the spatial wavenumber ( $k_1 = 2\pi \lambda^{-1}$ ) (Panofsky and Dutton 1984). Since the one dimensional variance spectrum is defined as the Fourier transform of the autocorrelation (Panofsky and Dutton 1984),

$$\phi_T(k_1) = \frac{2}{\pi} \int_0^\infty R_T(\xi_1) \cos(k_1 \xi_1) d\xi \quad (3.15)$$

it can be shown using the relation of the structure function to variance and the autocorrelation, that

$$\phi_T(k_1) = 0.25 C_T^2 k_1^{-5/3} \quad (3.16)$$

in which 0.25 is the result of combining several constants. Now, the so-called Corrsin relation is obtained from 3.14 and 3.16 (Tatarskii 1971).

$$C_T^2 = 4 \beta_T \chi_T \epsilon^{-1/3} \quad (3.17)$$

$\beta$  has been determined for temperature,  $\beta_T=0.8$ , and velocity,

$\beta_u=0.5$  (Champagne et al. 1977; Panofsky and Dutton 1984).  $\beta_q$  is assumed to be equal to  $\beta_T$ . Since  $\chi_u=\epsilon$  for velocity, a simplified Corrsin relation is obtained

$$C_u^2 = 4 \beta_u \epsilon^{2/3} = 2 \epsilon^{2/3} \quad (3.18)$$

Using this relation, it is simple to calculate  $\epsilon$ , the turbulent kinetic energy dissipation rate.

$\epsilon$  is an important term in the variance budget equations for a turbulent layer. These equations, neglecting transport (Ottersten 1969), are (Fairall and Markson 1984)

$$de/dt + \overline{u'w'} \partial u/\partial z - g/\theta \overline{w'\theta'} = -\epsilon \quad (3.19)$$

$$\frac{1}{2} \frac{d\sigma_\theta^2}{dt} + \overline{w'T'} \partial \theta/\partial z = -\chi_T = -C_T^2 \epsilon^{1/3} / (4 \beta_T) \quad (3.20)$$

where primed quantities are fluctuations, barred quantities are means.  $e=1/2(\sigma_u^2+\sigma_v^2+\sigma_w^2)$  is the turbulent kinetic energy,  $g$  is the acceleration due to gravity,  $z$  is altitude,  $\sigma_\theta$  is variance of potential temperature,  $\chi_T$  is the rate of dissipation of one half the thermal variance, and  $u$ ,  $v$ , and  $w$  are the horizontal and vertical velocity components respectively. If the flux Richardson number is defined as

$$R_f = [(\overline{w'\theta'} g/\theta) / (\overline{u'w'} \partial u/\partial z)] \quad (3.21)$$

and the eddy diffusion coefficient is invoked

$$\overline{w'\theta'} = -K_H \partial \theta/\partial z \quad (3.22)$$

$$\overline{u'w'} = -K_m \partial u/\partial z \quad (3.23)$$

then the following ratio results when using the Corrsin relations in a ratio of equation 3.20 to 3.19. (Fairall and Markson 1984)

$$C_T^2 / C_u^2 = 1.6 (\theta/g) \partial\theta/\partial z R_f / (1 - R_f) \quad (3.24)$$

$$C_T^2 / C_u^2 = 1.6 (\theta/g) \partial\theta/\partial z R_i / (P_r - R_i) \quad (3.25)$$

where  $R_f$  is replaced by the gradient Richardson number,

$$R_i = g \partial \ln \theta / \partial z / (\partial u / \partial z)^2 \quad (3.26)$$

and the turbulent Prandtl number,

$$P_r = K_m / K_H \quad (3.27)$$

In an actively turbulent layer in the free troposphere,

$R_i \approx R_{icrit} = 0.25$  and  $P_r \approx 1$  (Dewan 1980), then

$$C_T^2 / C_u^2 \approx 1.6 (\theta/g) \partial\theta/\partial z R_i \quad (3.28)$$

Gradient Richardson number is the basis for a model developed by VanZandt et al. (1978, 1981). This model predicts  $C_n^2$ -optical and  $\epsilon$  based on measured values of  $N$  ( $=g/\theta \partial\theta/\partial z$ ) and  $S$  ( $=\partial u/\partial z^2 + \partial v/\partial z^2$ ), and input values of  $L$ , the outer scale or overturning size of the turbulent eddies. Note that the gradient Richardson number is equal to  $N/S$ . Based on equation 3.28, this model can also be related to the ratio of  $C_T^2$  and  $C_u^2$ . The model is based on Tatarskii's dimensional relationships

$$C_n^2 = a M^2 L^{4/3} \quad (3.29)$$

$$\epsilon = b S^{3/2} L^2 \quad (3.30)$$

where  $a$  and  $b$  are constants. A statistical integration is performed assuming that turbulence occurs in discrete layers with  $R_i \leq 0.25$ . Theoretical probability density functions are assumed for shear and temperature gradients. The internal model variable  $L$  is adjusted to give best match to radar-derived  $C_n^2$  profiles. The model is inherently based on averaging over a length much greater than the turbulent scale, of which only a fraction,  $F$ , is actively turbulent (VanZandt et al. 1981). Thus high resolution in situ measurements (such as measurements by aircraft) may differ from model predictions.

### 3.4 The Turbulent Kinetic Energy Dissipation Rate

Few in situ measurements of  $C_u^2$  or  $\epsilon$  have been made above the PBL. Barat and Bertin (1984) measured  $C_T^2$  and  $C_u^2$  with stratospheric balloons, and Fairall and Markson (1984) with an aircraft. Kennedy and Shapiro (1980) calculated various turbulence parameters from research aircraft observations of CAT episodes associated with jetstreams.

Substituting for  $C_u^2$  in equation 3.22 gives another relationship for  $\epsilon$

$$C_T^2 = 3.2 (\theta/g) \partial\theta/\partial z R_i \epsilon^{2/3} \quad (3.31)$$

This can be used to calculate  $\epsilon$  from  $C_T^2$  measurements, and from high altitude (where water vapor contribution is negligible) profiler measurements of  $C_n^2$ -optical (Tatarskii 1971) with

$$C_n^2 = [79 \times 10^{-6} P/T^2]^2 3.2 (\theta/g) \partial\theta/\partial z R_i \epsilon^{2/3} \quad (3.32)$$



or by assuming a Corrsin relation for  $C_n^2$

$$C_n^2 = 3.2 \chi_n \epsilon^{-1/3} \quad (3.33)$$

and assuming

$$\chi_n = K_n (\partial n / \partial z)^2 \quad (3.34)$$

$$K_H = R_i N^{-1} \epsilon \quad (3.35)$$

$$K_n = K_H \quad (3.36)$$

$$M^2 = (\partial n / \partial z)^2 \quad (3.37)$$

then

$$C_n^2 = 3.2 R_i M^2 N^{-1} \epsilon^{2/3} \quad (3.38)$$

where  $N$  is Brunt-Vaisala frequency squared and  $M$  is Tatarskii's refractivity gradient (Barat and Bertin 1984, Panofsky and Dutton 1984). Notice that equation 3.28 implies the factor  $R_i$  should actually be  $R_i / (P_r - R_i)$ .

### 3.5 Turbulence Size Scales

For oceanic turbulence, Gregg (1987) defines a turbulence bandwidth based on the ratio of Ozmidov scale  $L_o = [\epsilon / N^{3/2}]^{1/2}$  (a buoyancy scale at which buoyancy equals inertial force) and the Kolmogorov scale,  $\eta = [\nu / \epsilon^3]^{1/4}$  (the inner scale or cutoff wavelength for the inertial subrange where viscous equal inertial forces).

$$L_o / \eta = [\epsilon / \nu N]^{3/4} \quad (3.39)$$

where  $\nu$  is the kinematic viscosity. The eddy overturning scale is proportional to the buoyancy scale in actively turbulent layers. Thus, the inertial subrange occurs for size scales less than the buoyancy scale and greater than the inner scale. Gregg provides the following empirical guideline to interpret the bandwidth ratio parameter as a turbulence activity parameter.

<u>Value of <math>\epsilon/\nu N</math></u>	<u>Turbulence State</u>
<15	Decaying turbulence, fluxes negligible
>200	Fully isotropic
>10000	Fully developed flow

A spectrum begins to deviate from  $-5/3$  slope at size scales one order of magnitude greater than the Kolmogorov microscale (Hill and Clifford 1978). For  $L_0 \approx 10\eta$ , no inertial subrange should be apparent.

## CHAPTER 4

### THE EWAK EXPERIMENT

#### 4.1 Overview

Two segments of the EWAK experiment were analyzed in this thesis study. The first and major segment was performed from 14 April 1986 to 6 May 1986. This segment was conducted at the Meteorological Field Site, located several miles southwest of State College, PA, on the Rock Springs Agronomy Research Farm. The relevant instruments operating at various times during the experiment were an Air Force Geophysical Lab (AFGL) scintillometer, Rome Air Development Center (RADC) scintillometer, an AFGL thermosonde, an Air Force Weapons Lab (AFWL) isoplanometer, a Naval Postgraduate School (NPS)  $r_o$  scintillometer, a Penn State University (PSU) Doppler radar profiler, a PSU Doppler sodar, and the Airborne Research Associates (ARA) aircraft. A summary of the database relevant to this study is given in Table 1.

The aircraft was based at University Park Airport, several miles northwest of State College, PA. Data gathering flights were made over the field site and insofar as possible within a radius of 10 miles. Eight flights were made, six yielded useable results: flight 1 was a test flight and flight 5 had a total failure of the instrument recorder. Each flight consisted of a fairly rapid climb to maximum altitude (approximately 30 kft or 10 km) and then a slow descent (500 fpm). All descents were analyzed (because of the greater resolution), but for comparison purposes several ascents were also analyzed. Level

Table 1.  
Aircraft flight logistics and corresponding data from other  
instruments during EWAK.

Aircraft Flight	Site	Date	Type	GMT Time	Radar Wind Observ Time	Thermosonde Flight Time	Scintillimeter		Radar C <sup>2</sup> Observ <sup>n</sup> Time
							Run Time	RADC	
1	PSU	4/13/86	test flight				AFGL		
2	PSU	4/14/86	Descent Level	1534-1554 1611-1732	1500-1600				1600-1700
3	PSU	4/18/86	Descent	2107-2207	2000-2100				2100-2200
4	PSU	4/19/86	Descent	1710-1809	1700-1800				1600-1700
5	PSU	5/3/86	recording failure						
6	PSU	5/4/86	Ascent Descent	0400-0438 0439-0540	0500-0600	L4033	0408	0342-0513	0500-0600
7I	PSU	5/4/86	Descent	1725-1822	1700-1800				1800-1900
8	PSU	5/6/86	Ascent Descent	0259-0331 0332-0430	0300-0400	L4019	0328	0317-0420	0300-0400
9	RADC	8/11/86	Ascent Descent	2247-2324 2325-2357					
10	RADC	8/12/86	Ascent Descent	1557-1706 1707-1751					
11I	RADC	8/13/86	Ascent Descent	0219-0300 0301-0357					
11II	RADC	8/13/86	Level	1410-1452					
12	RADC	10/10/86	Level Descent	1738-1825 1911-1943					

flight data of return trips by the aircraft to Boston was also added to several flights.

The second segment of EWAK was conducted at Griffiss Air Force Base, Rome, NY, from 11 August through 15 August 1986. Both ARA aircraft and RADC scintillometer measurements were taken, however, scintillometer data taken during these flights was unavailable for this thesis. One additional flight was made on 20 October 1986. For these flights, the aircraft was based at Oneida County Airport and performed similar flight patterns centered around RADC's field site in Verona, NY.

#### 4.2 Aircraft Instrumentation

A summary of the instrumentation available on the aircraft is given by Fairall and Markson (1984; 1987). Thus only the relevant turbulence measurements are discussed here. Temperature and velocity signals were amplified, filtered, and recorded on FM tape. Recorder gain settings were correlated to tape counters and recorded manually. Filters were set for a bandpass between 2 and 200 Hz for the temperature signal, and 5 and 200 Hz for the velocity signal. The FM tape recorder was set at the 15/16 ips speed, which provided an additional low pass filtering at 256 Hz.

Temperature fluctuations were measured with a fast response resistance bridge driving microthermal sensor probes as the temperature sensitive resistance elements. The bridge used was a Thermo Systems, Inc. (TSI) type 1044, dc Wheatstone bridge with a frequency response of 800 hz. The microthermal probes were TSI type 1210 with T1.5 configuration (W wire, 4.5 $\mu$ m dia., ice point resistance

$R_i - 5\Omega$ ). A wingtip boom carried matched sensors that were connected to the two bridge arms. One sensor was covered so that bridge signal output was proportional to temperature fluctuations sensed by the exposed probe.

Velocity fluctuations were measured with hot-wire anemometry in a constant temperature circuit. The bridge used was a TSI model 1050. Probes used were the same TSI type 1210 T1.5 tungsten sensors with a 50% overheat.

Other measurements taken that were used in this analysis were air temperature (measured with a standard Rosemont sensor and bridge circuit), dew-point temperature (measured with a Cambridge Systems, Inc. aircraft chilled mirror instrument), pressure altitude (measured with a Rosemont sensor), and radar altitude (measured with a Bonzair Mark 10 altimeter).

#### 4.3 Additional Instrumentation

Both the RADC and the AFGL scintillometers are instruments that measure stellar scintillation amplitude fluctuations based on the NOAA model II instrument described in detail by Ochs et al. (1977). Additional modifications were made to the AFGL scintillometer as described by Murphy and Battles (1986). The AFWL isoplanometer and NPS  $r_0$  scintillometer are instruments also based on measuring stellar scintillations and may be regarded to be derivatives of the NOAA instrument. These instruments are described in some detail by Eaton et al. (1985), and Stevens (1985), respectively.

The AFGL thermosonde is essentially a special temperature turbulence measuring package attached to a radiosonde. The instrument package is described in detail by Brown et al. (1982).

Penn State's Doppler radar profiler is, basically, of the type described by Strauch et al. (1986). It is a VHF (6 m wavelength) pulsed Doppler radar with a phased array antenna located near McAlevys Fort, PA, on Shantytown Road, approximately 10 miles south of State Collage, PA. With the profiler, vertical profiles of wind speed and direction are obtained as well as radar reflectivity (backscatter cross section). Radar volume reflectivity can be used to calculate  $C_n^2$  values at each of the radar gates (VanZandt et al. 1978). The profiler produces both high and low resolution profiles. High resolution is ~290 m from ~1 km to 8 km MSL. Low resolution is ~870 m from ~1.5 km to 17.5 km MSL.

PSU Doppler sodar data was not used in this study.



CHAPTER 5  
DATA PROCESSING

The relation of the structure constant to the variance spectral density as a function of wavenumber (Equation 3.16) allows determination of  $C_T^2$  and  $C_u^2$  from spectral analysis of turbulence data. The aircraft data was a time series record of voltage fluctuations, which could be transformed into frequency spectra. Taylor's frozen turbulence hypothesis allows for translation of the spatial spectrum  $\phi(k_1)$  to a frequency spectrum  $\phi'(f)$  (Panofsky and Dutton 1984), by the relation

$$k_1 = 2\pi f/u \quad (5.1)$$

where  $k_1$  is the spatial wavenumber,  $u$  is the relative speed of the passing eddies (in this case,  $u=60$  m/s, the aircraft speed), and  $f$  is the frequency in Hz. Since total spectral intensity must be invariant (Panofsky and Dutton 1984), temporal and spatial spectra can be related by

$$\phi(k_1)dk_1 = \phi'(f)df \quad (5.2)$$

Substitution gives

$$\phi'(f) = \phi(2\pi f/u)dk_1/df = \phi(2\pi f/u) 2\pi/u \quad (5.3)$$

and then

$$\phi_T'(f) = 2\pi/u \phi_T(k_1) \quad (5.4)$$

$$\phi_T'(f) = 2\pi/u (0.25 C_T^2 k_1^{-5/3}) \quad (5.5)$$

$$\phi'_T(f) = (2\pi/u)^{-2/3} (0.25 C_T^2 f^{-5/3}) \quad (5.6)$$

Similarly for velocity

$$\phi'_u(f) = (2\pi/u)^{-2/3} (0.25 C_u^2 f^{-5/3}) \quad (5.7)$$

Rearranging gives the equation(s) relating the structure functions to the measured spectra

$$C_{T,u}^2 = 4 (2\pi/u)^{2/3} \phi'_{T,u}(f) f^{5/3} \quad (5.8)$$

where  $\phi'_{T,u}(f)$  is a representative value in the inertial subrange (Fairall and Markson 1984).

Another method to determine the structure constants (the single probe RMS method) is suggested by the relation of total variance to spectral density (Fairall and Markson 1984)

$$\text{Variance} = \text{mean square} = \int_{f_1}^{f_u} \phi'(f) df \quad (5.9)$$

where  $f_u$ —upper frequency limit, and  $f_1$ —lower frequency limit.

Thus the filtered RMS of the signal can be used to directly obtain the structure constant by integrating 5.6 or 5.7

$$\text{Variance} = (\text{RMS})^2 = (2\pi/u)^{-2/3} 0.25 C_{T,u}^2 \left(-\frac{3}{2}\right) (f_u^{-2/3} - f_1^{-2/3}) \quad (5.10)$$

Rearranging gives

$$C_{T,u}^2 = \frac{8}{3} (2\pi/u)^{2/3} (\text{RMS})^2 (f_1^{-2/3} - f_u^{-2/3})^{-1} \quad (5.11)$$

The thermosonde instrument calculated  $C_T^2$  directly using the double probe RMS method. If two probes with a known separation  $\xi$  are used, then with an RMS of the difference of the signal

(Brown et al. 1982)

$$C_T^2 = \langle (T_1 - T_2)^2 \rangle / \xi^{2/3} = (\text{RMS})^2 / \xi^{2/3} \quad (5.12)$$

The spectral method has the advantage of greater accuracy over the RMS method because a region of the spectrum can be selected which is relatively free of noise. The RMS variance includes all noise in the bandwidth analyzed (Fairall and Markson 1984). However, the disadvantage to the spectral method is the greatly increased computation time. RMS methods can be done on a virtually real time basis.

The aircraft temperature turbulence data was taken as voltage fluctuations in bridge output due to resistance fluctuations of the probes. Temperature fluctuations cause these resistance changes. This relation is given by

$$dV/dt = i G_B dR/dt \quad (5.13)$$

where the current to the probe sensor is  $i$ , and bridge amplification or gain is  $G_B$  ( $\approx 4000$ ) (Fairall and Markson 1984).

The resistance-temperature relation is linear for tungsten sensors over a broad temperature range, giving

$$R = R_i [1 + \alpha(T - T_i)] \quad (5.14)$$

where  $R_i$  and  $T_i$  are values at the ice point ( $R_i = 5\Omega$ ), and  $\alpha$  is the effective thermal resistance coefficient ( $\alpha = .0026 \text{ K}^{-1}$ ), which includes the loss of sensitivity due to probe support effects (Fairall and Markson 1984). Thus,

$$dR/dt = R_i \alpha dT/dt \quad (5.15)$$

and

$$dV/dt = i G_B G (R_i \alpha dT/dt) \quad (5.16)$$

where the added G term accounts for any additional signal conditioning or gains applied (usually G=10). The voltage variance spectrum is the Fourier transform of the square of voltage fluctuations which then can be related to the temperature variance spectrum (Fairall and Markson 1984).

$$\phi'_V = (i G G_B R_i \alpha)^2 \phi'_T(f) \quad (5.17)$$

Including noise sources, this would be

$$\phi'_V = (i G G_B R_i \alpha)^2 (\phi'_T + N_u + N_T + N_v/(iR_i\alpha)^2) \quad (5.18)$$

where  $N_v$  is broadband voltage noise in the system,  $N_T$  is temperature noise detected by the sensors but not due to turbulence (e.g., sonic adiabatic compression), and  $N_u$  is velocity contamination due to cooling rate variations associated with velocity fluctuations. An indepth study of signal-to-noise ratio was done by Fairall and Markson (1984). It was concluded that, in flight, most noise was temperature noise. Although the source of this noise could not be identified, it could be lessened by changing sensor location. Optimal sensor location proved to be on the wingtip. Sensor currents were kept at a maximum just below the velocity contamination threshold (i=5 mA).

Velocity turbulence data was also taken as a time series of voltage fluctuations. King's Law voltage relationship (Hinze 1975) was used

$$V^2 = V_o^2 + B u^{1/2} \quad (5.19)$$

where  $V_o^2$  and  $B$  are calibration constants (Fairall and Schacher 1977) computed for 50% overhear at STP as  $V_o^2 = 2.7 \text{ Volts}^2$  and  $B_o = 1.0 \text{ Volts}^2 / (\text{ms}^{-1})^{1/2}$ . Correcting for varying temperature and pressure gives

$$B = B_o (P/1013)^{1/2} (288/T)^{1/4} [(453-T)/288] \quad (5.20)$$

(Fairall and Markson 1984). Velocity fluctuations cause bridge output voltage variations as

$$dV/dt = [B G / (4 V u^{1/2})] du/dt \quad (5.21)$$

with  $G$  additional signal conditioning gains (usually  $G=100$ ) and  $V$  the mean bridge voltage (about 3 Volts for nominal aircraft speeds).

Relating the square of fluctuations to the variance spectrum gives

$$\phi'_V = (B G / 4 V \sqrt{u})^2 \phi'_u \quad (5.22)$$

The final forms used for calculating  $C_T^2$  and  $C_u^2$  from the aircraft data (Fairall and Markson 1984) were

$$C_T^2 = 4 (2\pi/u)^{2/3} (i G G_B R_i \alpha)^{-2} \phi'_{V(T)}(f) f^{5/3} \quad (5.23)$$

$$C_u^2 = 4 (2\pi)^{2/3} u^{1/3} (4 V / B G)^2 \phi'_{V(u)}(f) f^{5/3} \quad (5.24)$$

Flight 12 gain settings were not recorded. They were assumed to be the same as flight 11 for processing, but for that flight, this should be noted.

Initially, the temperature and velocity channels of the taped data were converted from analog to digital with an Infotek A/D board. Approximately two minutes of analog data were digitized. A 128 point Fast Fourier Transform (FFT) was done and a final spectrum produced from an average of 400 spectral blocks. This gave a vertical resolution of 0.3 to 0.5 km, about the same as the radar profile.

The log of power spectral density ( $\text{Volts}^2/\text{Hz}$ ) was plotted as decibels [ $10 \cdot \log (V^2/\text{Hz})$ ] against log of frequency (Hz) for 4 to 256 Hz. A key frequency was chosen that consistently appeared in the inertial subrange (in a region of high signal to noise) and the spectral density at this point was used to plot a  $-5/3$  slope through the spectrum to show goodness-of-fit to the Kolmogorov turbulence theory. Due to the small number of points, the spectra obtained with this method were somewhat crude and very difficult to interpret. Figure 1 shows three different spectra from flight 2 as examples (indicated as EWAK2BT-rec#). Record 1 has a high signal-to-noise ratio, record 31 is very noisy with little signal, and record 45 is an unusual steeply sloped spectra.

A second method gave far more satisfactory results. Roughly two minutes of data were analyzed by a dual channel Hewlett-Packard 3562A dynamic signal analyzer by linearly averaging 55 times with an overlap of 75%. A 1600 point FFT, using a Hanning window, produced a power spectrum from .125 to 100 Hz. This frequency range corresponds to a wavenumber range of 0.01 to  $10 \text{ m}^{-1}$ . Resolution of the spectra was greatly increased. The same three records from flight 2 are shown in Figure 2.

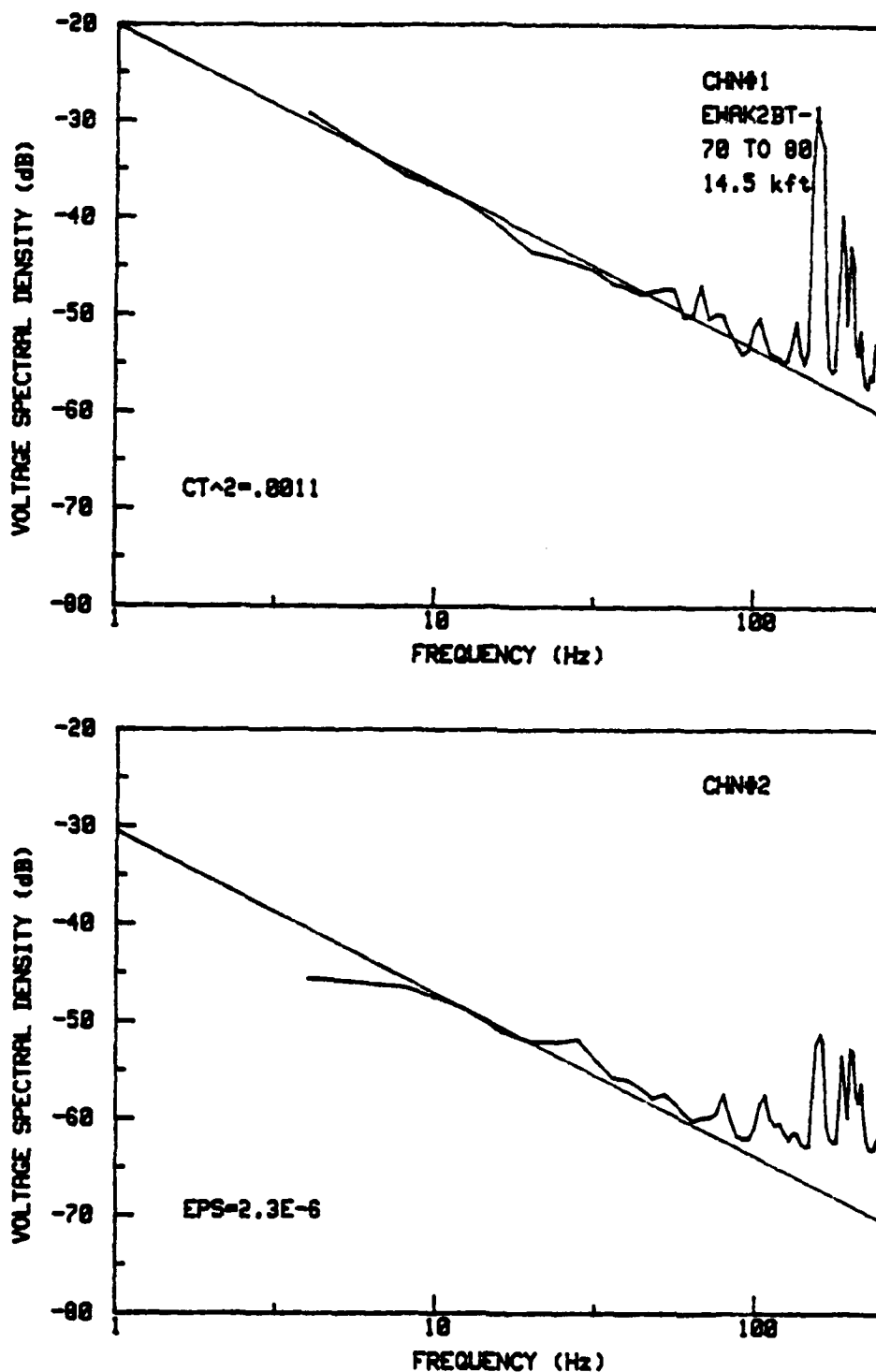


Figure 1. Voltage variance spectra from first FFT program (128 points). For each record, the top spectrum (channel #1) is temperature variance and the bottom spectrum (channel #2) is velocity variance. Voltage power spectral density (dB) is plotted against frequency (log Hz). The slanted line represents a  $-5/3$  slope for comparison. Coded flight name (e.g., EWAK2BT) and record number (e.g., - 1), tape footage, and altitude are shown interior to each channel #1 graph. Three different dual-channel records in flight 2 are shown: 1, 31, and 45.

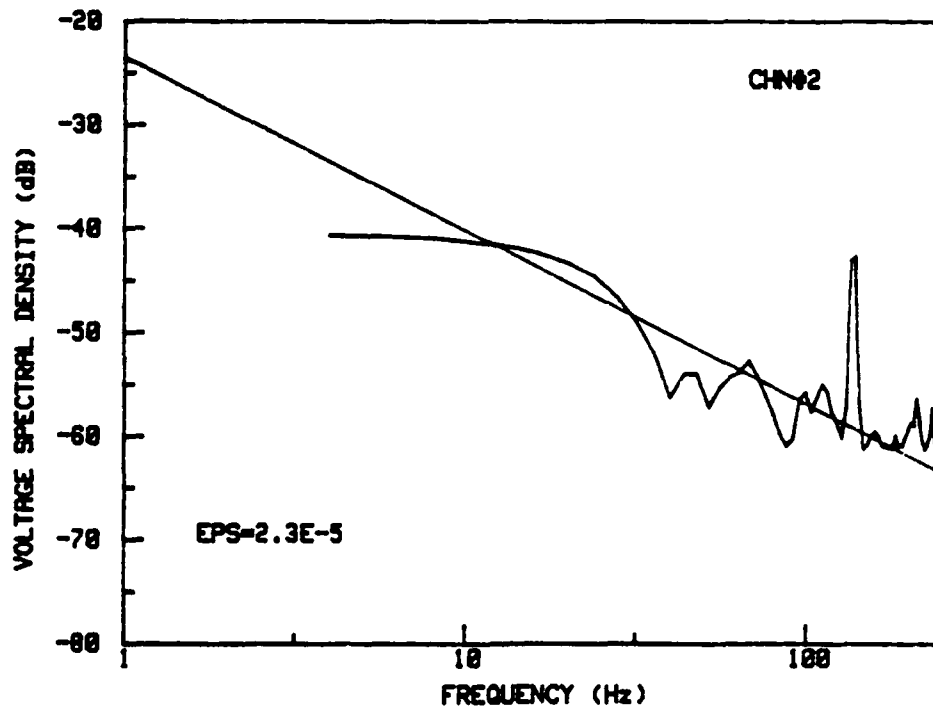
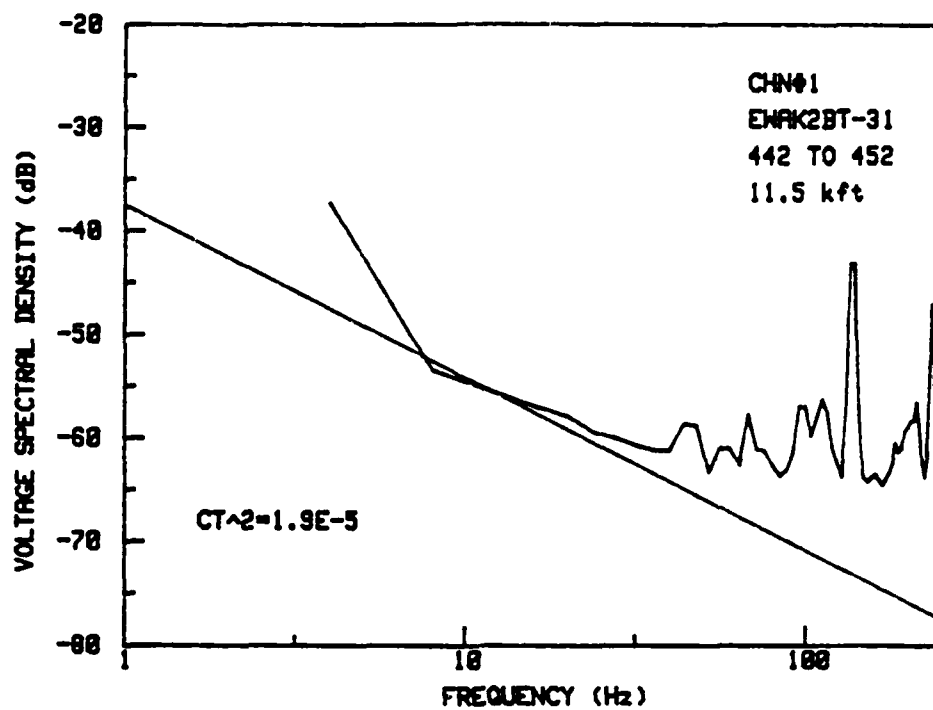


Figure 1. (continued)



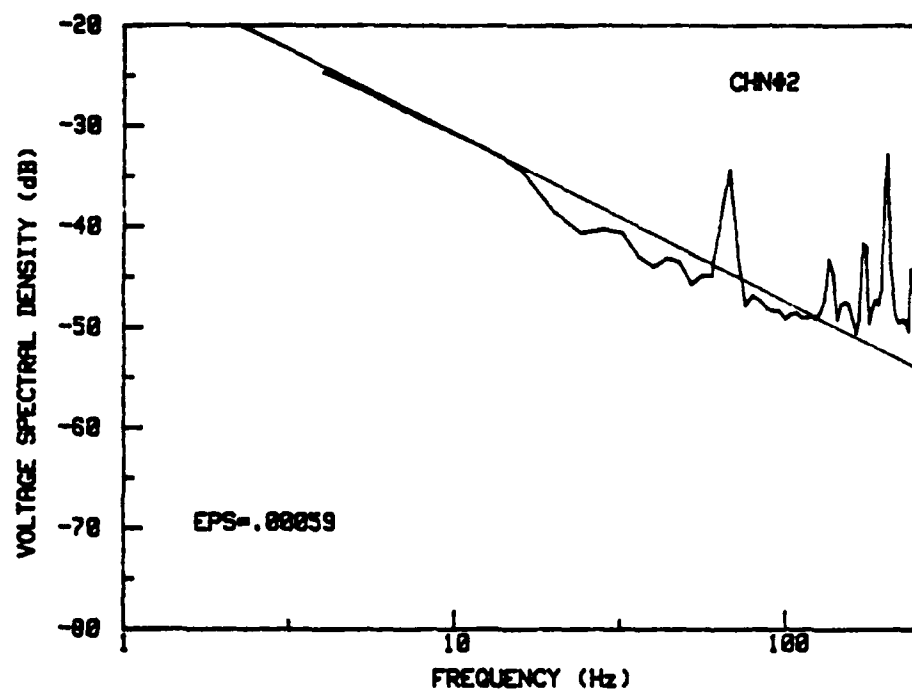
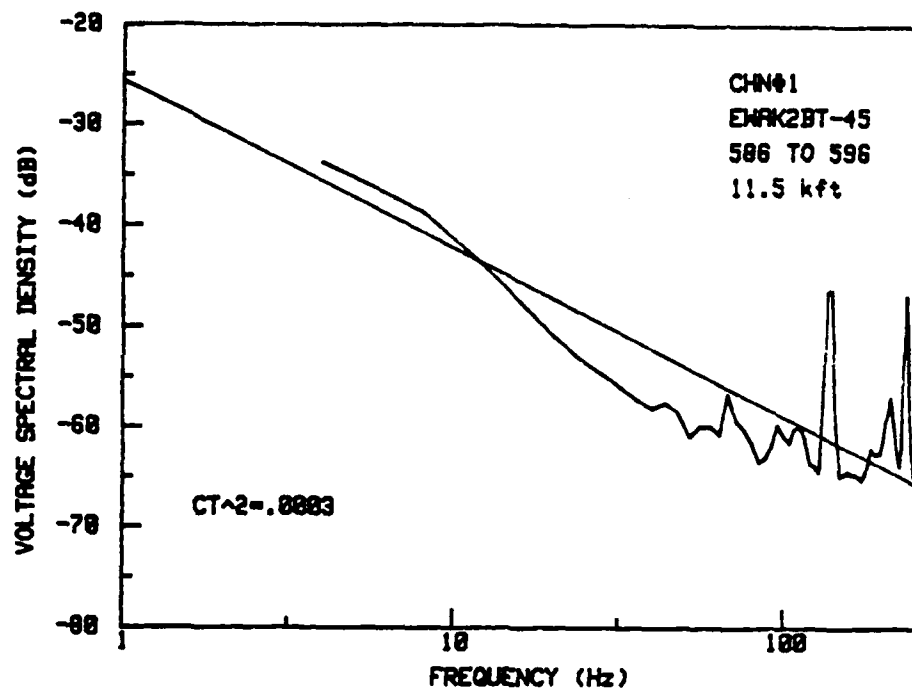


Figure 1. (continued)

X=10 Hz  
Ya=-39.721 dB

EAIR2-1  
TAPE 71-81 FT  
ALT 14.5 KFT

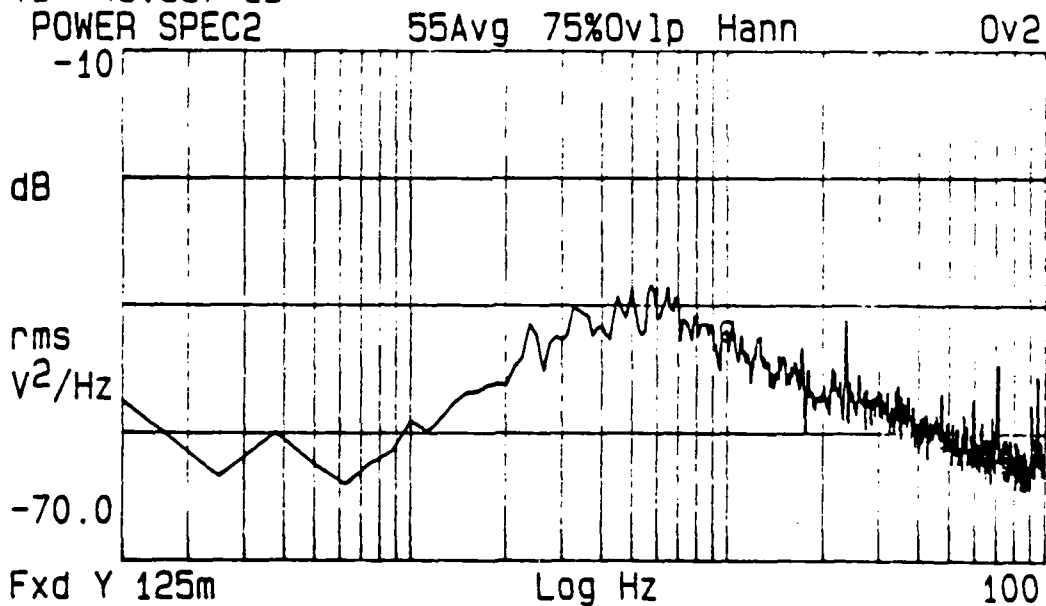
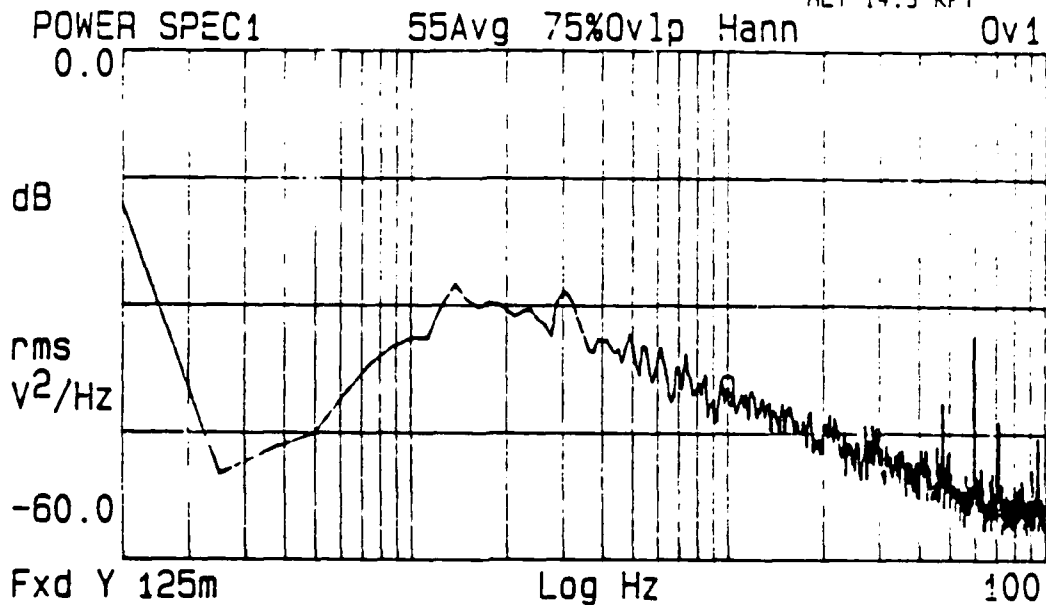
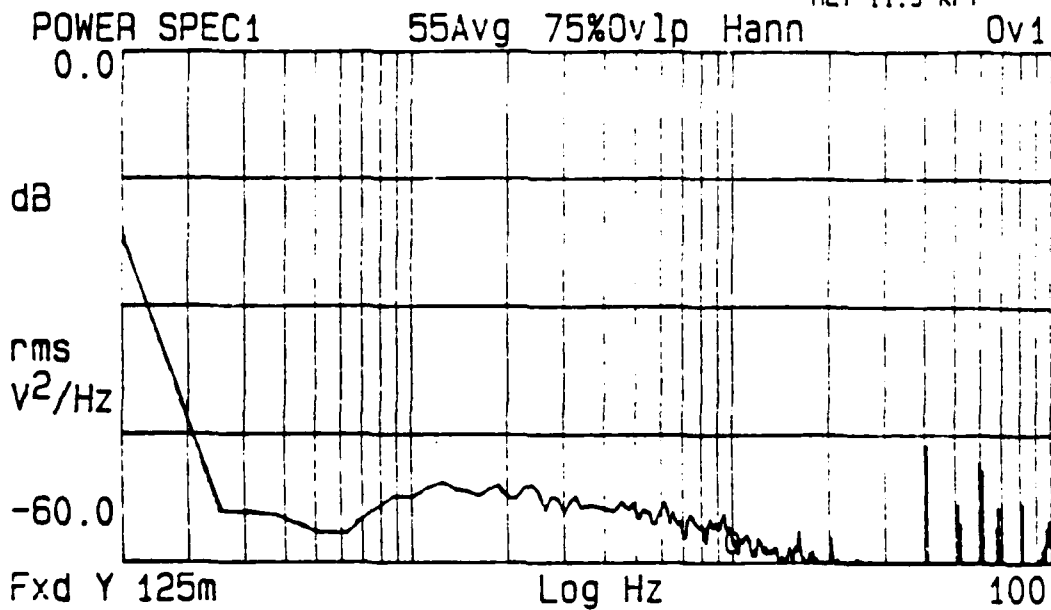


Figure 2. Voltage variance spectra produced by the signal analyzer's 1600 point FFT. For each record, Ov1 (top) is temperature variance and Ov2 (bottom) is velocity variance. Voltage power spectral density (dB) is plotted against frequency (log Hz). Processing parameters are stated above each spectrum. Coordinates of the cursor are given in the upper left corner of each spectrum. Vertical axis range has been fixed as stated in the lower left of each spectrum. Coded flight name (e.g., EAIR) and record number (e.g., - 1), tape footage, and altitude are annotated above each Ov1 graph. The same three dual-channel records in flight 2 are shown as in Figure 1.

Y=-10 Hz  
Ya=-57.921 dB

EAIR2-31  
TAPE 436-445 FT  
ALT 11.5 KFT



Fxd Y 125m  
Yb=-59.043 dB

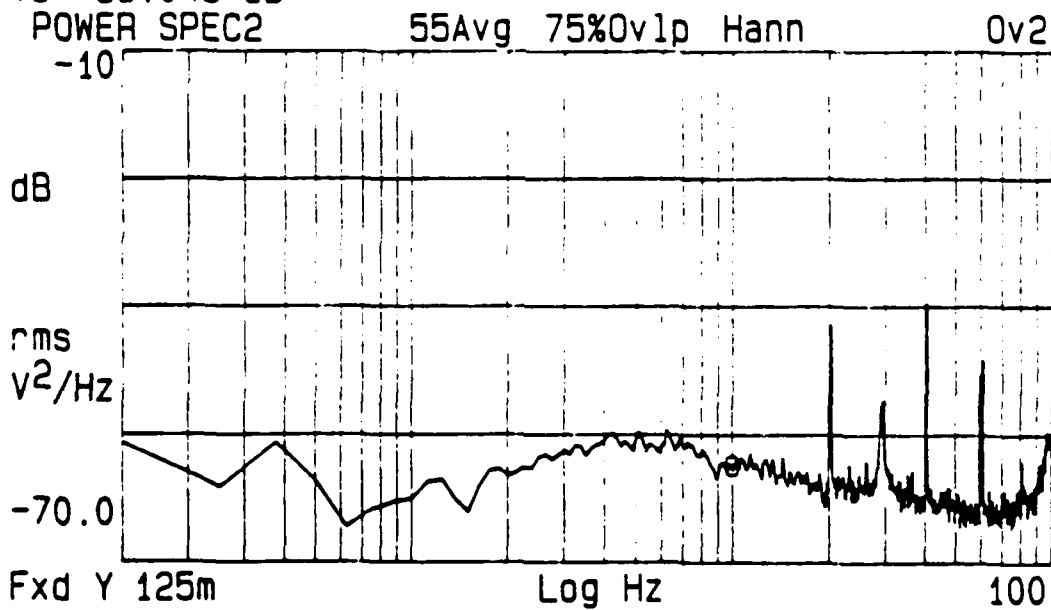
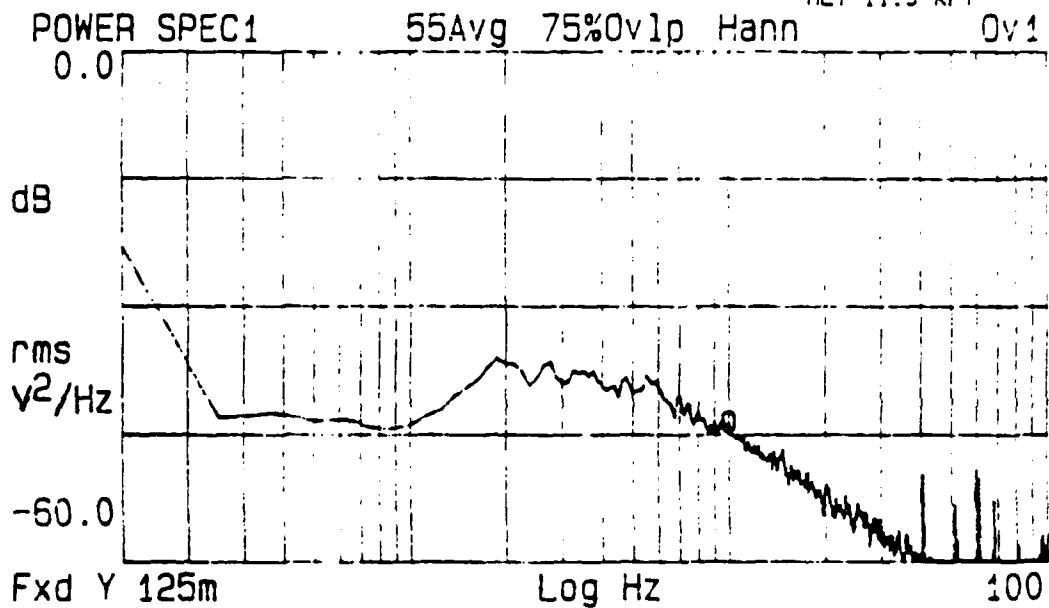


Figure 2. (continued)

X=10 Hz  
Ya=-43.891 dB

EAIR2-45  
TAPE 573-583 FT  
ALT 11.5 KFT



Yb=-51.657 dB

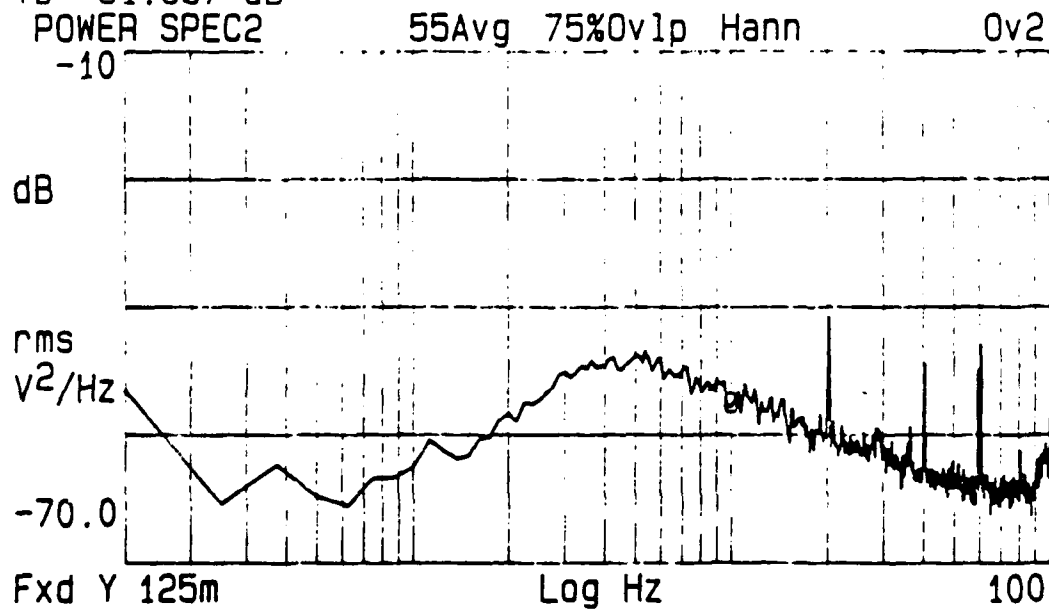


Figure 2. (continued)

## CHAPTER 6

### ANALYSIS METHODS

#### 6.1 Aircraft Turbulence Data Analysis

An indepth analysis on aircraft instrumentation/experimental error was done by Fairall and Markson (1984). Uncertainty due to measurement error will therefore not be discussed here. However, for this thesis, much effort was put into detailed analysis of the aircraft turbulence data in attempts to improve analysis precision. These processes are described in this chapter.

To quantify goodness-of-fit, a linear regression analysis was performed on the log-log spectral data and percent error was calculated for deviation from  $-5/3$  slope. Most spectra exhibited the  $-5/3$  dependence out to the broadband noise level of the instruments,  $\approx 3 \times 10^{-7} \text{ K}^2 \text{ m}$  for temperature and  $\approx 1 \times 10^{-6} (\text{m/s})^2 \text{ m}$  for velocity (Fairall and Markson 1985). Because of this background noise level, notable in the high frequency range (over 20 Hz), it was determined that the best fit would be obtained at the lowest frequency possible within the inertial subrange. Unfortunately, the temperature data had been low pass filtered at 2 Hz and the velocity data at 5 Hz. Filters of the type used on the aircraft (Thermo Systems, Inc. model 1057 signal conditioner with TSI model 1051-2 monitor and power supply) were analyzed with white noise input on the signal analyzer. Then a power spectrum ratio of unfiltered noise to filtered noise was calculated (Figures 3a and 3b). This function could then be multiplied point by point to essentially "defilter" the data.

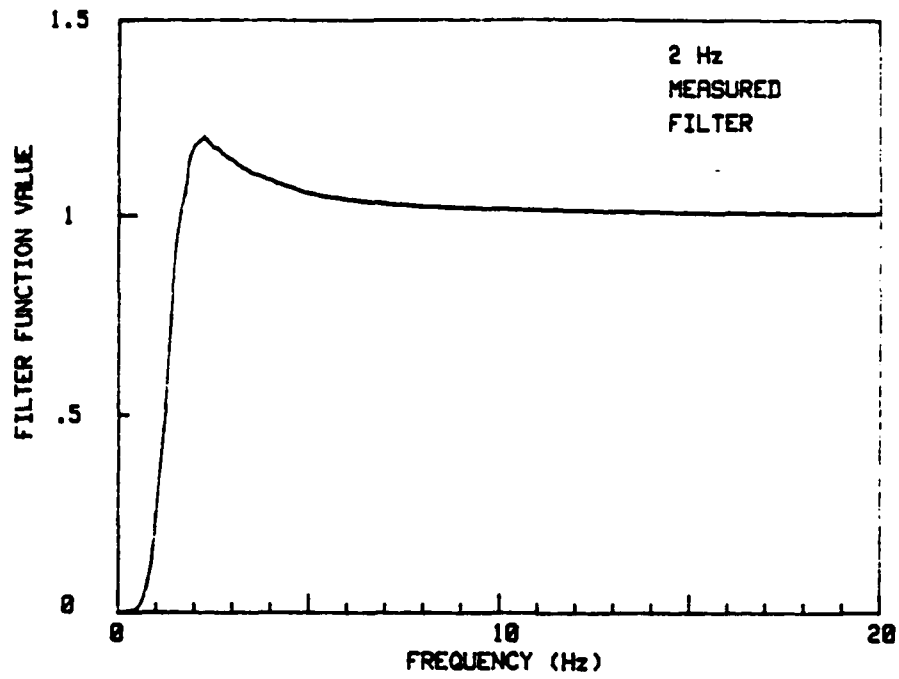


Figure 3a. The measured 2 Hz high pass temperature turbulence channel filter.

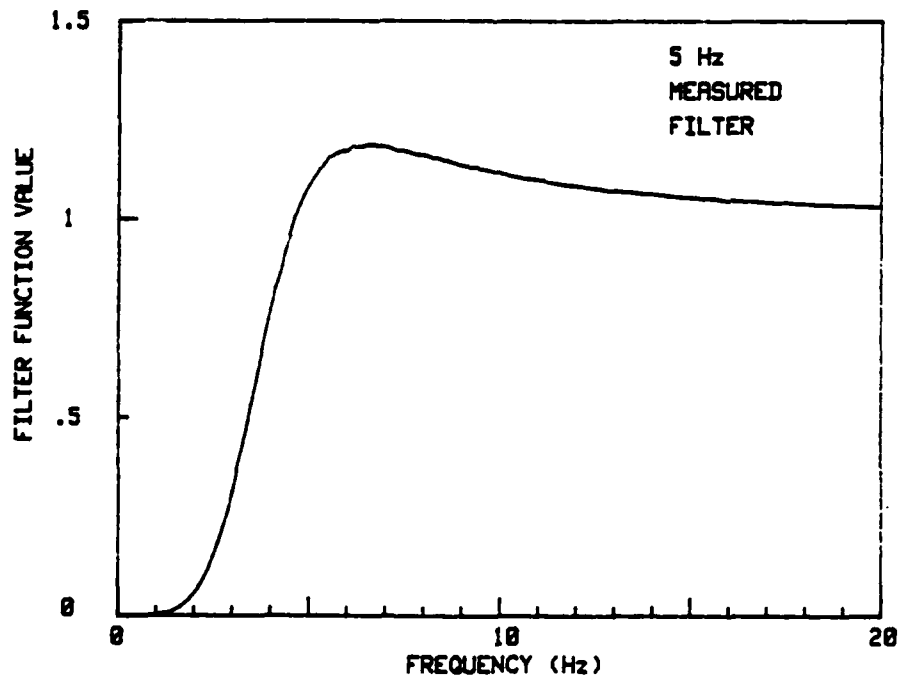


Figure 3b. The measured 5 Hz high pass velocity turbulence channel filter.

Spectral drop-off was still noted in the low frequency end (<1 Hz) of the spectra after this filter function was applied. Several reasons for this drop-off were proposed: a real phenomenon (i.e., the outer scale of the inertial subrange or the production size of the turbulence), a non-linear characteristic of the filter when the signal is log-distributed and not linearly distributed like the white noise, or individual error in the filter (two identical filters were tested and found to have different signatures). Assuming  $f$  is 1 Hz and  $u$  is 60 m/s, the frozen turbulence theory ( $\lambda^{-1} = 2\pi f/u$ ) gives  $\lambda$  of 10 m as the production scale. For the altitudes flown, this is within an order of magnitude of typical estimates (VanZandt et al. 1981; Gregg 1987; Barat and Bertin 1984). For comparison to the characteristics of the measured filter function, an atmospheric filter function was derived to compensate for non-linear filter effects and any unknown atmospheric effects (e.g., variable production size scale). Several sample spectra from the boundary layer with exceptionally high signal-to-noise ratio and -5/3 slope were used to derive a function based on -5/3 slope (Figures 4a and 4b).

All spectra were then run through a three pass progressive editing program. If the percent error on a regression fit from 5 to 18 Hz was greater than 20%, the spectrum was rejected on pass 1. Figure 5a again shows records 1, 31, and 45 of flight 2 for pass 1. On the second pass, the atmospheric filter was used to defilter the data from 0.1 to 5.6 Hz (the cutoff frequency where both 2 and 5 Hz filters were approximately equal to one). Figure 5b shows the same three records for pass 2. If percent error was greater than 15% on a second regression fit from 2 to 18 Hz, then the spectrum was run

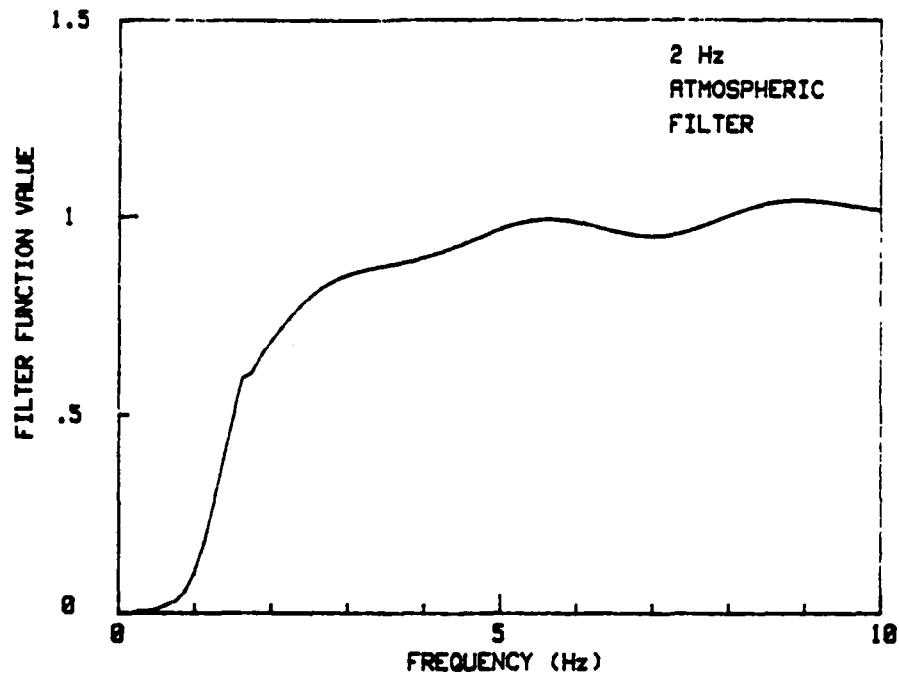


Figure 4a. The derived atmospheric 2 Hz high pass temperature turbulence channel filter.

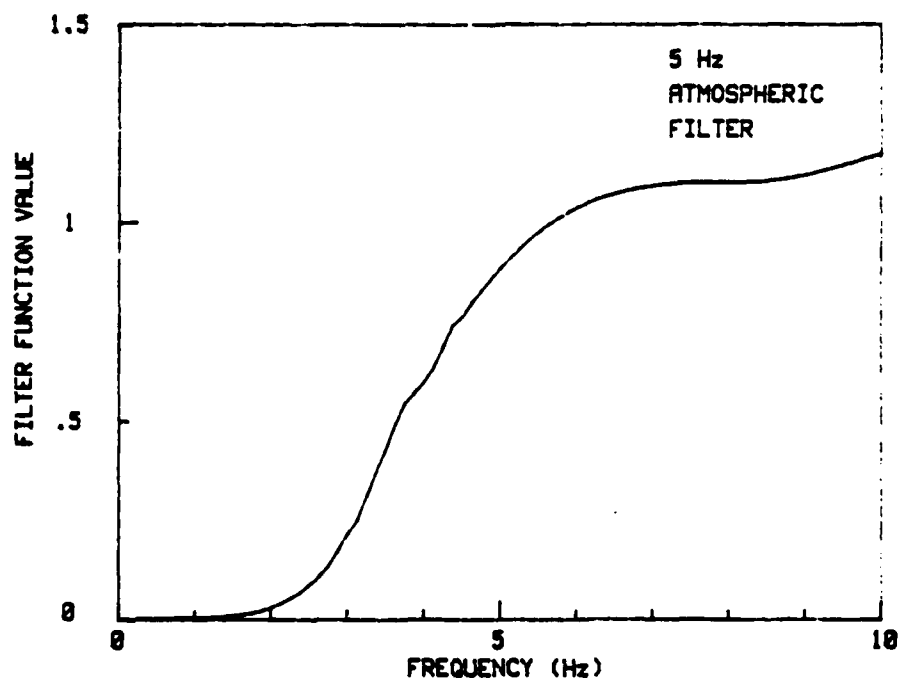


Figure 4b. The derived atmospheric 5 Hz high pass velocity turbulence channel filter.



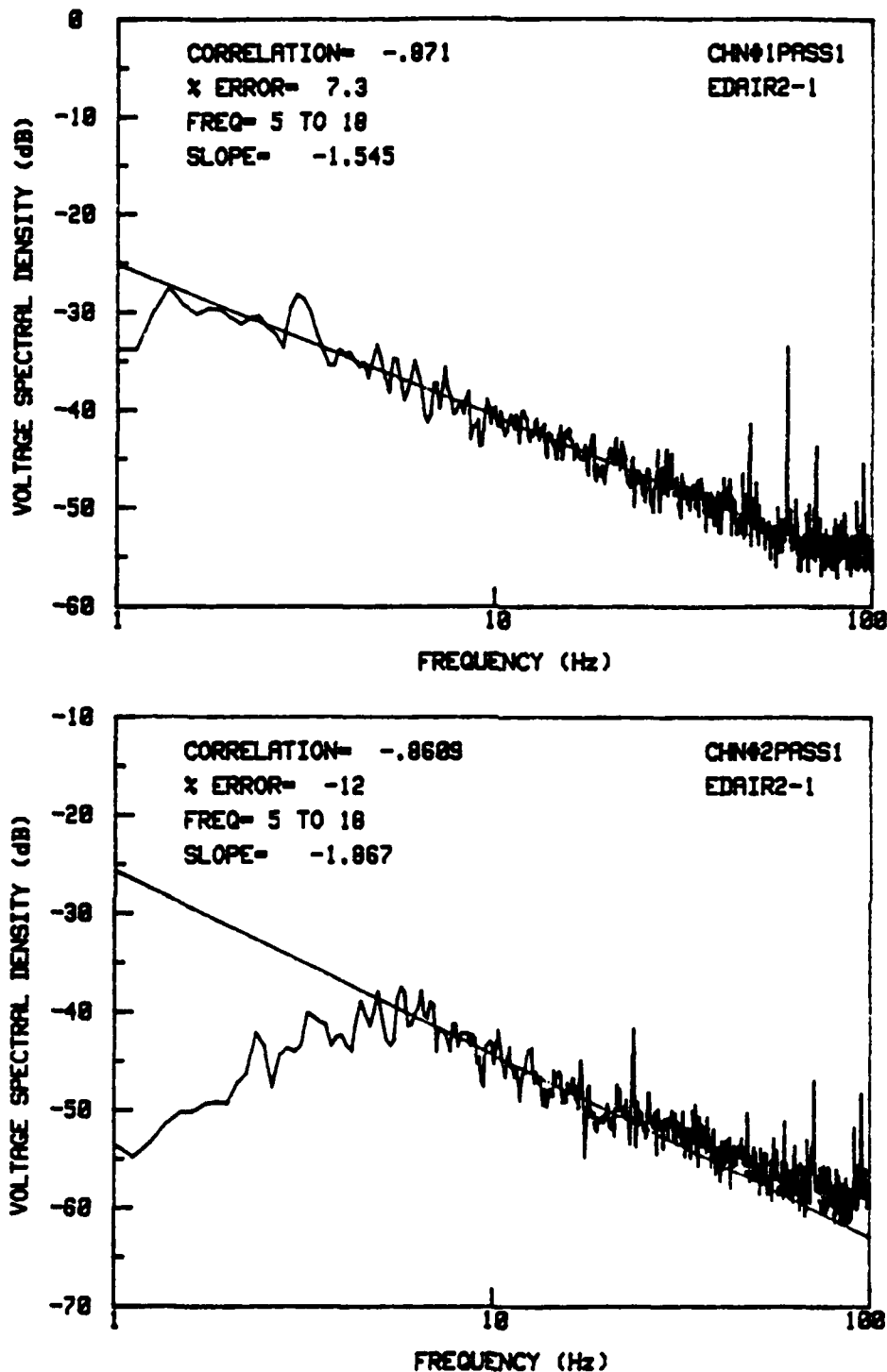


Figure 5a. Voltage variance spectra showing editing procedure. These spectra are filtered spectra derived from the taped data. This represents editing pass 1. Voltage power spectral density (dB) is plotted against frequency (log Hz). For each record, channel 1 (top) is temperature variance and channel 2 (bottom) is velocity variance. Channel number, pass number, and coded flight name and record number are shown interior to each graph. The slanted line represents the regression fit. Regression slope, correlation coefficient, and percent error are given in the upper left corner of each spectrum. The same three dual-channel records in flight 2 are shown as in Figure 1.

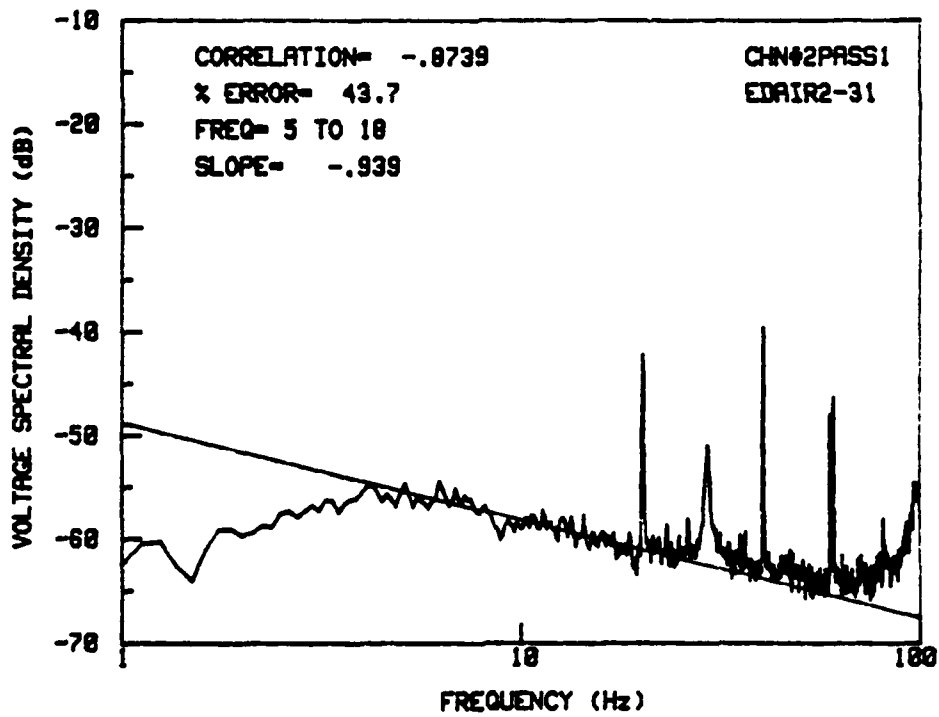
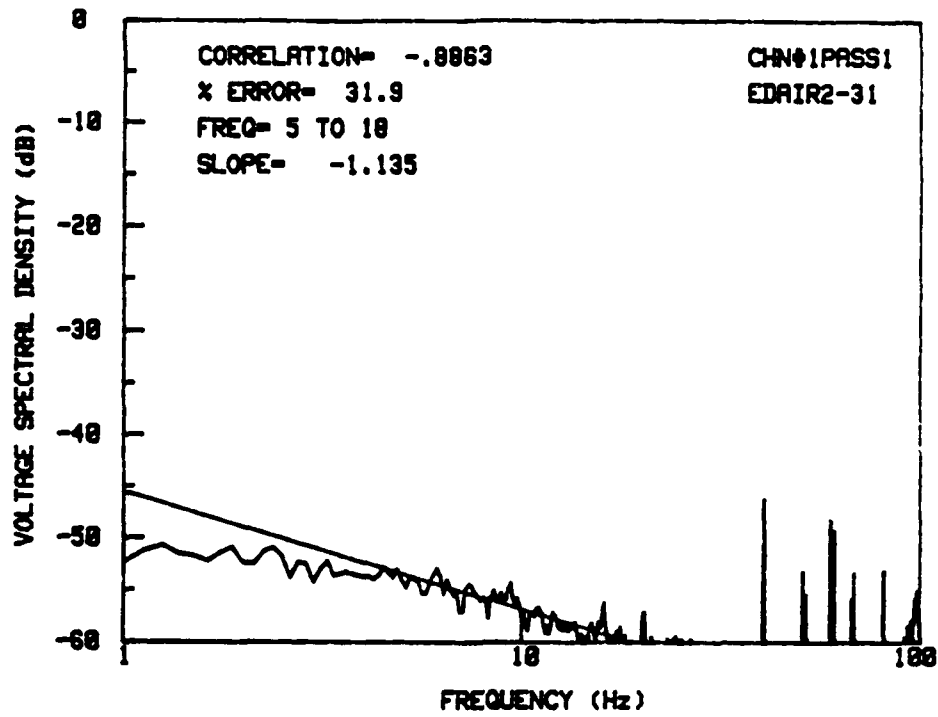


Figure 5a. (continued)

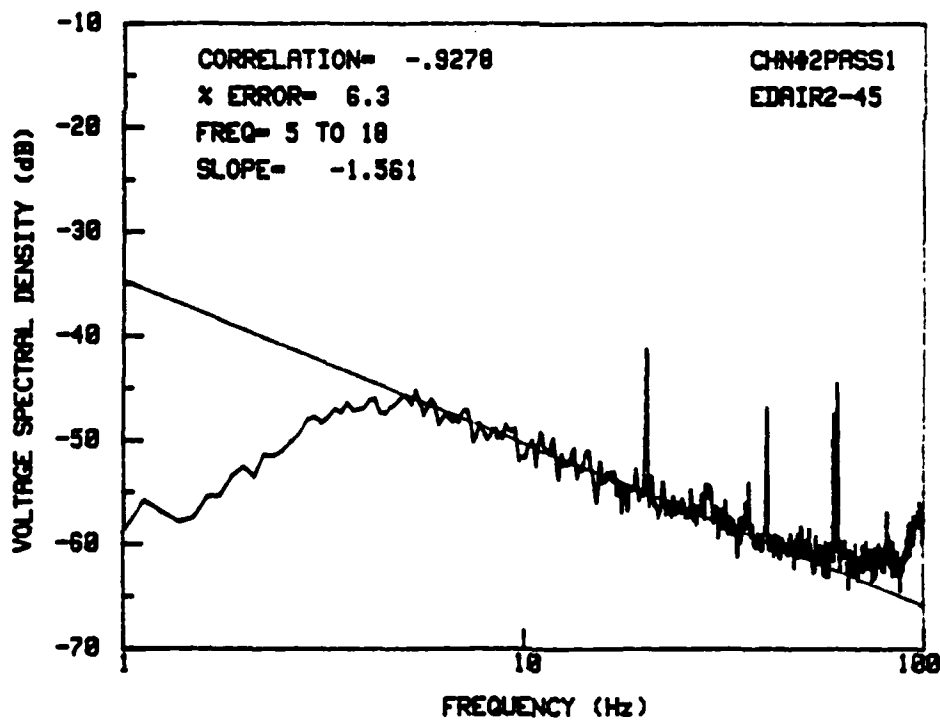
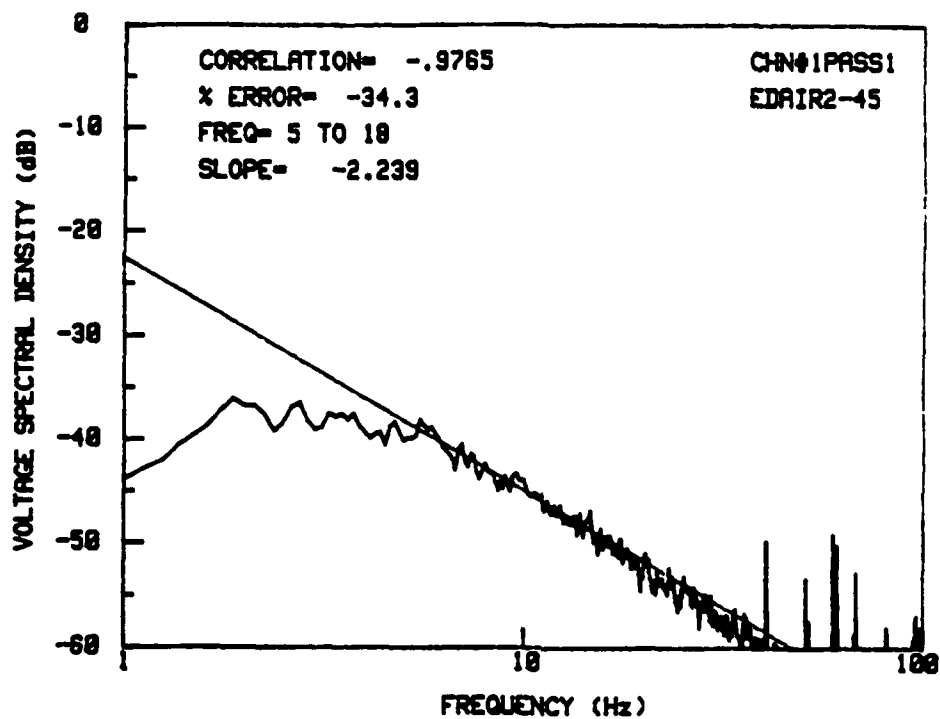


Figure 5a. (continued)

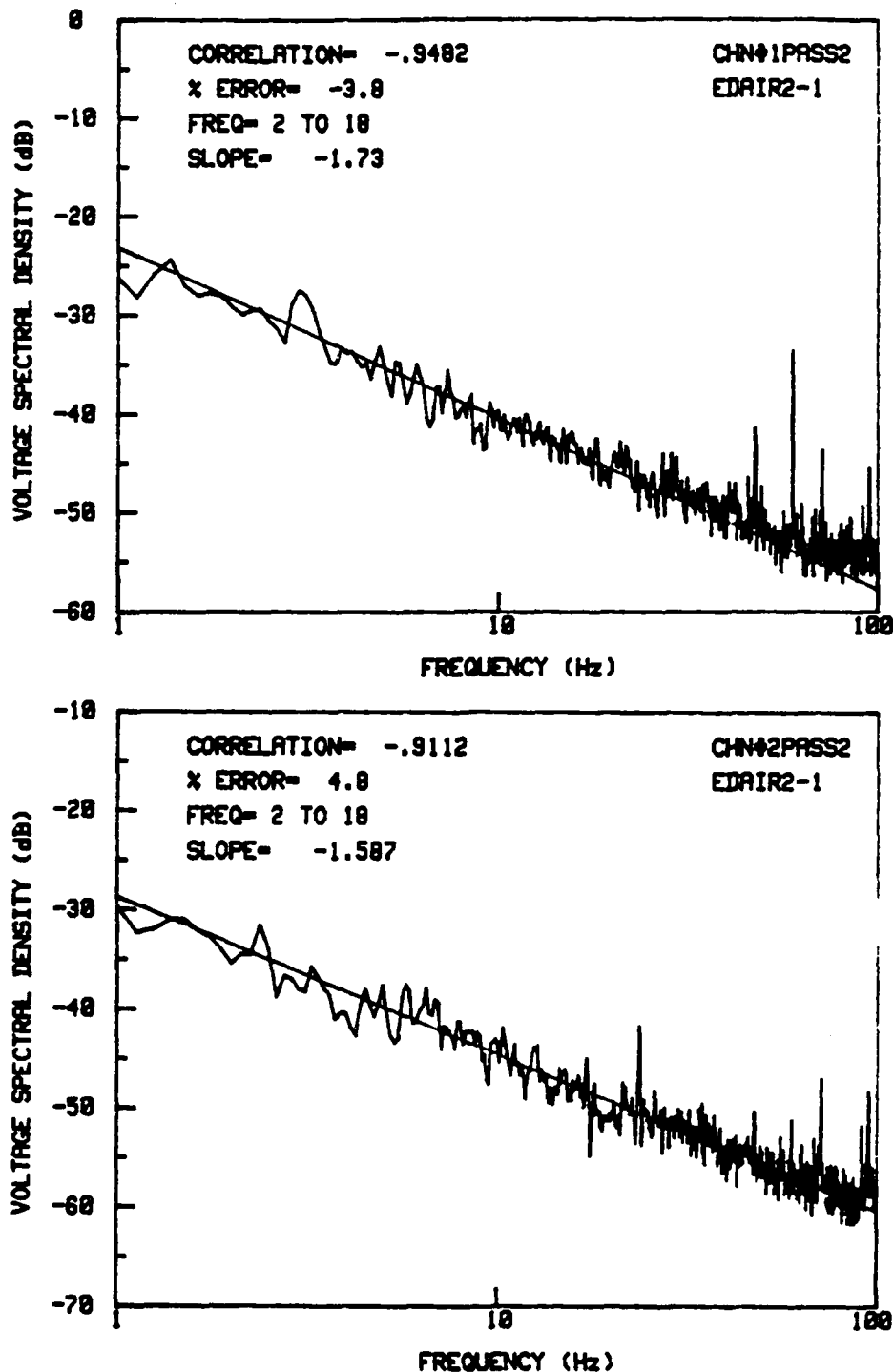


Figure 5b. Voltage variance spectra showing editing procedure. These spectra have been defiltered with the atmospheric filter function. This represents editing pass 2. Voltage power spectral density (dB) is plotted against frequency (log Hz). For each record, channel 1 (top) is temperature variance and channel 2 (bottom) is velocity variance. Channel number, pass number, and coded flight name and record number are shown interior to each graph. The slanted line represents the regression fit. Regression slope, correlation coefficient, and percent error are given in the upper left corner of each spectrum. The same three dual-channel records in flight 2 are shown as in Figure 1.

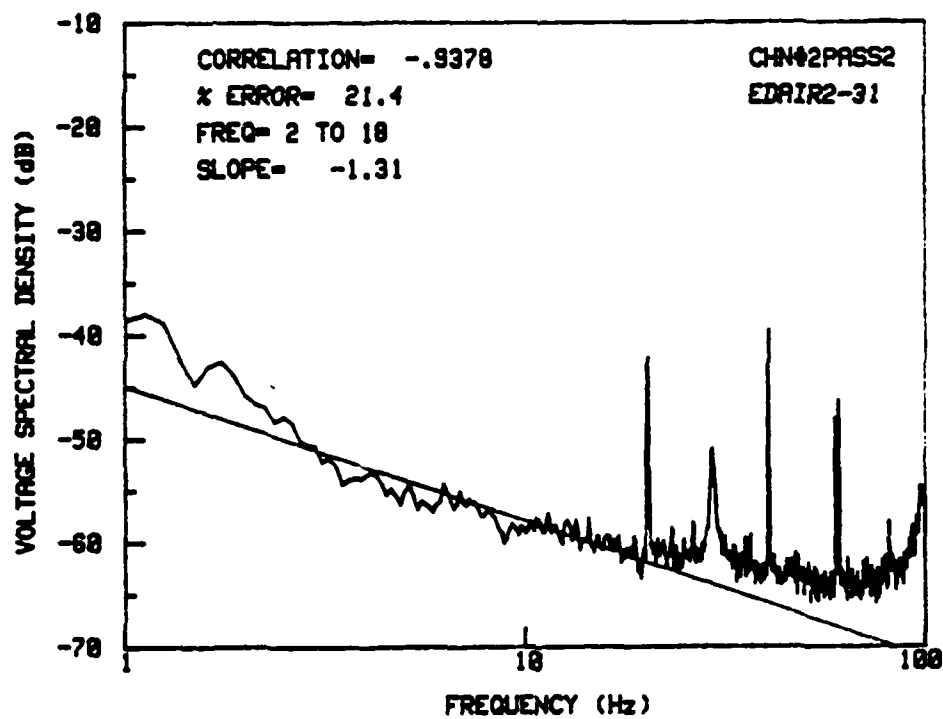
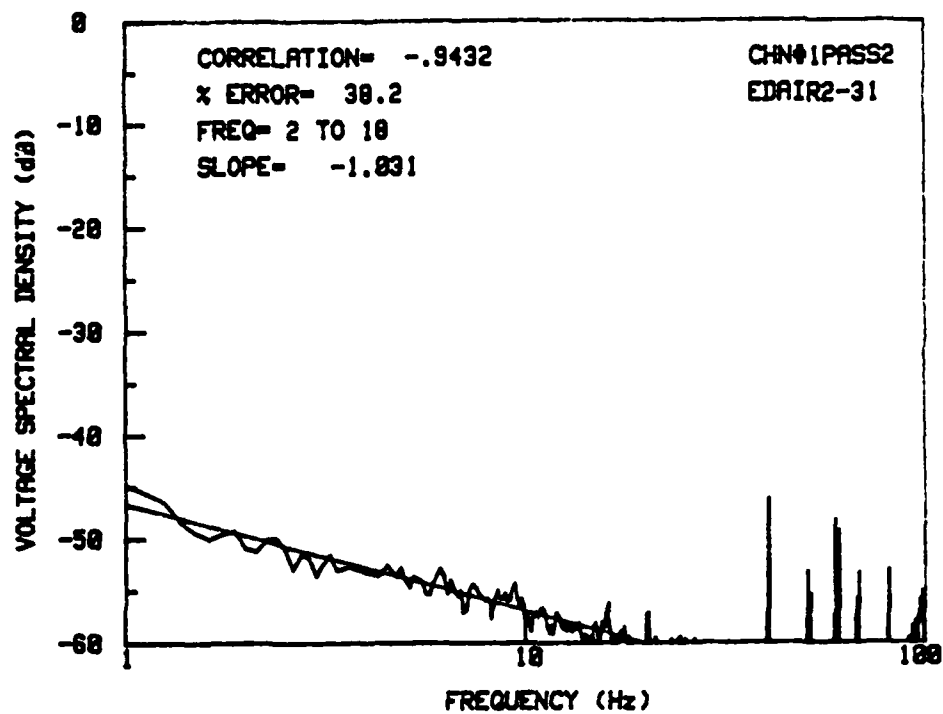


Figure 5b. (continued)

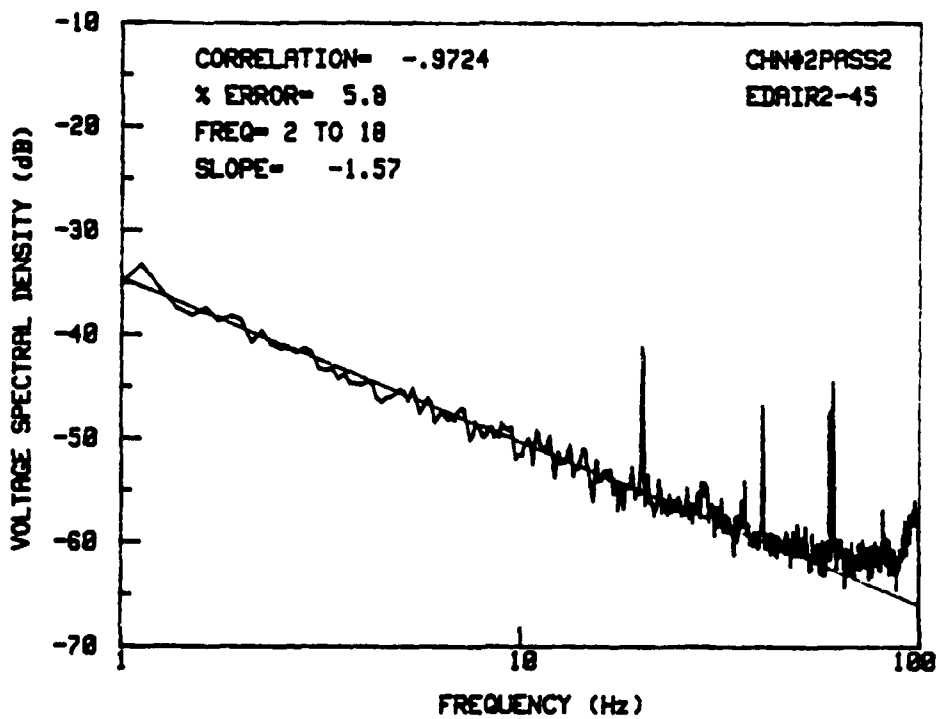
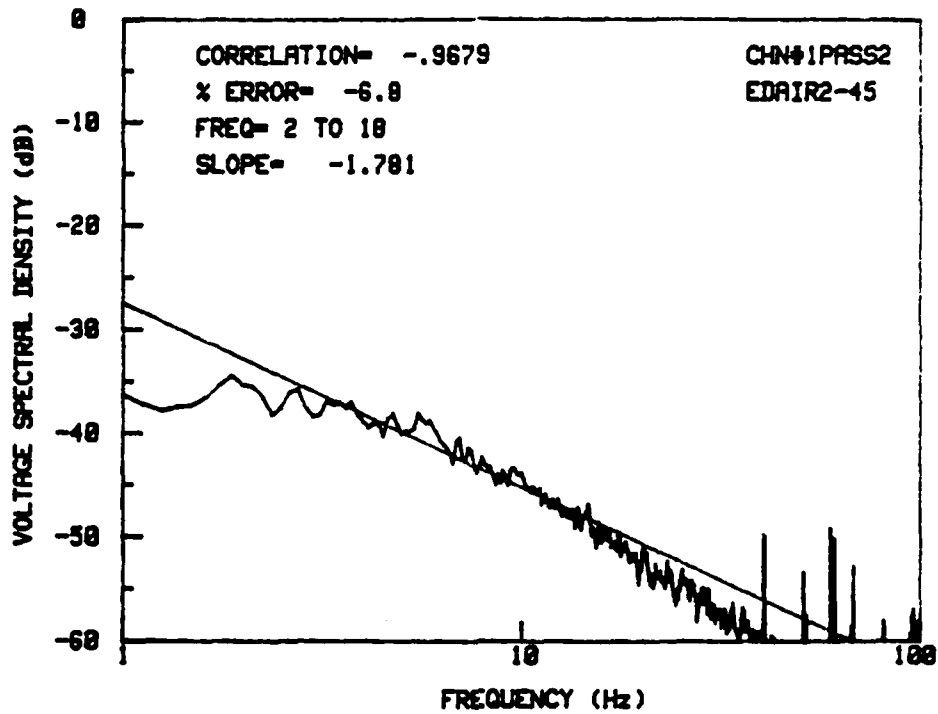


Figure 5b. (continued)

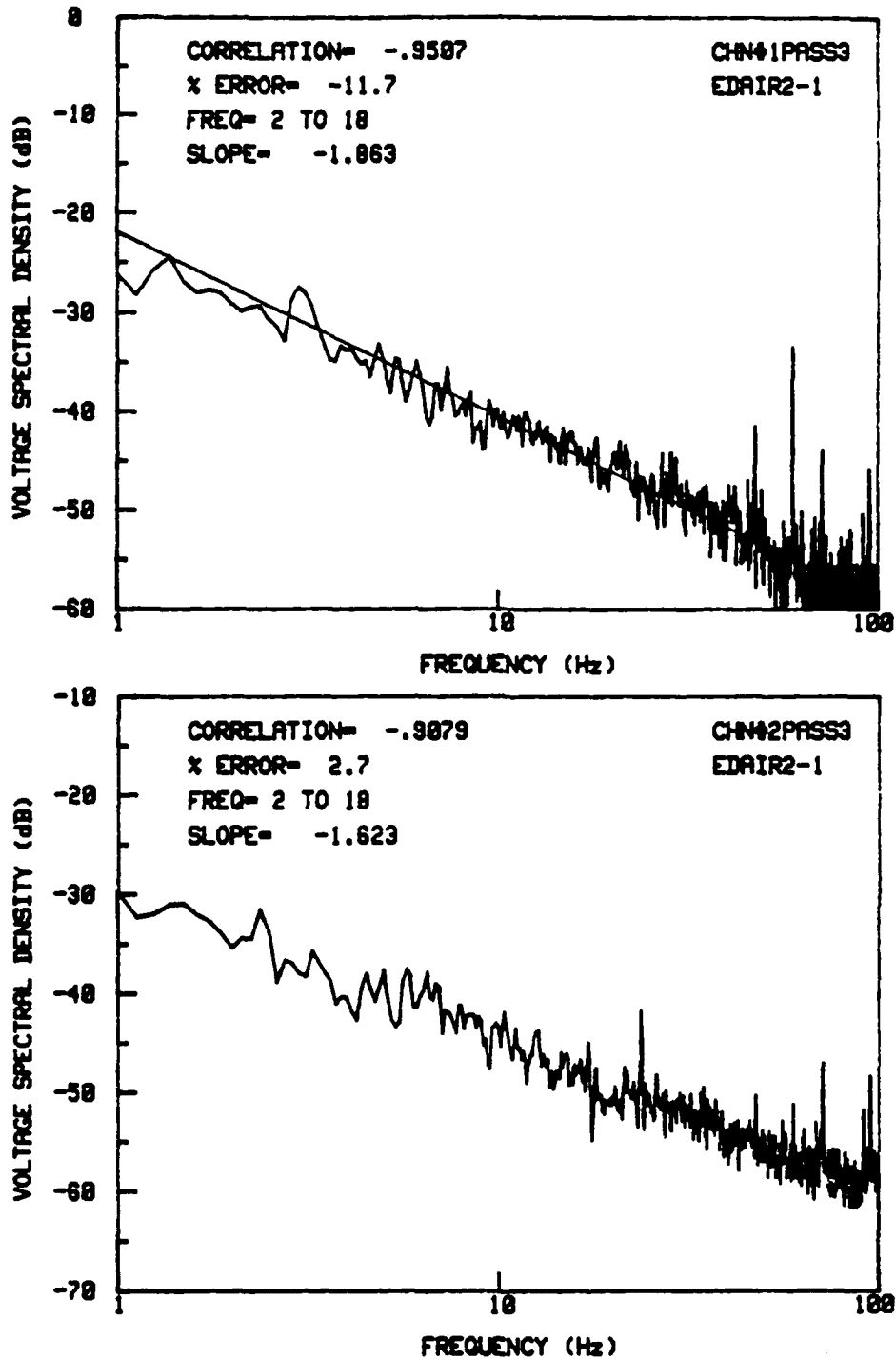


Figure 5c. Voltage variance spectra showing editing procedure. Average noise level has been subtracted from each defiltered spectrum. This represents editing pass 3. Voltage power spectral density (dB) is plotted against frequency (log Hz). For each record, channel 1 (top) is temperature variance and channel 2 (bottom) is velocity variance. Channel number, pass number, and coded flight name and record number are shown interior to each graph. The slanted line represents the regression fit. Regression slope, correlation coefficient, and percent error are given in the upper left corner of each spectrum. The same three dual-channel records in flight 2 are shown as in Figure 1.

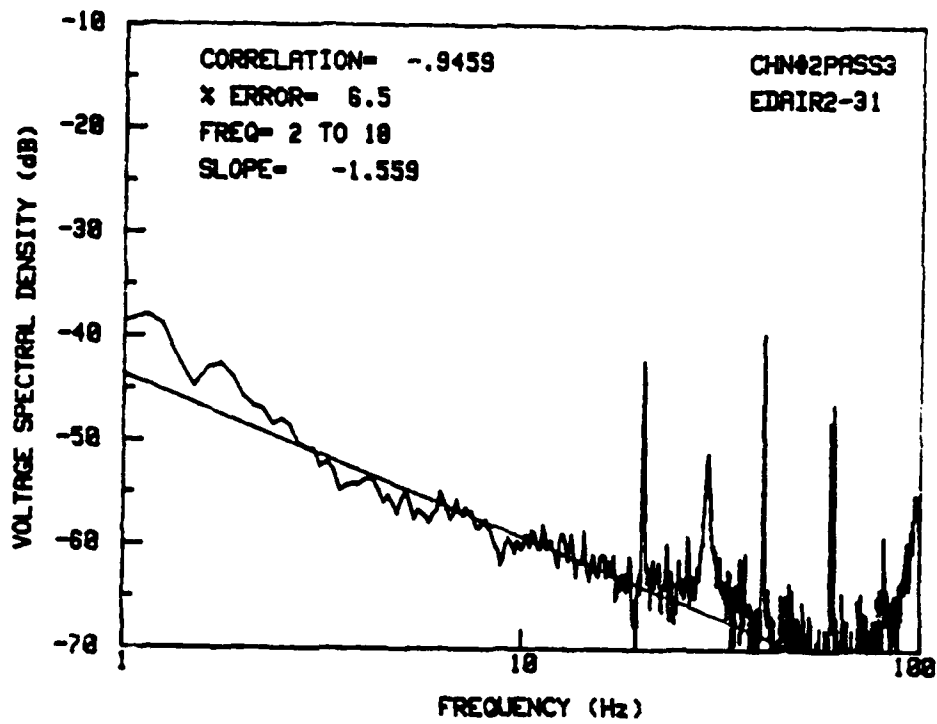
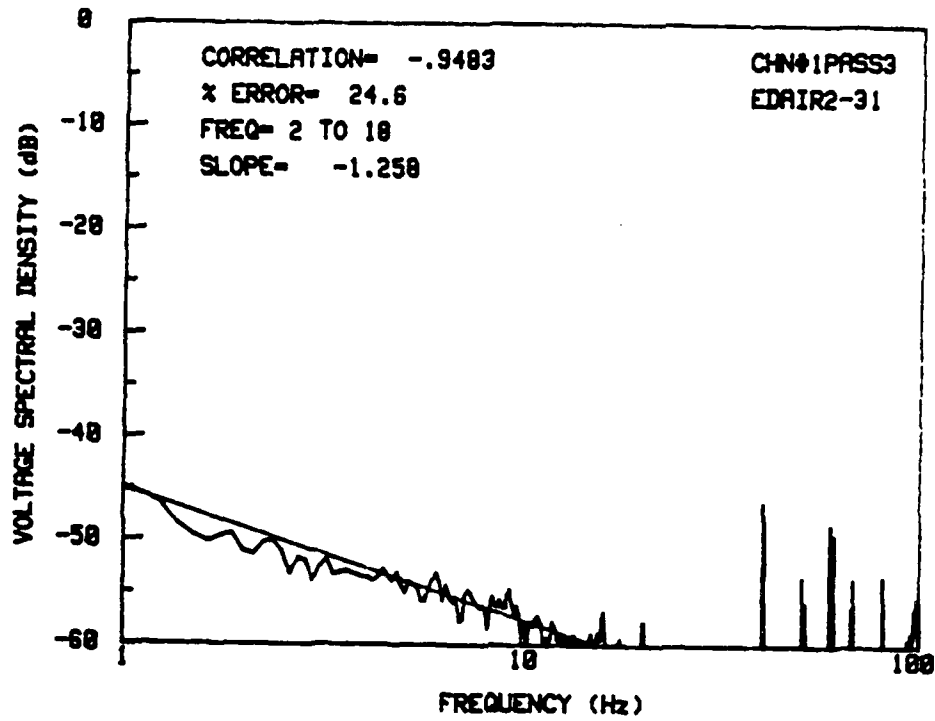


Figure 5c. (continued)



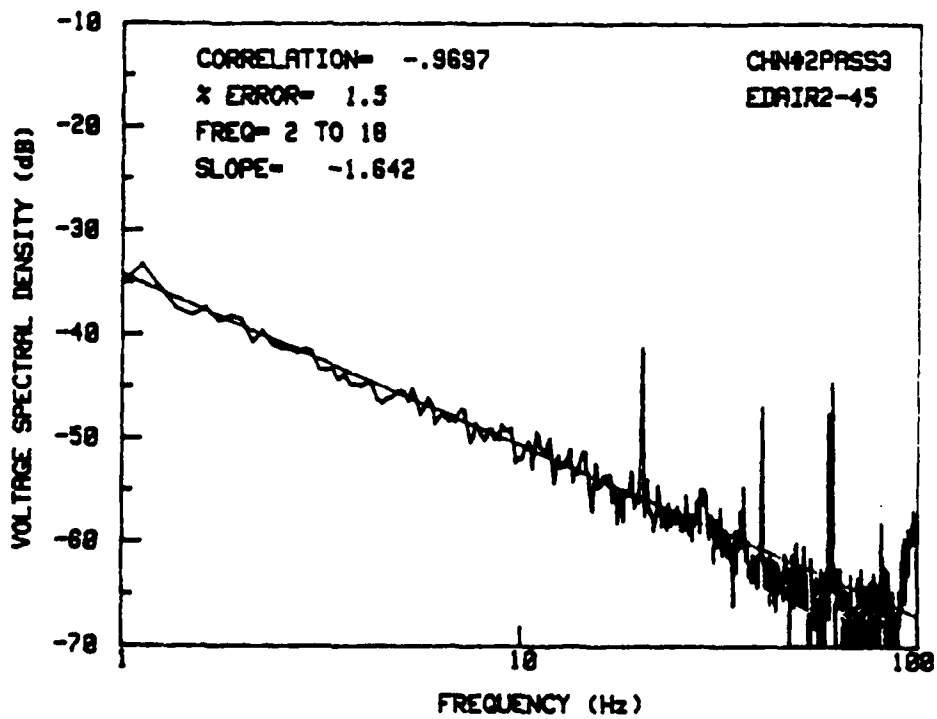
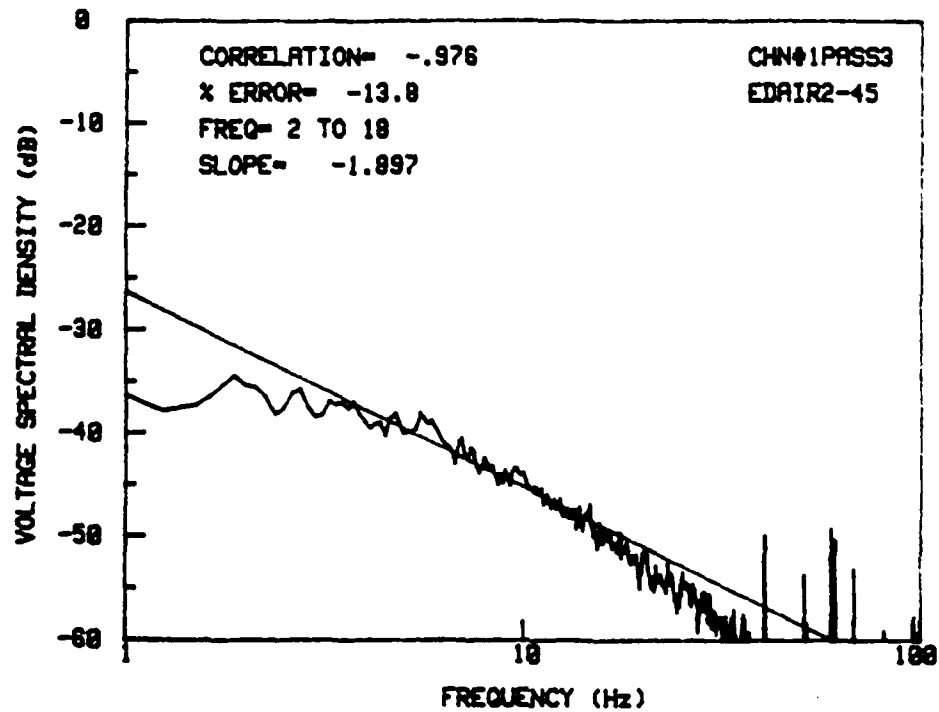


Figure 5c. (continued)

through pass 3. An average noise level was calculated from the twenty lowest spectral density values and subtracted from the entire spectrum. Figure 5c shows the same three records for pass 3. If the percent error on a new regression fit from 2 to 18 Hz was still greater than 15%, the spectrum was rejected on pass 3 and flagged. Spectra accepted on one of the above three passes were coded as "1". Flagged spectra were then manually examined. If a spectrum contained a visible portion of the inertial subrange that was represented by the regression fit, it was coded "2". Spectra with too small a signal-to-noise ratio (no visible inertial subrange) were coded "3". Unreal spectra were coded as "4". These unreal spectra were steeply sloped in log-log space. No theory predicts such a spectrum. Thus, these spectra were thought to be byproducts of measurement error, either overdriving the filter (i.e., amplitude fluctuations so great that filter saturation occurred) or noise distortion (e.g., change of aircraft power setting or a radio transmission). Code 4 spectra were eliminated from the analysis. All other analysis was performed on code 1 and 2 spectra, unless otherwise noted. Table 2 gives a representative breakdown of spectra by editing codes.

Based on the regression analysis, the following formulas were used to derive the spectral density necessary to calculate the structure parameters,  $C_T^2$  and  $C_u^2$ . 'X' was assigned to frequency and 'Y' to Volts<sup>2</sup>/Hz (spectral density). Using the power-law equation,

$$Y = a X^m \quad (6.1)$$

$$X^{5/3} Y = a X^{(m + 5/3)} \quad (6.2)$$

Table 2.

Representative editing results for each flight and in total. The breakdown of spectra in each pass for code 1 is shown, as well as the number of spectra in the remaining codes.

Temperature Spectra							
<u>Flight</u>	<u>Cold 1 :</u>			<u>Code 2</u>	<u>3</u>	<u>4</u>	
	<u>Pass</u>	<u>1</u>	<u>2</u>	<u>3</u>			
2		12	2	12	13	0	9
3		10	4	2	6	0	5
4		12	2	3	5	0	3
6		28	1	10	8	0	0
7I		21	0	1	4	0	0
7II		33	2	1	2	0	0
8		21	0	3	11	0	2
9		19	3	5	5	1	0
10		34	6	5	9	0	0
11I		17	1	7	17	0	0
11II		2	2	3	13	0	0
12		13	2	3	19	0	2

Table 2.  
(continued)

Velocity Spectra						
<u>Flight</u>	<u>Code 1 :</u>			<u>Code 2</u>	<u>3</u>	<u>4</u>
	<u>Pass 1</u>	<u>2</u>	<u>3</u>			
2	27	4	9	2	5	1
3	21	0	4	1	1	0
4	6	0	0	0	0	19
6	34	0	3	7	1	2
7I	25	0	0	1	0	0
7II	36	0	2	0	0	0
8	28	2	3	2	1	1
9	28	0	3	1	0	1
10	53	1	0	0	0	0
11I	33	0	2	2	0	5
11II	16	0	2	2	0	0
12	21	1	5	2	0	10

TOTALS

Temperature Spectra

<u>Code 1 :</u>	<u>Pass 1</u>	<u>2</u>	<u>3</u>	<u>Code 2</u>	<u>3</u>	<u>4</u>
	222	25	55	112	0	21

Velocity Spectra

<u>Code 1 :</u>	<u>Pass 1</u>	<u>2</u>	<u>3</u>	<u>Code 2</u>	<u>3</u>	<u>4</u>
	328	8	33	20	8	39

$$Q = X^{5/3} Y \quad (6.3)$$

$$a = Y / X^m \quad (6.4)$$

$$Q = 10^{(\langle \log Y \rangle - m \langle \log X \rangle)} 10^{(m + 5/3) \langle \log X \rangle} \quad (6.5)$$

$$Q = 10^{(\langle \log Y \rangle + 5/3 \langle \log X \rangle)} \quad (6.6)$$

$$Q = 10^{[(\Sigma \log Y)/N + 1.667 (\Sigma \log X)/N]} \quad (6.7)$$

where Q is the spectral density times frequency to the 5/3 and is based on the spectral density and frequency values midrange in the regression fit. Q is a necessary input parameter for the  $C_T^2$  and  $C_u^2$  equations (equations 5.23 and 5.24), calculated from the temperature and velocity turbulence spectra, respectively.

## 6.2 Mean Aircraft Meteorological Profiles

The aircraft temperature and humidity profiles were digitized at levels corresponding to the profiler high resolution range gate heights. Dewpoint temperature was converted to vapor pressure, e, over water using the following formula (Iribarne and Godson 1981).

$$\log e = -(2937.4 / T) - 4.9283 \log T + 23.5471 \quad (6.8)$$

where e is vapor pressure in mb and T is in Kelvin. Vapor pressure was then converted to specific humidity, q, using the approximation  $e = (P q)/0.622$ . Potential temperature and temperature have the defined relationship

$$\theta = T (1000 \text{ mb}/P)^{0.286} \quad (6.9)$$

with pressure from the standard atmosphere relationship

$$P = P_0 e^{-(z/8)} \quad (6.10)$$

where  $P_0$  is 1013.2 mb, altitude  $z$  is in km and scale height  $H$  is  $\approx 8$  km (Iribarne and Godson 1981; Wallace and Hobbs 1977). Aircraft potential temperature profiles are shown for all flights in Figure 6. Aircraft specific humidity profiles for only the PSU flights are shown in Figure 7.

### 6.3 Other Data Sources

Profiler data was logged at one hour intervals denoted by the GMT time (zulu time, "z") at the end of the average period. Height is given in m, wind speed in m/s, direction in degrees, and  $C_n^2$  (radar) in  $m^{-2/3}$  (Mike Moss, letter to author, July 1987; Mike Moss, letter to author, November 1987). Radar wind profiles for the PSU flights are shown in Figure 8.

AFGL thermosonde data was available at 20 m resolution. The following information was available for each level: altitude (km), pressure (mb), temperature ( $^{\circ}\text{C}$ ), relative humidity (%),  $C_n^2$  ( $m^{-2/3}$ ), wind speed (m/s), and direction (degrees) (Robert Beland, letter to William Syrett, September 1986). AFGL thermosonde potential temperature profiles corresponding to aircraft flights are shown in Figure 9. Corresponding AFGL thermosonde specific humidity, mean wind, and calculated raw  $C_n^2$  profiles are shown in Figures 10, 11, and 12, respectively.

AFGL scintillometer data was provided as seven-level profiles with  $C_n^2$  in  $m^{-2/3}$ , and height (corrected for zenith angle) in km

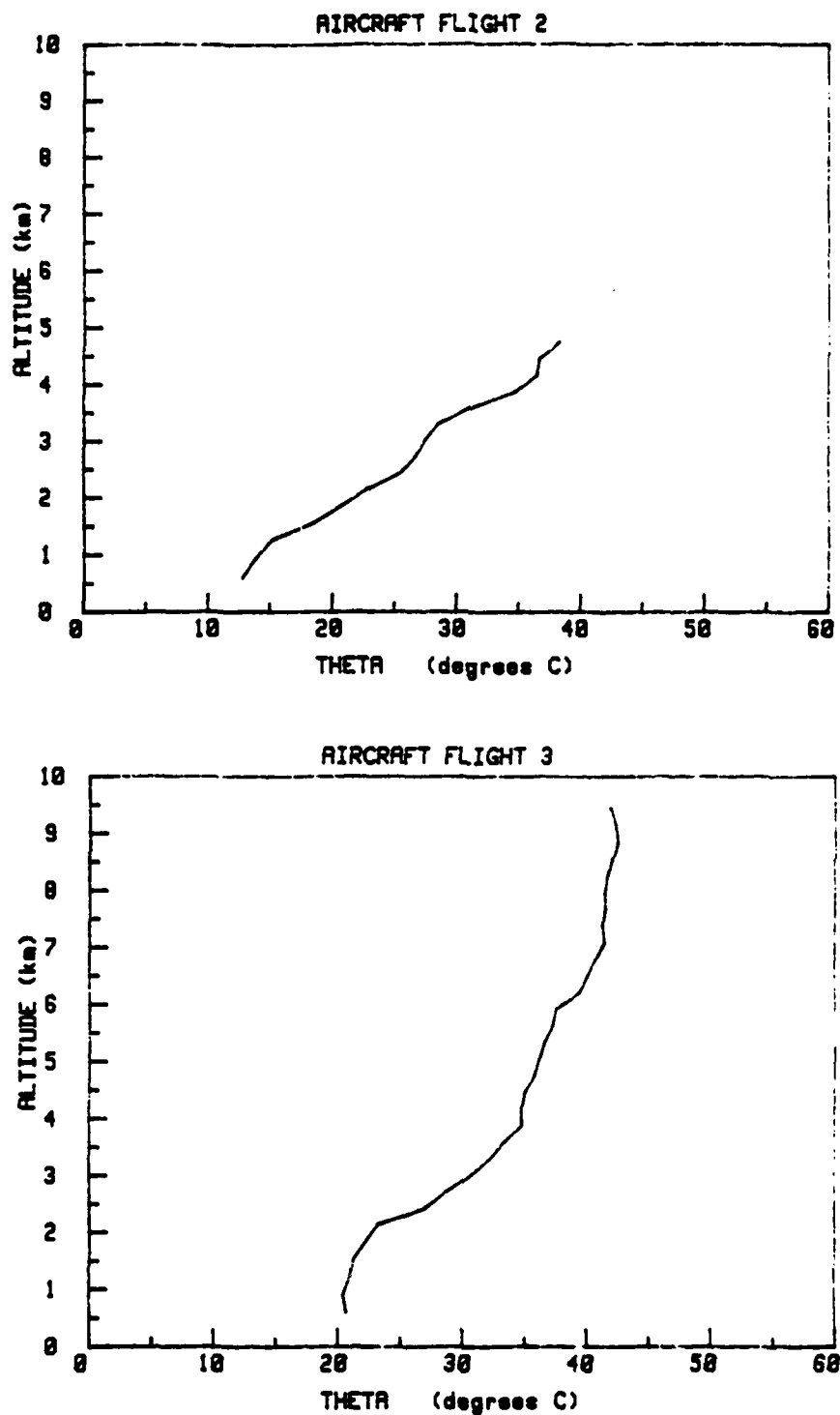


Figure 6. Potential temperature (theta) vertical profiles as measured by aircraft instrumentation. Altitude is MSL. Flights 2-12 are shown (labeled above each graph).

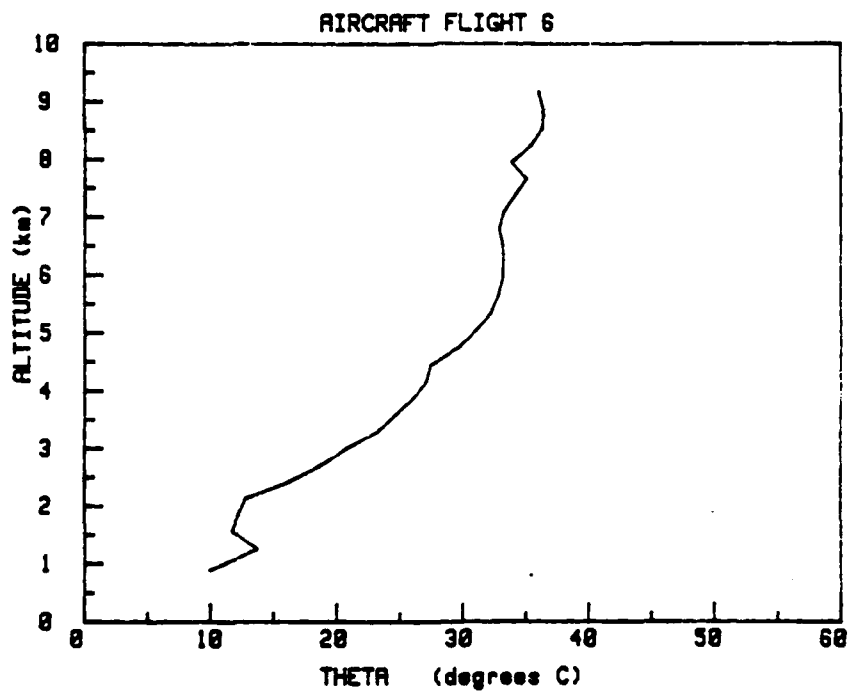
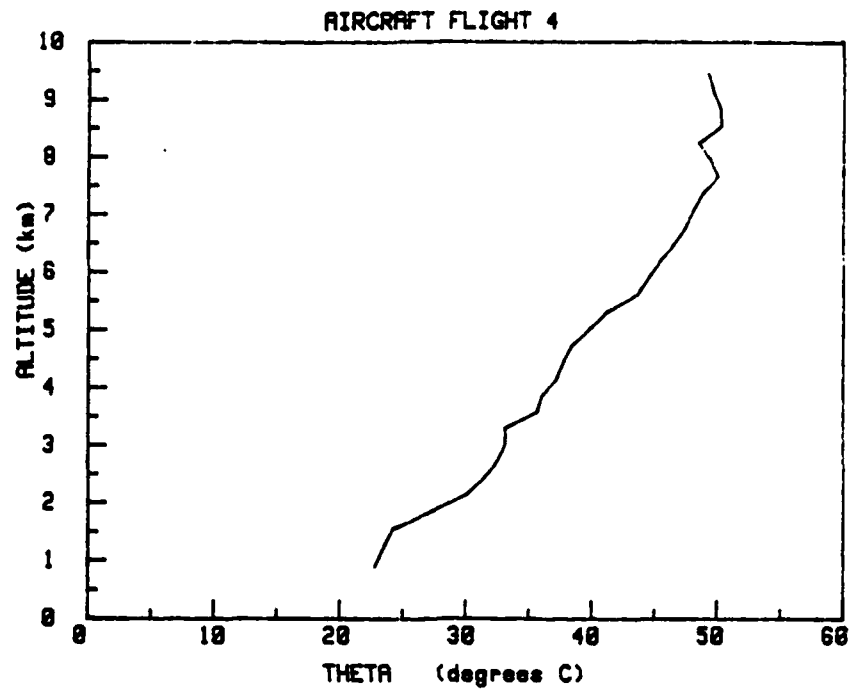


Figure 6. (continued)



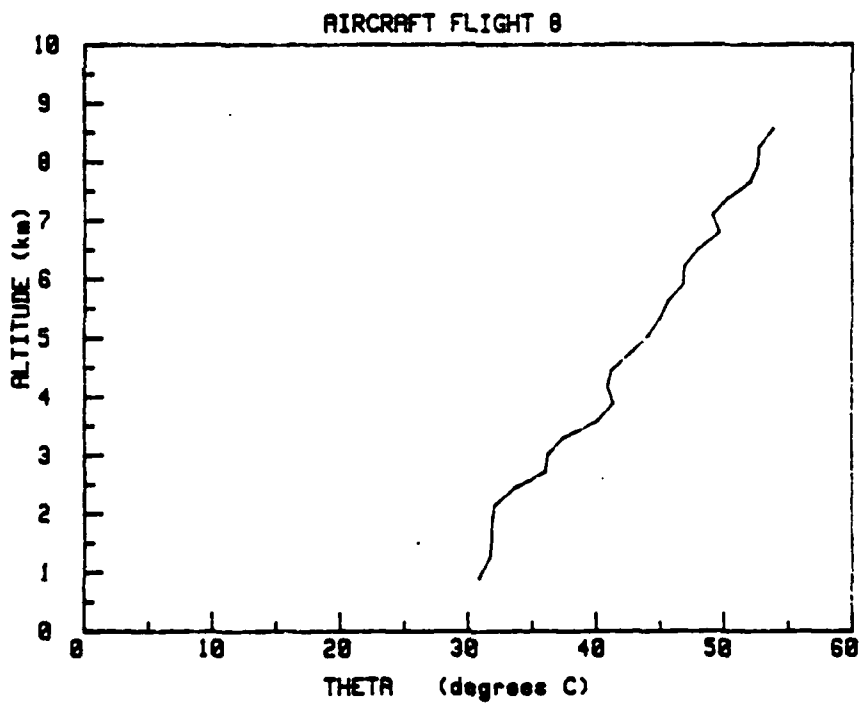
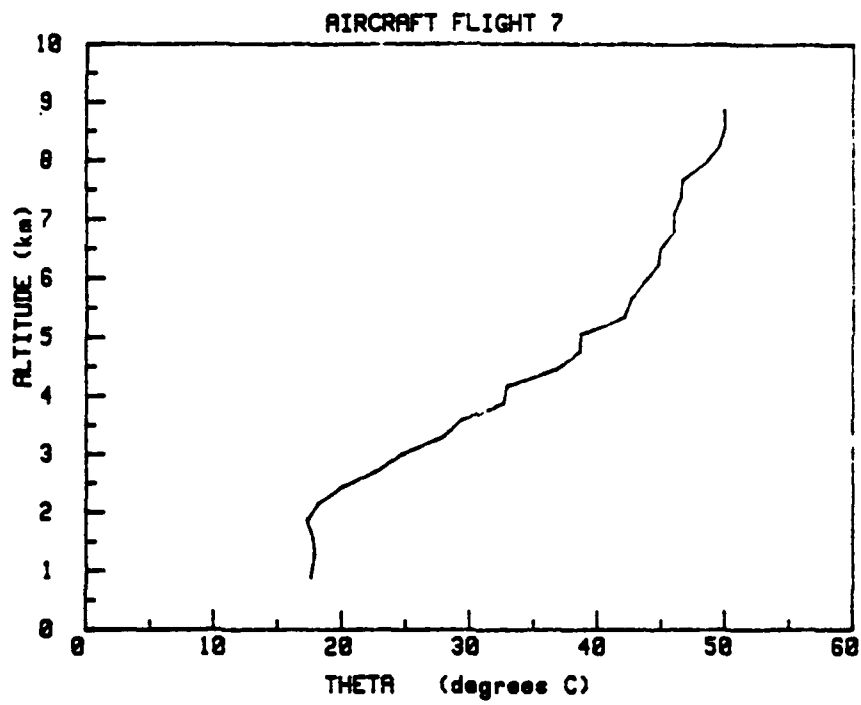


Figure 6. (continued)

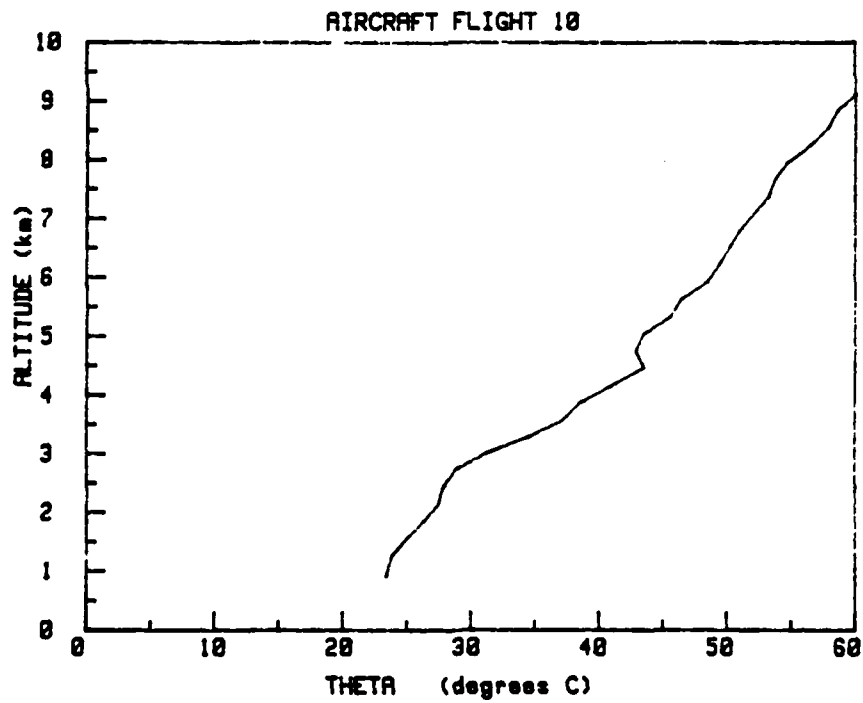
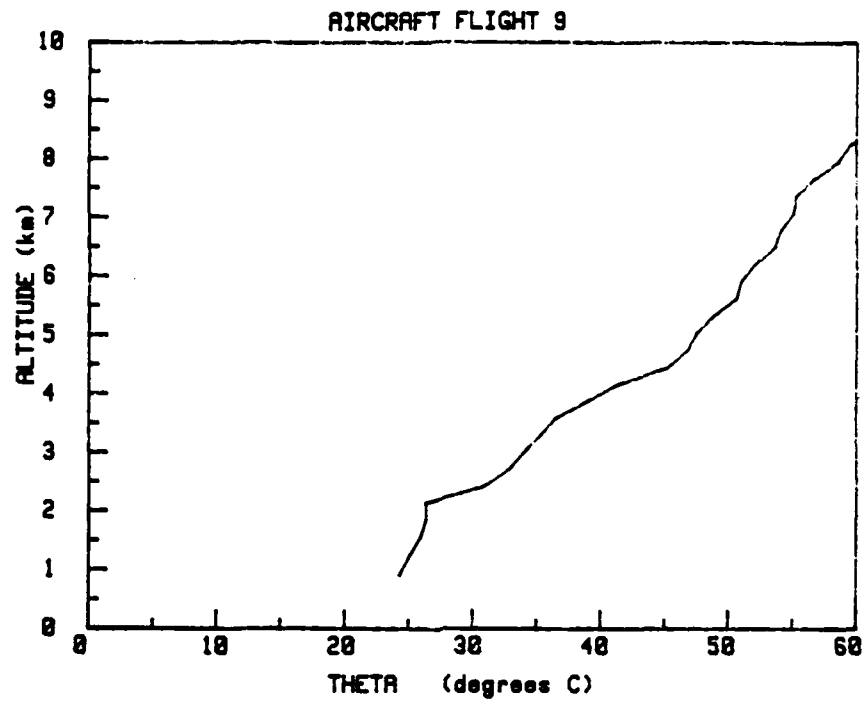


Figure 6. (continued)

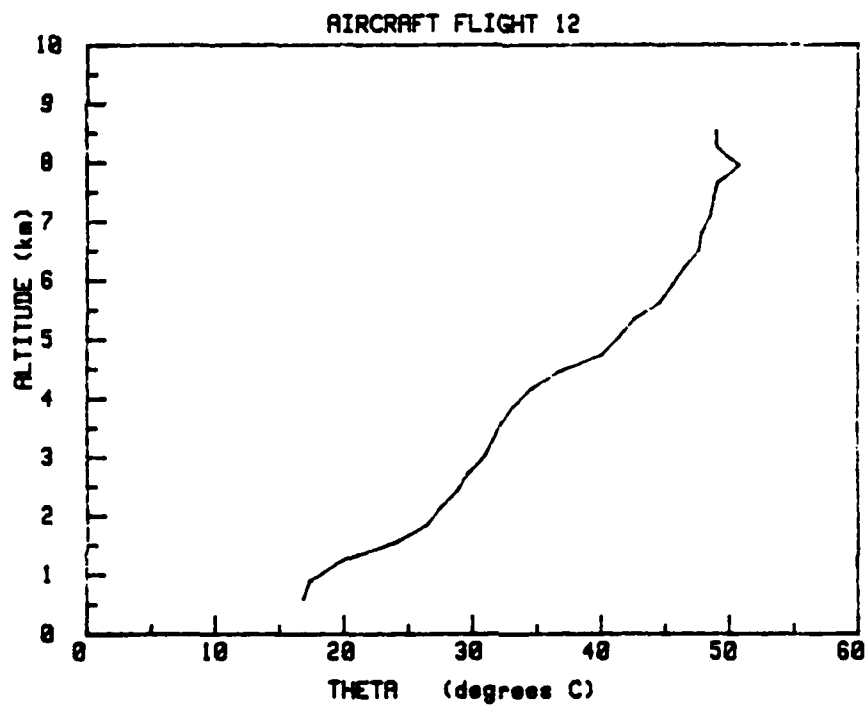
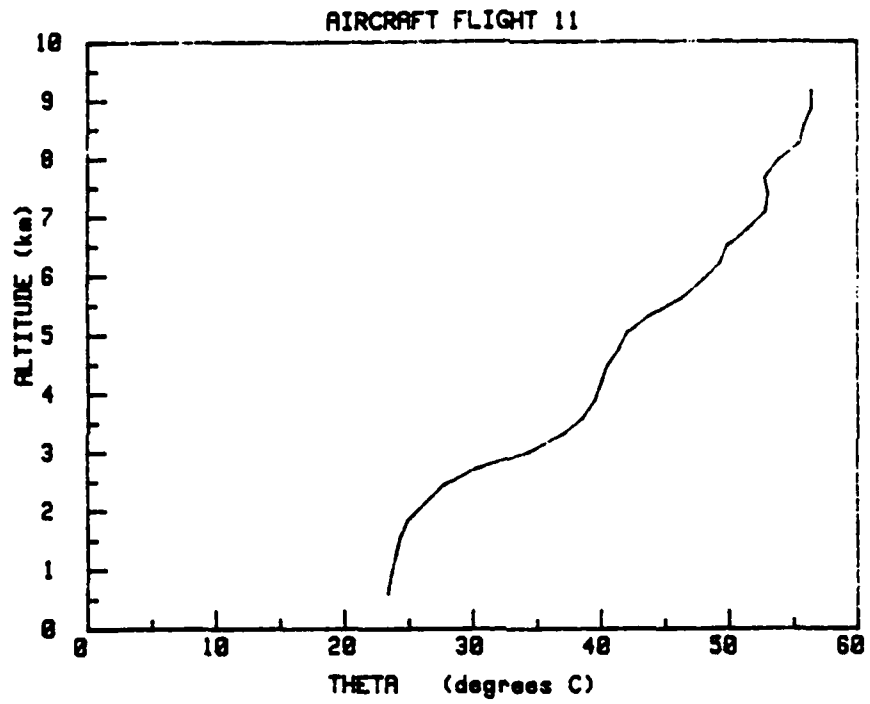


Figure 6. (continued)

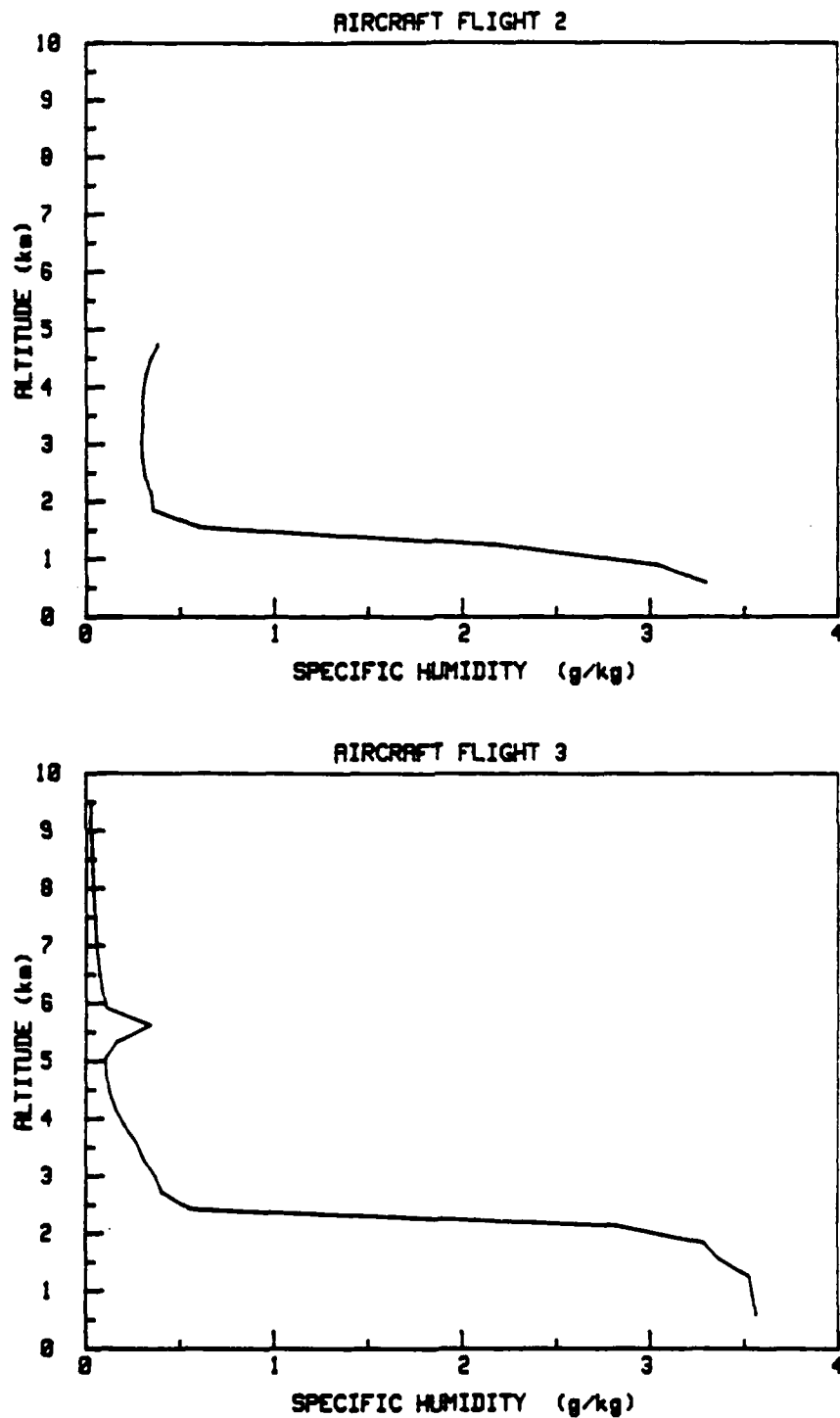


Figure 7. Specific humidity vertical profiles as measured by aircraft instrumentation. Altitude is MSL. Only flights during which the PSU profiler operated are shown, Flights 2-8 (labeled above each graph).

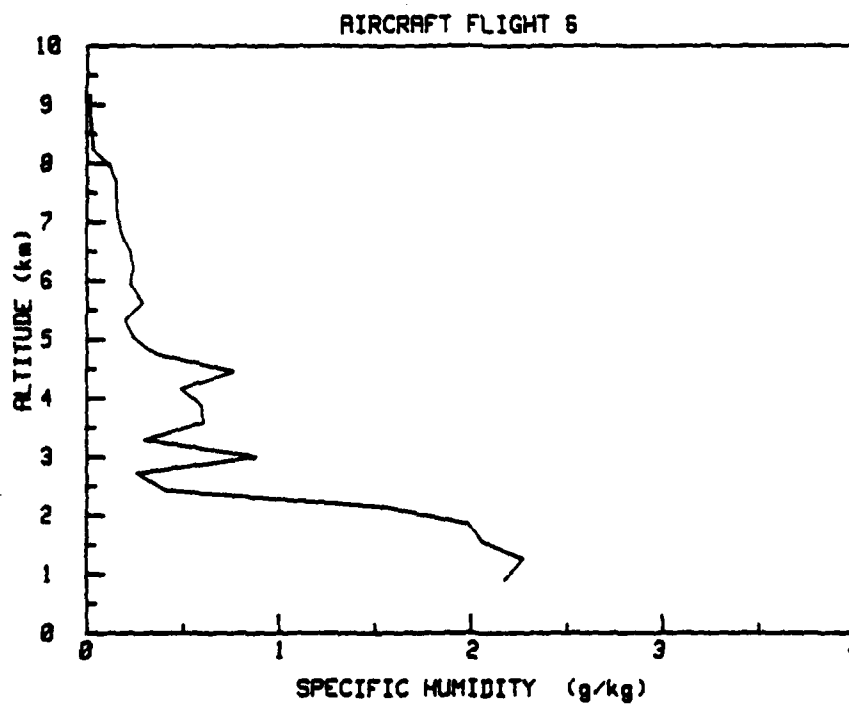
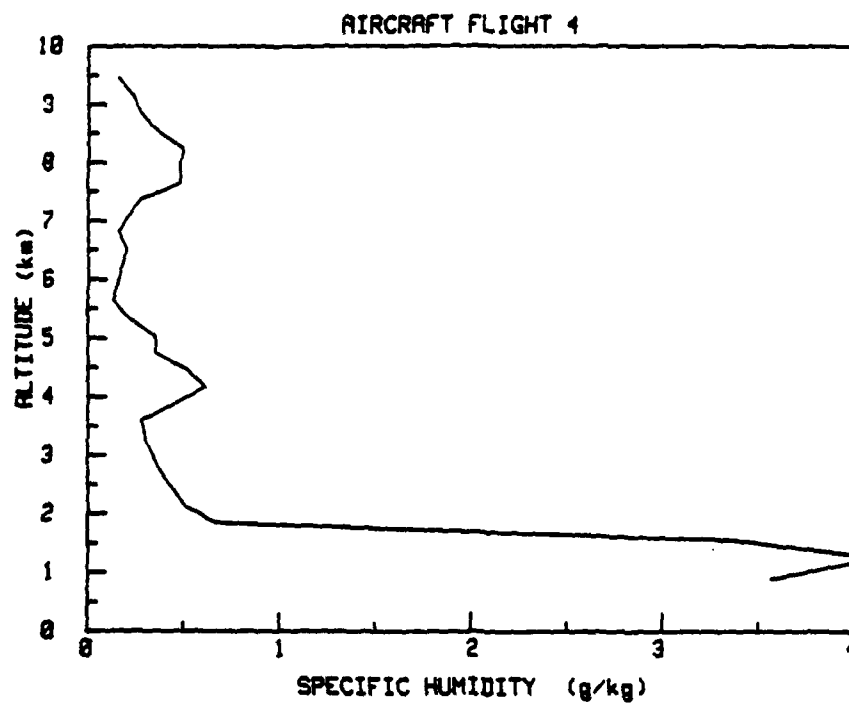


Figure 7. (continued)

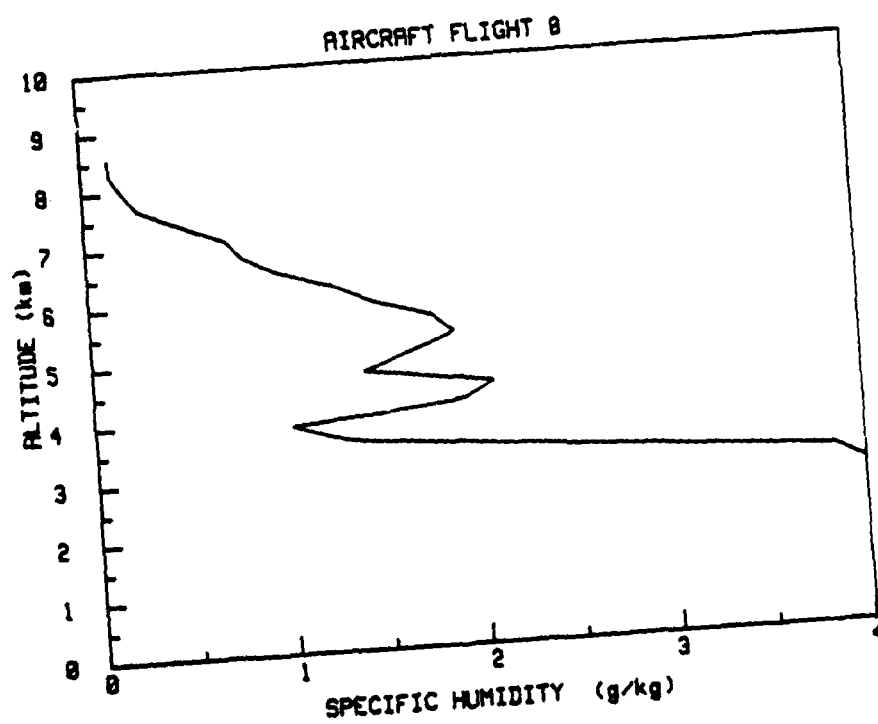
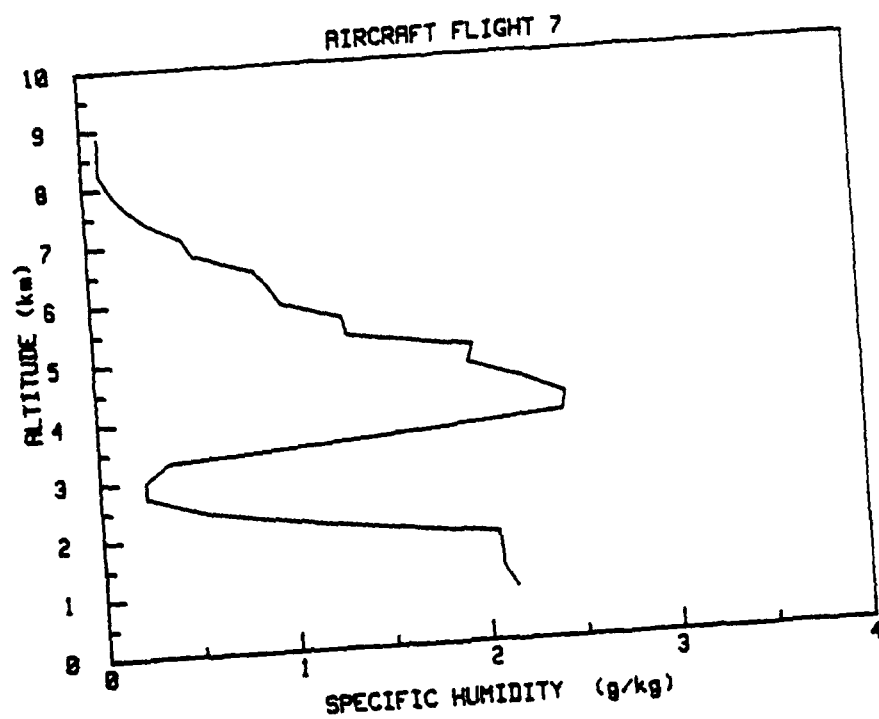


Figure 7. (continued)

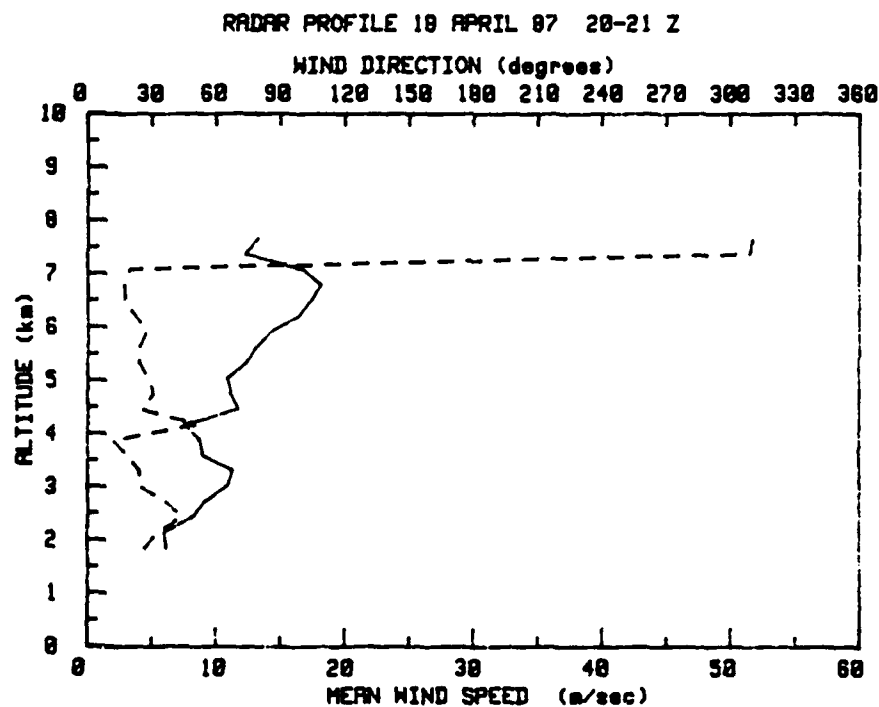
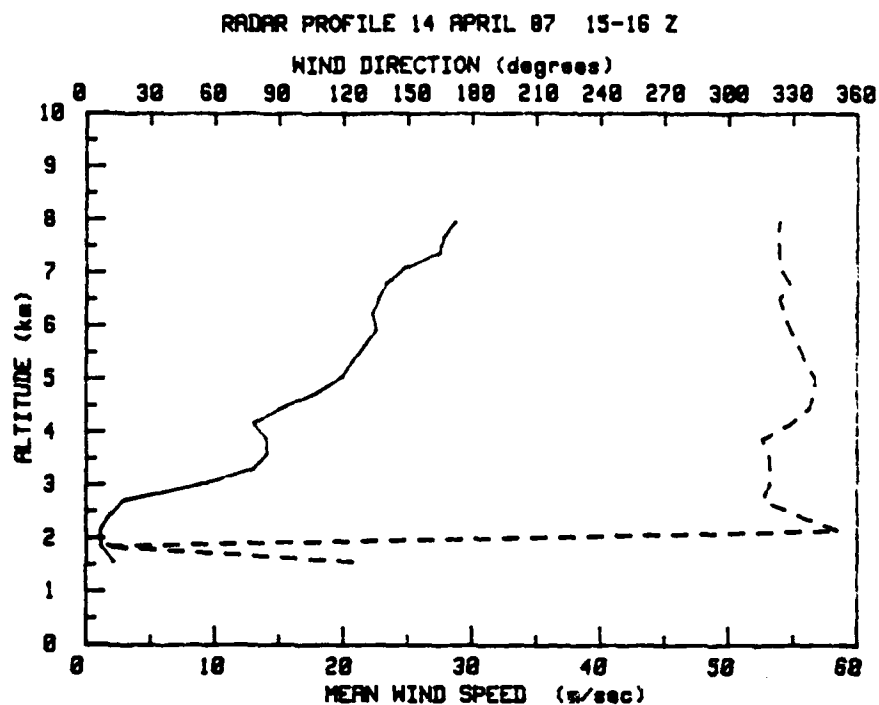


Figure 8. Mean wind speed (solid line) and direction (broken line) as measured by the profiler. Date and the hour interval averaged are given above each graph. Altitude is MSL.

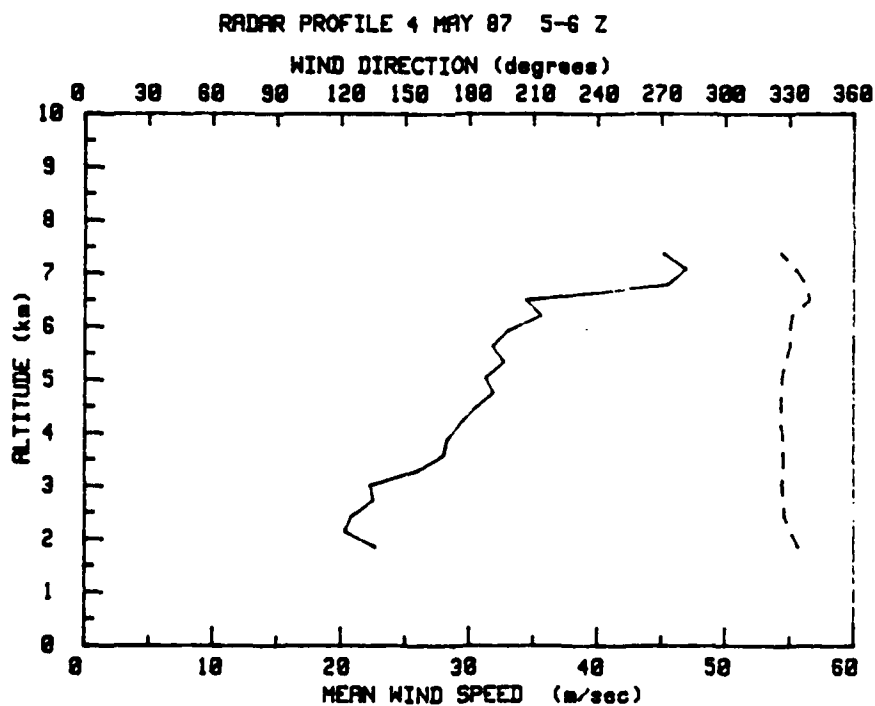
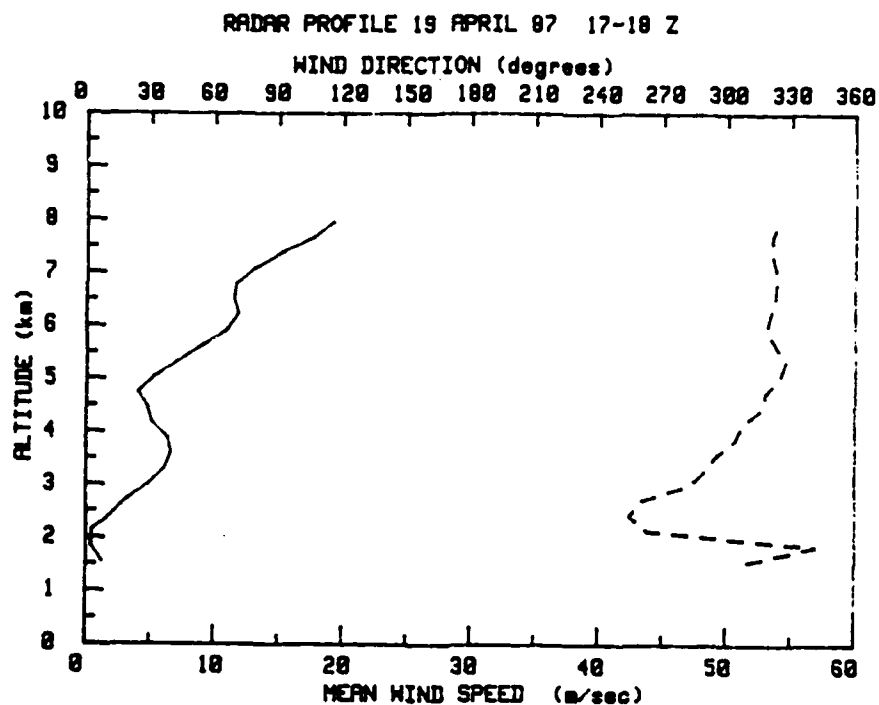


Figure 8. (continued)



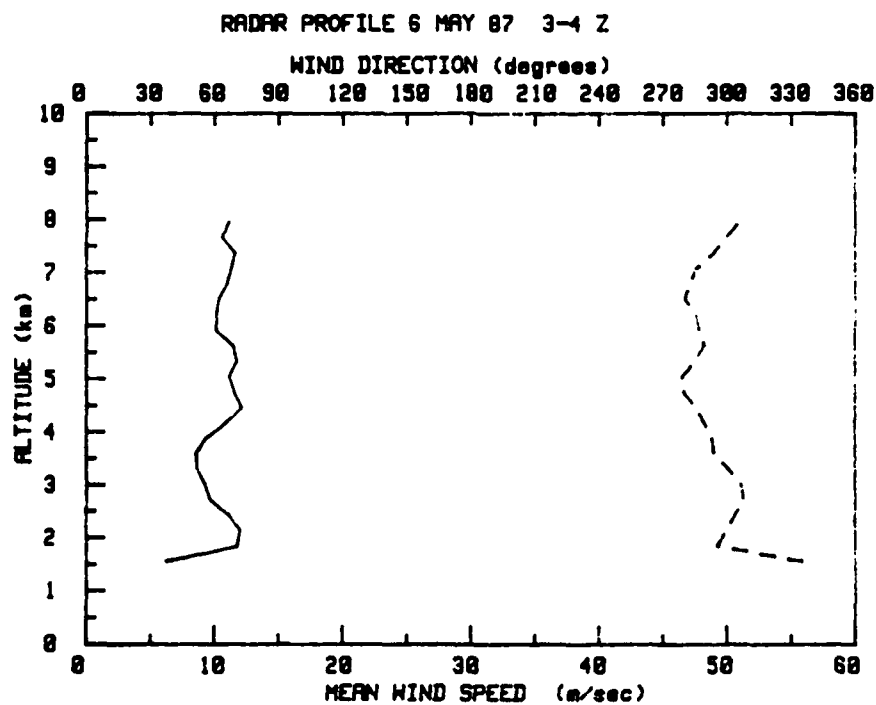
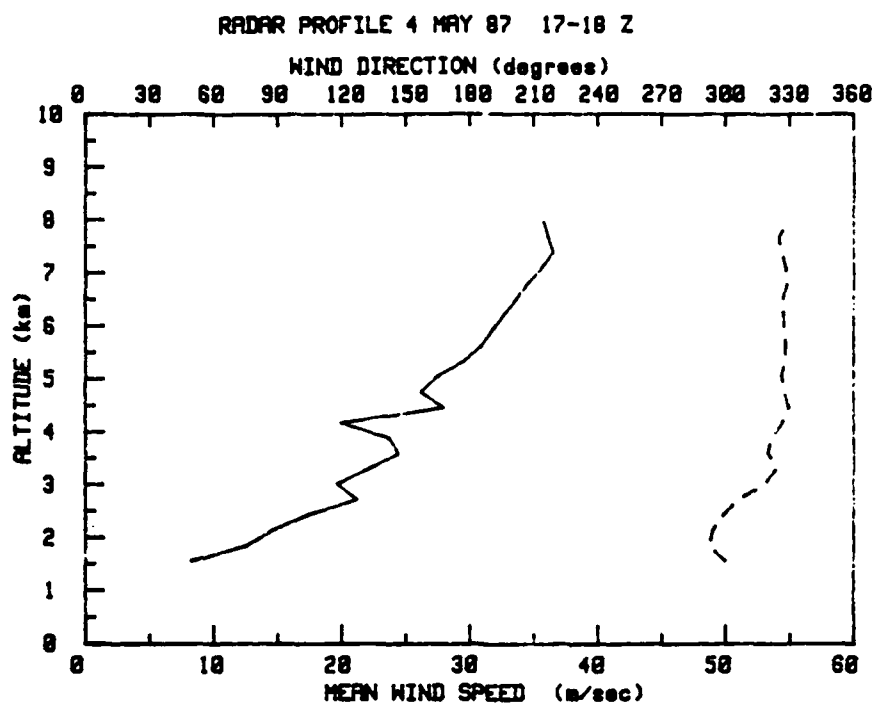


Figure 8. (continued)

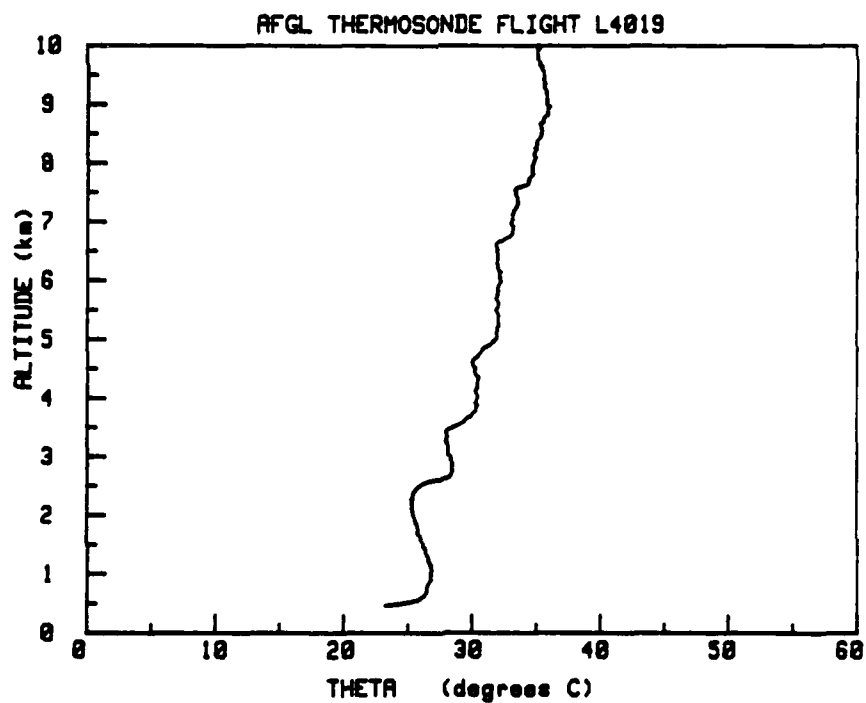
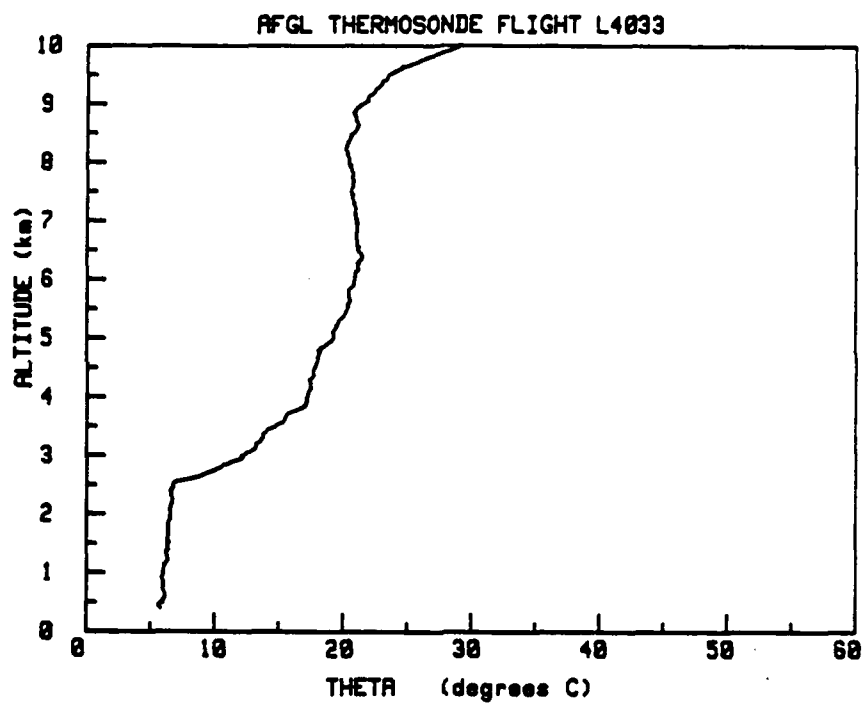


Figure 9. AFGL thermosonde-measured potential temperature vertical profiles correlating to aircraft flights. Altitude is MSL. Thermosonde flight number is given above each graph.

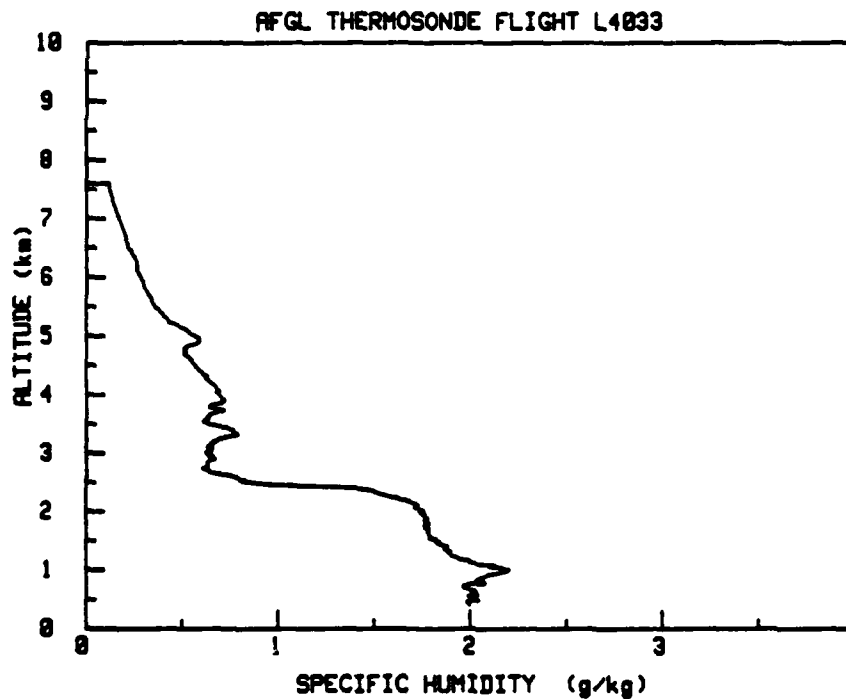
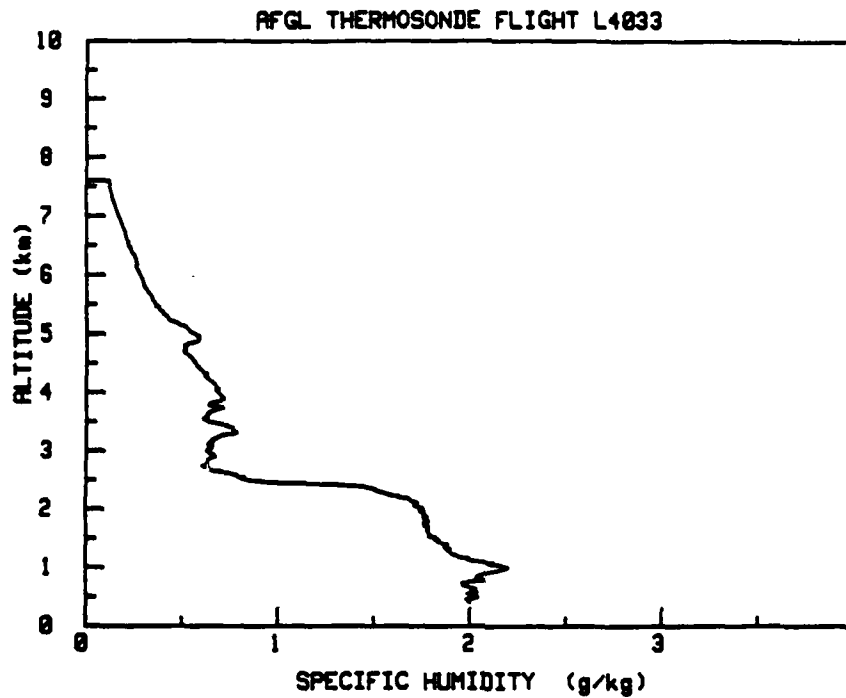


Figure 10. AFGL thermosonde-measured specific humidity vertical profiles correlating to aircraft flights. Altitude is MSL. Thermosonde flight number is given above each graph.

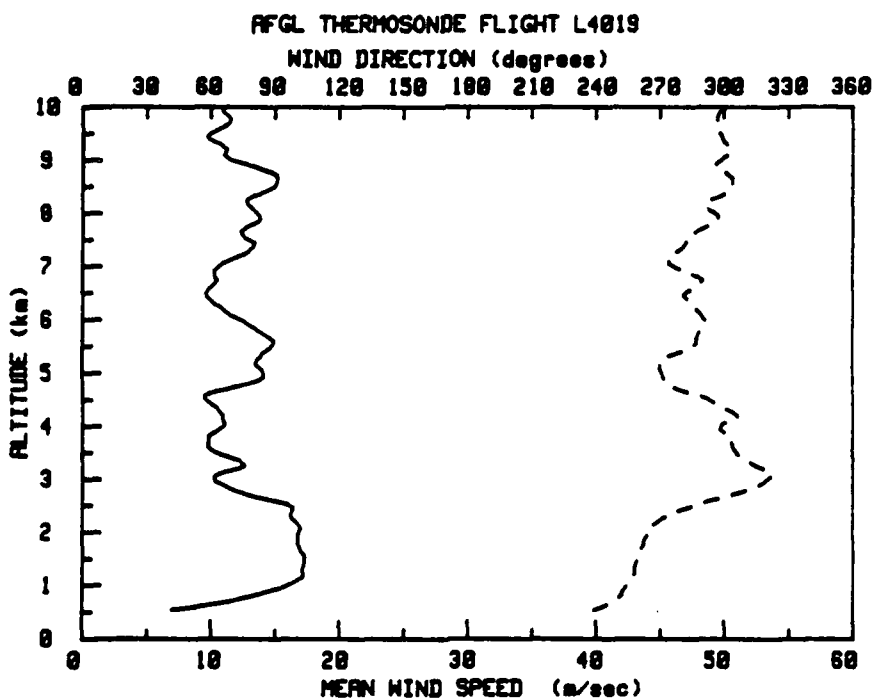
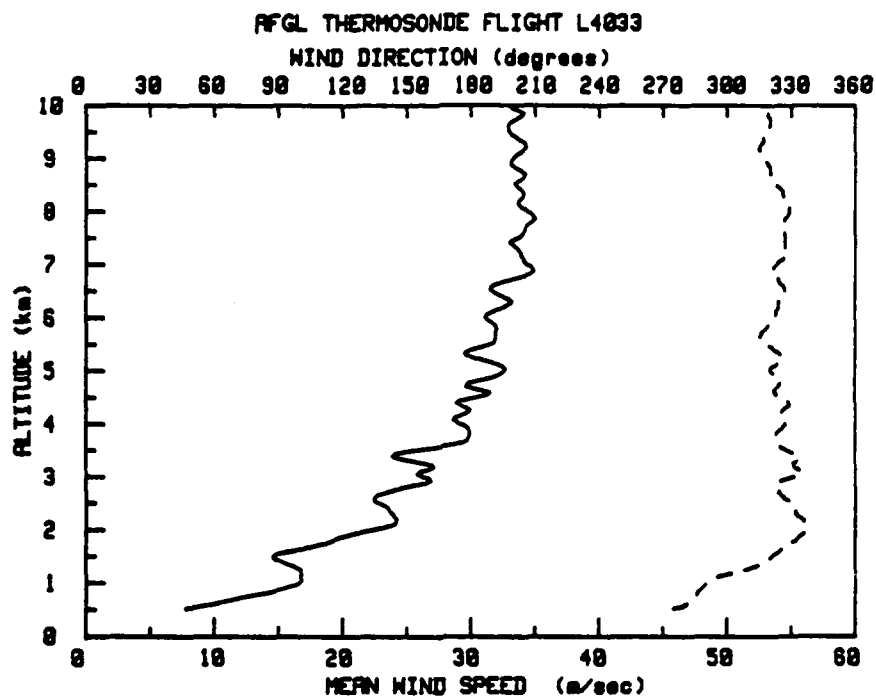


Figure 11. AFGL thermosonde-measured vertical profiles of mean wind speed (solid line) and direction (broken line). Altitude is MSL. Thermosonde flight number is given above each graph.

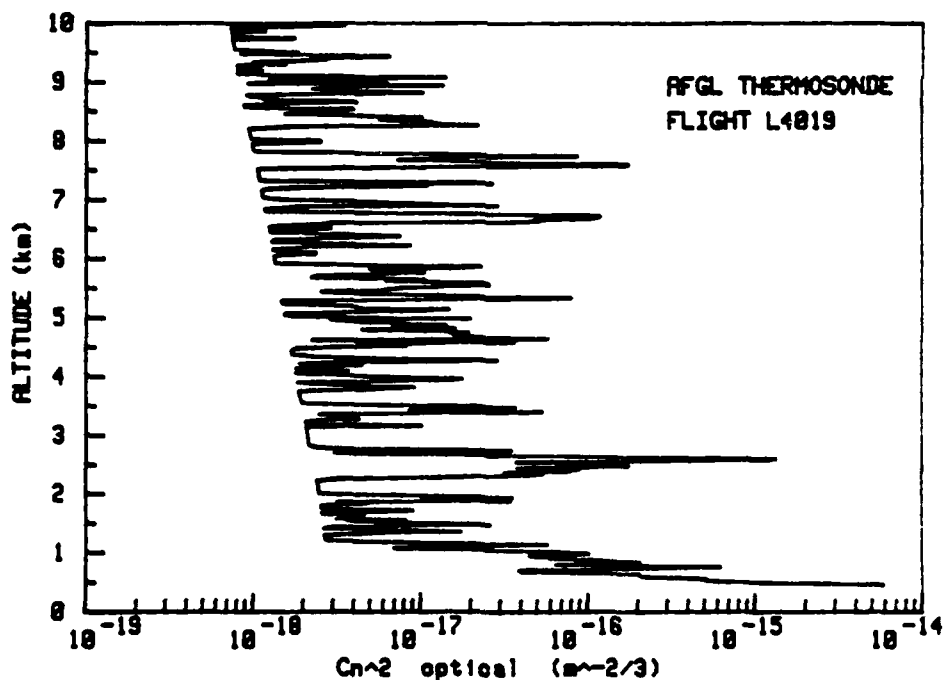
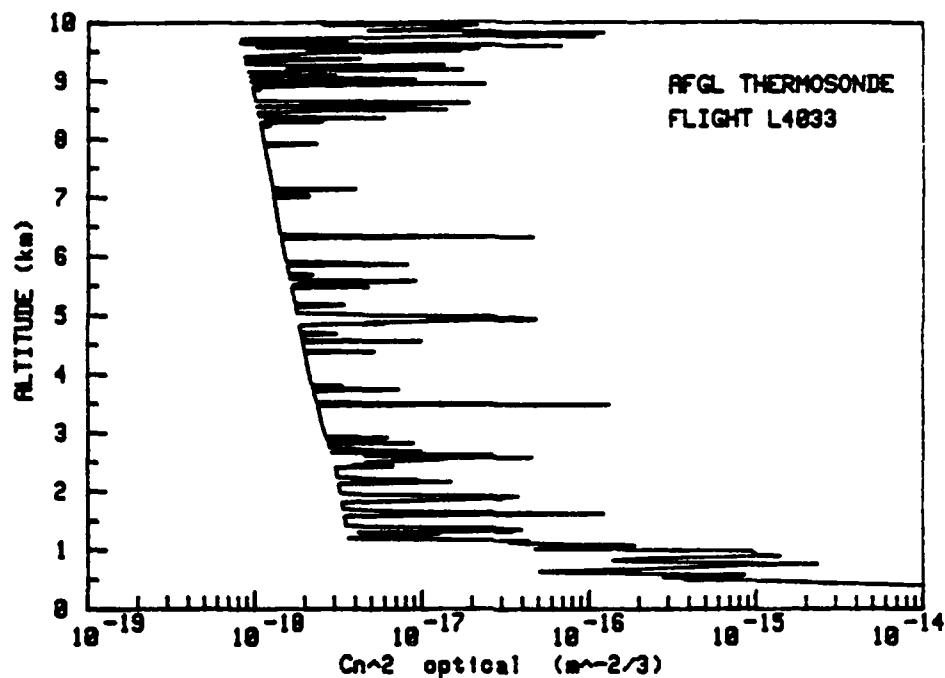


Figure 12. AFGL thermosonde-calculated vertical profiles of raw  $C_n^2$ -optical based on measured  $C_T$ . Altitude is MSL. Thermosonde flight number is given interior to each graph.

(Murphy and Battles 1986). AFGL scintillometer profiles corresponding to aircraft flights are shown in Figure 13.

RADC scintillometer data was provided as seven-level profiles with  $C_n^2$  in  $m^{-2/3}$  at the standard kernel levels (AGL altitude assuming zenith angle of zero) (Donald Stebbins, letter to author, September 1986). Only one data run corresponded to the aircraft flight times. It is shown in Figure 14.

NPS  $r_o$  scintillometer data was provided as  $r_o$  in cm as a function of zulu time (Donald Walters, telephone conversation, November 1987). Data taken during aircraft flight was limited to one night, 4 May 1986. The average value of  $r_o$  during this time segment, 0400-0540 Z, was 5 cm.

AFWL isoplanometer data was unavailable for use in this comparison.

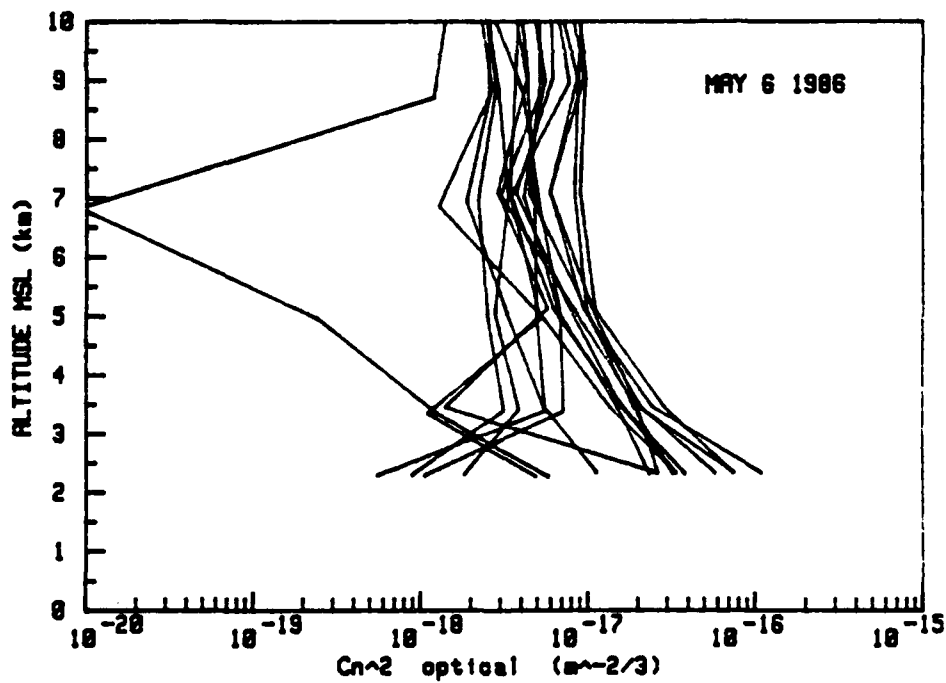
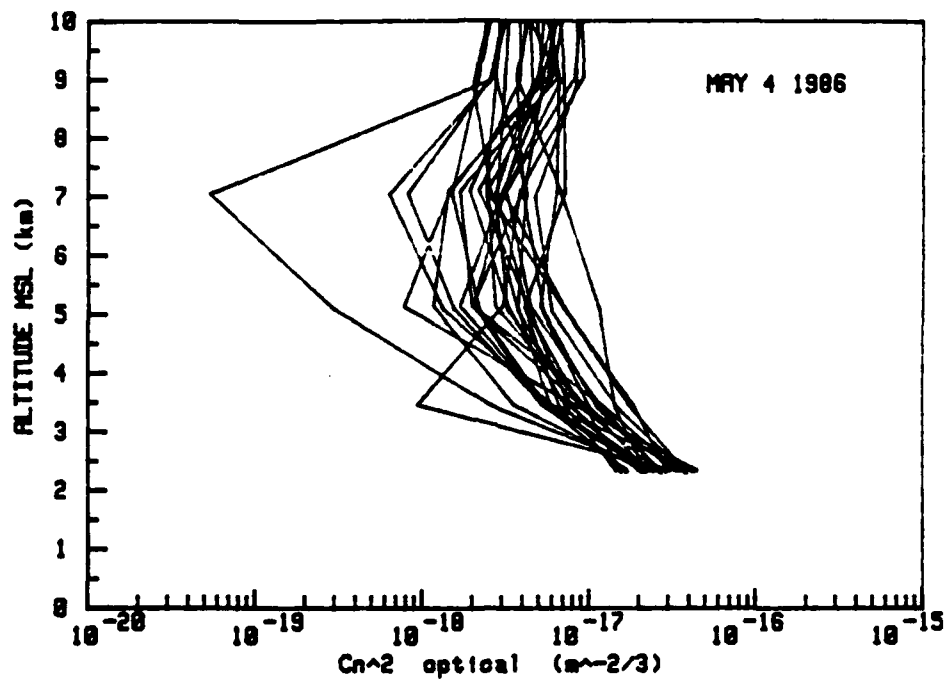


Figure 13. AFGL scintillometer-measured vertical profiles of  $C_n^2$ -optical taken during the aircraft flight time period. Altitude AGL has been adjusted to MSL. Date is given interior to each graph.

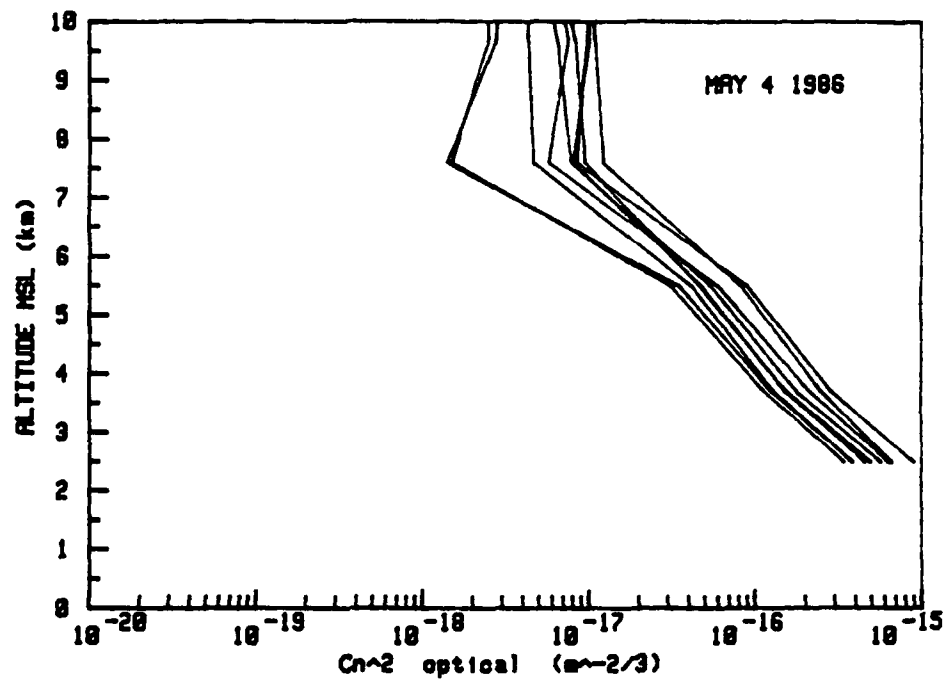


Figure 14. RADC scintillometer-measured vertical profiles of  $C_n^2$ -optical taken during the aircraft flight time period. Altitude AGL has been adjusted to MSL. Date is given interior to the graph.



## CHAPTER 7

### RESULTS AND DISCUSSION

#### 7.1 Analysis of $C_T^2/C_u^2$

The vertical profiles of  $C_u^2$  and  $C_T^2$  calculated from the aircraft data show strong correlation for flights 2, 6(ascent and descent), 8(ascent and descent), 9(ascent), 10(descent), 11, and 12 (Figure 15). The other flights also show some correlation, but not at all levels. Correlation of higher values of these turbulence parameters indicates regions of the atmosphere that contain turbulent layers (Ottersten 1969).  $C_T^2$  and  $C_n^2$  are directly correlated at all levels for all flights, as is to be expected since  $C_n^2$  is a function of  $C_T^2$ .

A rough estimate of boundary layer height can be determined by spectral signal-to-noise ratio for these profiles, since the signal is much stronger in the turbulent boundary layer. For this purpose spectra were examined in detail manually. Table 3 gives an estimate of PBL height for each flight. If  $C_T^2$  versus  $C_u^2$  is graphed (for values above the boundary layer where the TKE and variance budget approximations discussed in Chapter 3 are valid), a power-law relation is evident (Figures 16 and 17). This ratio is proportional to Richardson number and temperature gradient (right hand side of equation 3.28). All flights except 6(ascent and descent), 7(descent), and 11(ascent) show distinct sloped correlations. All flights were plotted simultaneously and a regression analysis was done to determine slope and goodness-of-fit (Figure 18). The plot of flight 6 had high scatter. Removal of this flight decreased the scatter and thus

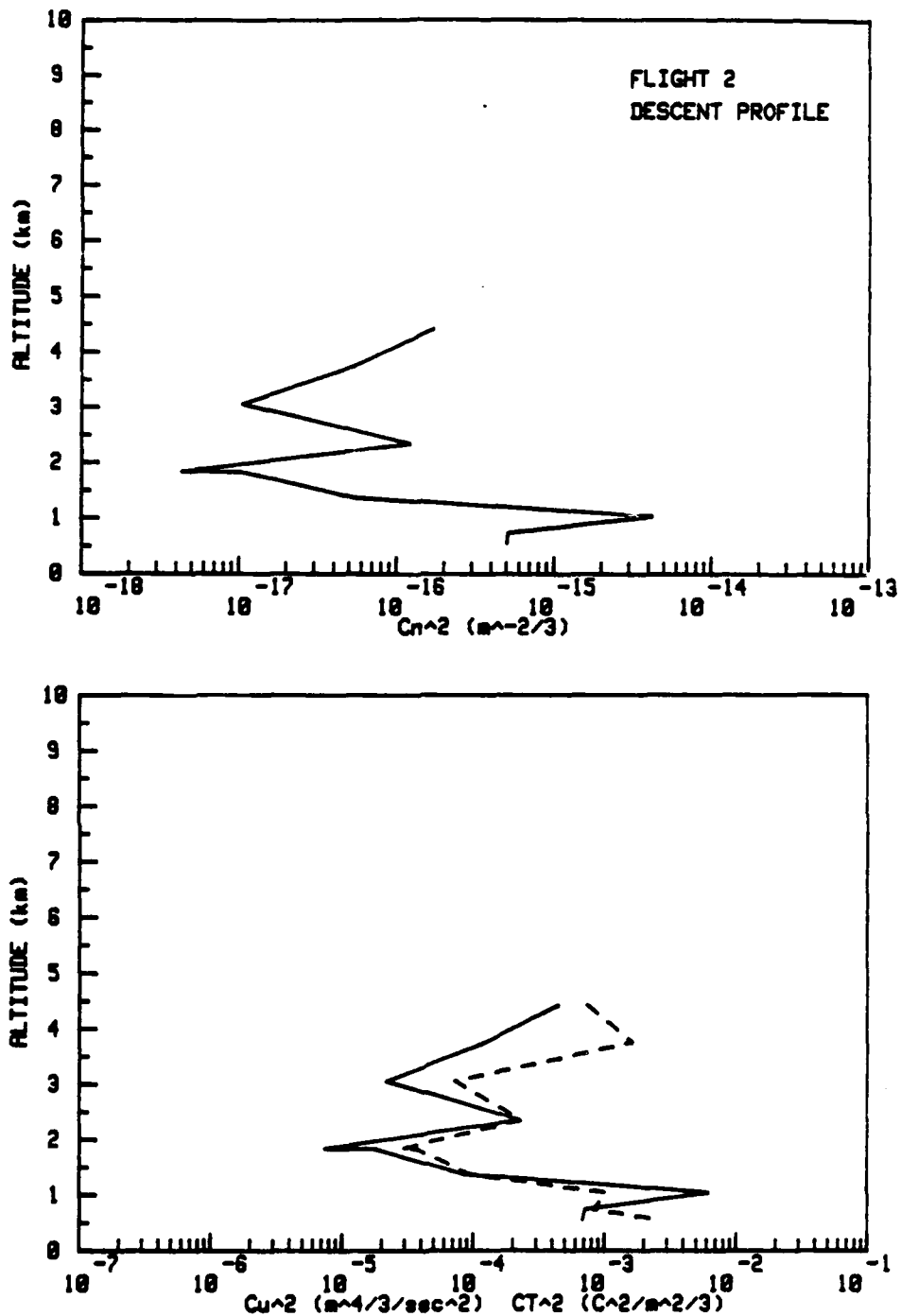


Figure 15. Vertical profiles of  $C_n^2$ ,  $C_T^2$ , and  $C_u^2$ . The top graph shows the  $C_n^2$  profile calculated from the  $C_T^2$  profile.  $C_T^2$  (solid line) and  $C_u^2$  (broken line) are shown on the bottom graph versus MSL altitude. These values were calculated from the aircraft spectral data. The flight number and ascent/descent designation for the profile is given interior to the top graph. Dual graphs are shown for flights 2-12.

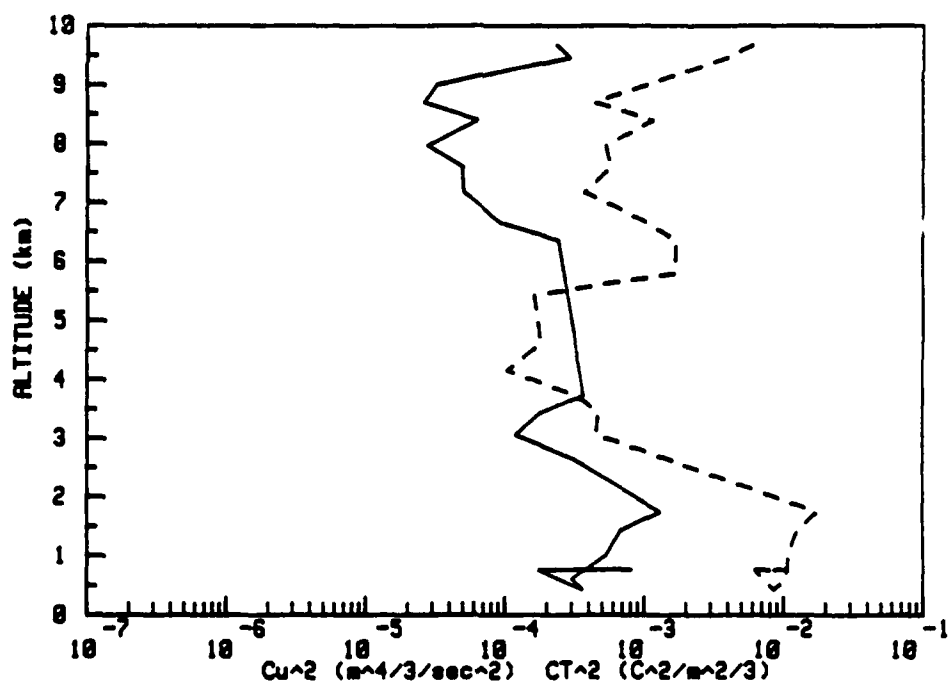
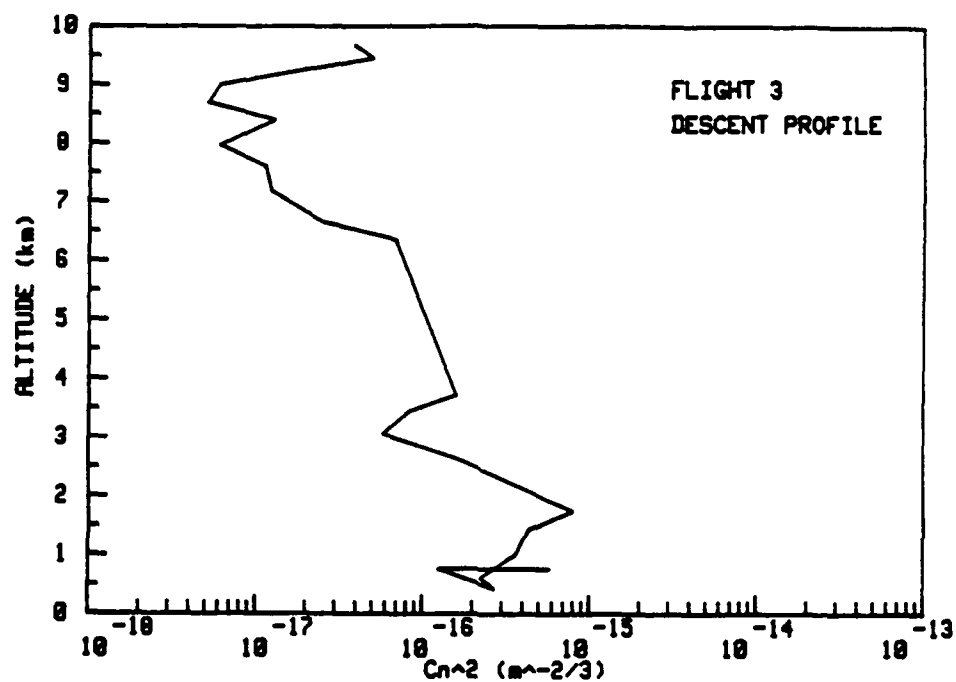


Figure 15. (continued)

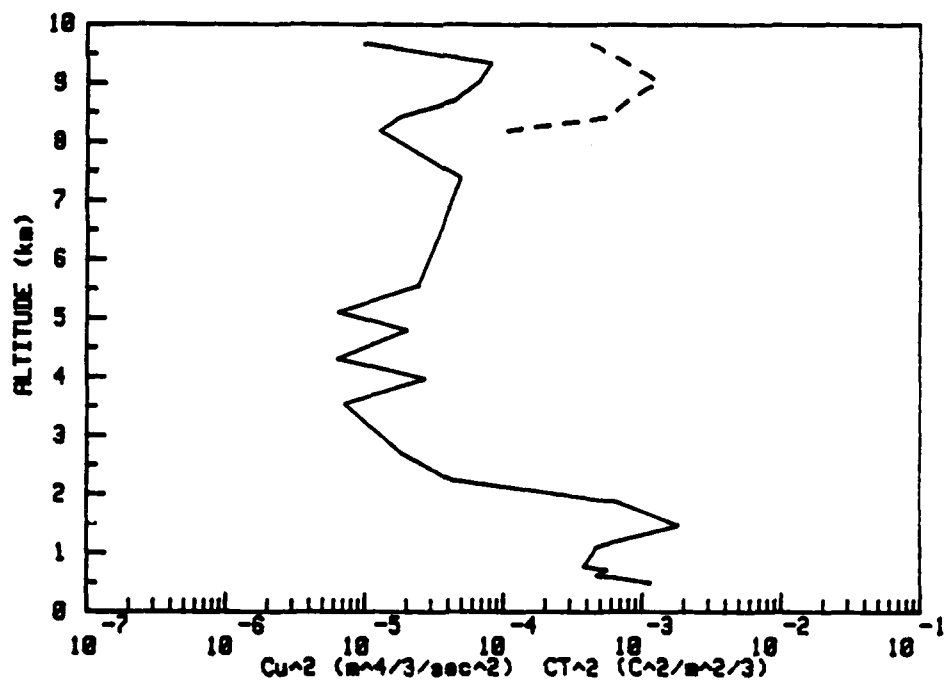
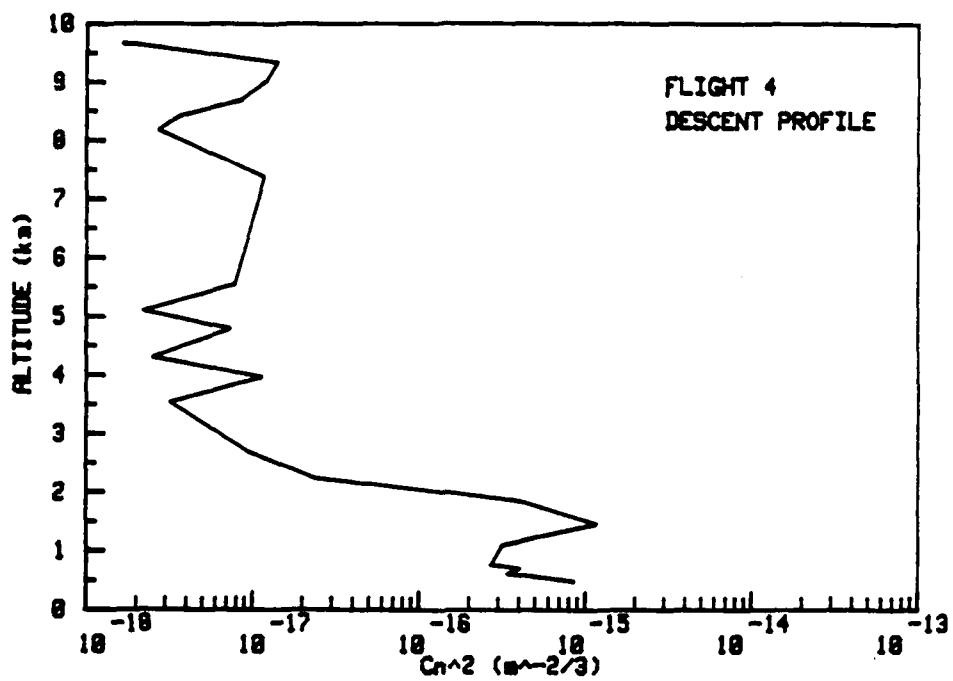


Figure 15. (continued)

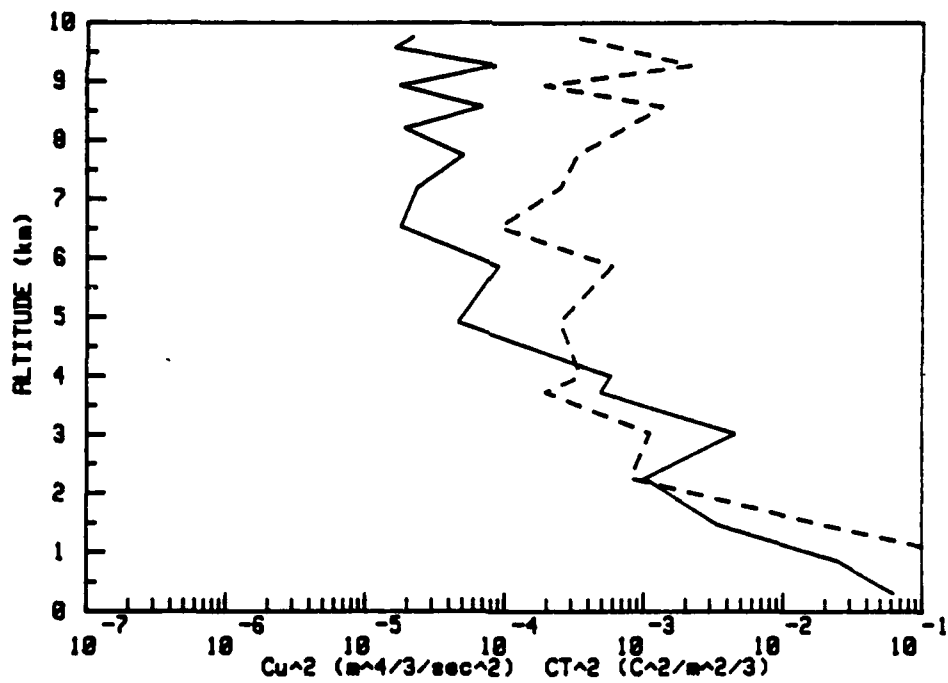
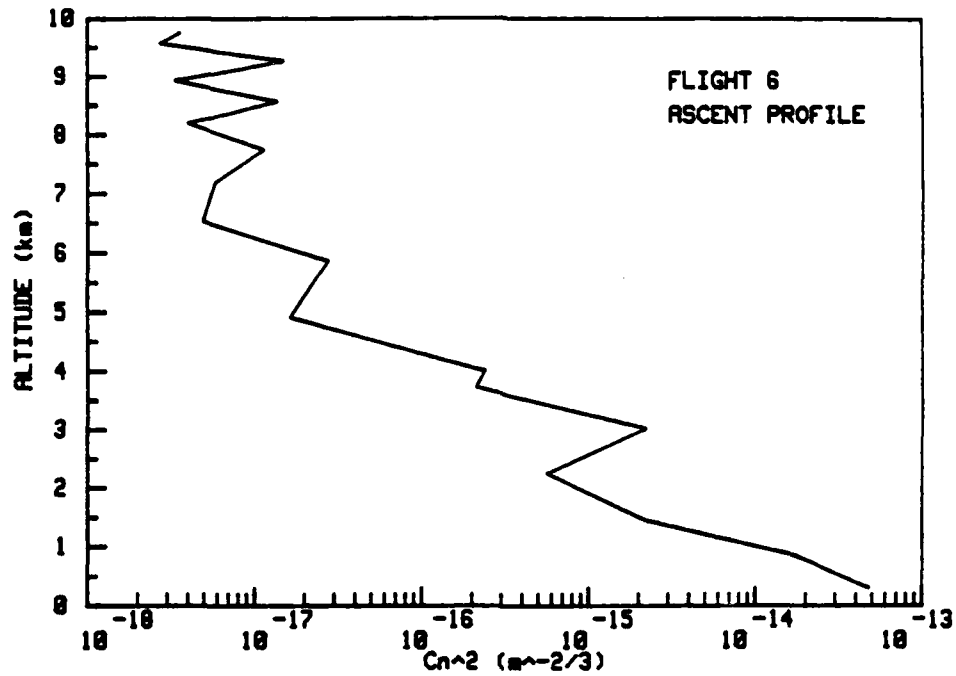


Figure 15. (continued)

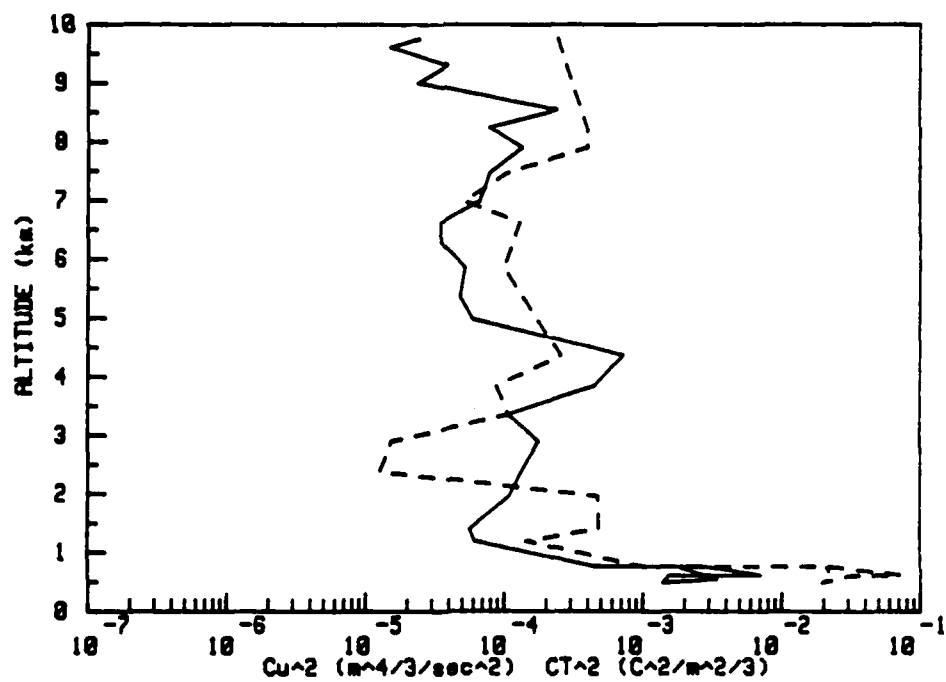
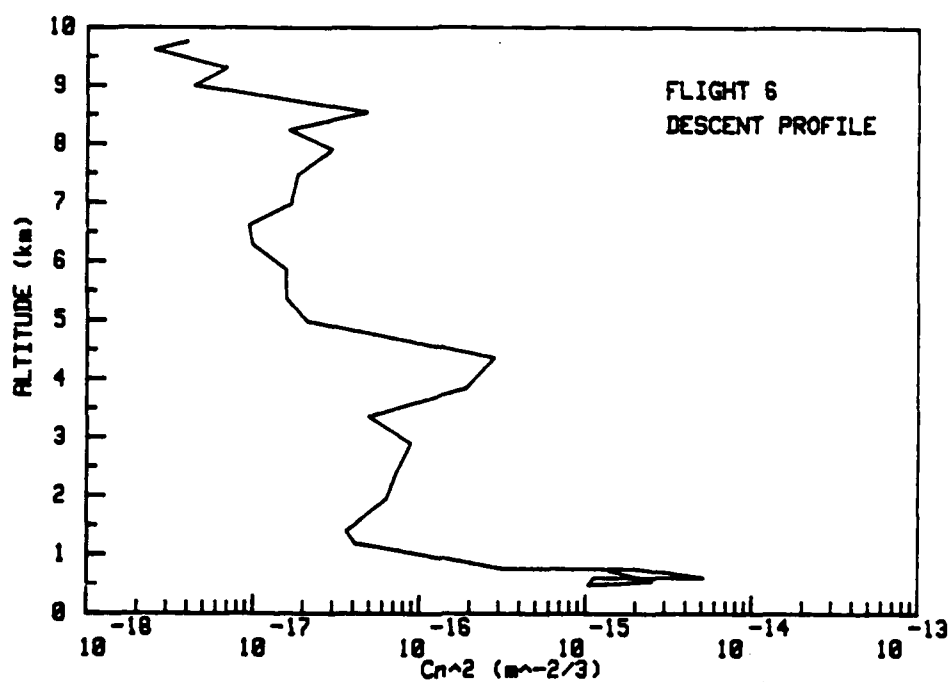


Figure 15. (continued)

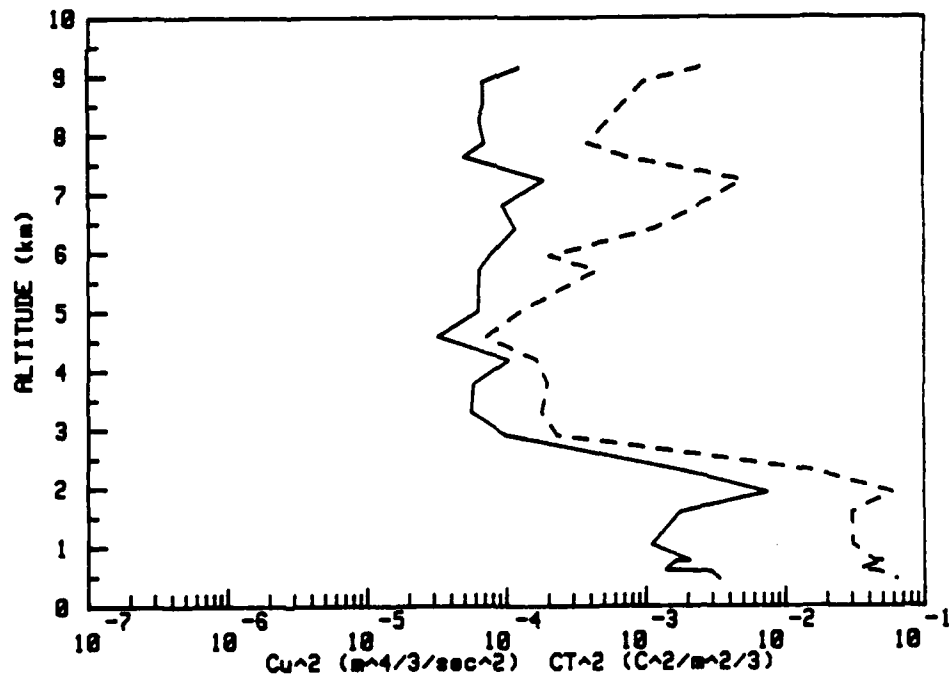
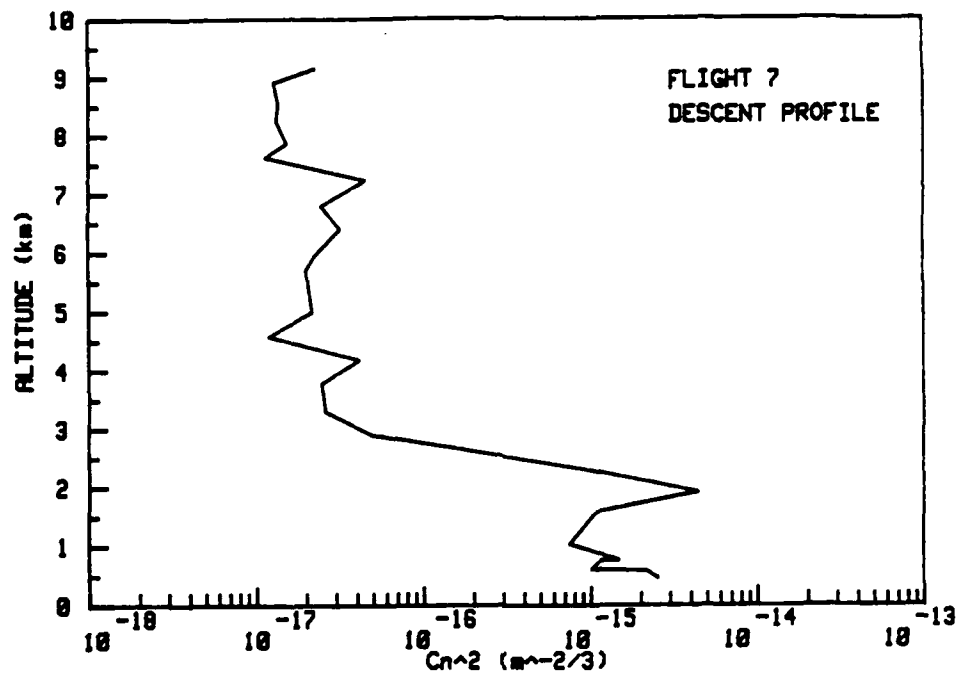


Figure 15. (continued)

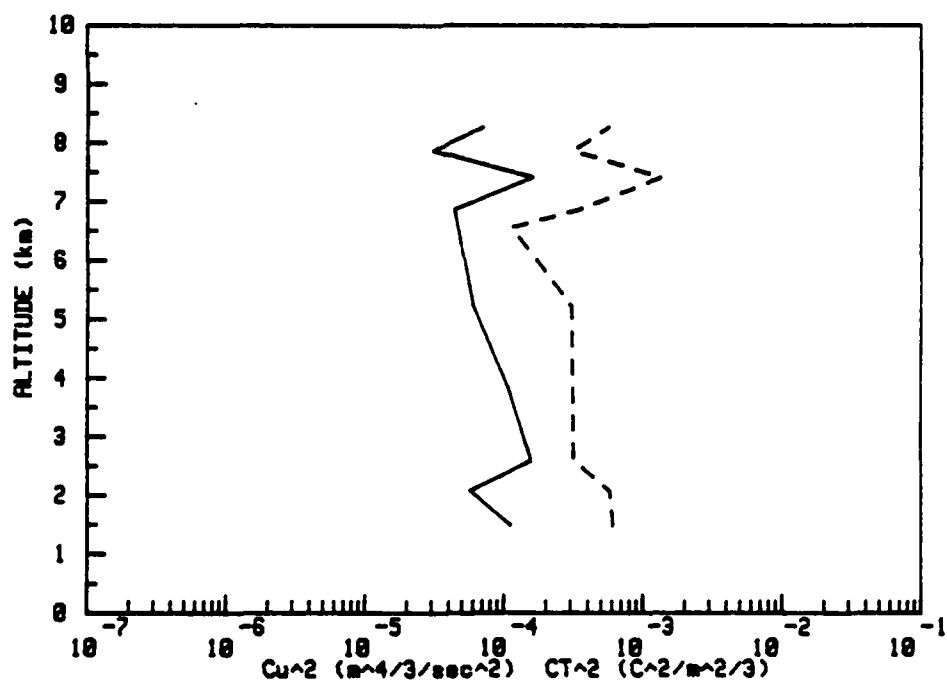
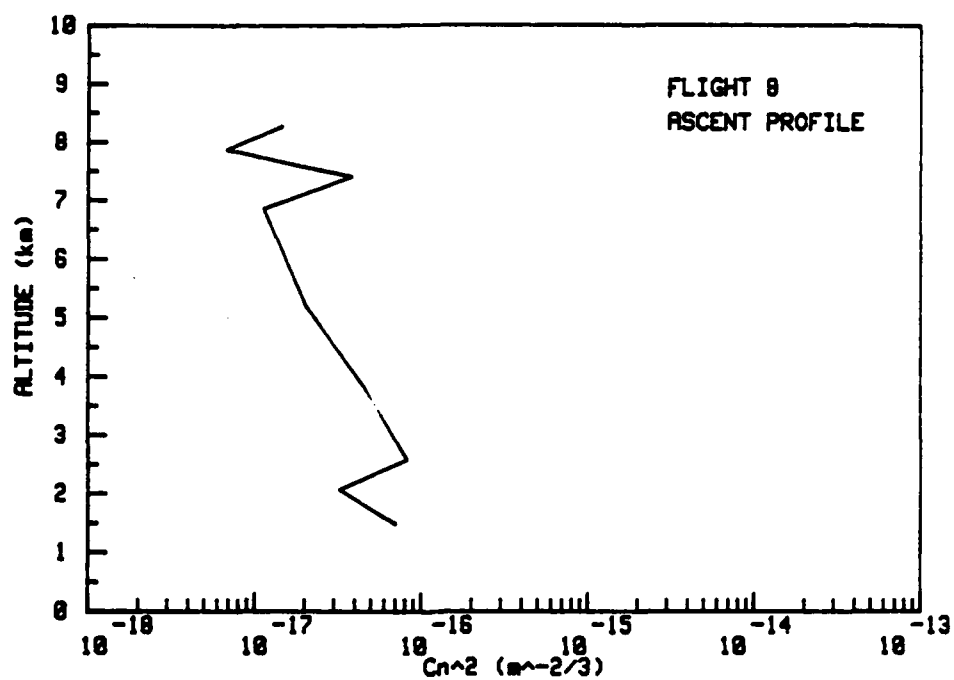


Figure 15. (continued)



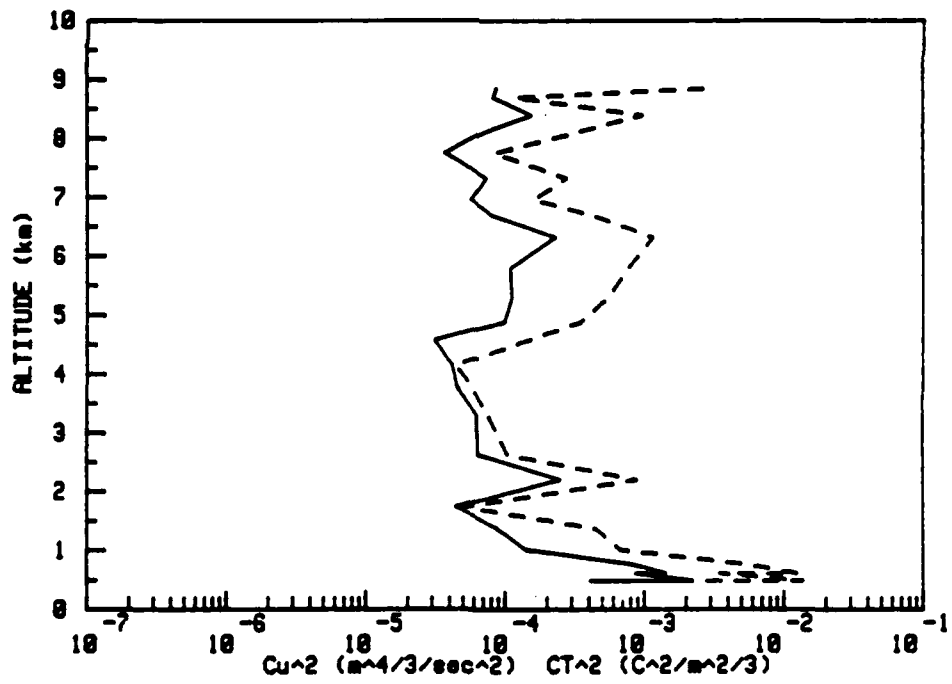
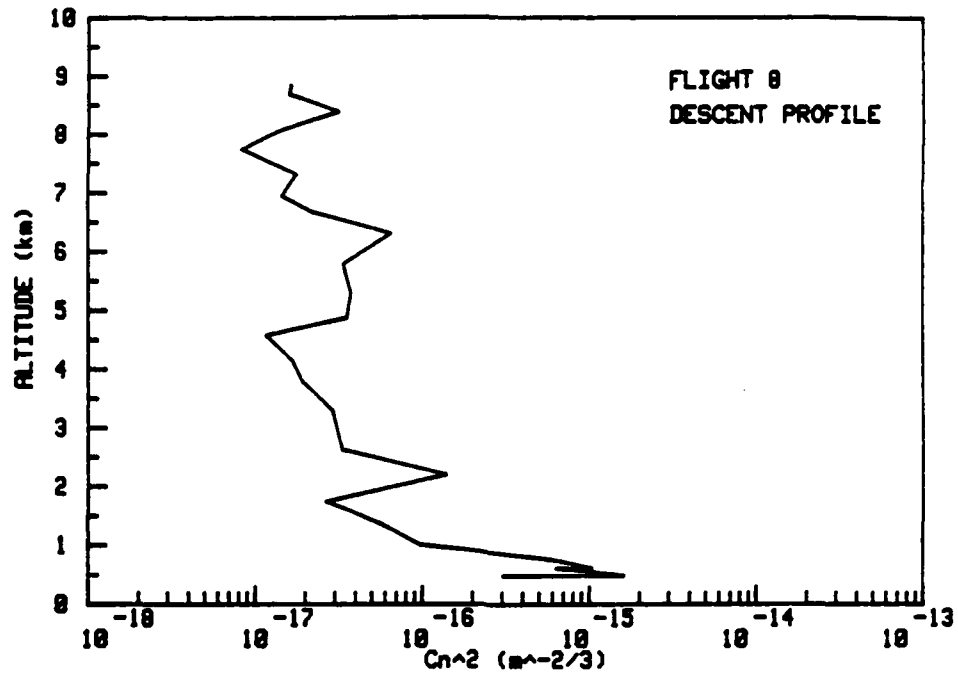


Figure 15. (continued)

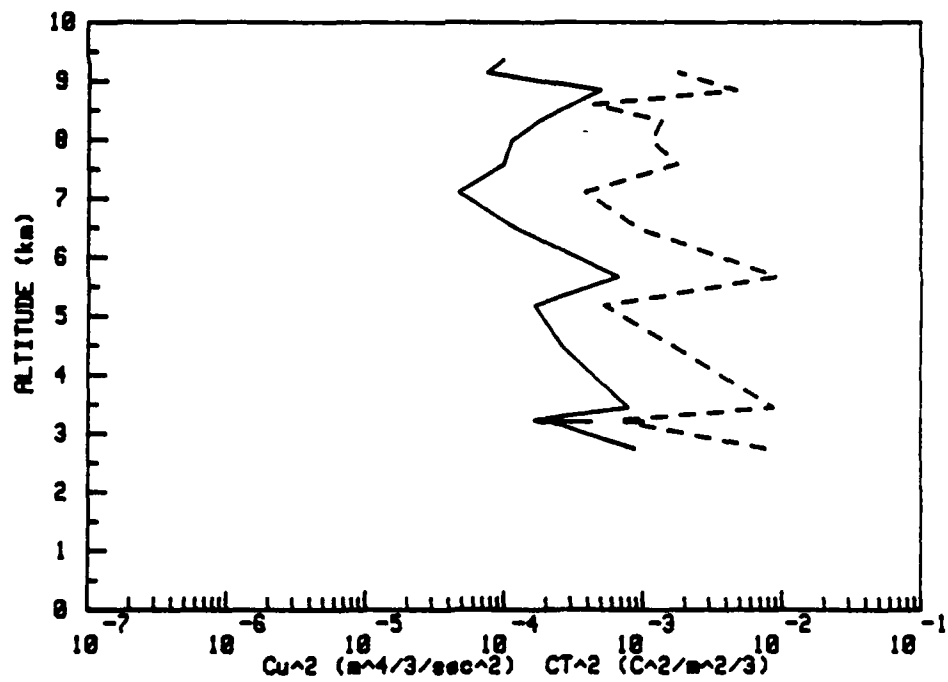
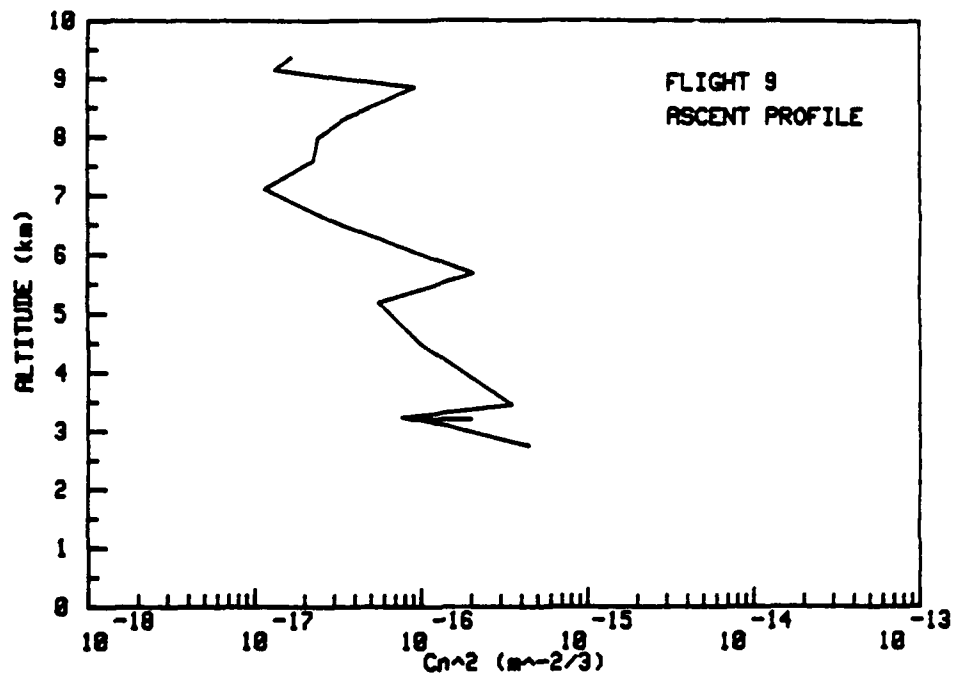


Figure 15. (continued)

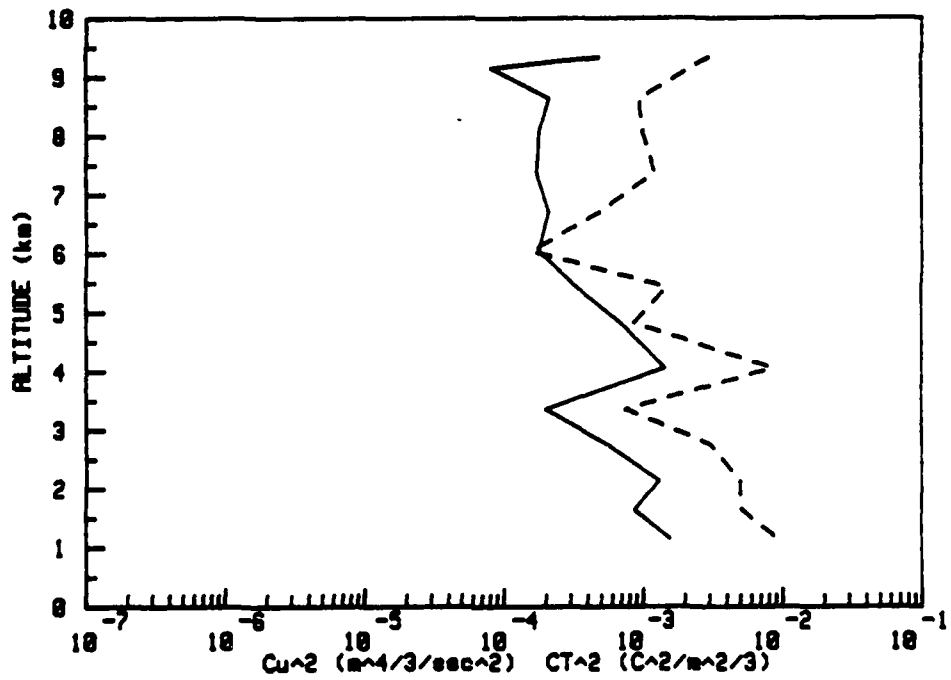
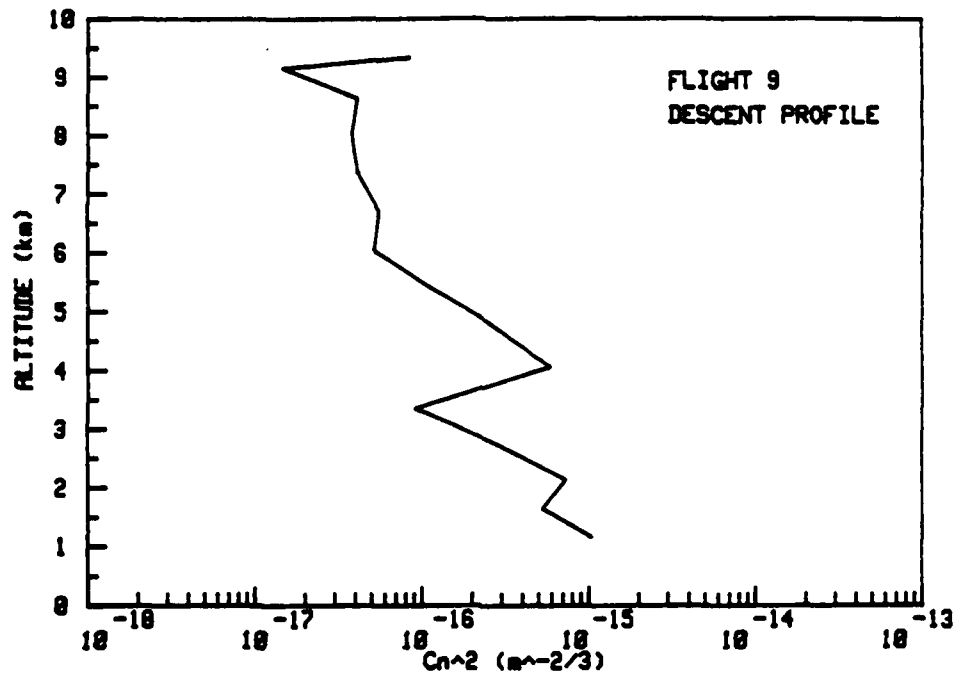


Figure 15. (continued)

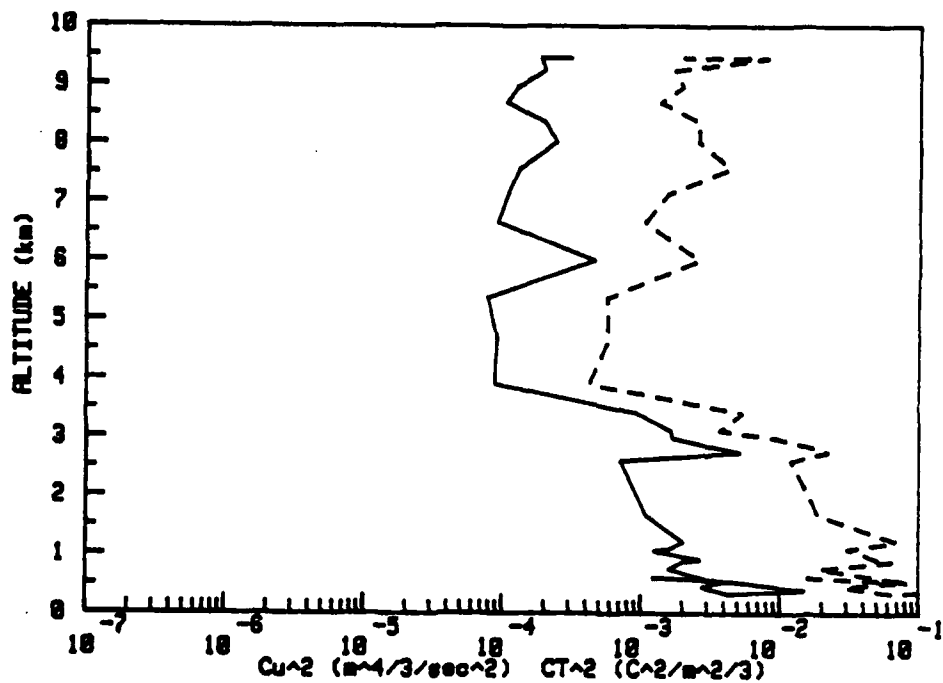
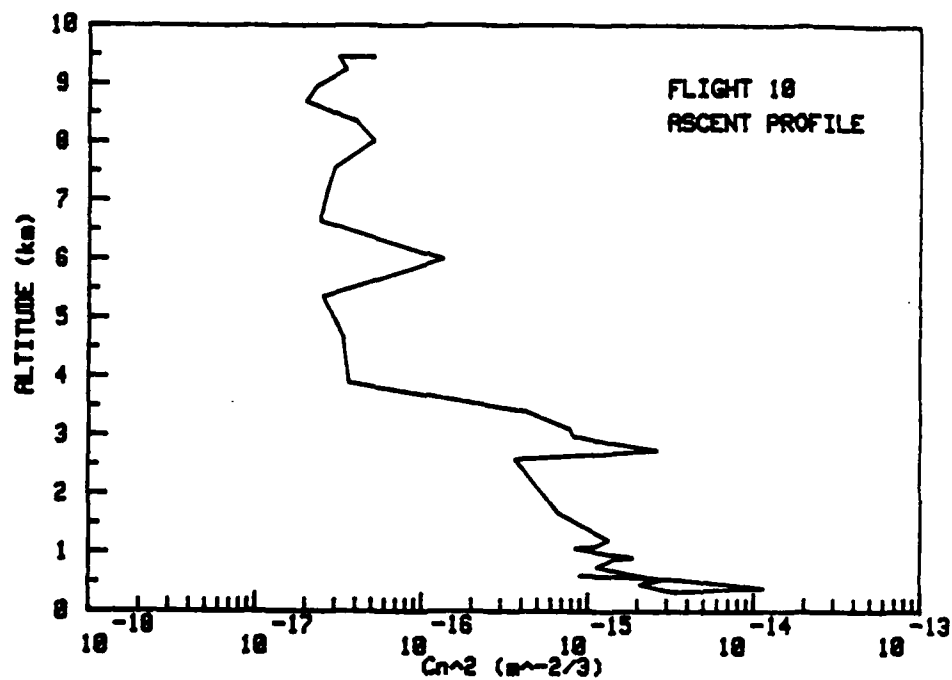


Figure 15. (continued)

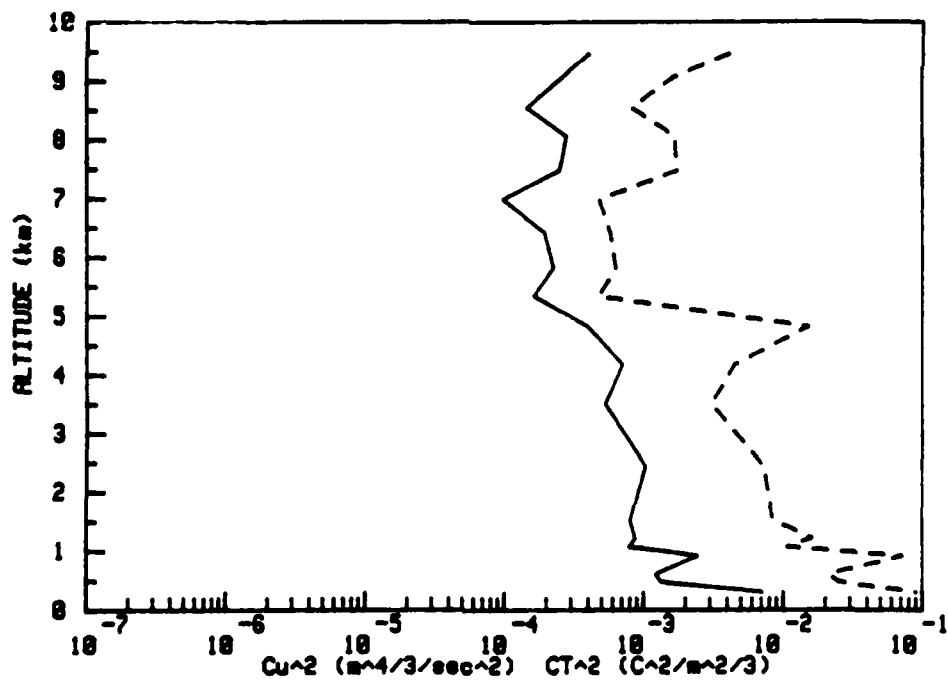
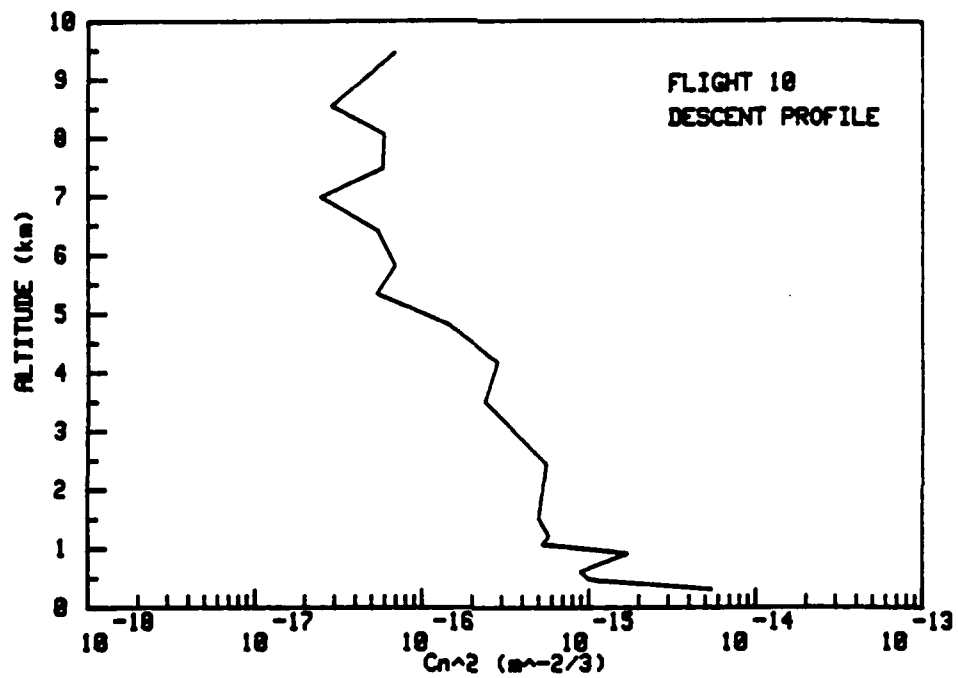


Figure 15. (continued)

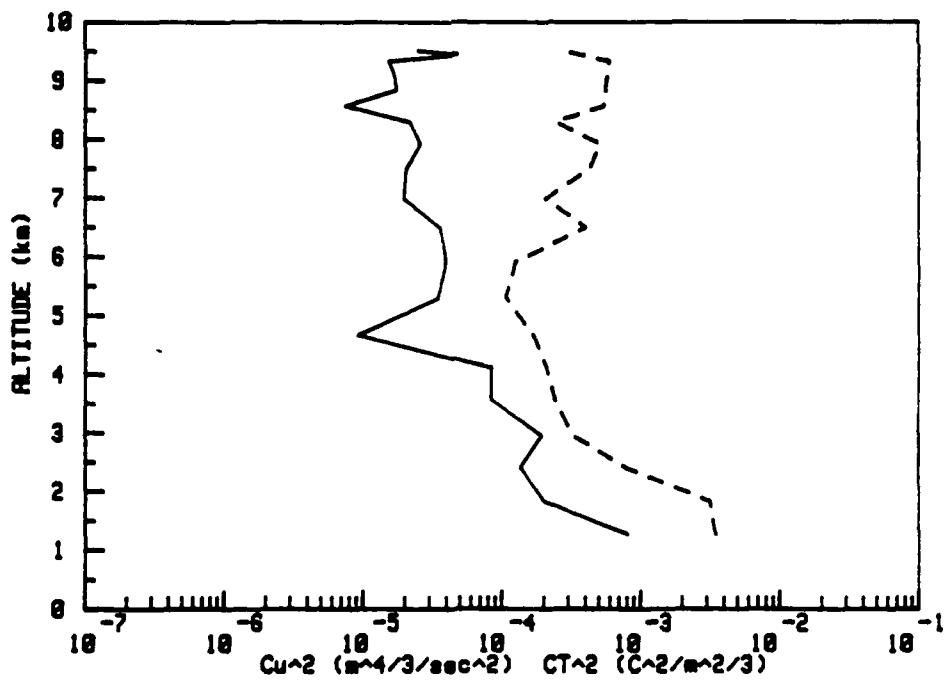
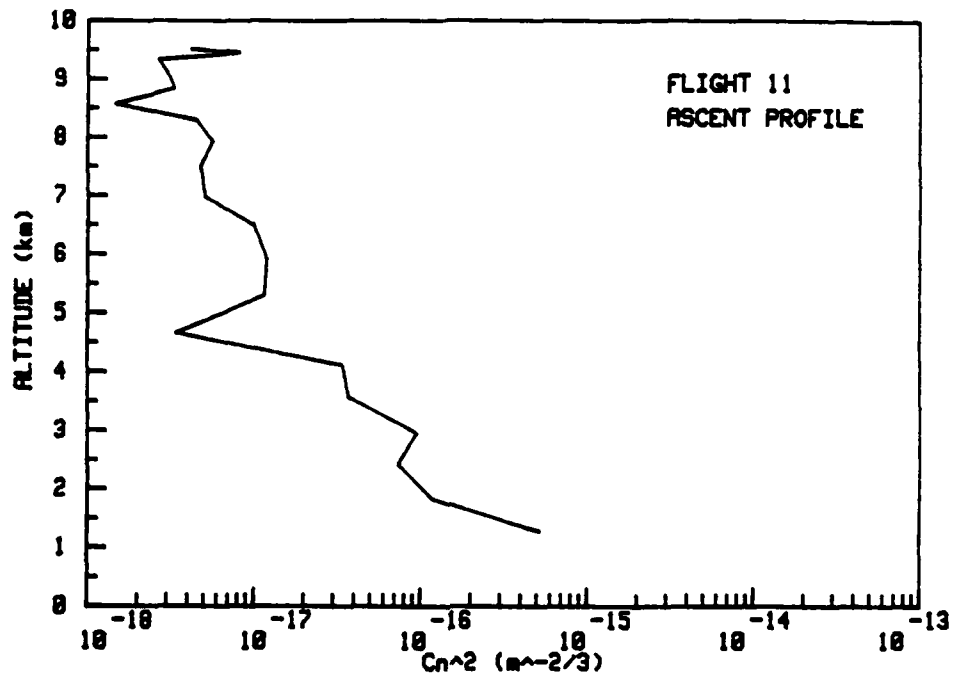


Figure 15. (continued)

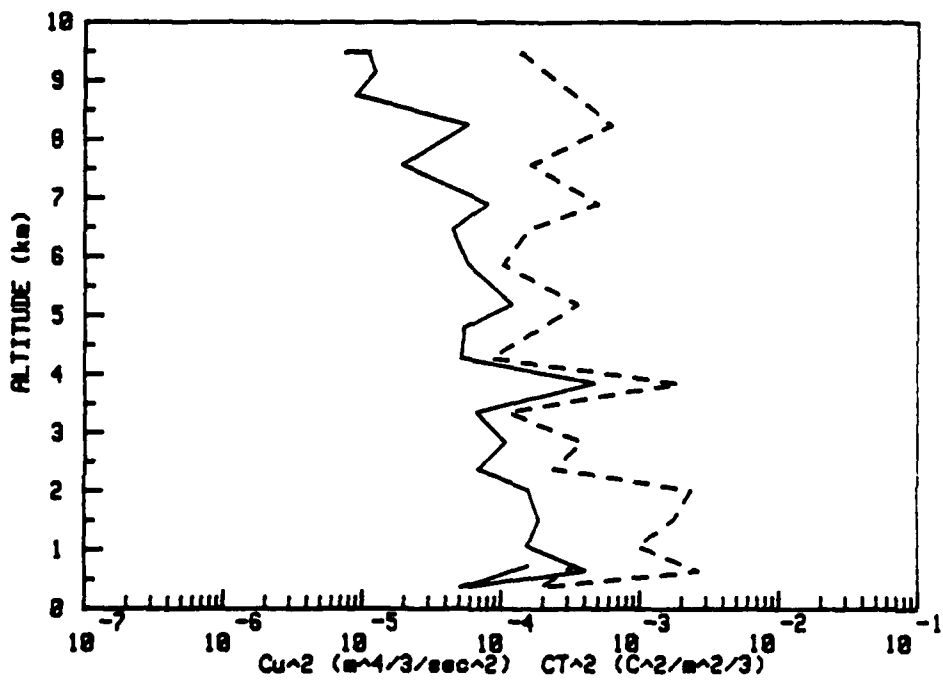
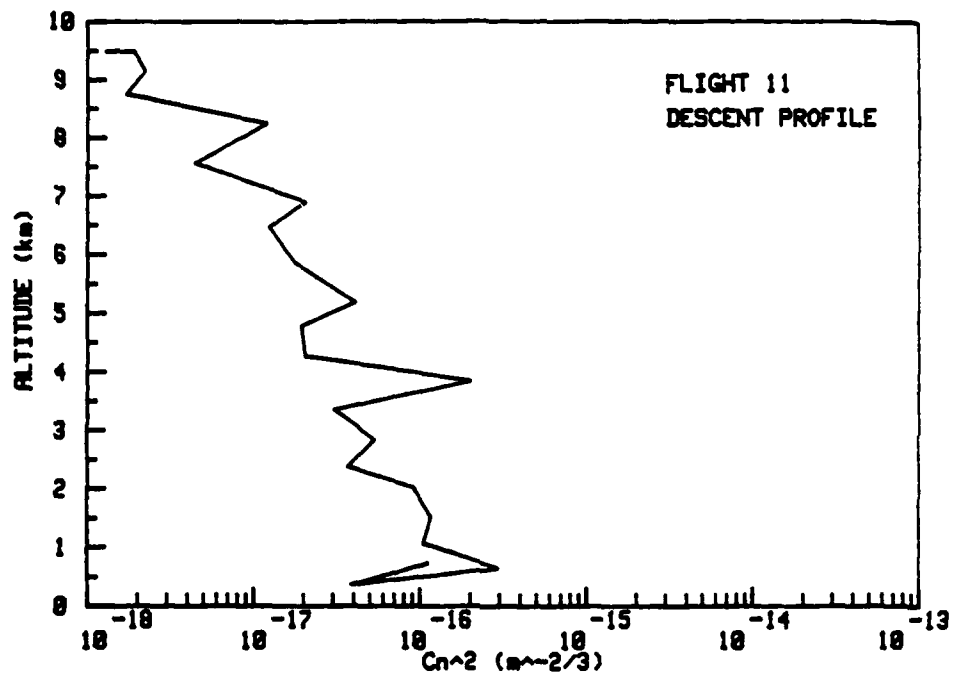


Figure 15. (continued)

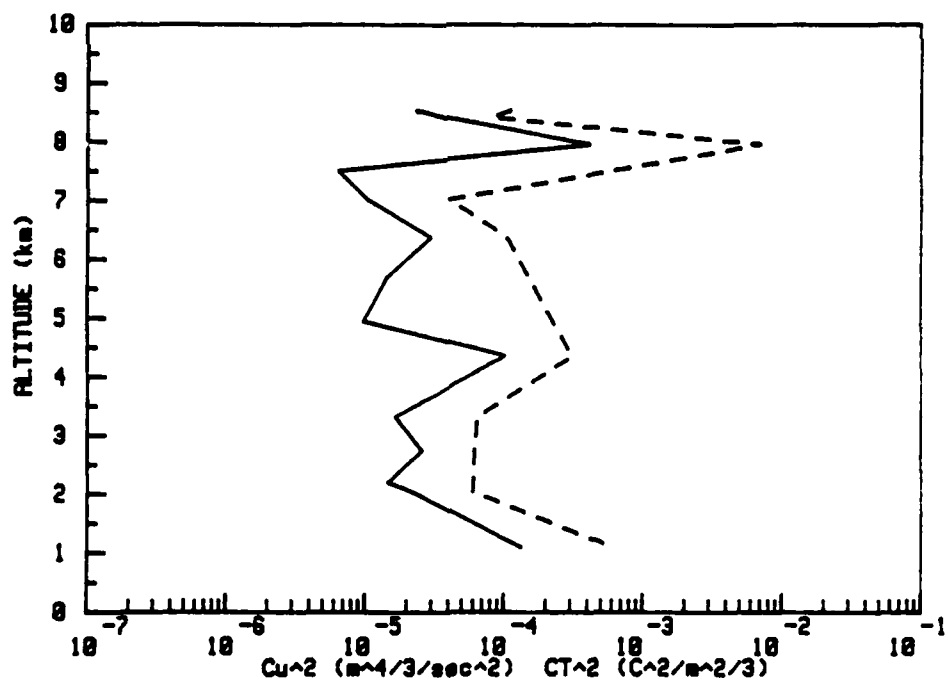
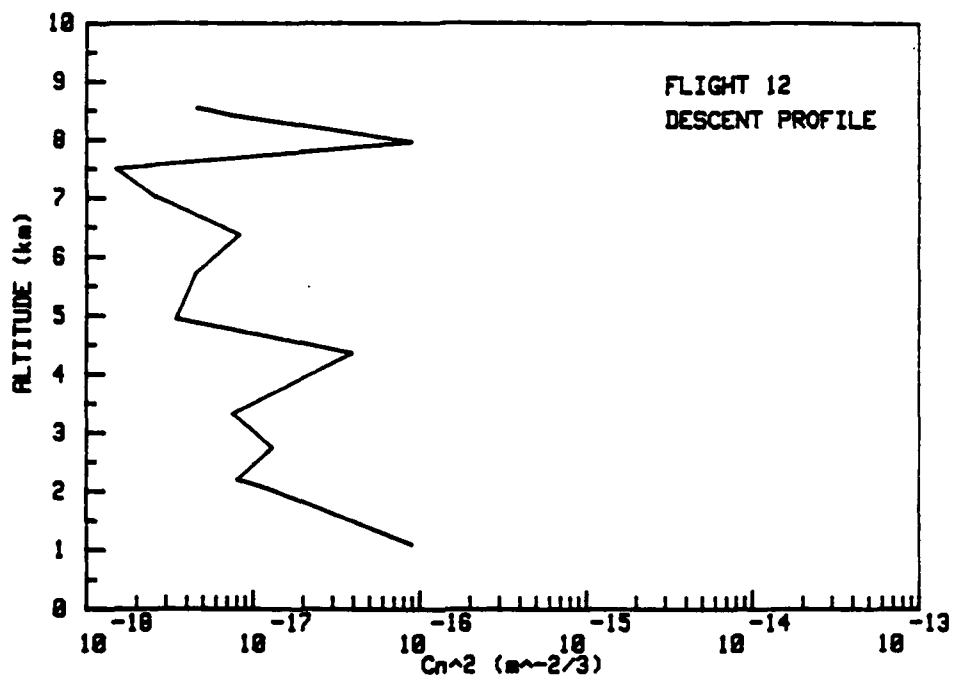


Figure 15. (continued)



Table 3.

Estimates of the height of the PBL based on the strength of the signal-to-noise ratio exhibited in the spectra.

<u>Flight</u>	PBL Height (MSL km)
2	1.3
3	2.3
4	1.5
6	2.2
7	2.2
8	2.4
9	2.2
10	2.8
11	2
12	1

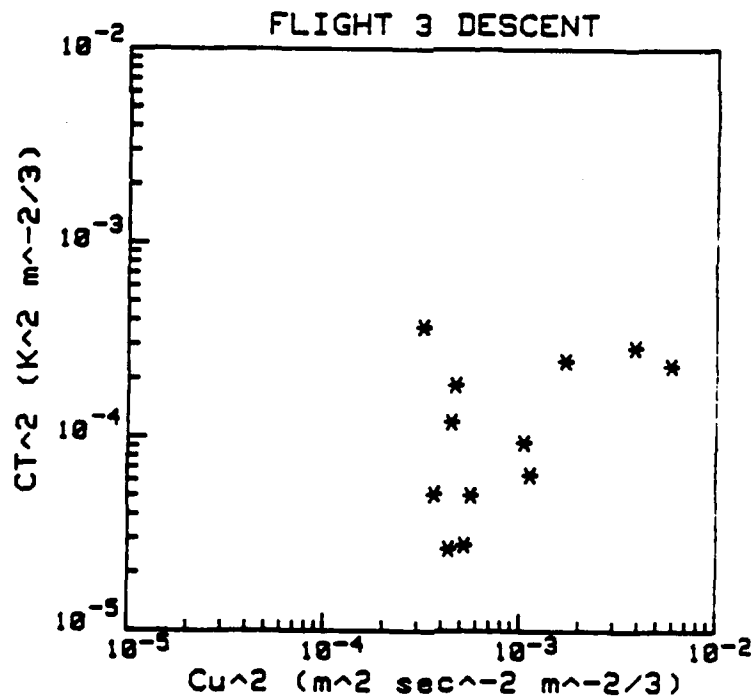
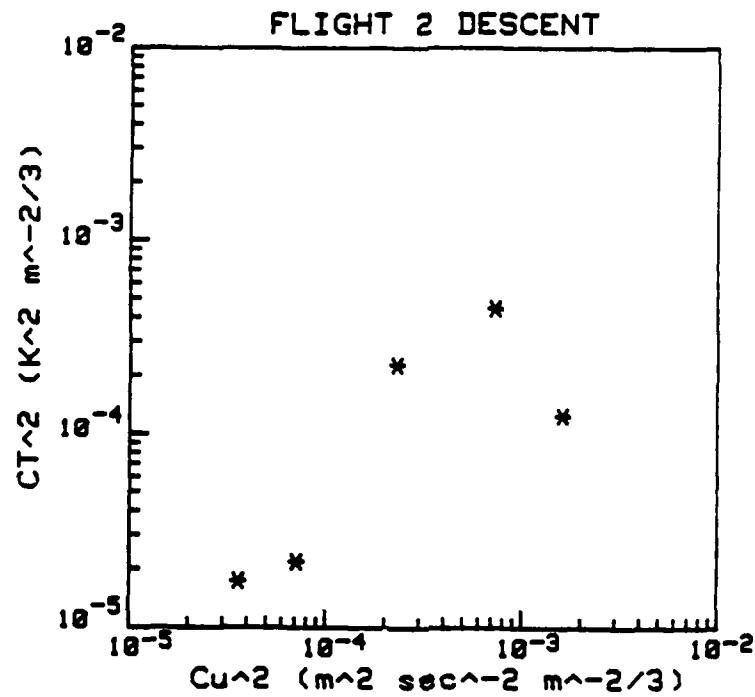


Figure 16. A comparison for each vertical flight of  $C_T^2$  versus  $C_u^2$  for spectra above the PBL. Flights 2-12 are shown (labeled above each graph).

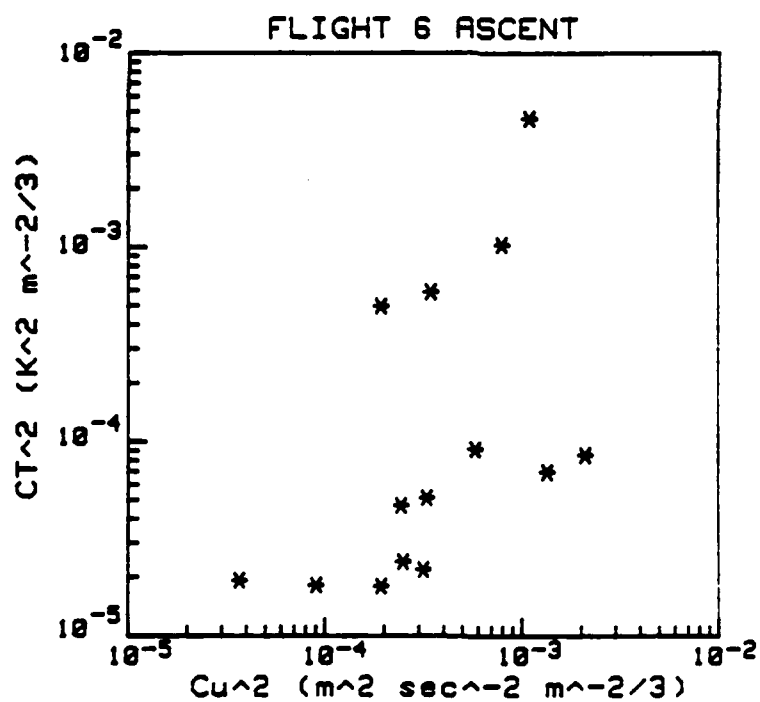
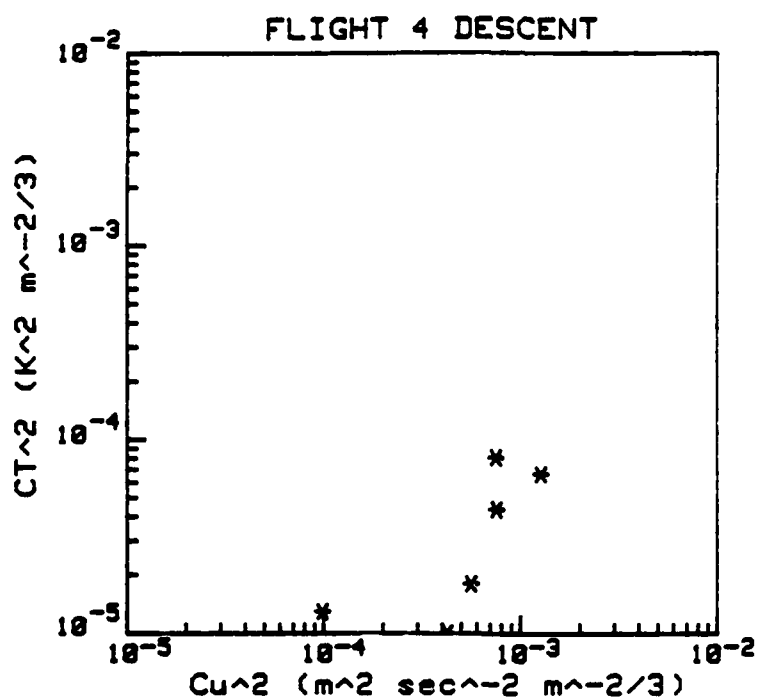


Figure 16. (continued)

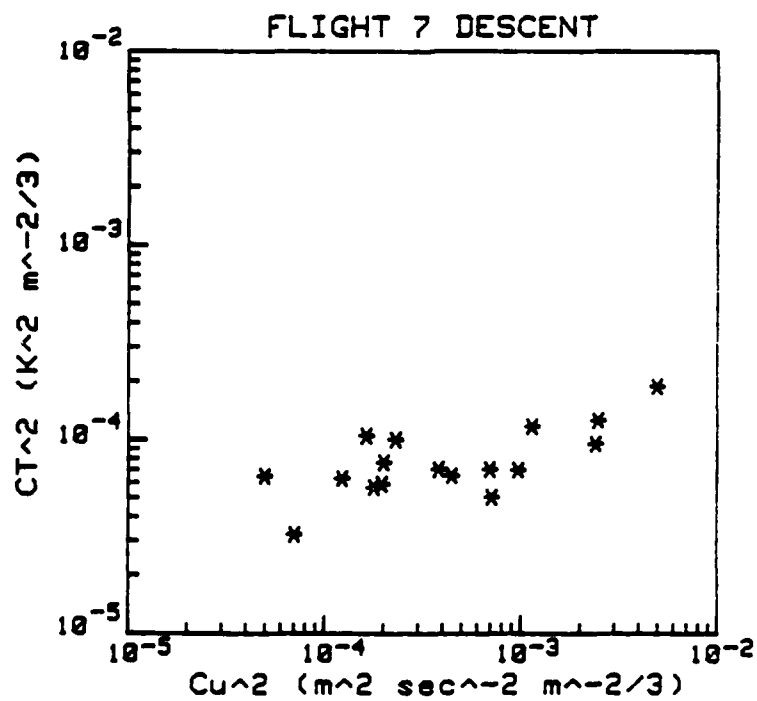
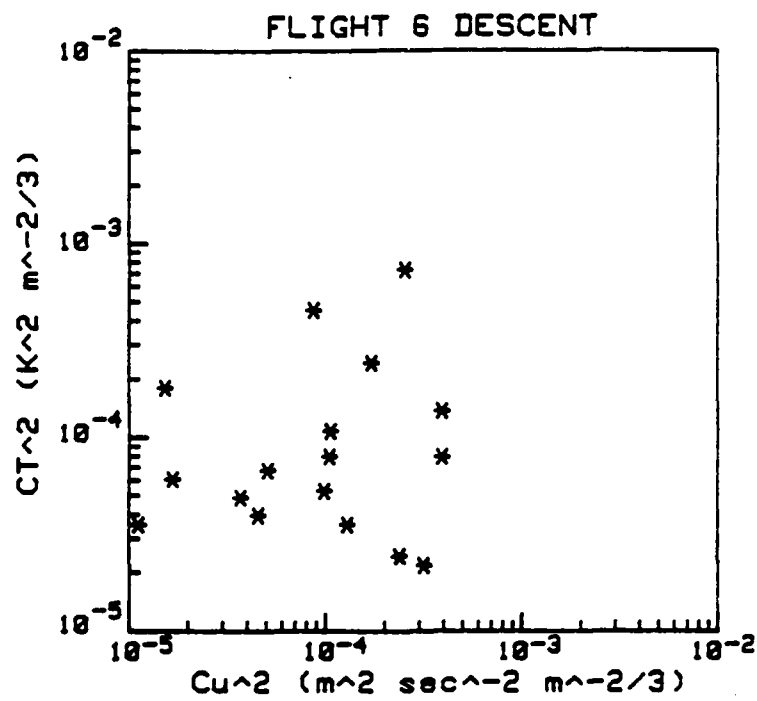


Figure 16. (continued)

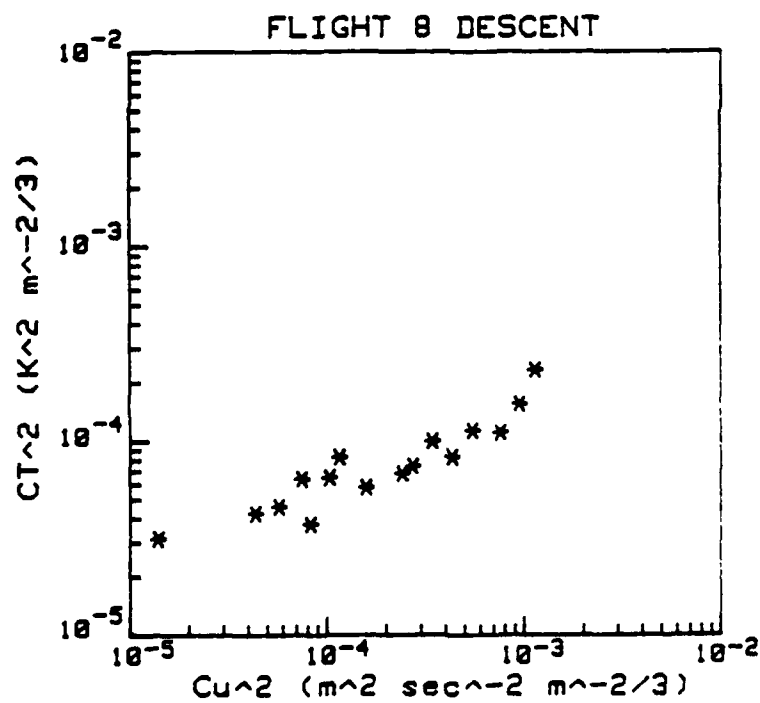
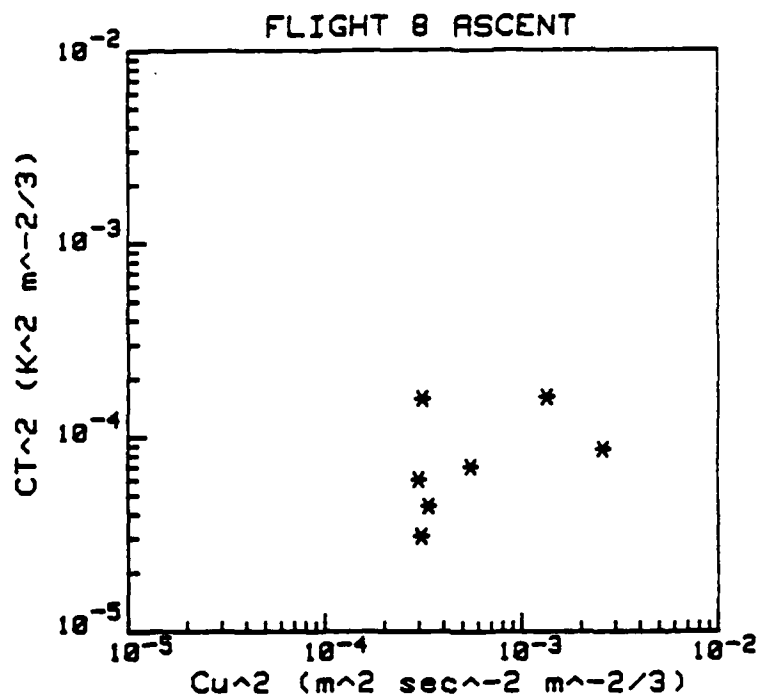


Figure 16. (continued)

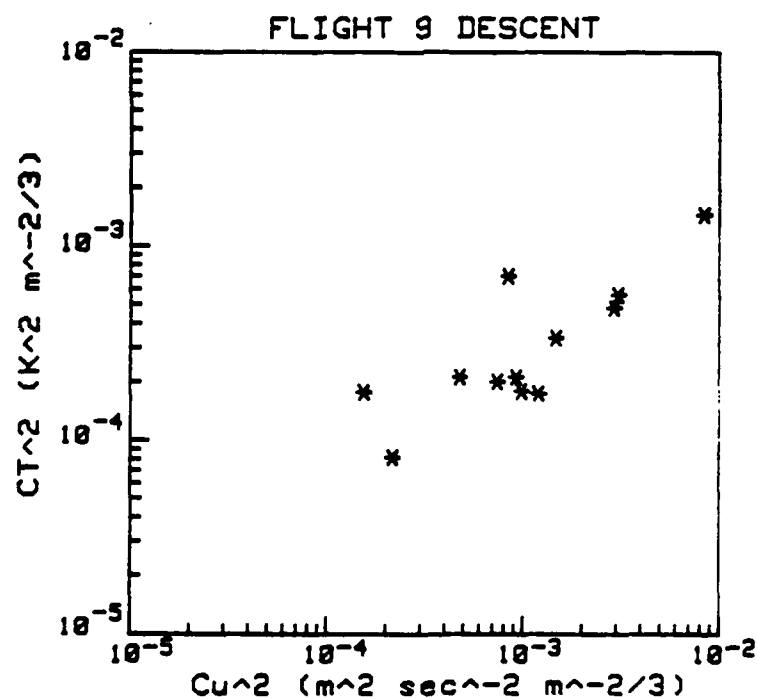
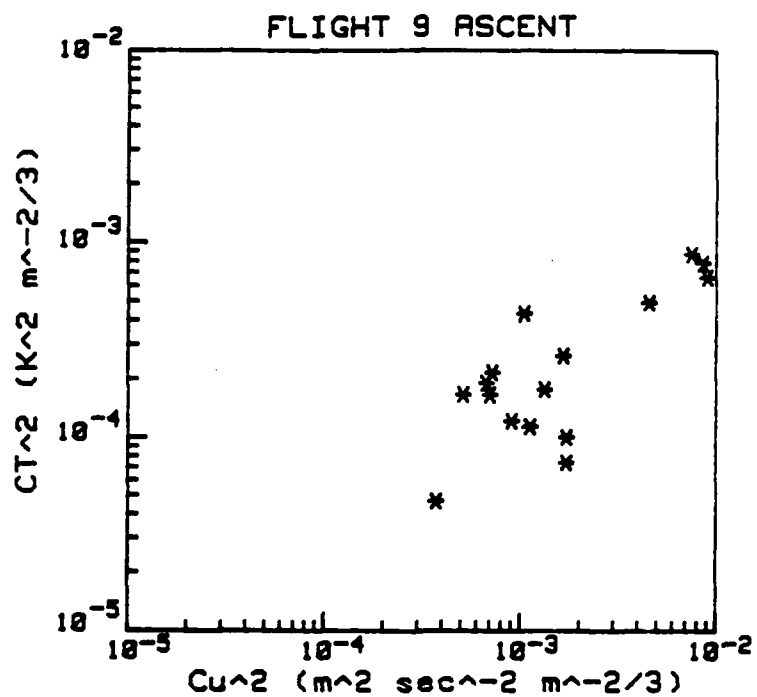


Figure 16. (continued)

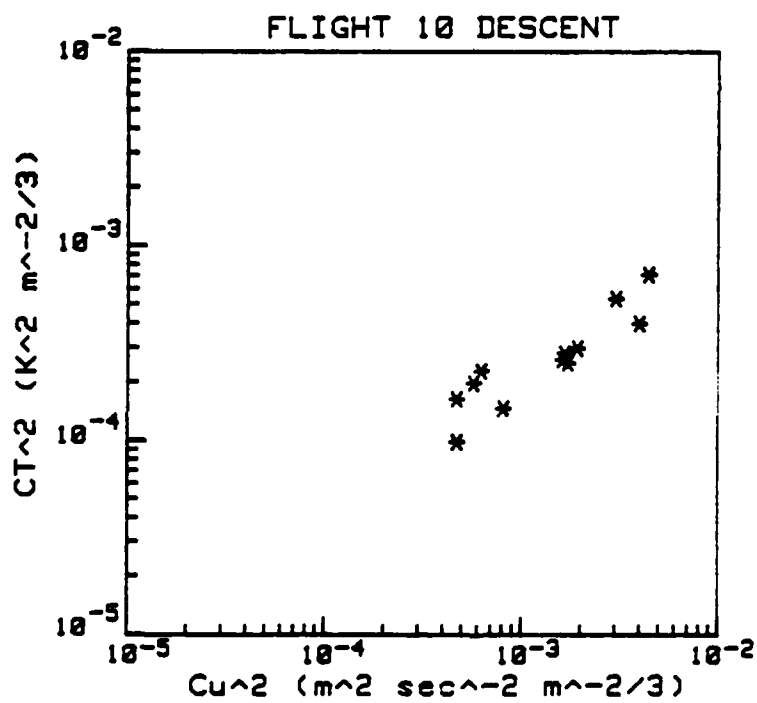
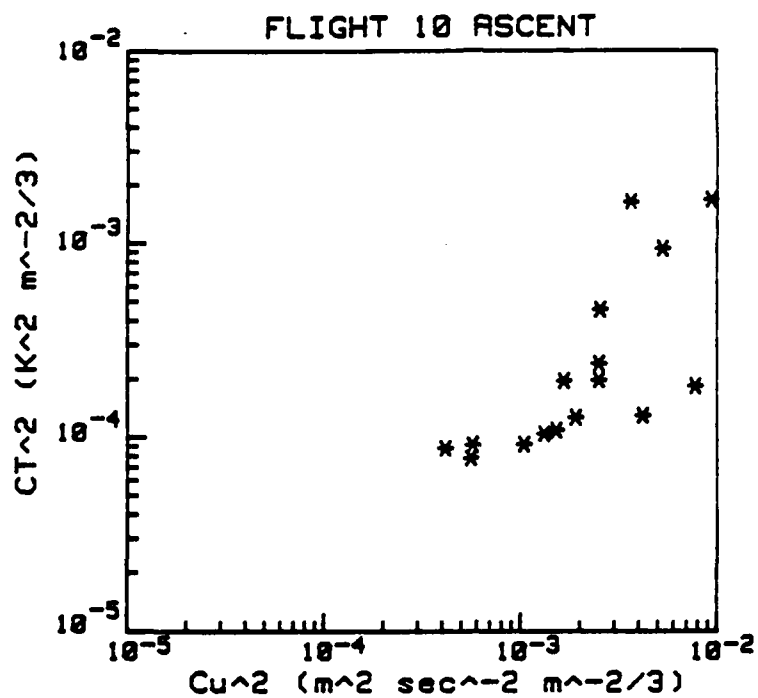


Figure 16. (continued)

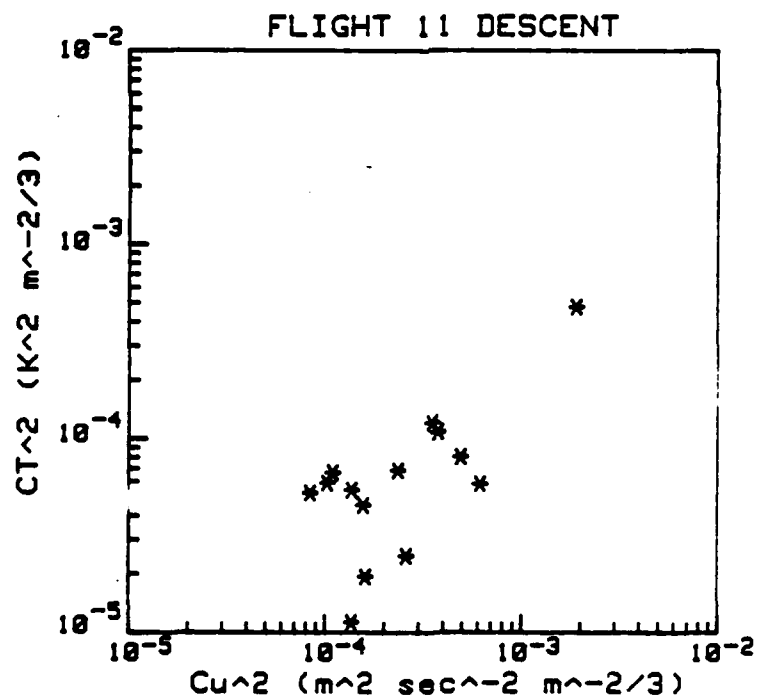
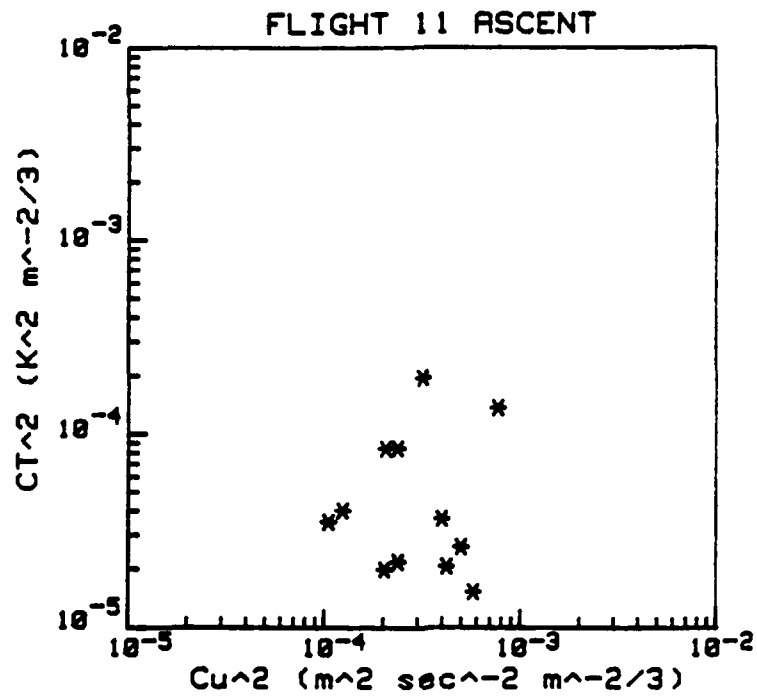


Figure 16. (continued)



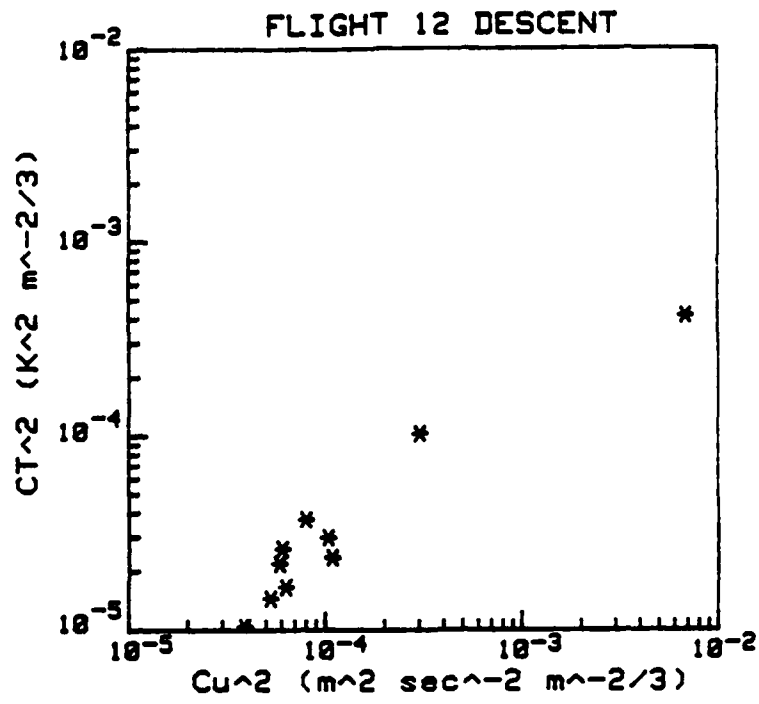


Figure 16. (continued)

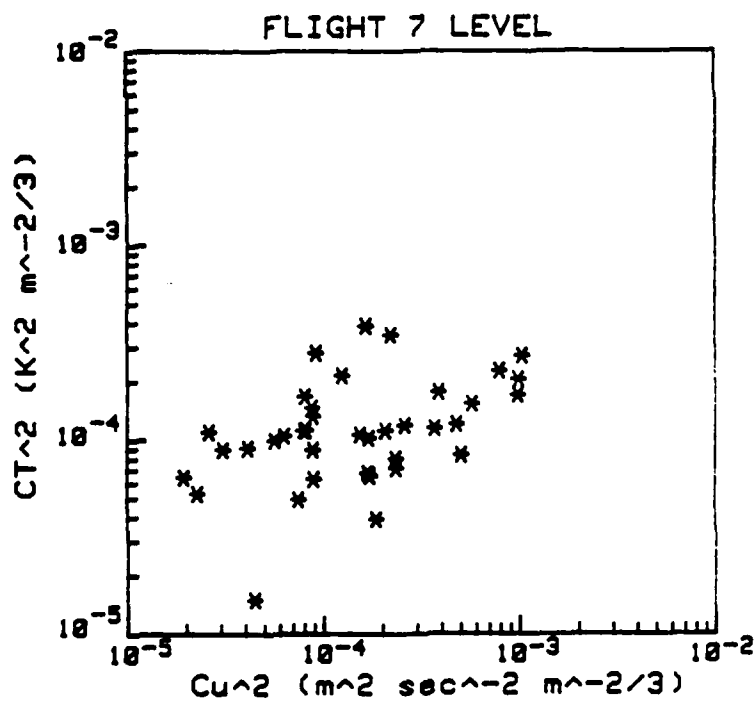
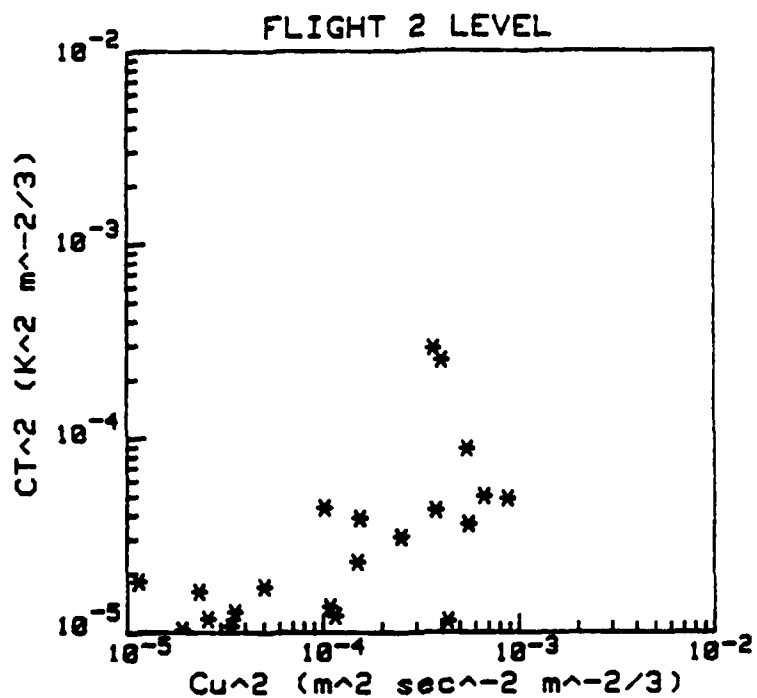


Figure 17. A comparison for each level flight of  $C_T^2$  versus  $C_u^2$  for spectra above the PBL. Flights 2, 7, 11, and 12 are shown (labeled above each graph).

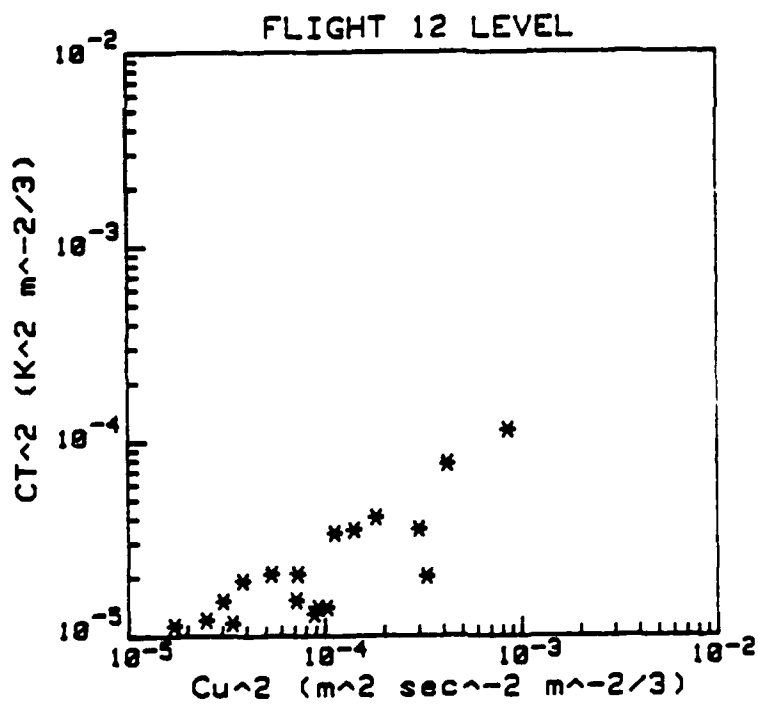
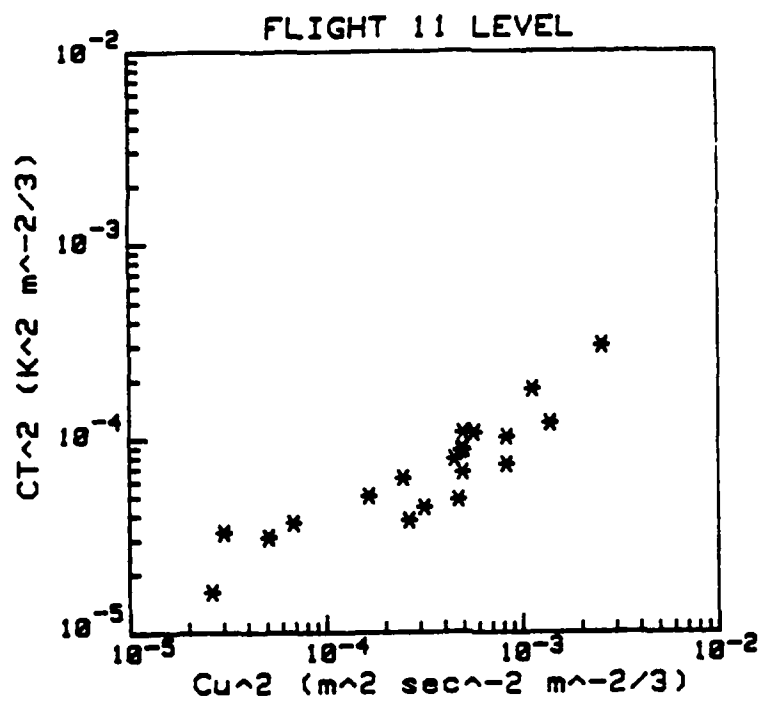
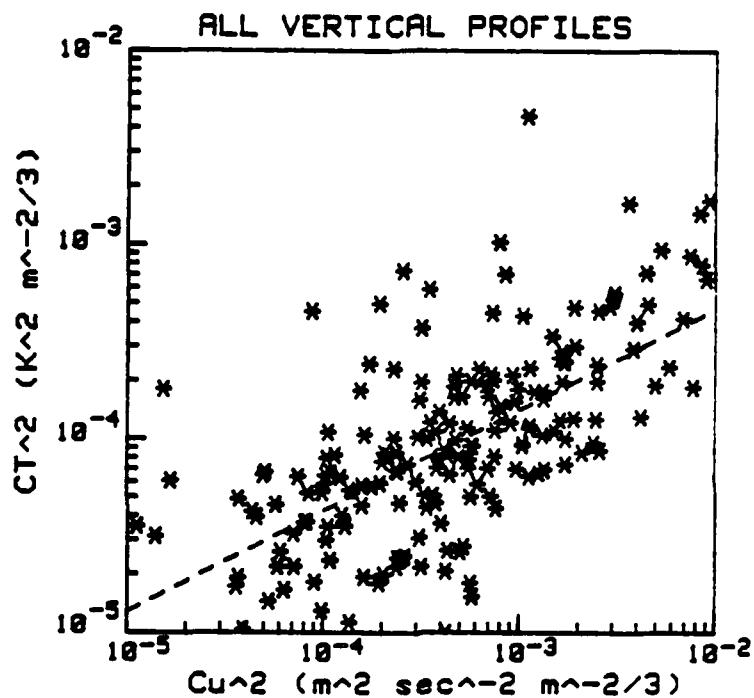


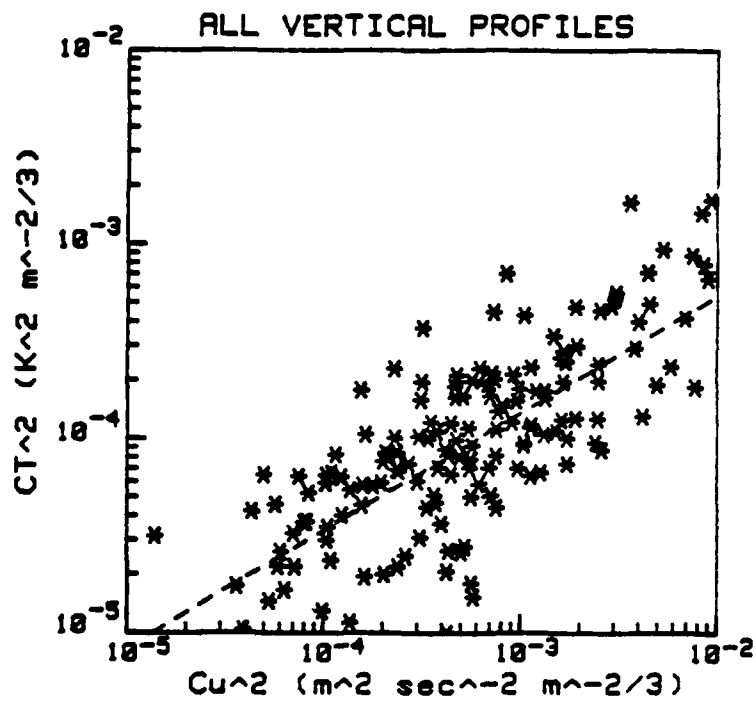
Figure 17. (continued)



Slope = .520

Correlation Coefficient = .647

Figure 18. A composite comparison of  $C_T^2$  versus  $C_u^2$  for all vertical profiles. The broken line represents a regression analysis. Slope and correlation coefficient are given below each graph.



Excluding flight 6  
Slope = .605  
Correlation Coefficient = .749

Figure 18. (continued)

increased correlation of the entire data base (Figure 18). The slope for all the vertical profiles was close to 3/5. Correlation and slope for all the level flights showed approximately the same scatter (correlation) and slope as the vertical profiles (Figure 19).

In Figure 20,  $C_T^2$  was plotted versus  $C_u^2$  multiplied by

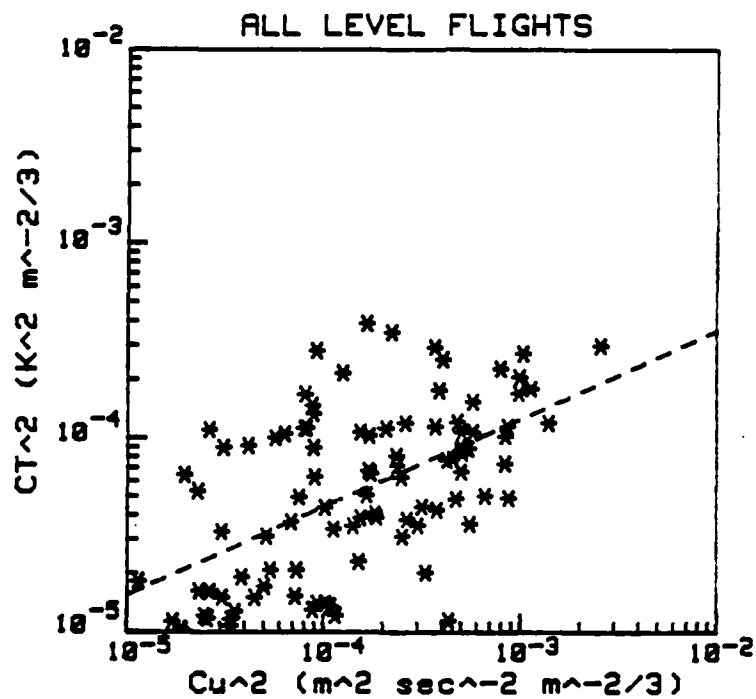
$$\theta/g (\partial\theta/\partial z) = T/g (\partial T/\partial z + \Gamma) \quad (7.1)$$

for all vertical flights (having associated temperature profiles). Again, flight 6 had high scatter and flight 7 showed little slope. A combined plot of all flights showed slightly higher correlation without flight 6 and again roughly a slope of 3/5 (Figure 20). This ratio corresponds to values of  $1.6 R_i / (P_r - R_i)$  that range from 0.3 for high values of  $C_T^2$  to as much as 10 for low values of  $C_T^2$ .

As an additional comparison,  $C_T^2 / (C_u^2 \theta/g \partial\theta/\partial z)$  was plotted against a turbulence activity parameter (Gregg 1987),  $\epsilon/\nu N$  (Figure 21).  $N$  was calculated as  $g \partial \ln \theta / \partial z$  from a polynomial fit to the aircraft potential temperature profile. The formula used to derive kinematic viscosity was taken from the U. S. Standard Atmosphere Supplements, 1966 (Environmental Science Services Administration et al. 1966).

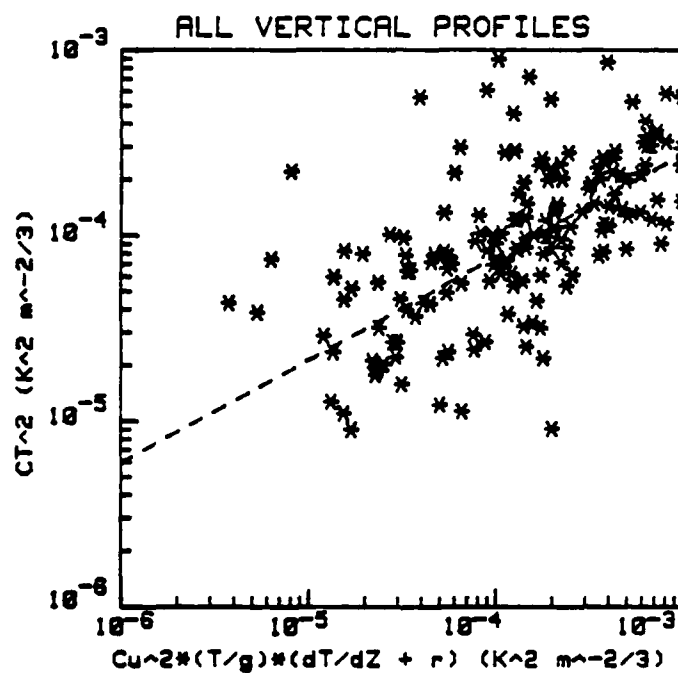
$$\mu = (\beta T^{3/2}) / (T + S) \quad (7.2)$$

where  $\mu$  is the dynamic viscosity,  $\beta = 1.458E-6 \text{ kg sec}^{-1} \text{ m}^{-1} \text{ K}^{-1/2}$ , and  $S = 110.4$  Kelvin. Kinematic viscosity,  $\nu$ , equals  $\mu/\rho$ . Density was calculated as  $\rho = \rho_0 \exp(-Z/8 \text{ km})$  where  $\rho_0$  is  $1.225 \text{ kg m}^{-3}$ .  $T$  was taken from the aircraft profiles.  $C_T^2$ ,  $C_u^2$ ,  $\epsilon$ , and  $N$



Slope = .454  
Correlation Coefficient = .571

Figure 19. A composite comparison of  $C_T^2$  versus  $C_u^2$  for all level profiles. The broken line represents a regression analysis. Slope and correlation coefficient are given below each graph.

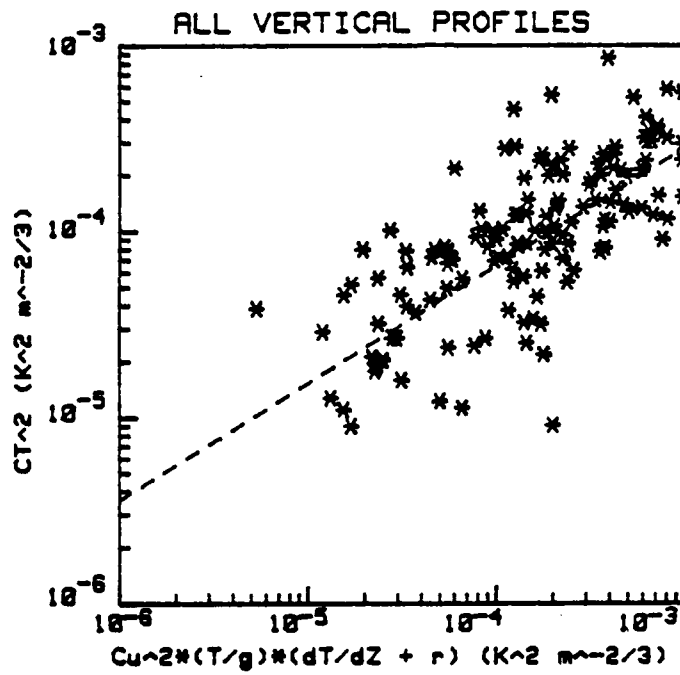


Slope = .554

Correlation Coefficient = .703

Figure 20. A composite comparison of  $C_T^2$  versus  $C_u^2$  normalized by the expression  $[T/g (\partial T/\partial Z + \Gamma)]$ . The broken line represents a regression analysis. Slope and correlation coefficient are given below each graph.





Excluding flight 6  
Slope = .630  
Correlation Coefficient = .797

Figure 20. (continued)

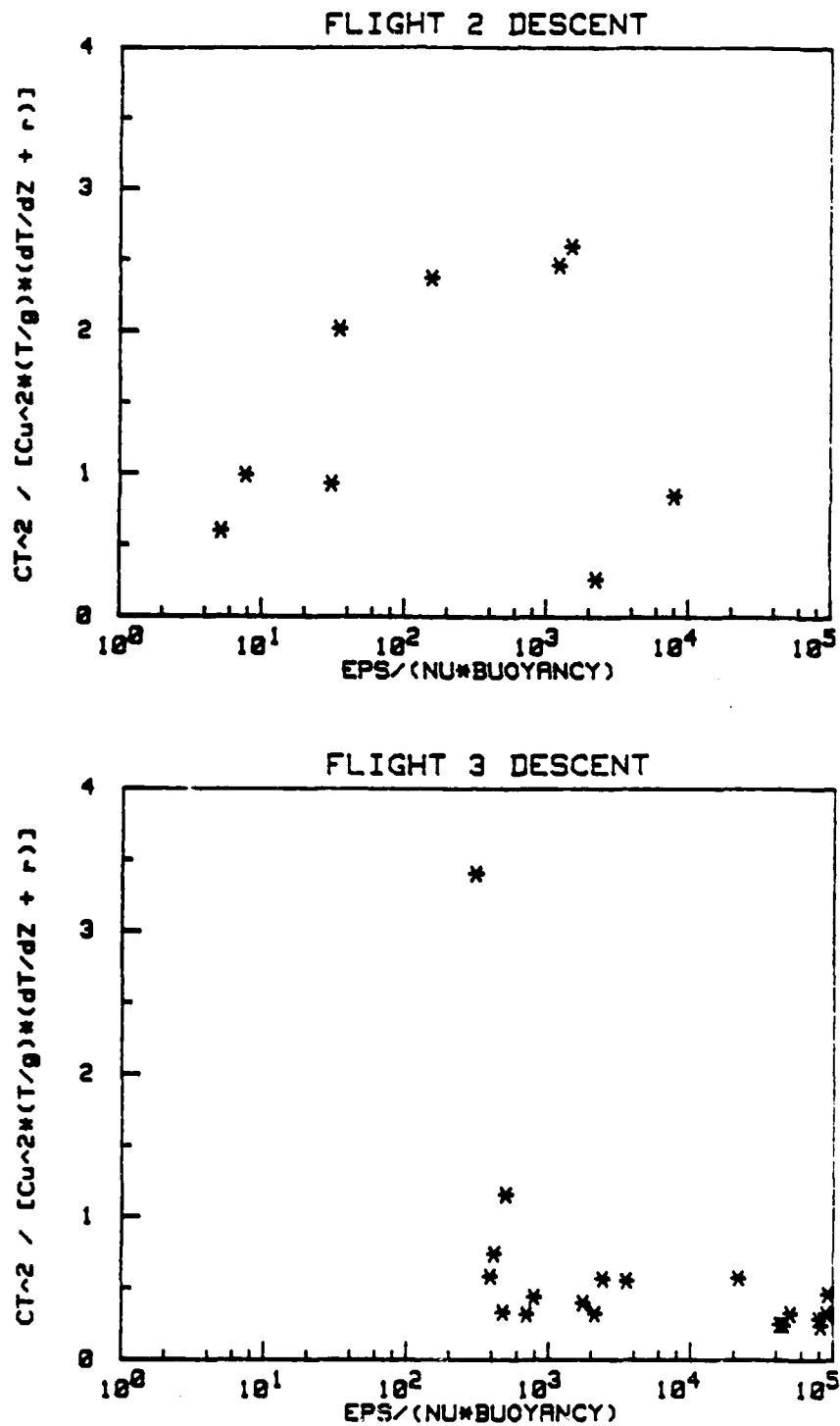


Figure 21. Comparison for each vertical profile of  $C_T^2$  divided by  $C_u^2$  normalized as in Figure 20 versus a turbulent activity parameter,  $\epsilon/(\nu N)$ . Flights 2-12 are shown (labeled above each graph).

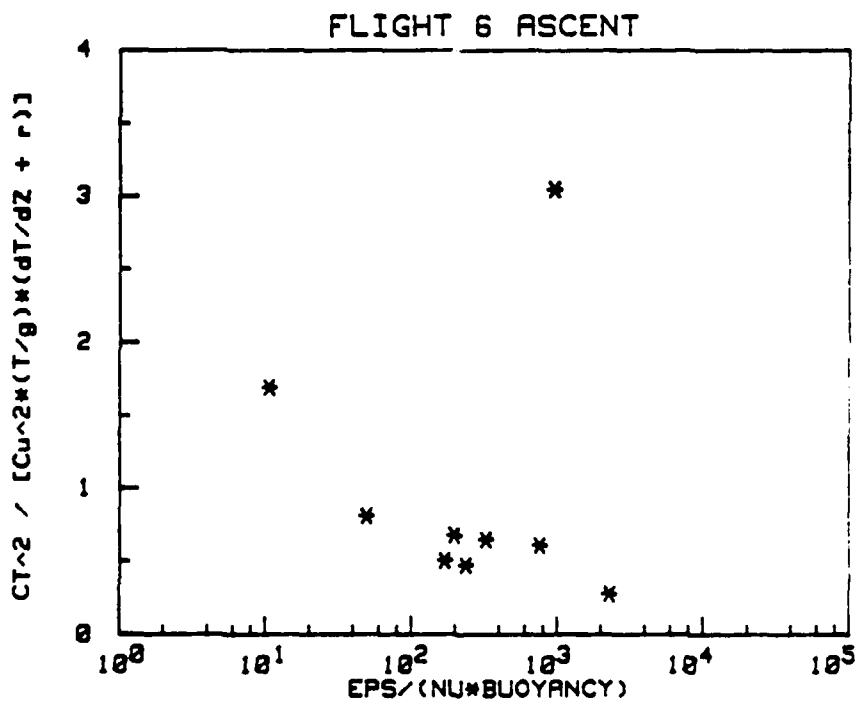
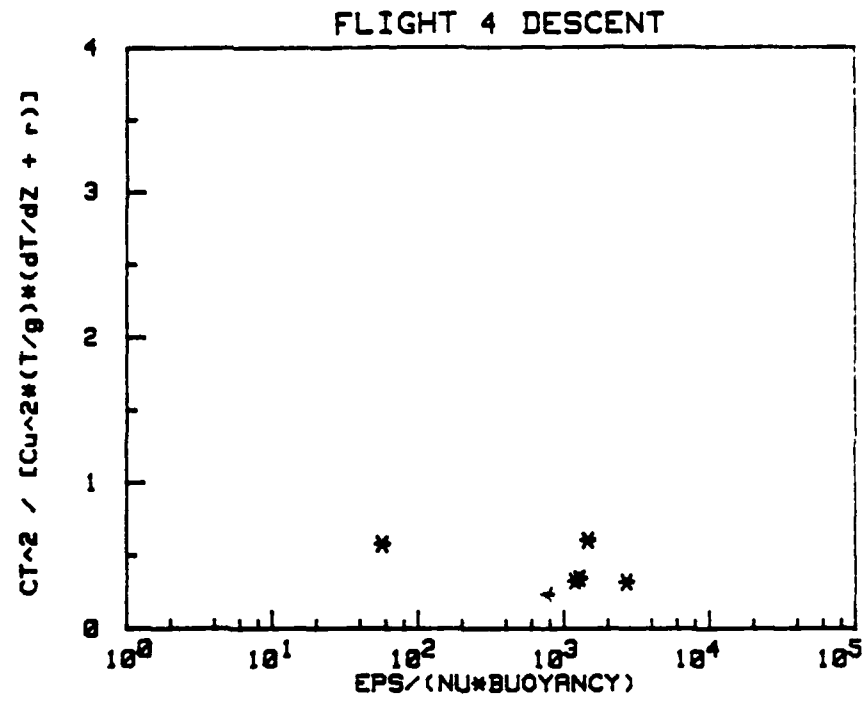


Figure 21. (continued)

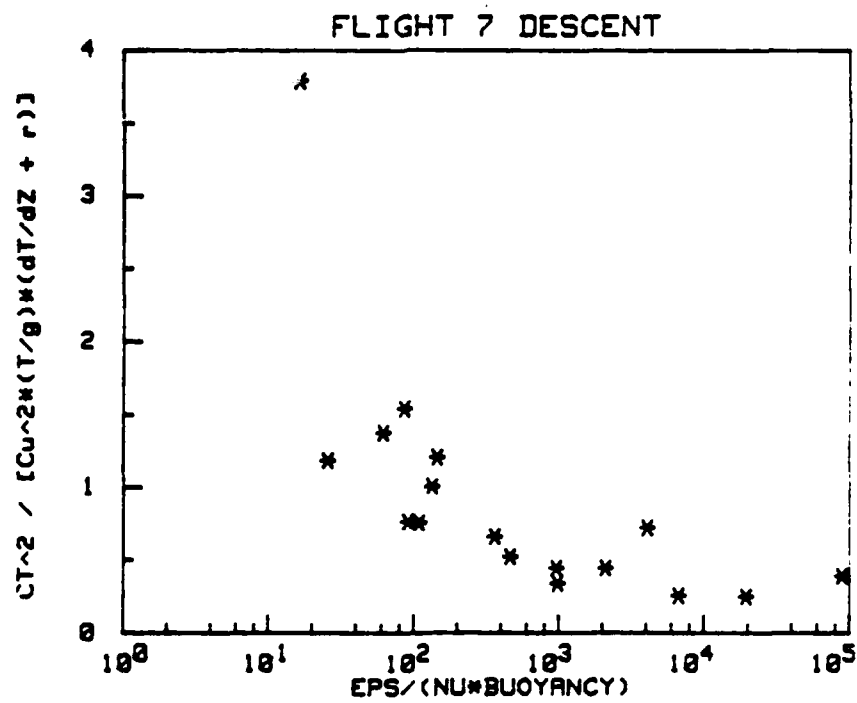
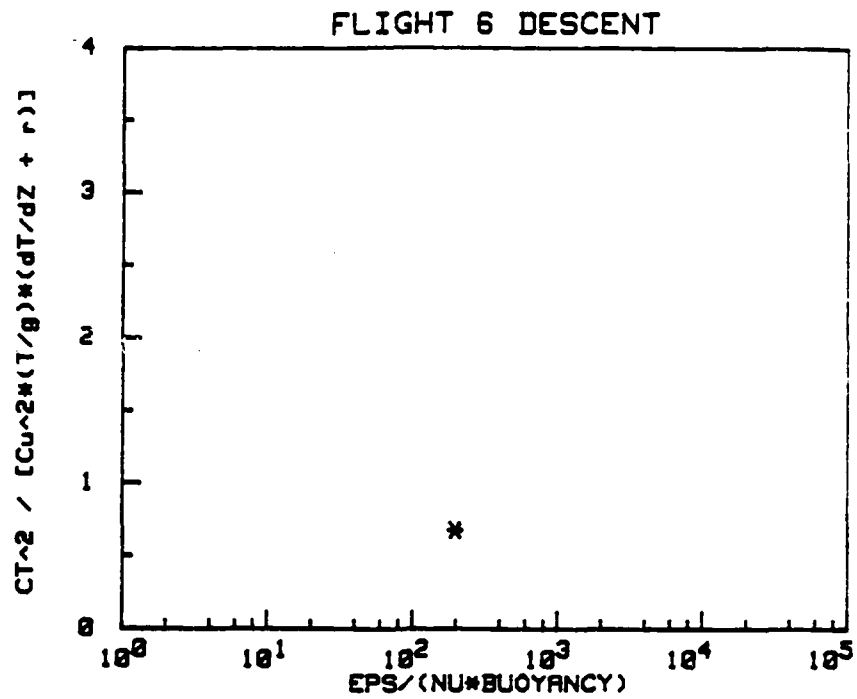


Figure 21. (continued)

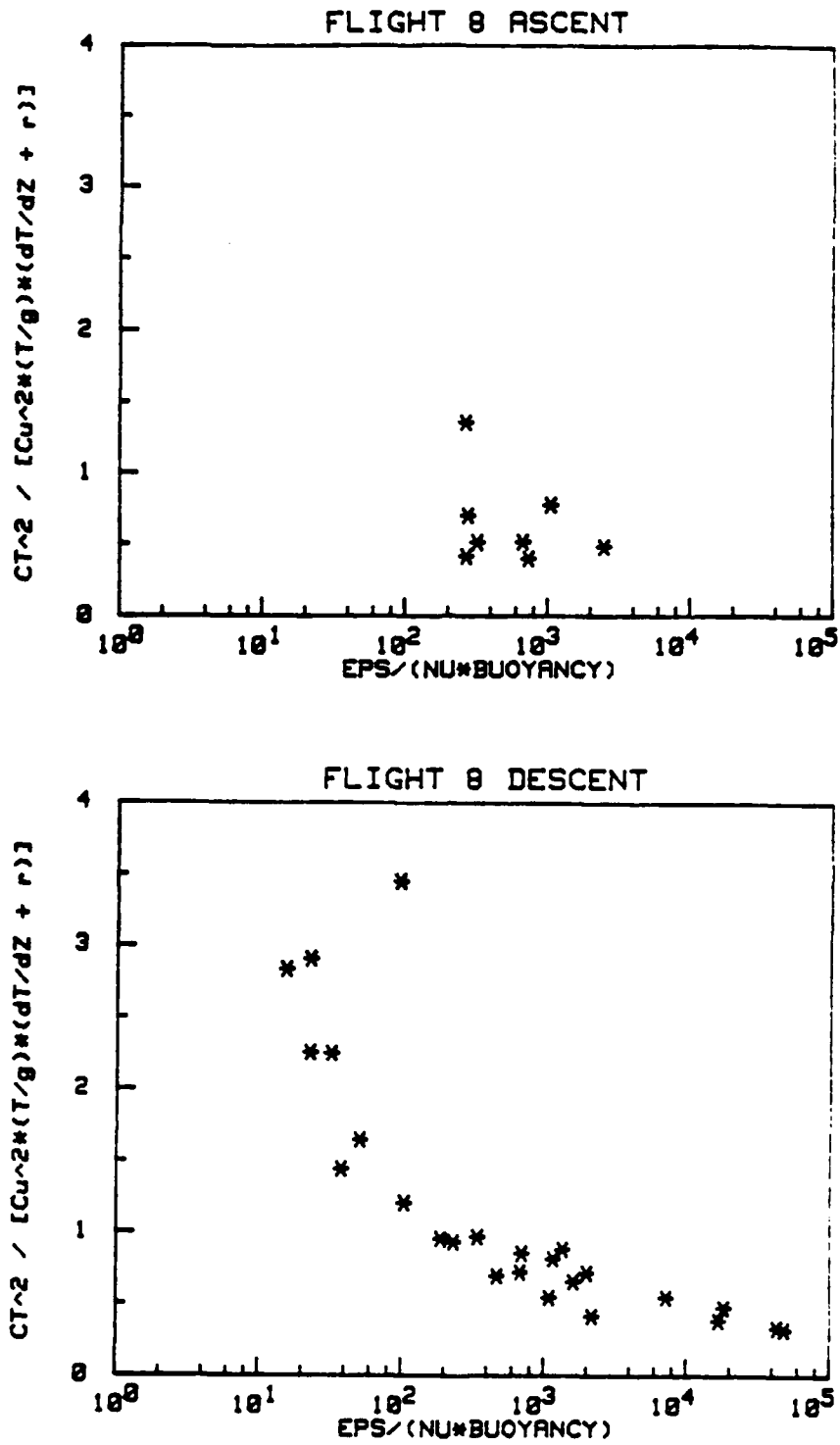


Figure 21. (continued)

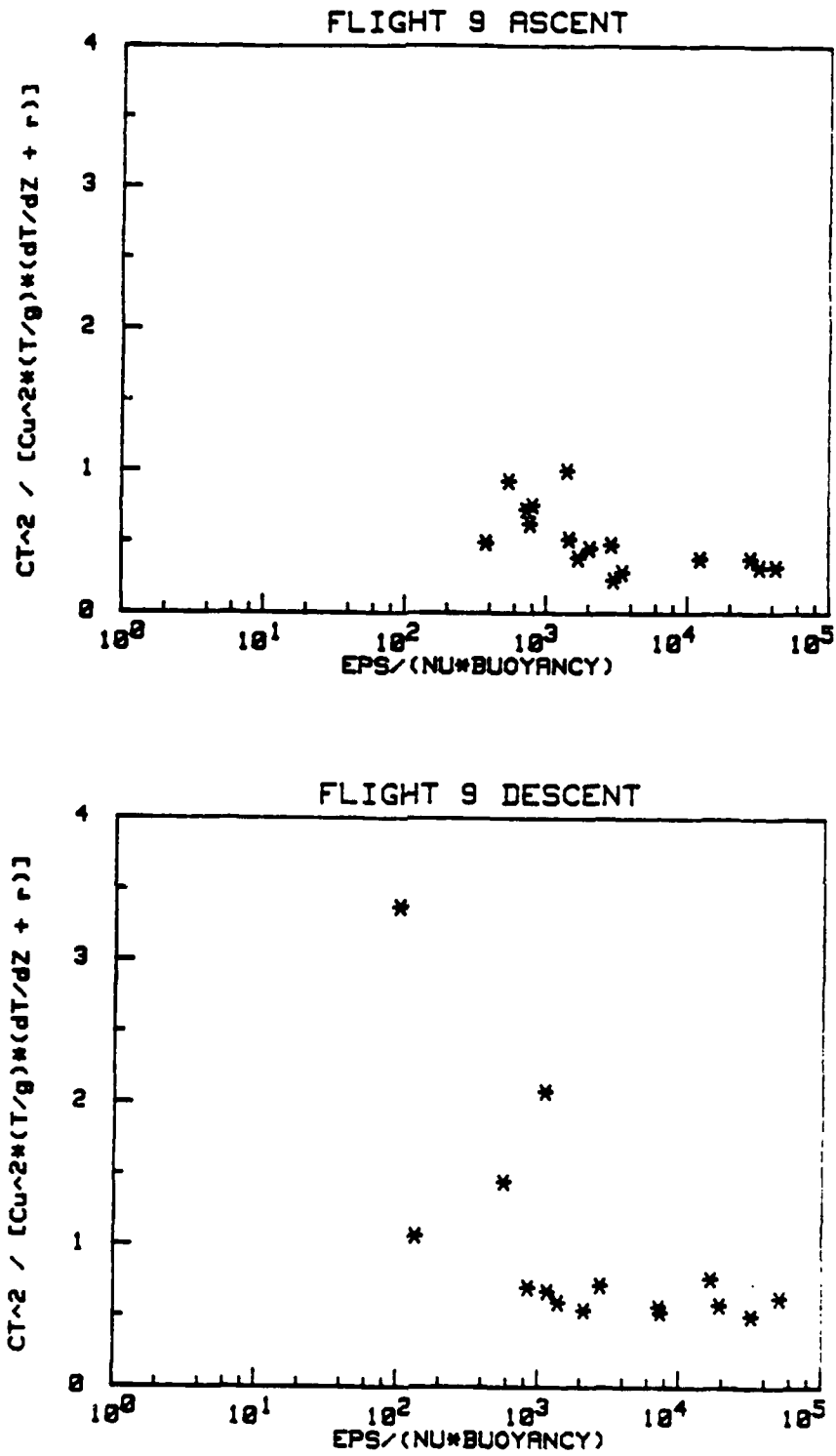


Figure 21. (continued)

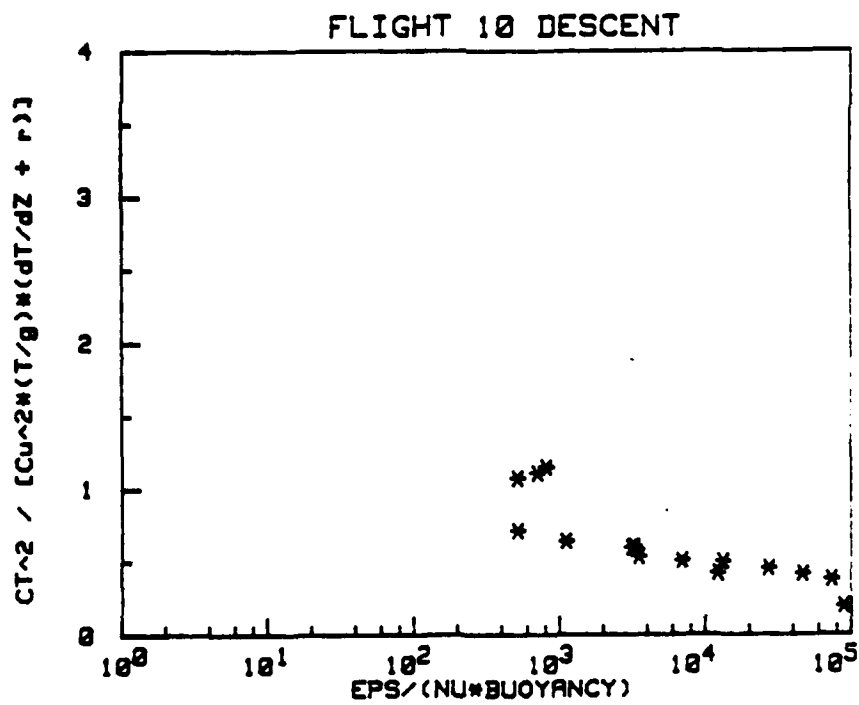
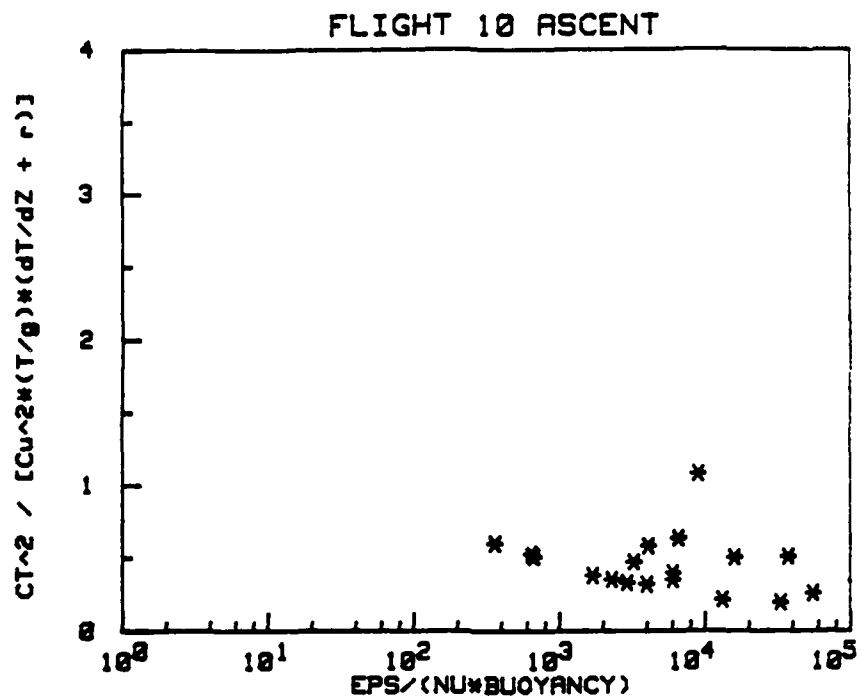


Figure 21. (continued)

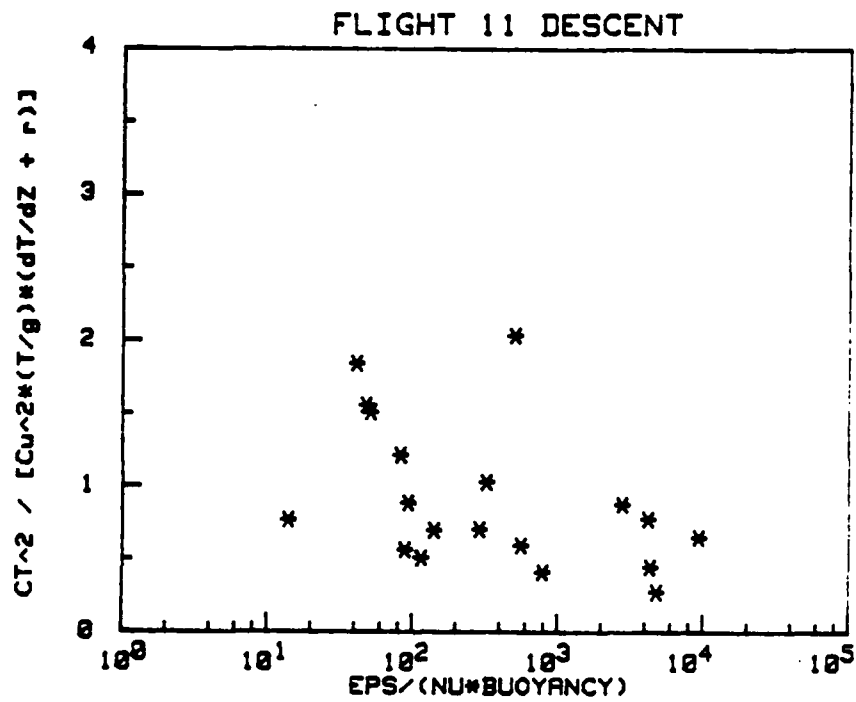
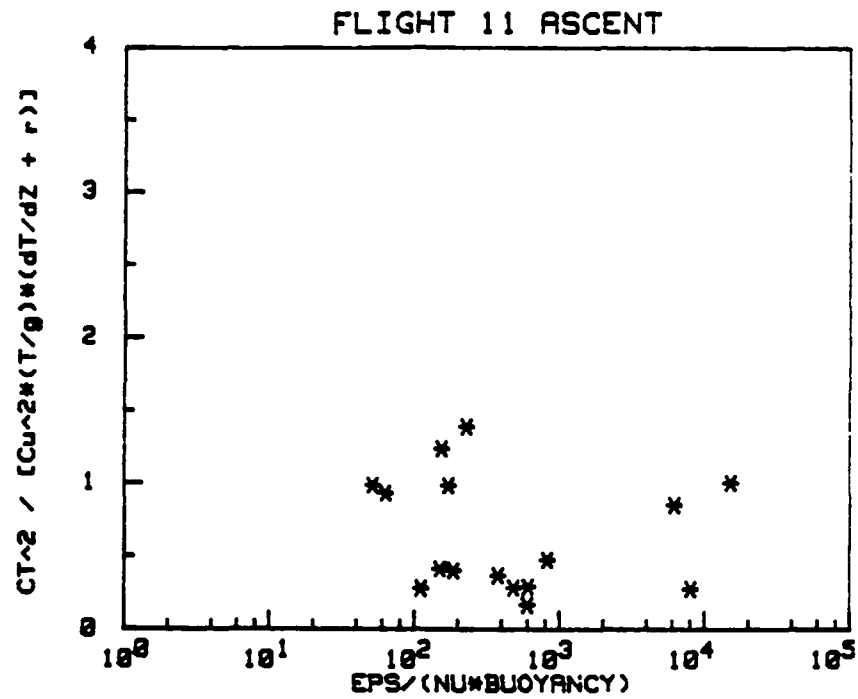


Figure 21. (continued)



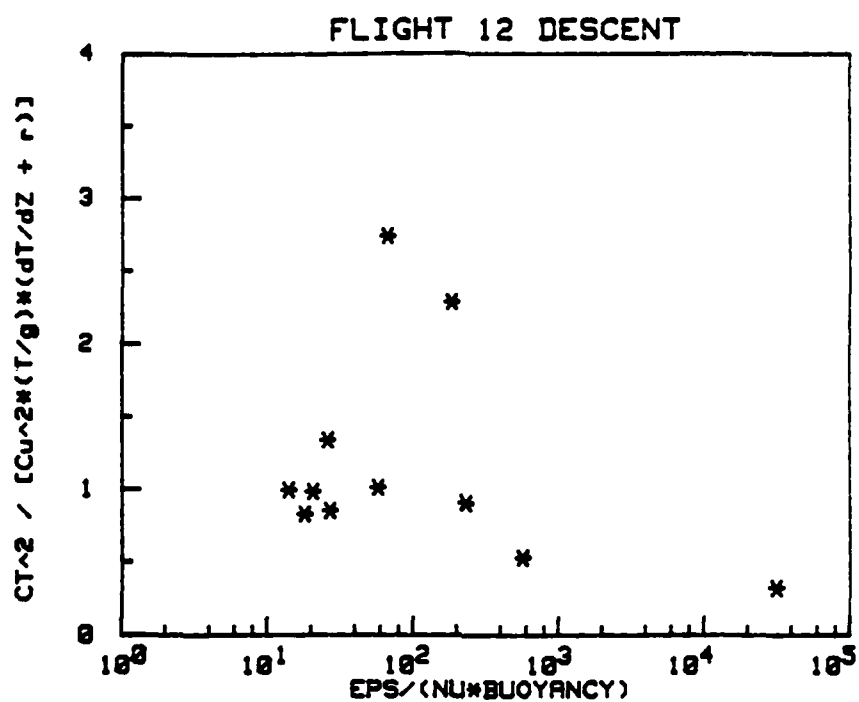


Figure 21. (continued)

were all calculated from the aircraft data. Figure 22 is a composite of all vertical flights. This plot clearly shows that as turbulence activity goes down, the ratio of  $C_T^2$  to normalized  $C_u^2$  goes up. For activity values above  $10^2$ , the  $C_T^2/C_u^2(\text{norm})$  ratio becomes constant at about 0.4.

## 7.2 Mean Gradients and Richardson Number

Next, the Richardson number was evaluated. Since VanZandt et al. (1981) defined  $R_i$  as  $N/S$ ,  $N$  versus  $S$  was plotted, thus showing Richardson number as a slope (Figure 23).  $N$  was calculated by a finite difference derivative between each level in the digitized aircraft potential temperature profiles, while  $S$  was calculated by finite difference from the profiler hourly average taken during the time the aircraft was collecting data (Table 1).  $S$  was calculated as  $(\partial u/\partial z)^2 + (\partial v/\partial z)^2$ . Figure 24 is a composite of all flights shown in Figure 23. Most values show  $R_i > 0.25$  above the broken line, with the shear term on the order of  $10^{-5}$  and the buoyancy term ranging from  $10^{-5}$  to  $4 \times 10^{-4}$ . Richardson number profiles for each flight were directly calculated (Table 4), and then averaged (Table 5).

These values of  $N$  and  $S$  are the necessary input parameters for the VanZandt et al. model which was used to predict vertical profiles of  $C_n^2$  and  $\epsilon$ . This was done for each flight conducted at Penn State where profiler data was available (Figure 25). The model output is normalized optical  $C_n^2$ . Standard pressure calculated from the geometric height and the aircraft temperature profile were used to

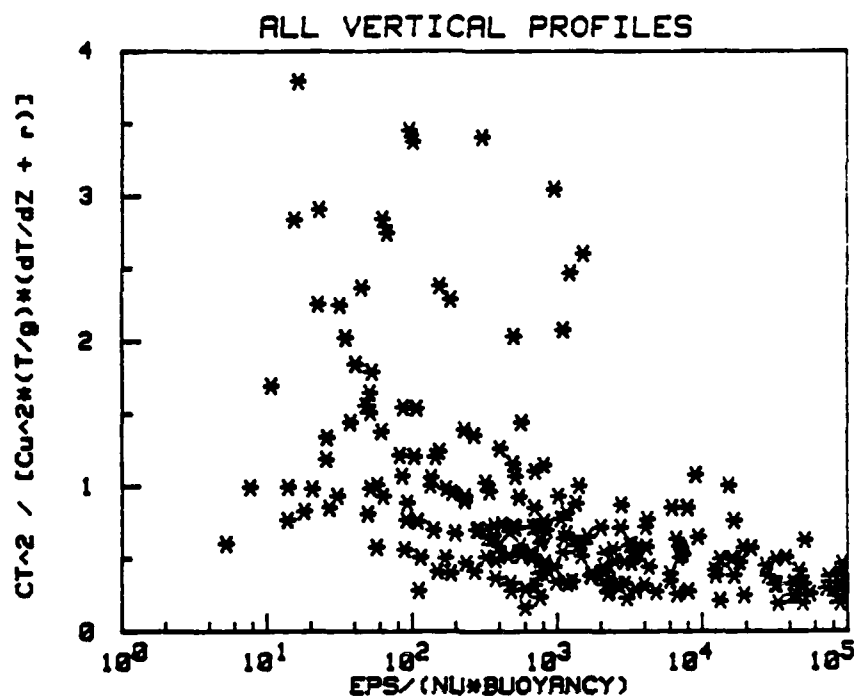


Figure 22. A composite comparison of  $C_T^2$  divided by  $C_u^2$  normalized as in Figure 20 versus a turbulent activity parameter  $\epsilon/(\nu N)$  for all vertical profiles.

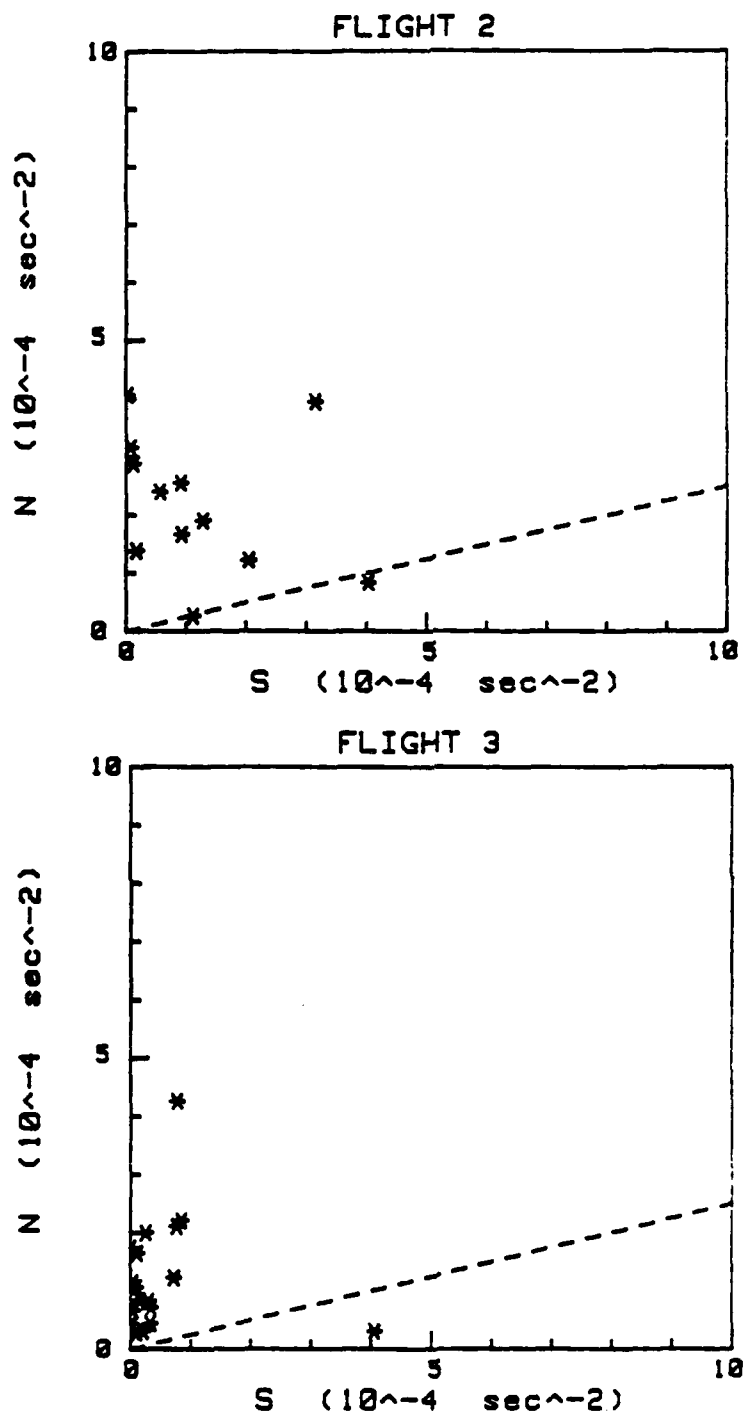


Figure 23. Comparisons of the VanZandt et al. parameters  $N$ , the Brunt-Vaisala frequency squared, and  $S$ , the shear squared. Comparison is shown for each vertical aircraft flight during which the radar operated (labeled above each graph).  $N$  was calculated using aircraft potential temperature profiles and  $S$  was calculated using radar wind profiles. Note units. Broken line represents  $R_i = 0.25$ .

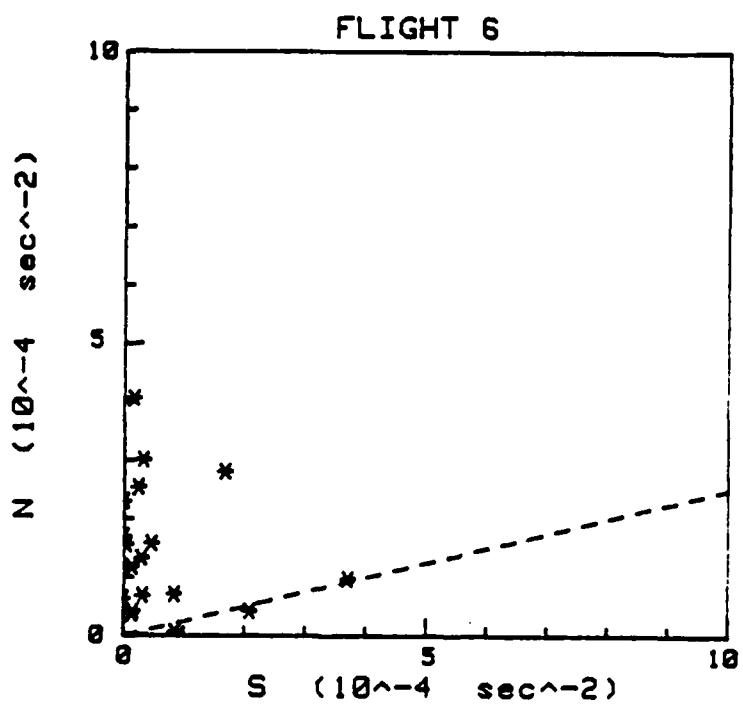
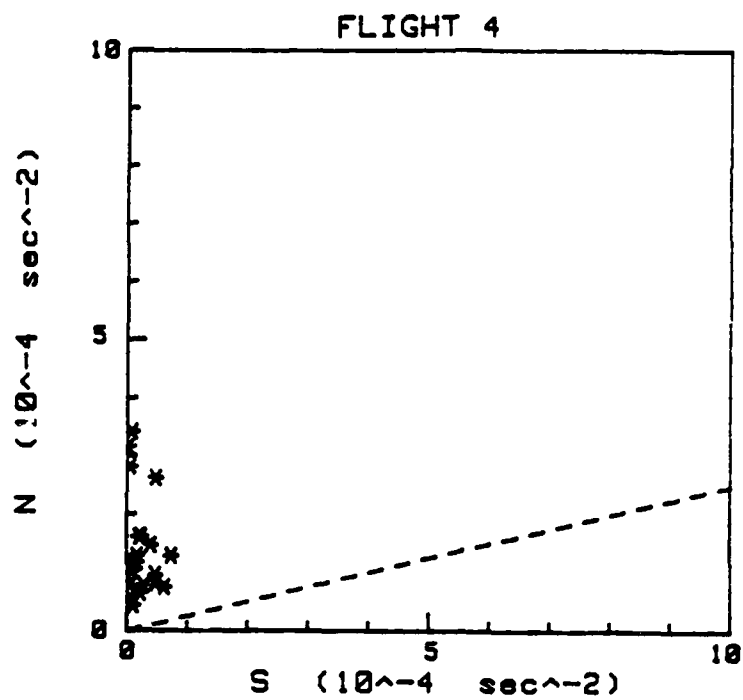


Figure 23. (continued)

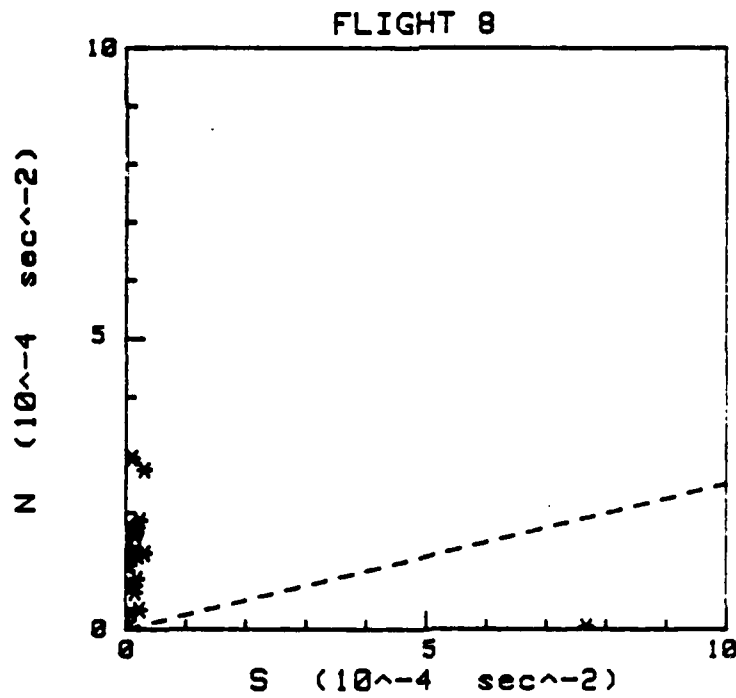
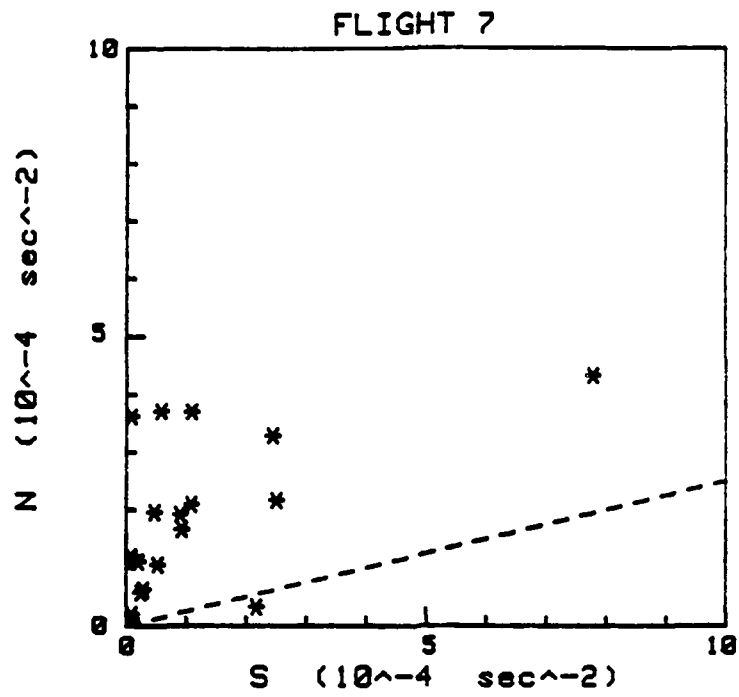


Figure 23. (continued)

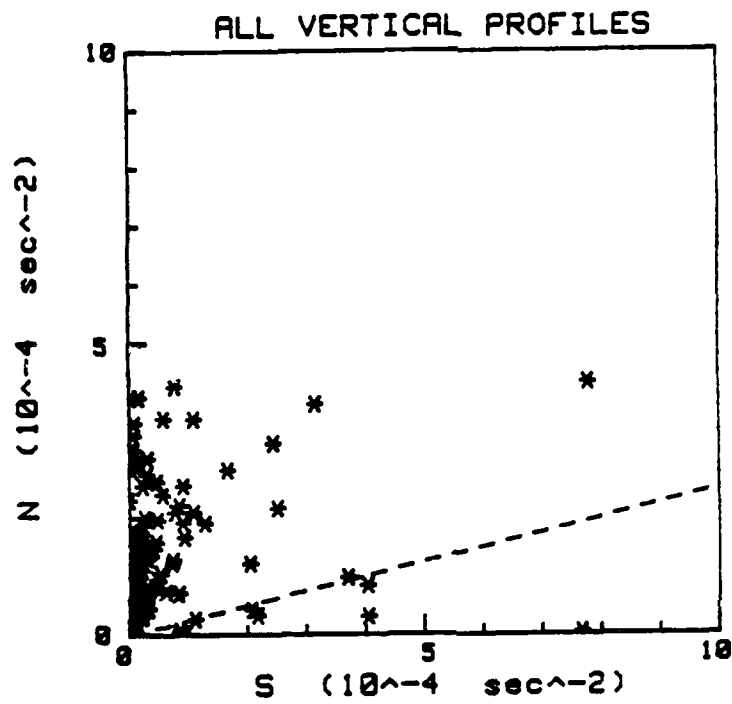


Figure 24. A composite comparison of  $N$  versus  $S$  for all flights shown in Figure 23. Note units. Broken line represents  $R_f = 0.25$ .

Table 4.

Calculated vertical profiles of Richardson number based on  $R_i = N/S$  and using N and S values shown in Figure 17. Altitude shown is MSL and is the average altitude between each vertical radar observation level.

Flight 2		Flight 3	
<u>Alt (km)</u>	<u><math>R_i</math></u>	<u>Alt (km)</u>	<u><math>R_i</math></u>
1.4	1.2	1.7	9.04
1.7	2.61	2	20.99
2	3.92	2.3	5.18
2.3	31.98	2.6	6.99
2.6	6.73	2.9	2.45
2.9	.19	3.2	88.53
3.2	.56	3.4	1.58
3.4	18.94	3.7	11.59
3.7	74.74	4	0
4	1.4	4.3	.07
4.3	.21	4.6	4.51
4.6	1.68	4.9	10.18
		5.2	1.15
		5.5	11.4
		5.8	1.17
		6.1	2.56
		6.4	1.83
		6.6	8.96
		6.9	2.39
		7.2	0
		7.5	2.02



Table 4.  
(continued)

Flight 4		Flight 6	
<u>Alt (km)</u>	<u>R<sub>i</sub></u>	<u>Alt (km)</u>	<u>R<sub>i</sub></u>
1.4	2.45	1.4	-.03
1.7	34.24	1.7	142.19
2	86.56	2	.78
2.3	5.99	2.3	21.71
2.6	5.87	2.6	8.65
2.9	1.09	2.9	179.84
3.2	-.02	3.2	1.6
3.4	39.34	3.4	3.2
3.7	3.23	3.7	181.64
4	6.27	4	7.6
4.3	6.21	4.3	2.24
4.6	10.47	4.6	9.6
4.9	6.66	4.9	27.89
5.2	3.32	5.2	4.13
5.5	5.11	5.5	1.92
5.8	1.84	5.8	2.19
6.1	9.16	6.1	.05
6.4	31.57	6.4	-.02
6.6	138.56	6.6	-.02
6.9	2.49	6.9	.19
7.2	1.53	7.2	.25
7.5	1.6	7.5	0
7.8	-1.53		

Table 4.  
(continued)

Flight 7		Flight 8	
<u>Alt</u> (km)	<u>R<sub>i</sub></u>	<u>Alt</u> (km)	<u>R<sub>i</sub></u>
1.4	-.05	1.4	.02
1.7	-.21	1.7	0
2	1.82	2	2.31
2.3	1.81	2.3	8.51
2.6	1.28	2.6	8.05
2.9	.82	2.9	8.64
3.2	3.21	3.2	8.93
3.4	1.67	3.4	23.48
3.7	32.94	3.7	17.85
4	.13	4	-1.22
4.3	.53	4.3	1.22
4.6	3.81	4.6	8.08
4.9	4.54	4.9	67.55
5.2	4.94	5.2	3.82
5.5	2.02	5.5	6.6
5.8	10.74	5.8	5.3
6.1	11.11	6.1	7.18
6.4	1.56	6.4	11.93
6.6	4.67	6.6	23.27
6.9	6.6	6.9	-8.82
7.2	1.9	7.2	3.68
7.5	1.1	7.5	7.03
7.8	1.99	7.8	3.3

Table 5.

The arithmetically averaged Richardson number at each height for all vertical flights.

Average Richardson Number

<u>Alt (km)</u>	<u>R<sub>i</sub></u>
1.4	0.72
1.7	31
2	19
2.3	12
2.6	6
2.9	32
3.2	17
3.4	15
3.7	54
4	2.36
4.3	1.75
4.6	6
4.9	23
5.2	3.67
5.5	5
5.8	4.25
6.1	6
6.4	9
6.6	35
6.9	0.57
7.2	1.47
7.5	2.35
7.8	1.25

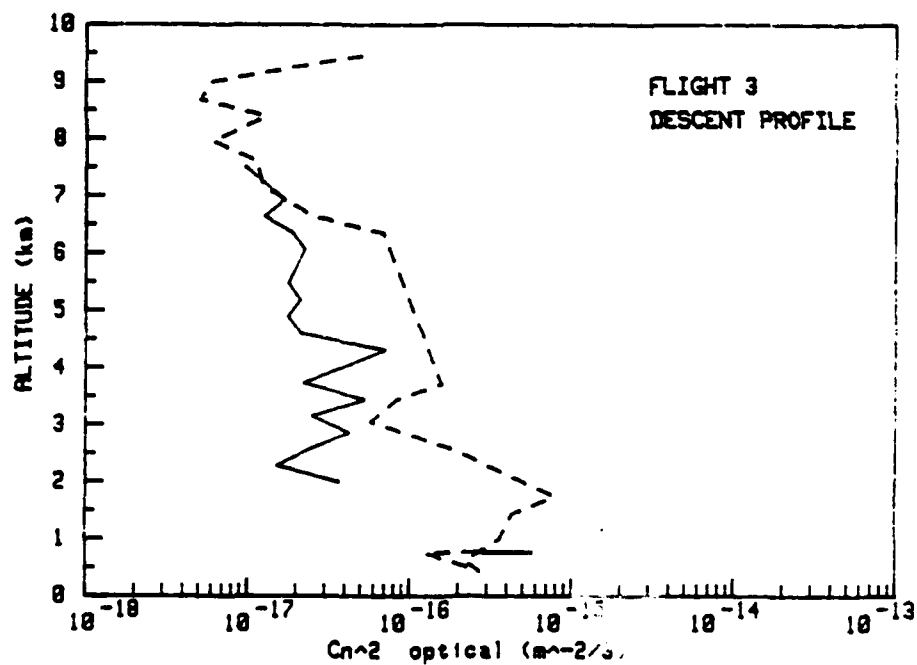
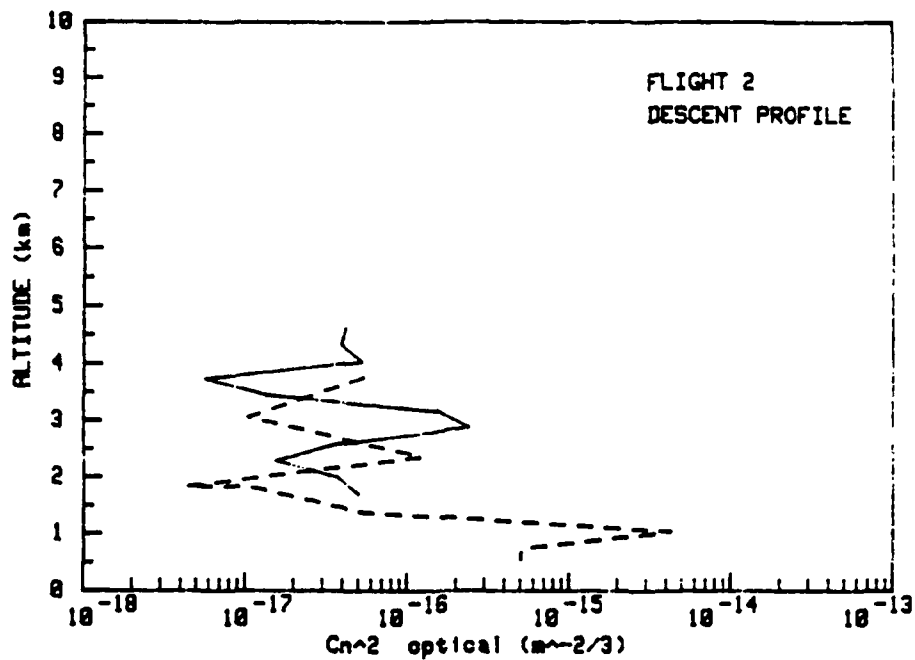


Figure 25. Comparison of the VanZandt et al. model vertical profile prediction of  $C_n^2$ -optical (solid line) and the aircraft  $C_n^2$ -derived vertical profile of  $C_n^2$ -optical (broken line). PSU flights are shown (labeled interior to each graph).

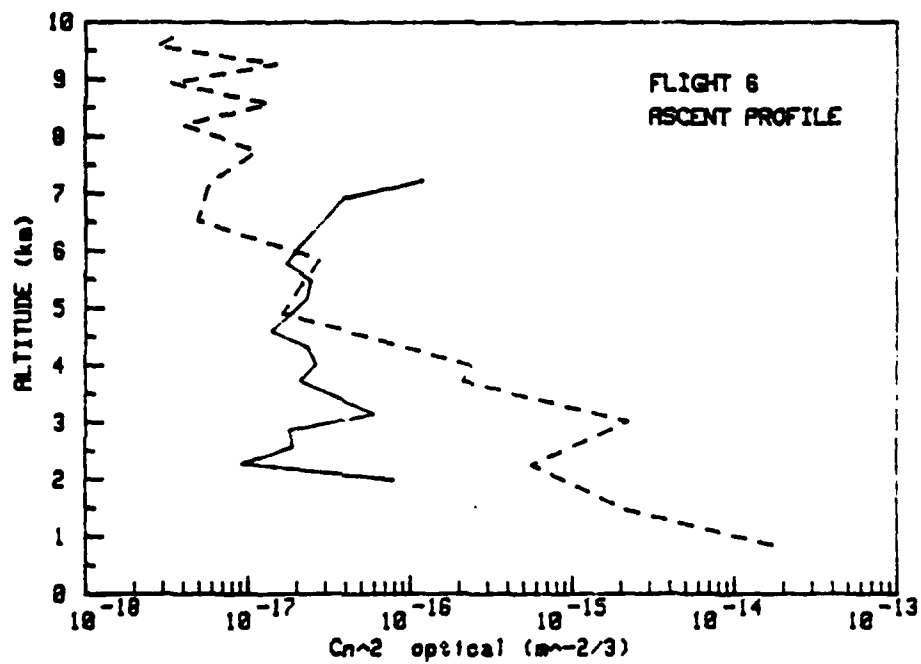
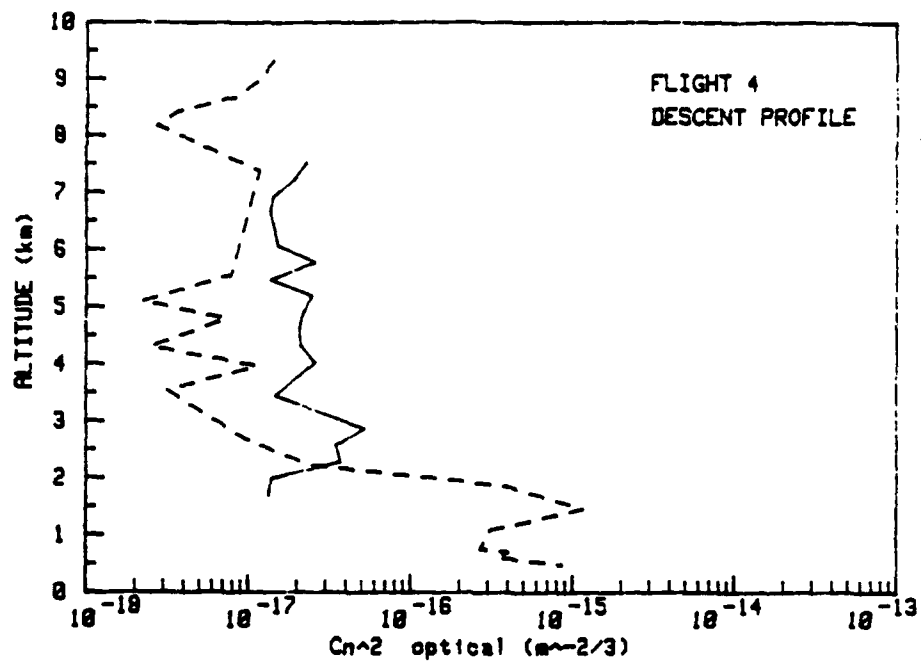


Figure 25. (continued)

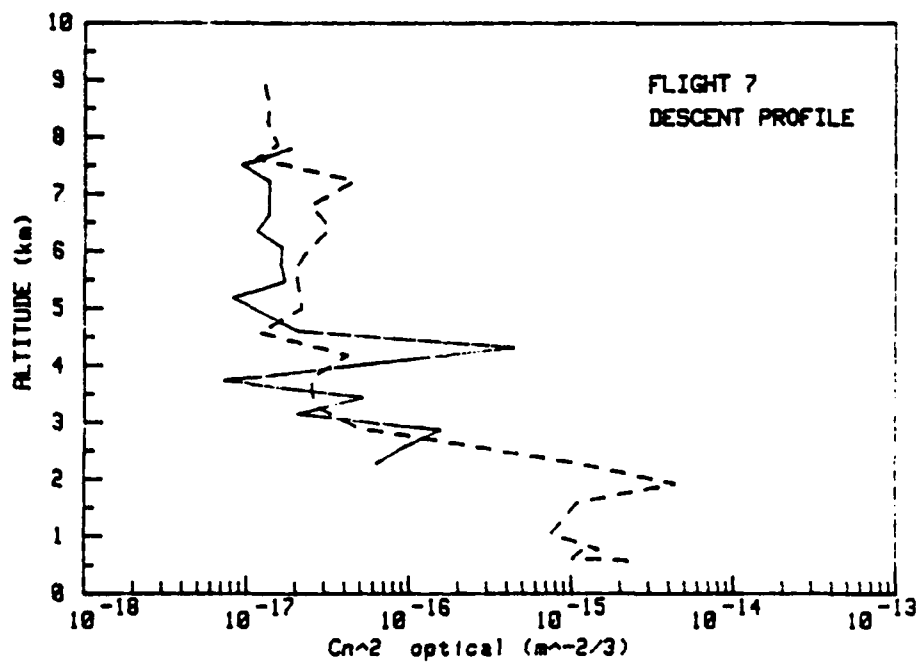
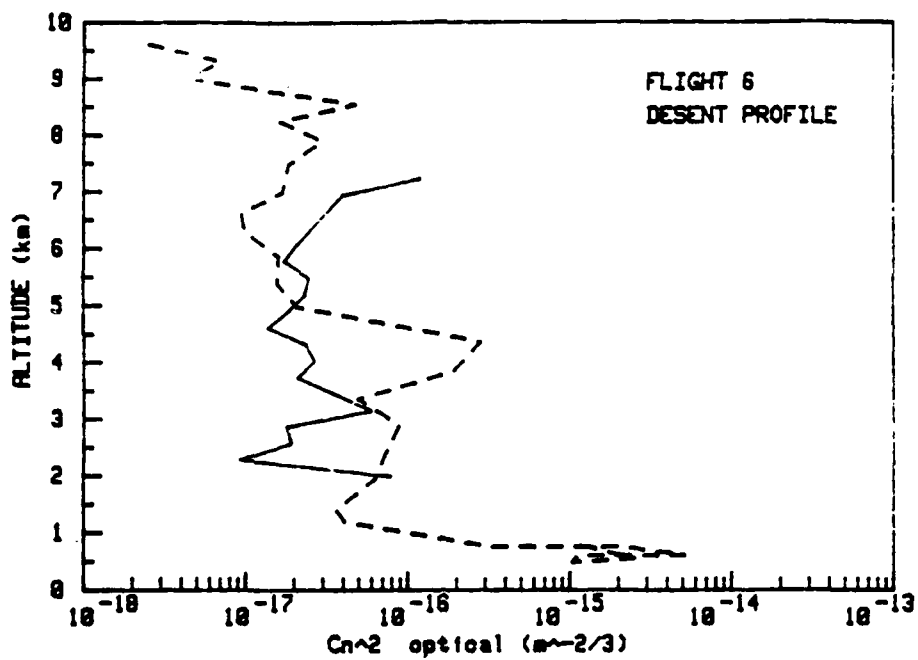


Figure 25. (continued)

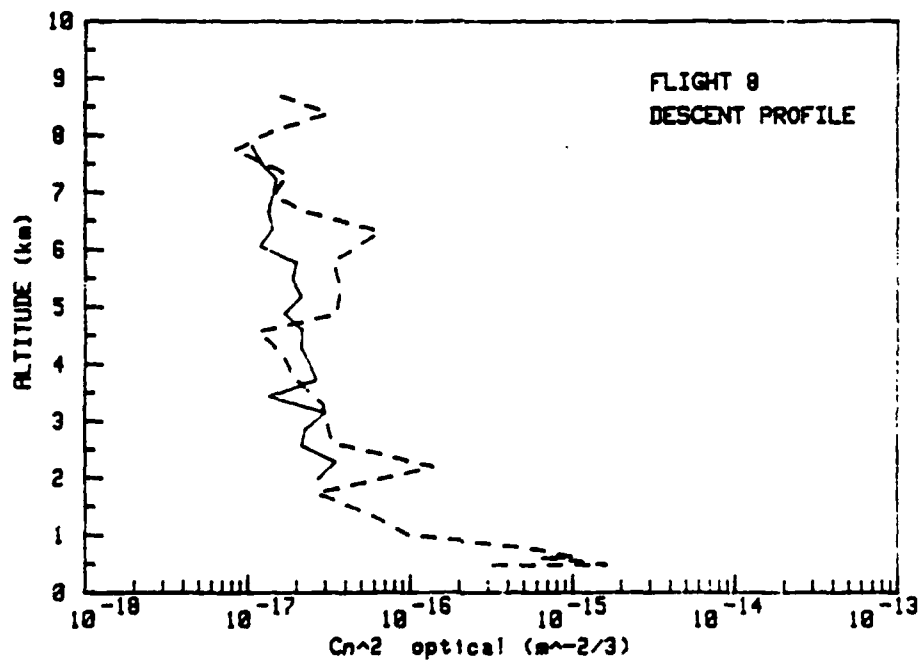
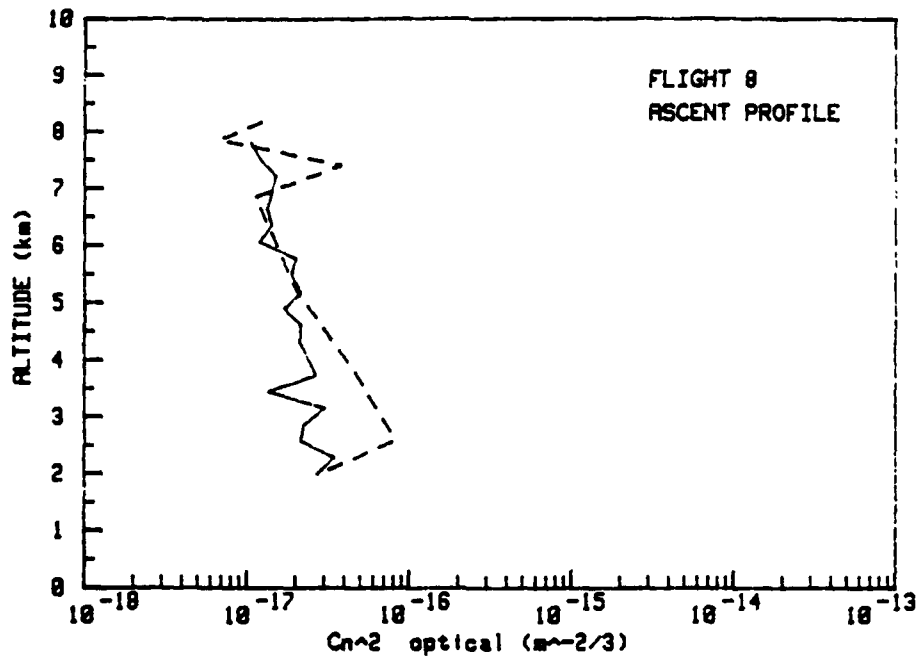


Figure 25. (continued)

"de-normalize" the model-derived parameter. Since only the high resolution profiler range gates were used to calculate  $S$  at a resolution of 290 m, the prediction was only calculated from 1410 m MSL to 7515 m MSL. An average MSL altitude for State College, PA, is 300 m. Except for flight 6 (ascent) the model and aircraft profiles agreed to within an order of magnitude. This particular discrepancy in flight 6 is thought to be the result of errors in gain records for the flight.

### 7.3 Profiles of $C_n^2$

The VanZandt et al. model can also be used to give radar  $C_n^2$ . The relationship between profiler measured  $C_n^2$ -radar and  $C_n^2$ -optical is a function of temperature and humidity (Tatarskii 1971). This parameter, previously referred to as  $X^2$ , has been calculated using the aircraft specific humidity and temperature data.  $X^2$  is the ratio of  $C_n^2$ -radar to  $C_n^2$ -optical.  $X^2$  at each aircraft average observation level was calculated with a polynomial fit to the temperature profile and a finite difference derivative from the humidity profile. Smoothing of the vertical profiles was achieved by setting negative or zero temperature derivatives equal to 0.00001 K/m and positive specific humidity profiles equal to zero. This calculation is given in Table 6.  $X^2$  at each average profiler high resolution gate height was also calculated with finite difference derivatives from both temperature and humidity digitized profiles. Smoothing was performed as before. This calculation is given in Table 7. An arithmetically averaged  $X^2$  profile from Table 7 is given in Table 8. High humidity in the boundary layer gives extremely high



Table 6.  
 $X^2$  vertical profiles for each flight during which the profiler operated, calculated at each aircraft observation level in MSL altitude with aircraft-measured temperature and specific humidity profiles.

Flight 2	Descent	Flight 3	Descent
<u>Alt (km)</u>	<u><math>X^2</math></u>	<u>Alt (km)</u>	<u><math>X^2</math></u>
4.4	1	9	1
3.8	1	8.7	1
3	1	8.4	1.6
2.3	1.2	8	1.3
1.8	1.1	7.6	1.3
1.4	42.8	7.2	1.2
1	25.5	6.6	1.4
.7	12.5	6.3	1.6
.5	148.6	5.8	1.9
		5.4	1
		5	1
		4.6	1.5
		4.1	1.8
		3.7	2.3
		3.4	1.7
		3	1.9
		2.6	1.5
		1.7	12.4
		1.4	2.6
		1	2.3
		.6	1914
		.4	13019
		.8	3717
		.3	12907

Table 6.  
(continued)

Flight 4	Descent	Flight 6	Descent
<u>Alt</u> (km)	<u>X<sup>2</sup></u>	<u>Alt</u> (km)	<u>X<sup>2</sup></u>
9	76189	9	1
8.7	106301	8.5	1.3
8.4	104241	8.2	1.2
8.2	232623	7.9	6.4
7.4	1	7.5	1.1
6.8	1	7	1.8
6.1	1	6.6	18.9
5.6	1	6.3	4.6
5.1	4.6	5.9	1
4.8	1	5.4	1
4.3	3.8	5	1.9
4	1.1	4.4	12.8
3.5	1	3.8	2.4
3	1.8	3.4	1
2.7	1.6	2.9	13.4
2.2	1.8	2.4	3.2
1.9	3.4	2	13.9
1.5	227.8	1.4	7.7
.8	1.4	1.2	7.7
.7	2.33E+6	.8	1.3
.6	2.32E+6	.7	4.2
.5	2.3E+6	.6	3.7
		.5	3.2

Table 6.  
(continued)

Flight 7 Alt (km)	Descent $\chi^2$	Flight 8 Alt (km)	Descent $\chi^2$
8.5	1	8.4	1.9
8.3	1	8.1	3.5
7.9	2.6	7.7	3.3
7.6	3.5	7.3	10.8
7.2	13.4	7	11.6
6.8	4.1	6.7	3.8
6.4	39.2	6.3	21.7
5.9	3.3	5.8	15.3
5.7	17.8	5.3	6.1
5	24.6	4.9	1.2
4.6	5.8	4.6	54.8
4.2	4	4.1	1.2
3.8	1.3	3.8	1.1
3.3	1	3.3	87.5
2.9	1	2.8	6.6
2.3	21.4	2.6	6.8
1.9	81.9	2.2	101.9
1.6	1.9	1.7	5.8
1	351269	1.4	2.2
.8	34447	1	1.6
.6	16	.8	1.6
.5	3.2	.6	1.5
		.5	1.5

Table 7.

$\chi^2$  vertical profiles for each flight during which the profiler operated, calculated at each profiler observation level in MSL altitude with aircraft-measured temperature and specific humidity profiles.

Flight 2 Alt (km)	$\chi^2$	Flight 3 Alt (km)	$\chi^2$
1.3	46.9	1.3	5.7
1.6	3.5	1.6	2.5
1.9	1.1	1.9	11.9
2.1	1.3	2.1	138.2
2.4	1.2	2.4	3.2
2.7	1.1	2.7	1.5
3	1	3	1.9
3.3	1	3.3	1.6
3.6	1	3.6	2.2
3.9	1	3.9	2.2
4.2	1	4.2	1.8
4.5	1	4.5	1.5
		4.8	1.2
		5	1
		5.3	1
		5.6	25.5
		5.9	1.9
		6.2	1.6
		6.5	1.4
		6.8	1.4
		7.1	1.2
		7.4	1.2
		7.7	1.3
		8	1.3

Table 7.  
(continued)

Flight 4		Flight 6	
Alt (km)	$\chi^2$	Alt (km)	$\chi^2$
1.3	34.9	1.3	7.8
1.6	210.3	1.6	2.9
1.9	3.4	1.9	14.9
2.1	1.8	2.1	56.2
2.4	1.9	2.4	3.2
2.7	1.6	2.7	1
3	1.8	3	13.2
3.3	1.3	3.3	1
3.6	1	3.6	1.2
3.9	1.1	3.9	2.5
4.2	3.8	4.2	1.1
4.5	6.9	4.5	13.9
4.8	1	4.8	4.2
5	4.6	5	2
5.3	2.8	5.3	1
5.6	1	5.6	5.9
5.9	1	5.9	1
6.2	1	6.2	4.2
6.5	1.9	6.5	20.4
6.8	1	6.8	6.1
7.1	1	7.1	1.7
7.4	1	7.4	1.1
7.7	1.5	7.7	2.4
8	1.1	8	6.2

Table 7.  
(continued)

Flight 7		Flight 8	
<u>Alt</u> (km)	$\chi^2$	<u>Alt</u> (km)	$\chi^2$
1.3	1.2	1.3	2.3
1.6	1.9	1.6	1.6
1.9	12.9	1.9	5.4
2.1	27.4	2.1	107.4
2.4	6.5	2.4	7.7
2.7	1	2.7	6.7
3	1	3	112.1
3.3	1	3.3	87.6
3.6	1.2	3.6	9.6
3.9	1.3	3.9	1.1
4.2	4	4.2	1.2
4.5	5.5	4.5	50.9
4.8	1.2	4.8	1.2
5	25.6	5	1.2
5.3	1.5	5.3	6.1
5.6	16.3	5.6	25.8
5.9	3.3	5.9	15.3
6.2	4.7	6.2	22.4
6.5	41.3	6.5	10.3
6.8	4.1	6.8	3.7
7.1	14.8	7.1	11.1
7.4	6.5	7.4	10.8
7.7	3.5	7.7	3.2
8	2.6	8	3.1

Table 8.  
Arithmetically averaged  $X^2$  vertical profiles from the Table 7  
profiles.

Average Radar $X^2$ Alt (km)	Profile $X^2$
1.3	16.5
1.6	37.1
1.9	23.3
2.1	55.4
2.4	3.9
2.7	2.1
3	21.8
3.3	15.6
3.6	2.7
3.9	1.5
4.2	2.2
4.5	13.3
4.8	1.8
5	6.9
5.3	2.5
5.6	14.9
5.9	4.5
6.2	6.8
6.5	15
6.8	3.3
7.1	6
7.4	4.1
7.7	2.4
8	2.9

values of  $C_n^2$ -radar at these levels. Aircraft profiles of  $C_n^2$ -optical adjusted with  $X^2$  to give  $C_n^2$ -radar show agreement with the profiler derived  $C_n^2$ -radar profiles (Figure 26).

For the two night flights during which multiple instruments took data, comparisons of  $C_n^2$ -optical vertical profiles are shown. The level at which  $C_n^2$  was measured by the AFGL scintillometer varied because the instrument was measuring at different zenith angles. To aid in graphical interpretation, for each night, all the AFGL scintillometer profile  $C_n^2$  values were log averaged and the heights arithmetically averaged, at each level. RADC data (Figure 14) was available for one night only and was omitted for clarity. Figure 27 shows a comparison of  $C_n^2$ -optical from the averaged AFGL scintillometer profiles, the aircraft, the VanZandt et al. model predictions, the AFGL thermosonde, and the profiler (unadjusted raw  $C_n^2$ -radar). The ascent profile for the aircraft on flight 6 is thought to have been an incorrect gain setting which leads to the unrealistically high values in the lower part of the profile. Figure 28 is the same comparison except that the radar profile has been converted to  $C_n^2$ -optical using the calculated  $X^2$  profiles of Table 7. These plots show again the agreement between the model and the aircraft, while the thermosonde has good agreement with the scintillometer. The profiler  $C_n^2$ -optical values (from the hourly average observation during the aircraft flight) show some agreement with the thermosonde.



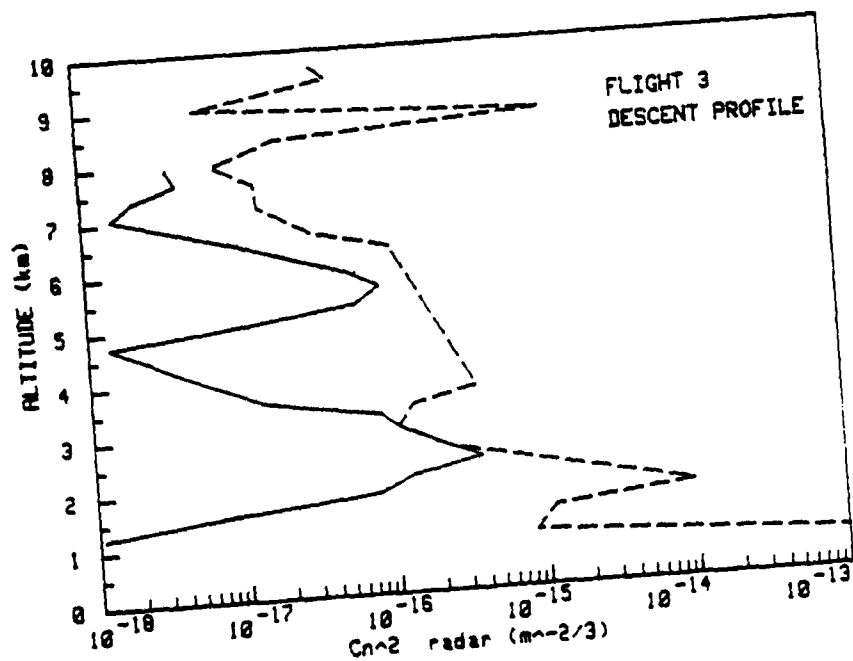
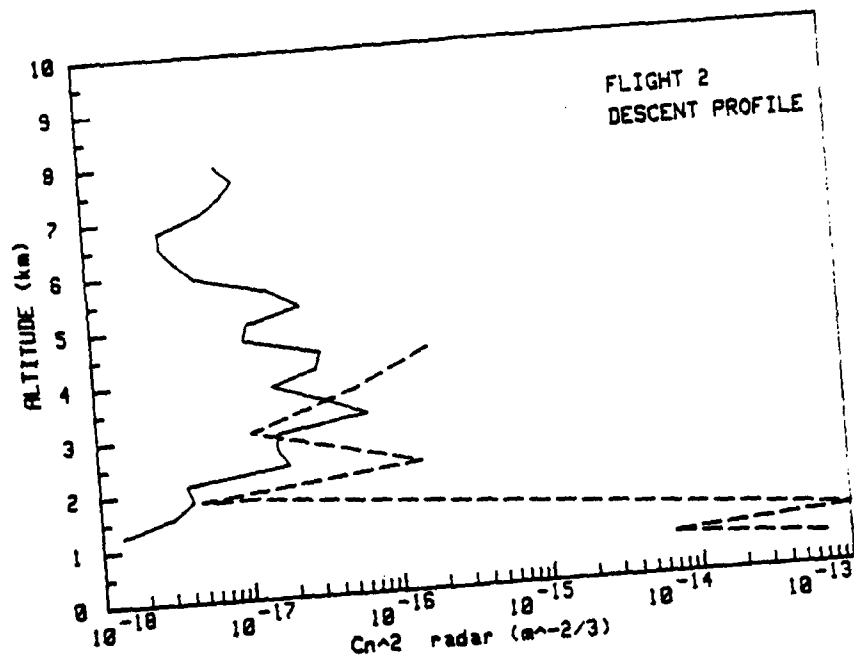


Figure 26. Comparison of  $C_n^2$ -radar as derived from profiler (solid line) and from aircraft  $C_n^2$ -optical, multiplied by the conversion factor  $X^2$  to give  $C_n^2$ -radar (broken line). PSU flights are shown (labeled interior to each graph).

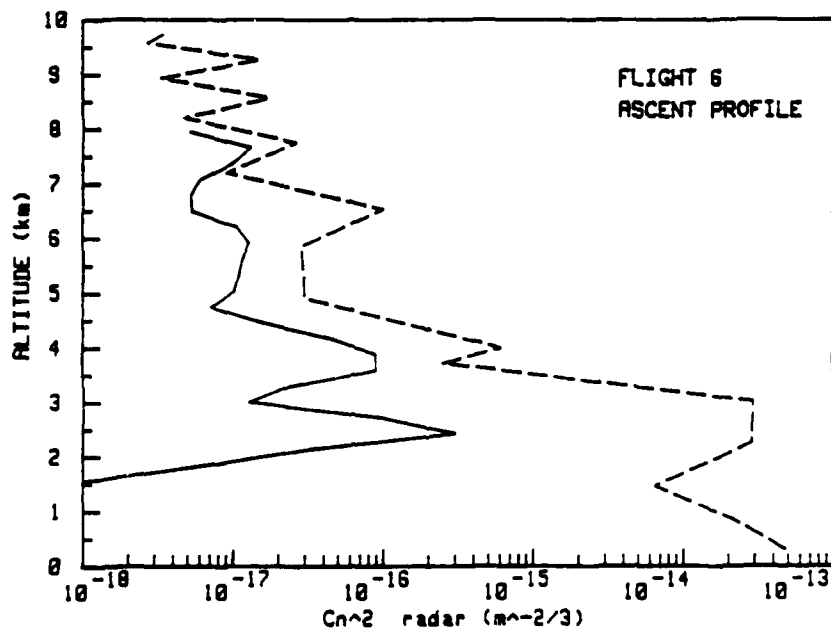
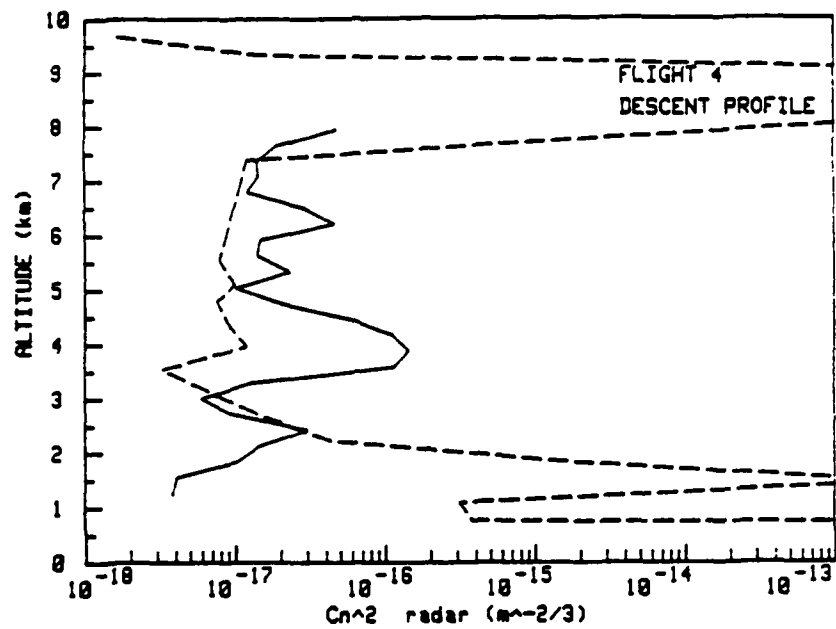


Figure 26. (continued)

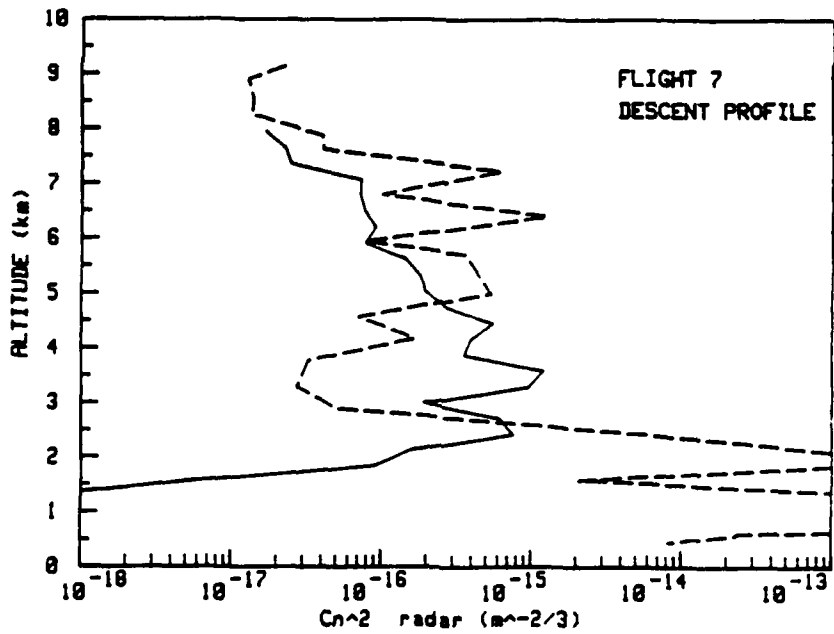
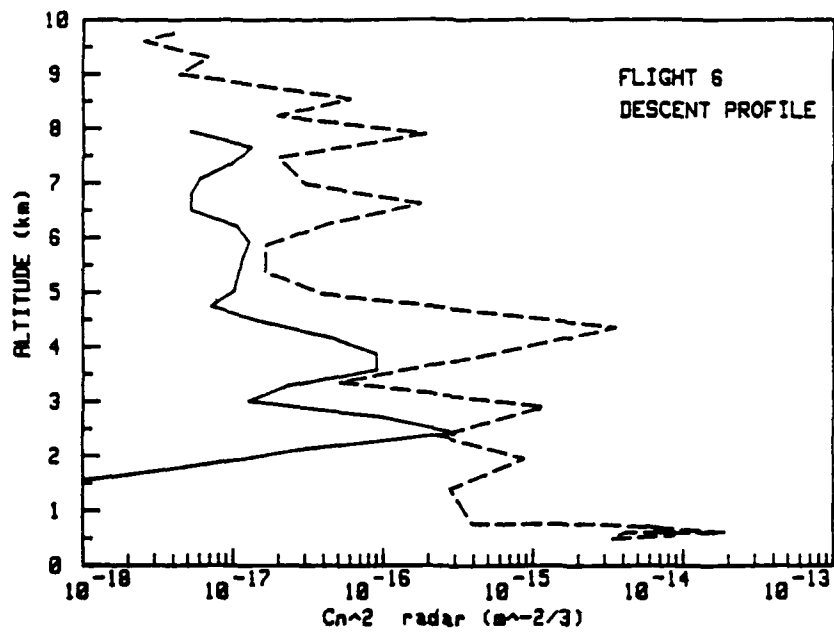


Figure 26. (continued)

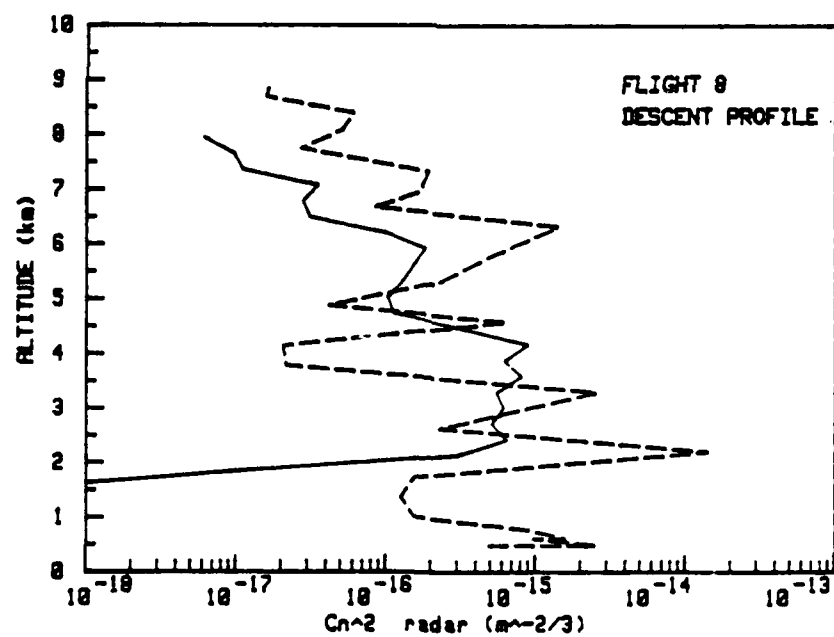
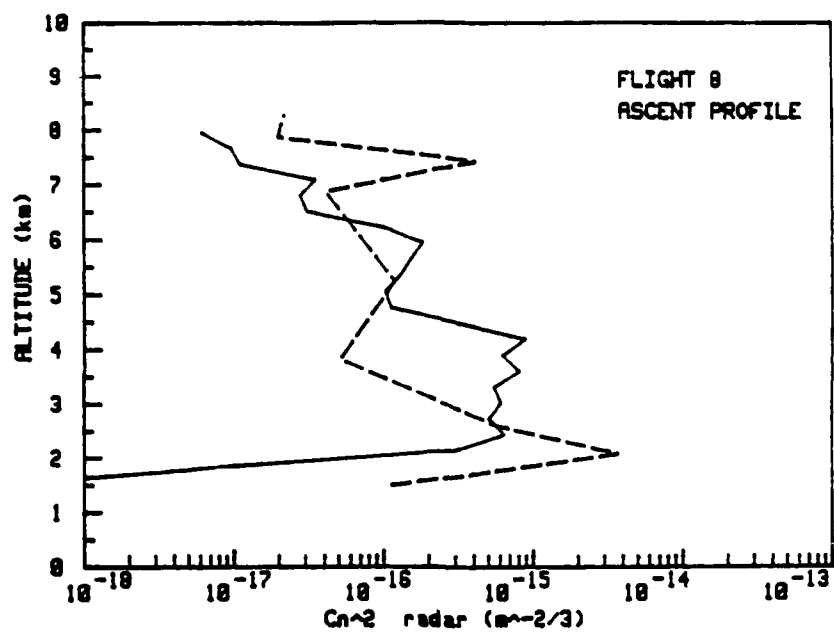


Figure 26. (continued)

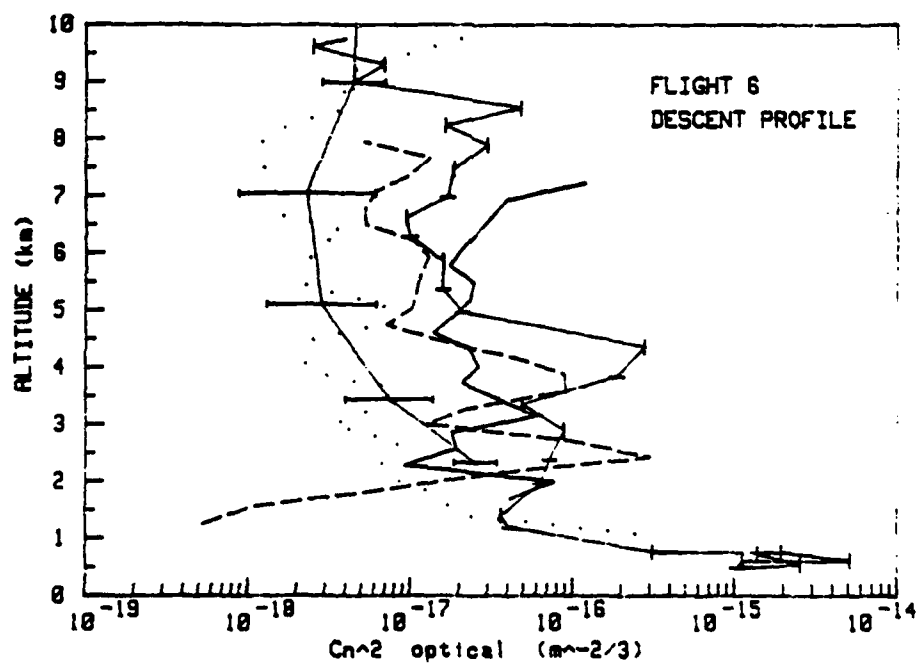
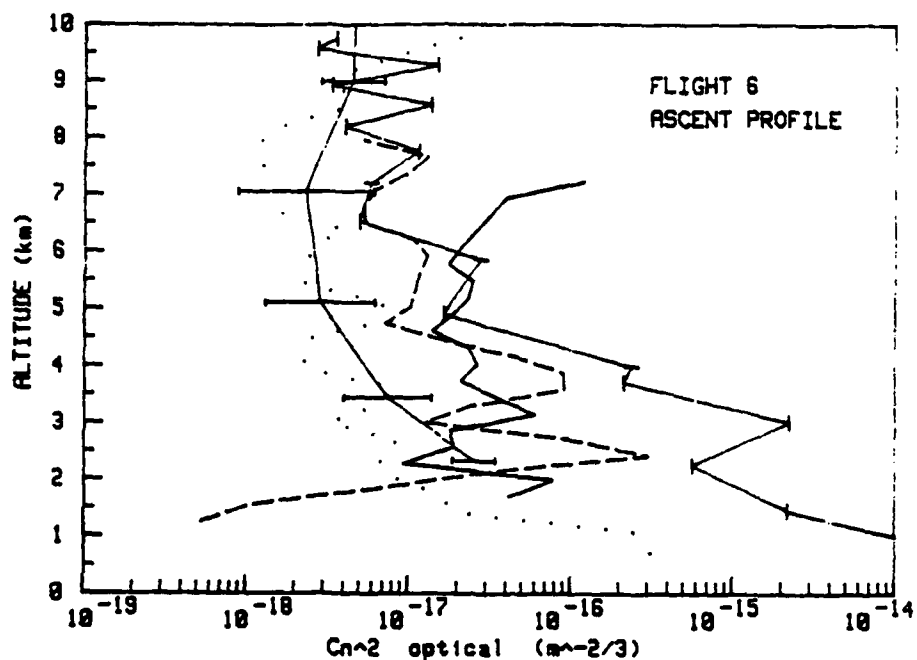


Figure 27. Comparison of vertical profiles of  $C_n^2$ -optical. Altitude is MSL. Bars represent standard deviation of AFGL scintillometer data. Profiler values are raw  $C_n^2$ -radar (not converted to  $C_n^2$ -optical). Aircraft flight designations are labeled interior to each graph.

Log averaged scintillometer	— —	Aircraft	— —
VanZandt et al. model	—	Profiler	- - -
Arithmetically smoothed thermosonde	.....		

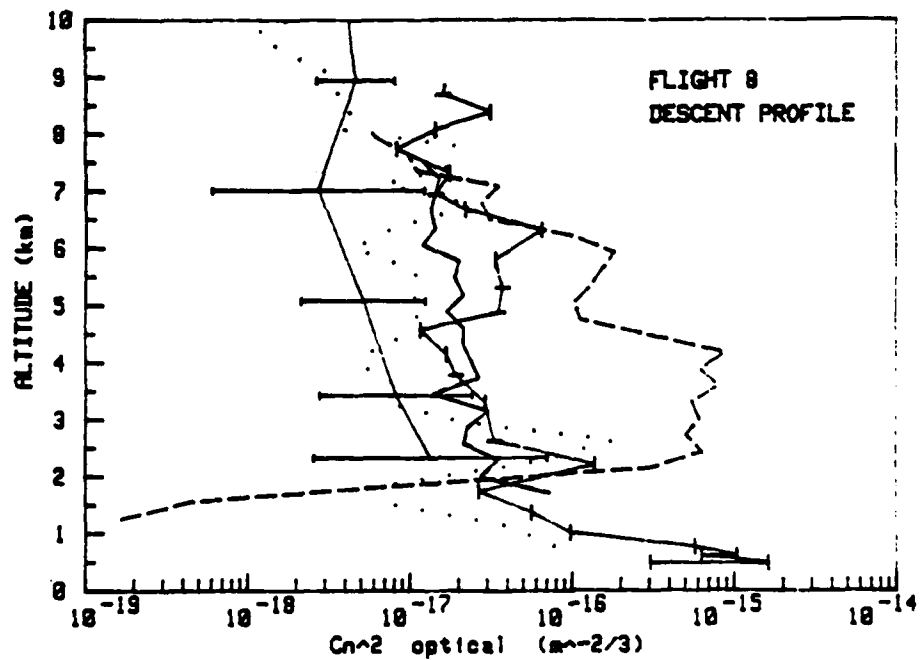
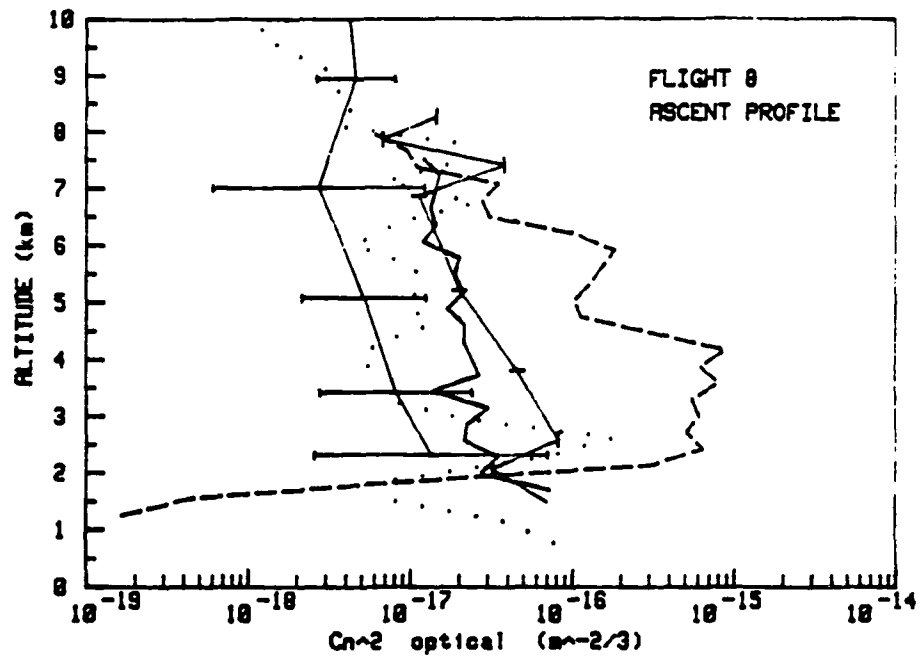


Figure 27. (continued)

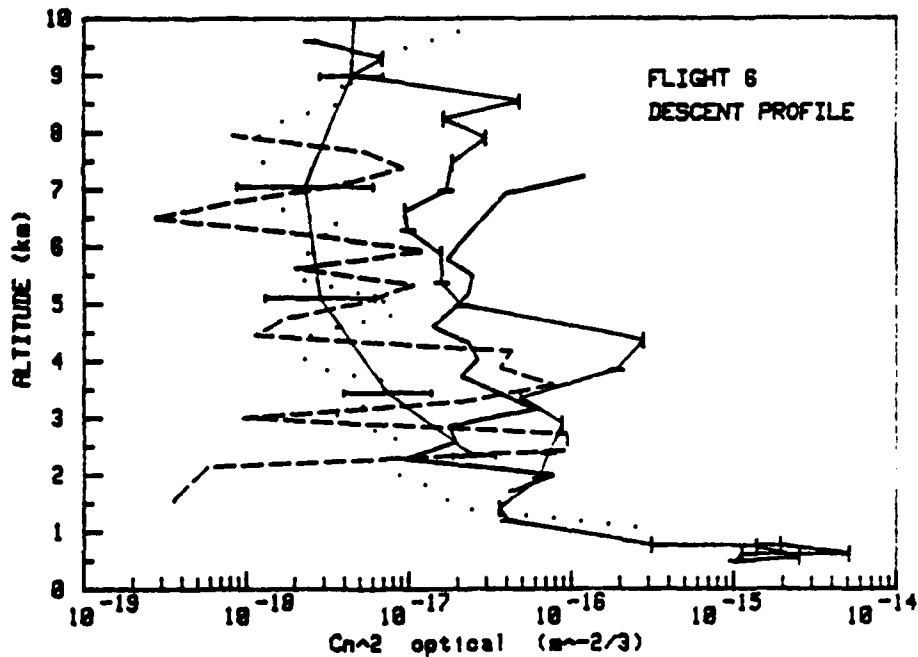
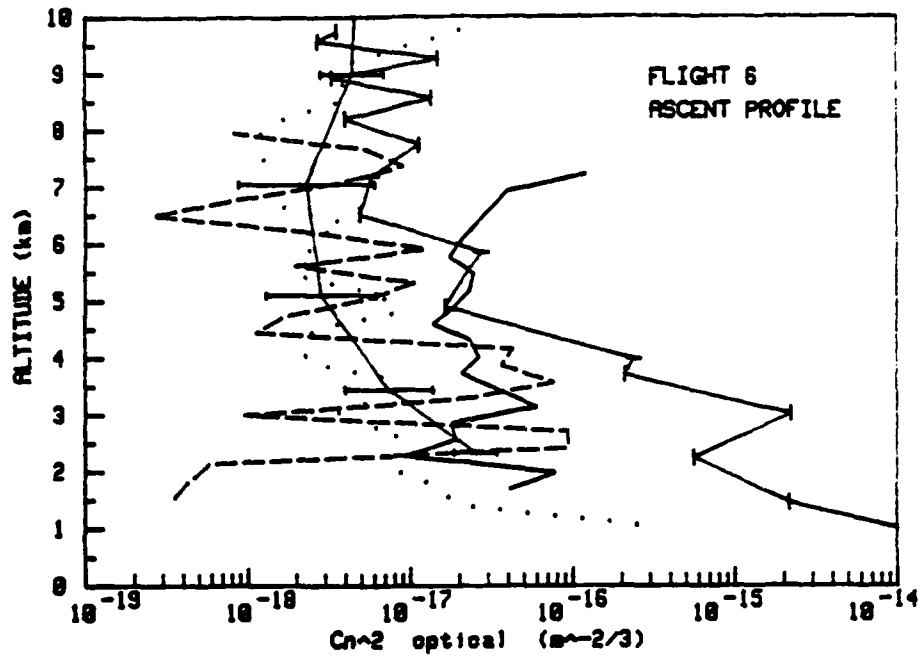


Figure 28. Comparison of vertical profiles of  $C_n^2$ -optical. Altitude is MSL. Bars represent standard deviation of AFGL scintillometer data. Profiler values have been converted to  $C_n^2$ -optical. Aircraft flight designations are labeled interior to each graph.

Log averaged scintillometer	— —	Aircraft	———
VanZandt et al. model	-----	Profiler	-----
Arithmetically smoothed thermosonde	.....		

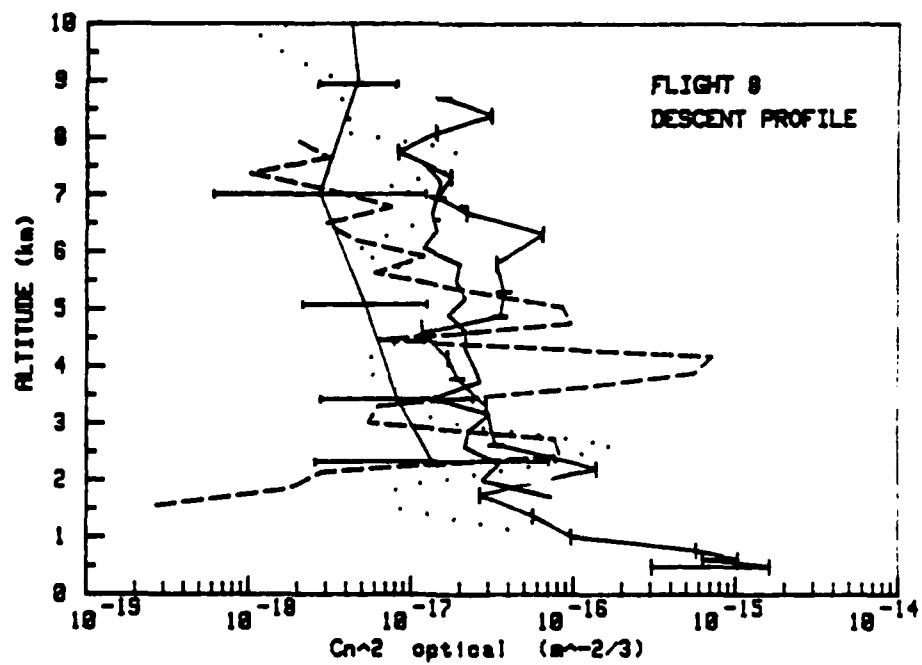
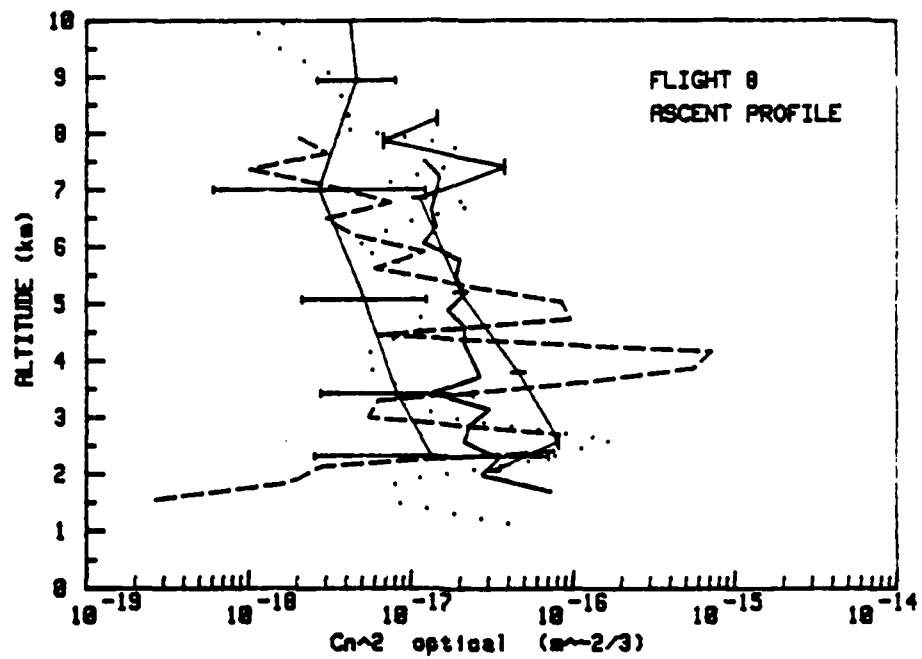


Figure 28. (continued)



#### 7.4 Propagation Parameters

Other optical parameters of interest are the coherence length  $r_o$  and isoplanatic angle  $\theta_o$ . These are related to vertical integrals of  $C_n^2$  (Murphy and Battles 1986)

$$r_o = k_r \left[ \int_0^\infty C_n^2(z) dz \right]^{-3/5} \quad (7.3)$$

$$\theta_o = k_t \left[ \int_0^\infty C_n^2(z) z^{5/3} dz \right]^{-3/5} \quad (7.4)$$

where  $k_t$  and  $k_r$  are functions of wavelength ( $\lambda^{1.2}$  dependence).

Assuming a wavelength, and a linear relation between observations of  $C_n^2$ -optical at each level, the integrals can be evaluated numerically. But contributions from above and below the measured profile must be calculated based on theoretical assumptions. In the boundary layer, Murphy and Battles (1986) assumed  $C_n^2$  to go as

$$C_n^2(z) = C_n^2(z_b) (z/z_b)^{-2/3} \quad (7.5)$$

where  $z_b$  is the lowest level of the measured profile. In the upper atmosphere,  $C_n^2$  was modeled by an exponential decrease

$$C_n^2(z) = C_n^2(z_t) e^{-a(z-z_t)} \quad (7.6)$$

where  $a = (\ln 10) DR$ , and  $DR$  (the atmospheric drop off rate) =  $1.3 \times 10^{-4}$ . With these relationships, the integral portions for  $\theta_o$  above and below become (Murphy and Battles 1986)

$$\int_{\text{Above}} = z_t^{5/3} (C_n^2(z_t)/a) \left[ 1 + (5/3)(az_t)^{-1} + (10/9)(a^2 z_t^2)^{-1} \right] \quad (7.7)$$

$$\int \text{Below} = \frac{1}{2} z_b^{8/3} C_n^2(z_b) \quad (7.8)$$

and for  $r_o$

$$\int \text{Above} = C_n^2(z_t)/a \quad (7.9)$$

$$\int \text{Below} = 3 z_b C_n^2(z_b) [1 - (6/z_b)^{1/3}] \quad (7.10)$$

As part of the AFGL thermosonde flights,  $r_o$  and  $\theta_o$  were calculated using equations 7.3 and 7.4 linearly integrated for just the thermosonde profile, assuming  $\lambda = .3 \mu$  (Robert Beland, letter to William Syrett, September 1986; Robert Beland, telephone conversation, November 1987). These values are shown in Table 9.  $r_o$  and  $\theta_o$  were also calculated by Murphy and Battles (1986) with all the above integral equations and theoretical assumptions for the atmosphere above and below, for the AFGL scintillometer data, using  $\lambda = 0.5 \mu$ . An average value for each night is given in Table 10. No  $r_o$  values are shown for the AFGL scintillometer because the boundary layer has a large contribution to the  $r_o$  integral. The lowest scintillometer measurement level is roughly 2 km AGL. Comparisons of contributions to the total integral showed that the theoretical extrapolations below the measured profile were contributing the major percentage to the computed value. Calculated  $r_o$  values were thus considered unreliable (Murphy and Battles 1986). To facilitate comparison, this same method and assumptions were used to compute  $r_o$  and  $\theta_o$  from the aircraft data at  $0.3 \mu$  and  $0.5 \mu$  wavelength (Table 11). Both the aircraft and thermosonde profiles start at much lower AGL altitudes and thus the measured profile is a significant contributor to the  $r_o$  calculations for both these instruments (Robert Beland, telephone

Table 9.  
AFGL-calculated optical parameters from thermosonde data.

AFGL Thermosonde Optical Data  
(calculated with  $\lambda = .3\mu$ )

<u>Flight</u>	$r_o$ ( <u>cm</u> )	$\theta_o$ ( <u><math>\mu</math>rad</u> )
L4033	4.3	3.2
L4019	4.4	4.5

Table 10.

Average of AFGL-calculated optical parameters from scintillometer data.

AFGL Scintillometer Data  
(calculated with  $\lambda = .5\mu$ )

<u>Date</u>	<u>GMT Time</u>	$\theta_0$ ( $\mu$ rad)	<u>Percent Contribution</u>	
5/4/86	0342-0513	8.02	a	56.5
			b	42.2
			c	1.3
5/6/86	0317-0420	10.29	a	61.4
			b	36.8
			c	1.8

a- Scintillometer Measurement

b- Atmosphere Above

c- Atmosphere Below

Table 11.

Optical parameters from aircraft data calculated with the Murphy and Battles assumptions.

Aircraft Data  
(calculated with  $\lambda = .5\mu$ )

<u>Date</u>	<u>Flight</u>	$\theta_0$ ( $\mu$ rad)	<u>Percent Contribution</u>
4 May	6	8.3	a 84.8 b 15 c 0.2
6 May	8	7.9	a 49.2 b 50.7 c 0

Aircraft Data  
(calculated with  $\lambda = .3\mu$ )

<u>Date</u>	<u>Flight</u>	$\theta_0$ ( $\mu$ rad)	<u>Percent Contribution</u>
4 May	6	4.5	a 84.8 b 15 c 0.2
6 May	8	4.3	a 49.2 b 50.7 c 0

<u>Date</u>	<u>Flight</u>	$r_0$ (cm)	<u>Percent Contribution</u>
4 May	6	2.4	a 68.5 b 0.5 c 31
6 May	8	4.8	a 82.2 b 6.4 c 11.3

a- Thermosonde Measurement  
b- Atmosphere Above  
c- Atmosphere Below

conversation, November 1987)). The  $\theta_0$  integral, inversely, weights the upper atmosphere most heavily. Since the aircraft is limited in altitude to  $\approx 10$  km, the contribution to  $\theta_0$  is limited. However, due to the integral approximation, profiles in which  $C_n^2$  drops off sharply with altitude will weight the measured layer more heavily. This is seen in the profile of flight 6.  $\theta_0$  values from the scintillometer and the aircraft (at  $\lambda = 0.5 \mu$ ) were similar on 4 May, but disagreed on 6 May. The thermosonde and aircraft  $\theta_0$  values (at  $\lambda = 0.3 \mu$ ) disagreed on 4 May, but agreed on 6 May.

$r_0$  was also measured at optical wavelengths during the EWAK experiment by the NPS  $r_0$  scintillometer. The measured  $r_0$  average for the aircraft flight time on the night of 4 May 1986 was 5 cm. The thermosonde and aircraft  $r_0$  values (at  $\lambda = 0.5 \mu$ ) differed by a factor of two on 4 May. The night of 6 May, the thermosonde and aircraft  $r_0$  values were similar.

#### 7.5 VanZandt et al. Model for $\epsilon$

The VanZandt et al. model  $\epsilon$  predictions are compared to  $\epsilon$  profiles from the aircraft data (Figure 29). The hot wire failed during flight 4, so that only a small amount of data is available. The model shows predictions generally ranging in the area of  $5 \times 10^{-4}$  for all flights. There is poor agreement between the aircraft and model, the aircraft (except for flight 3) often giving values three or four orders of magnitude smaller. Aircraft values also vary much more, ranging from  $10^{-3}$  to  $10^{-7}$ .

A crude average profile of  $\eta$ , the microscale, based on the aircraft  $\epsilon$  profiles is shown in Figure 30.  $\eta = (\nu^3/\epsilon)^{.25}$  was

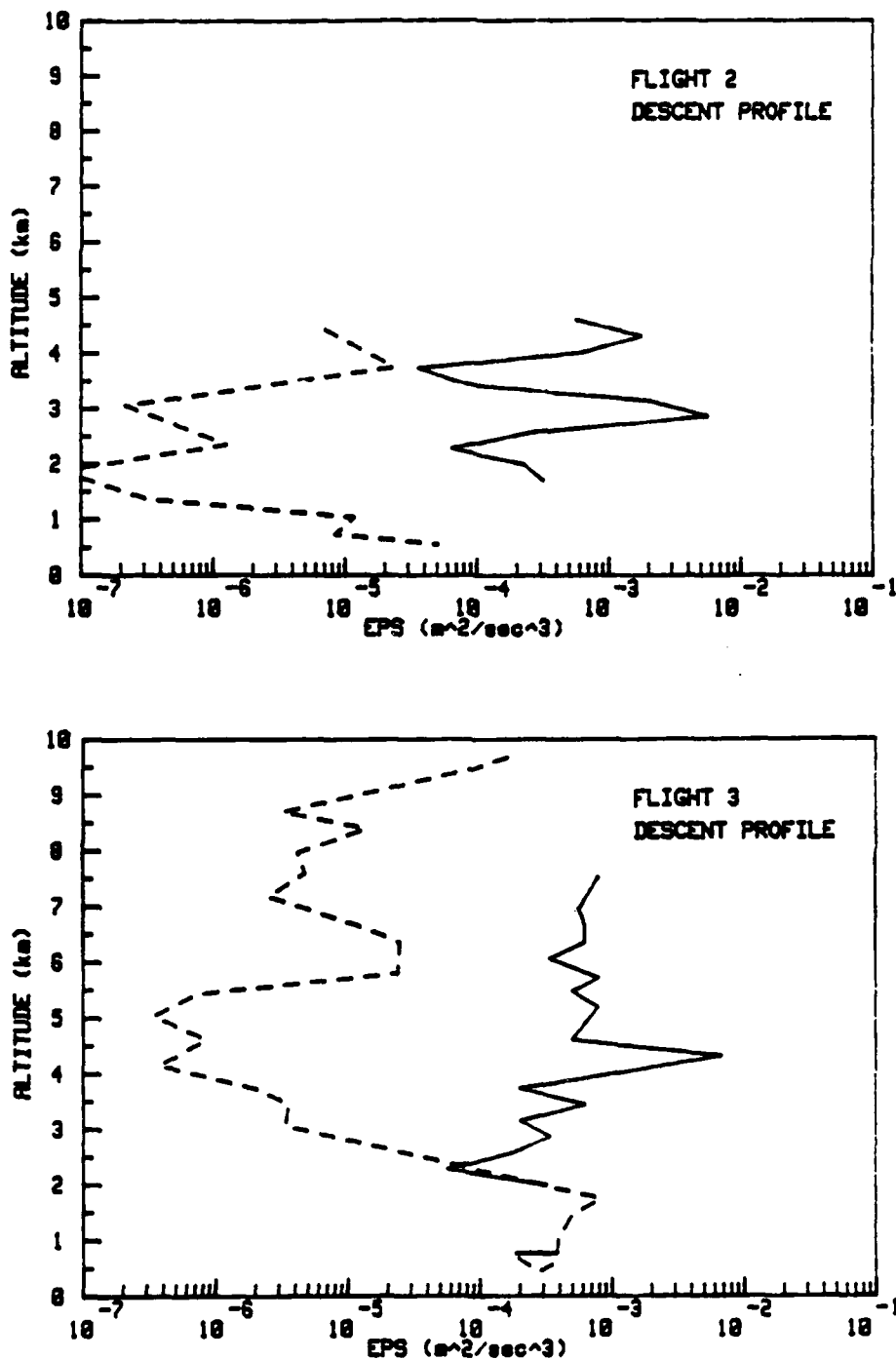


Figure 29. Comparison of vertical profiles of epsilon ( $\epsilon$ ), the turbulent kinetic energy dissipation rate, predicted by the VanZandt et al. model (solid line) and measured by the aircraft (broken line). Altitude is MSL. Aircraft flight designations are given interior to each graph.

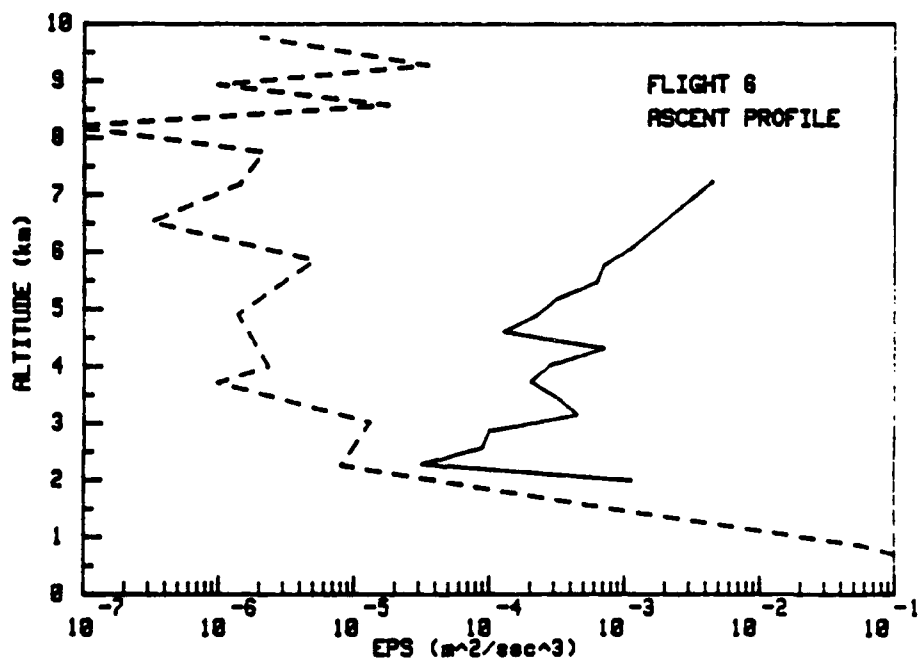
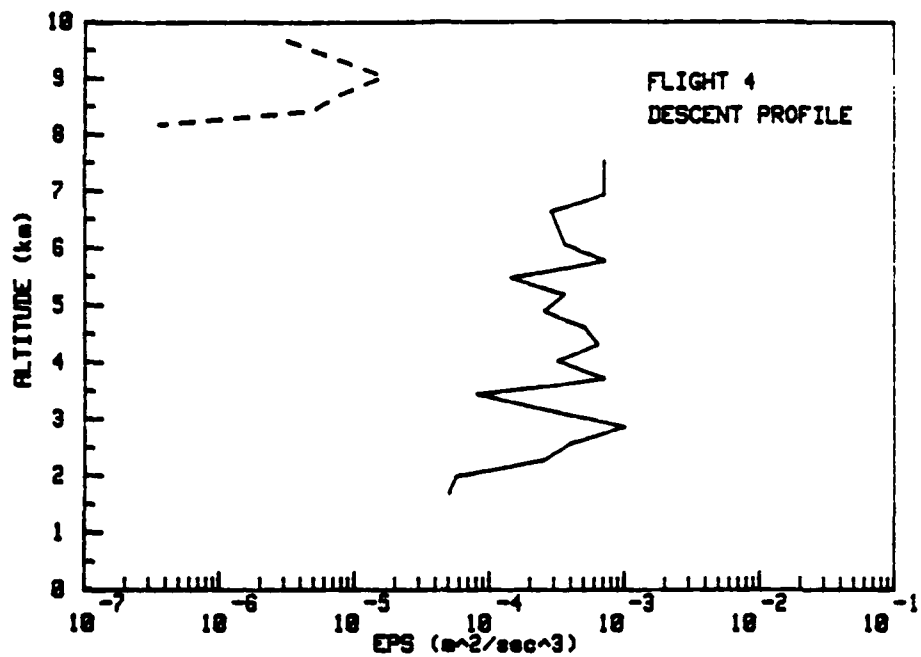


Figure 29. (continued)



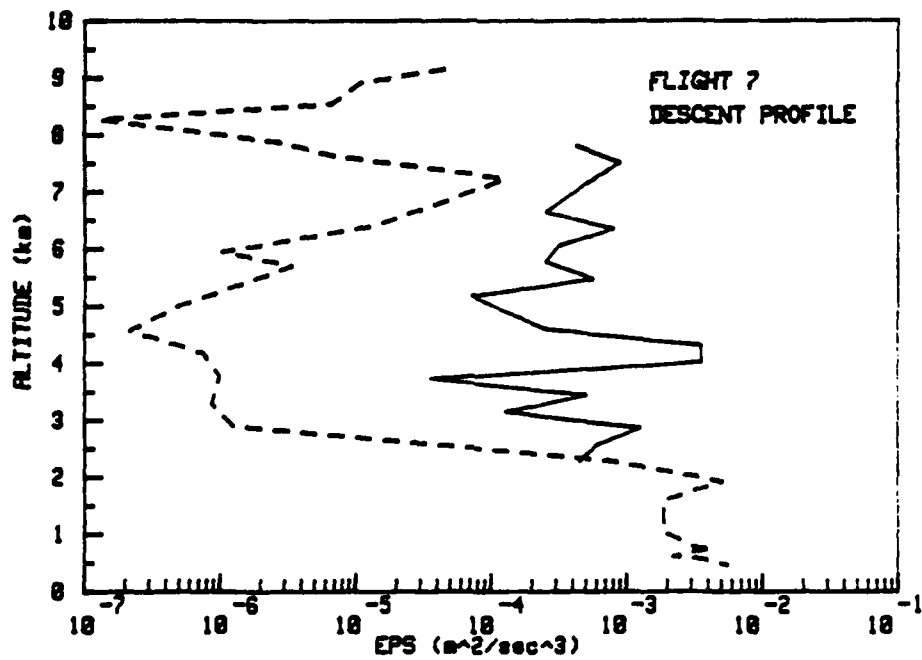
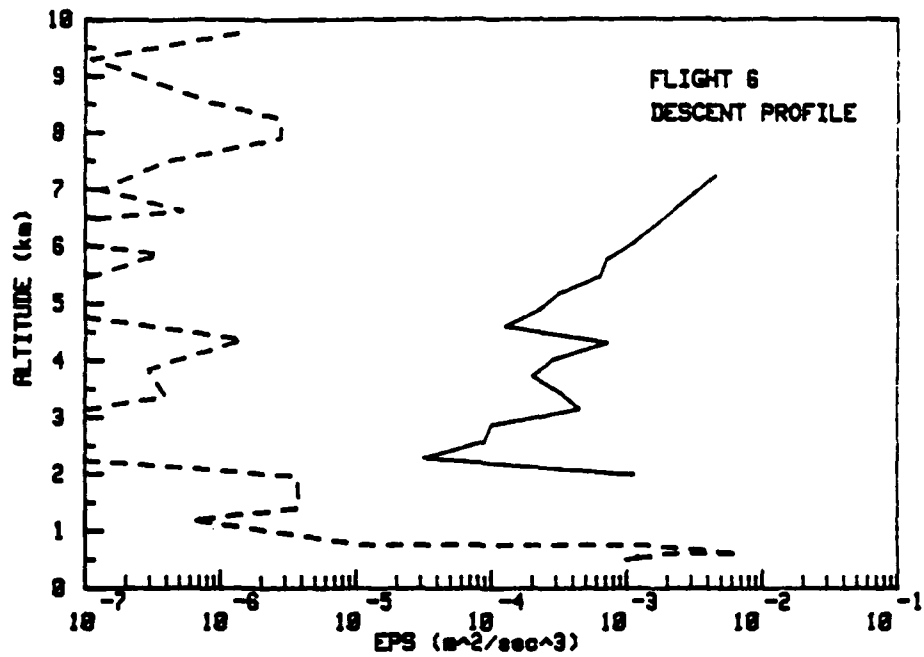


Figure 29. (continued)

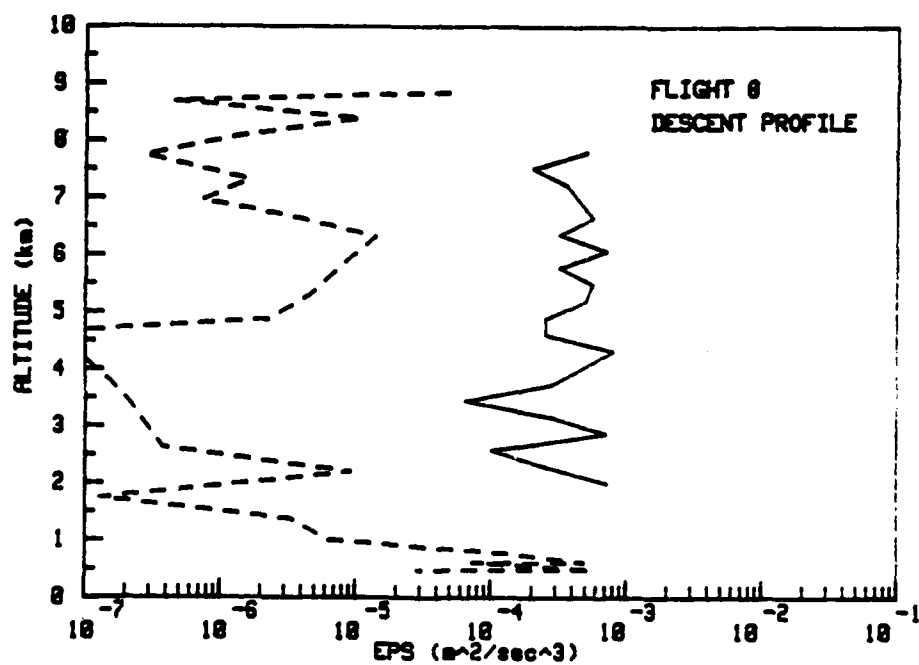
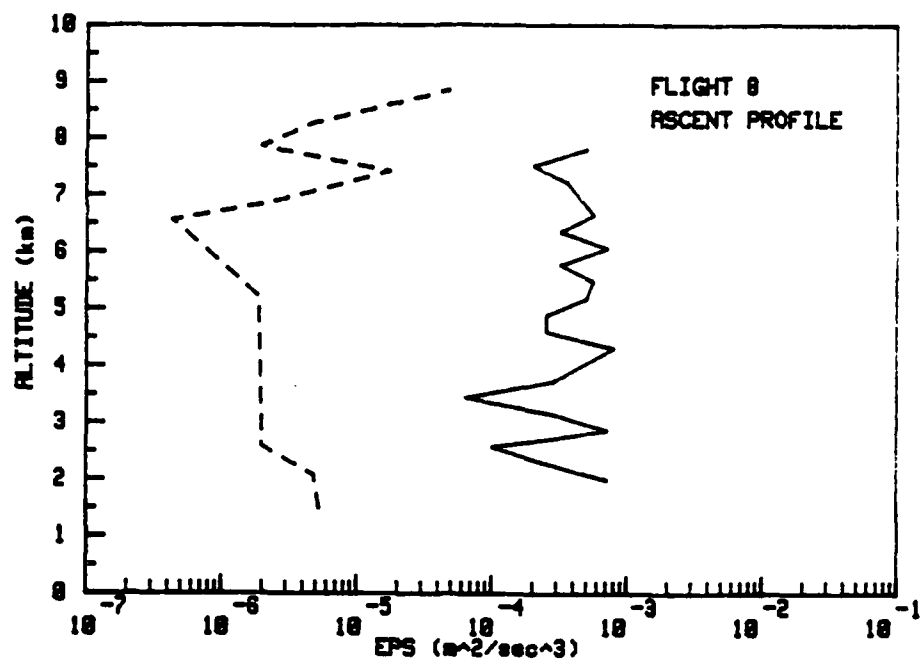


Figure 29. (continued)

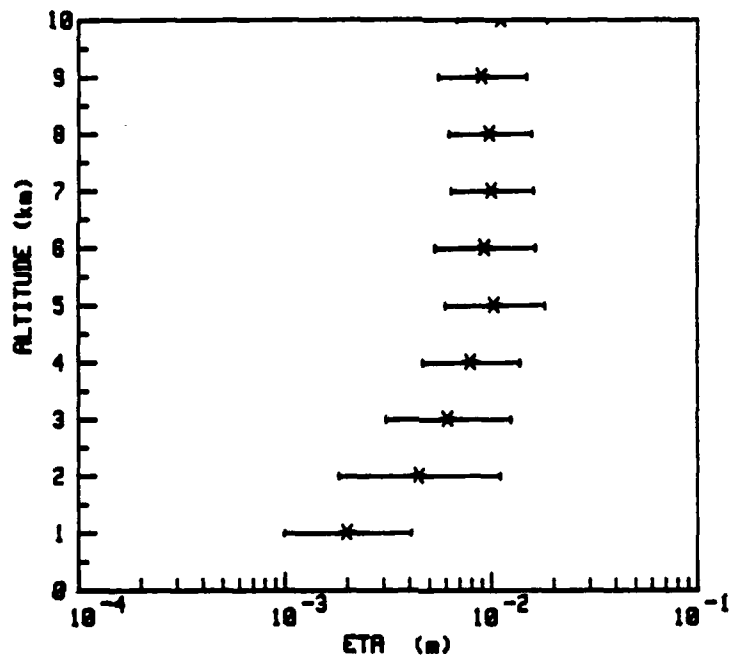


Figure 30. Average vertical profile of eta ( $\eta$ ), the turbulence inner size scale, from aircraft-measured epsilon profiles. Altitude is MSL.

computed for each  $\epsilon$  value using the previously mentioned formula for  $\nu$  with the standard atmosphere temperature profile, and then averaged in 1 km layers. The average value of  $\eta$  spans one order of magnitude, from 1 mm in the boundary layer to an average of 1 cm above the boundary layer.

## CHAPTER 8

### SUMMARY AND CONCLUSIONS

The atmosphere has a temporally and spatially variable refractive index due to its inherently turbulent nature. This can affect electromagnetic beam propagation by introducing beam steering, image dancing, beam spread, spatial coherence degradation, temporal coherence degradation, and scintillation (Dewan 1980). Refractivity is wavelength dependent. At microwave radar wavelengths, molecular composition (e.g., water content) dominates refractivity changes. At visible wavelengths, density (parameterized by temperature) dominates (Balsley and Gage 1980). For many quantification purposes, the refractive index turbulent structure constant,  $C_n^2$ , is a key parameter. This parameter can be inferred from optical turbulence (scintillometer), temperature turbulence (aircraft instrumentation or thermosonde) or radar backscatter (profiler) measurements. However,  $C_n^2$  from a radar profiler will differ because of the wavelength dependence of refractivity. Theoretically, this can be compensated for, if the humidity profile is known (VanZandt et al. 1981). Vertical integrals of  $C_n^2$  give transverse coherence length,  $r_0$ , and isoplanatic angle,  $\theta_0$ . These can also be measured remotely (based on optical turbulence) by an  $r_0$  scintillometer and isoplanometer, respectively.

During an atmospheric optics/meteorology experiment (acronym EWAK) conducted at Penn State University primarily during April and May of 1986, data was collected by the aforementioned instruments. AFGL and RADC scintillometers produced vertical profiles of

$C_n^2$ -optical. An AFGL thermosonde produced vertical profiles of  $C_T^2$  and other meteorological variables. A PSU profiler produced vertical profiles of wind direction and speed, and  $C_n^2$ -radar. The instrumented ARA research aircraft produced vertical profiles of temperature and velocity turbulence ( $C_T^2$  and  $C_u^2$ ) and other meteorological variables.

An indepth analysis of the aircraft turbulence data was performed. The turbulence instrumentation aboard consisted of cold-wire and hot-wire sensors (for temperature and velocity variations, respectively) and FM recording apparatus. The taped data was processed via FFT to produce one-dimensional variance spectra (wavenumber range 0.01 to 10  $m^{-1}$ ). Flights usually produced a 10 km vertical profile; the data was processed to give roughly 0.5 km vertical resolution, similar to that of the profiler.

An atmospheric filter function was derived, based on PBL spectra and -5/3 inertial subrange slope. This function was applied to compensate for low frequency dropoff, as part of a spectral editing program. Editing was based on percent error between a regression analysis and theoretical -5/3 slope. Noise subtraction was performed in some low signal cases. In general, PBL spectra clearly showed the classical -5/3 inertial subrange slope, out to the broadband instrument noise level. A majority of spectra in the free troposphere showed good evidence of the inertial subrange with -5/3 slope. Further data collection should emphasize the low frequencies, since this appears to be the low noise region. Occasional anomalous and low signal-to-noise spectra were encountered above the PBL. Low signal spectra represent quiescent layers.  $C_T^2$  and  $C_u^2$  were

calculated from the regression fit to the inertial subrange power spectral density. The rate of dissipation of turbulent kinetic energy,  $\epsilon$ , can be calculated by using the so-called Corrsin relation for velocity turbulence.  $C_n^2$  can be calculated from  $C_T^2$ .

Considerable interest has developed in models that relate microturbulence parameters to the mean gradients. One such model, proposed by VanZandt et al. (1978; 1981), has as a key variable the gradient Richardson number,  $R_i$ . In actively turbulent regions,  $R_i$  can be related to  $C_T^2$  and  $C_u^2$  as follows:

$$C_T^2 / C_u^2 = 1.6 R_i / (P_r - R_i) (\theta/g) (\partial\theta/\partial z) \quad (8.1)$$

A scatter plot of  $C_T^2$  versus  $(\theta/g \partial\theta/\partial z) C_u^2$  in the free troposphere has a slope that corresponds to  $1.6 R_i / (P_r - R_i)$ . This plot showed a range of values from 0.3 to 10 for high and low values of  $C_T^2$ , respectively. Scatter plots of  $C_T^2$  versus  $C_u^2$  showed high correlation of these two parameters, with  $\log C_u^2 = 1.7 \log C_T^2$ . This implies that the mean gradient structure of the free troposphere would have a probability density maximum (Fairall and Markson 1985). This could be illustrated as a single curve in N-S space, where N is the Brunt-Vaisala frequency squared, and S is the shear squared and  $R_i = N/S$ . Plots of this type were done using aircraft temperature data and profiler wind data. A distribution was obtained roughly corresponding to the curve depicted by Fairall and Markson (1985). Generally, regions of high shear are at or below the  $R_i = 0.25$  line, as expected.

Plots of  $C_T^2 / C_u^2 (\theta/g \partial\theta/\partial z)$  versus a turbulent activity parameter (Gregg 1987) clearly show agreement with the suggested

activity levels and associated values. As the ordinate value [corresponding to  $1.6 R_i / (P_r - R_i)$ ] decreases, turbulent activity increases. At high activity levels, the ordinate value approaches 0.4 (equivalent to  $1.6 R_i$  when approximating  $P_r$  as 1 and  $R_i$  as 0.25).

Values of N and S were used to obtain values of  $C_n^2$  and  $\epsilon$  with the model of VanZandt et al. Comparisons of  $C_n^2$  profiles measured by the various instruments showed good agreement between scintillometer and thermosonde, and between the VanZandt et al. model and the aircraft data. The profiler (converted optical values) had some agreement with the thermosonde. The difference in  $C_n^2$  profiles between methods varied. An average ratio of each profile versus the thermosonde profile gave the following factors for flight 6: aircraft 11.7 (standard deviation 23.4), model 11.5 (stand. dev. 18.5), profiler 4.3 (stand. dev. 5.3), and the scintillometer 1.6 (stand. dev. 0.5). In the lower levels of the flight 6 ascent, the aircraft profile is thought to have an error in gain setting. For flight 8, the factors were: aircraft 4.2 (stand. dev. 4.5), model 2.2 (stand. dev. 2), profiler 12 (stand. dev. 34), and the scintillometer 0.7 (stand. dev. 0.6). Similar differences between aircraft and thermosonde were noted by Brown and Good (1984). It was later thought that this difference might have been due to spectral analysis technique. However, the increased effort to improve spectral analysis in this paper apparently seemed to have little effect. Structure constant values obtained by the two spectral analysis methods examined in this work (FFT board and the signal analyzer) differed on the average by about a factor of two for  $C_T^2$ ; however individual



values differed by as much as two orders of magnitude.

To account for the difference in  $C_n^2$  profiles between instrument systems, further research might seek to determine the difference in values obtained by thermosonde and aircraft instrumentation, since they actually measure some of the same variables (e.g.,  $C_T^2$ ) in slightly different ways. Since the scintillometer tended to agree with the thermosonde and the VanZandt et al. model tended to agree with the aircraft, no clear choice is evident. The radar does not have an absolute calibration, so there is no significance to its agreement with either system (Christopher Fairall, personal communication, December 1987).

Another noticeable difference between the aircraft and thermosonde is the measured vertical profiles of potential temperature. Since potential temperature and its gradient are input parameters in the VanZandt et al. model, this difference could obviously affect model output. Barat and Bertin (1984) state the need for accurate temperature profiles and suggest changes in Richardson number depend more on temperature gradient than on shear. This study only used aircraft data as model input. Comparing model output from thermosonde and aircraft input could be another interesting comparison for further study. There is also an obvious need for additional simultaneous data collection. Logistical and weather problems contributed to make only two nights of simultaneous operation possible during EWAK.

Numerical integration of  $C_n^2$  gave estimates of  $r_0$  and  $\theta_0$ . Values from scintillometer, thermosonde and aircraft did not show consistent agreement. Based on the aircraft values, both the

scintillometer and thermosonde differed by an average of 17% for  $\theta_0$ , and the thermosonde differed by an average of 35% for  $r_0$ . With such a limited data set it is not possible at this time to conclude whether profiles of  $C_n^2$  can be used to estimate these optical parameters. Acceptable approximations for unmeasured segments of the atmosphere must also be further studied.

Despite good agreement on  $C_n^2$ , the aircraft data and the VanZandt et al. model output clearly disagreed on vertical profiles of  $\epsilon$ . This difference was also noted by Fairall and Markson (1985). They suggest this effect is due to the adjustment of the model parameter L, turbulent layer thickness, to produce the best fit of model output to profiler  $C_n^2$  data. Since few measurements of  $\epsilon$  have been done, there is a definite need for a larger data base. Other areas of study might include adjusting L to best fit aircraft  $\epsilon$  profiles. However, this would require either adjusting the constants (a and b) in the model equations or modifying the theory in order to preserve the good predictions for  $C_n^2$ . Raw high speed aircraft data could also be used to study turbulent "episodes" individually without vertical averaging. The fraction of the profile that is actually turbulent could be computed and the microturbulence ratio could be examined for each active layer.

Overall, EWAK provided a chance to compare methods of measuring  $C_n^2$ , as well as an opportunity to obtain microturbulence data that has some relation to the mean gradient structure. Hopefully, further research will provide a relationship that could be exploited in future predictive models.

## REFERENCES

- Balsley, B. B. and K. S. Gage. 1980. The MST radar technique: Potential for middle atmospheric studies. Pure Appl. Geophys. 118: 452-93.
- Barat, J. and F. Bertin. 1984. Simultaneous measurements of temperature and velocity fluctuations within clear air turbulence layers: Analysis of the estimate of dissipation rate by remote sensors. J. Atmos. Sci. 41: 1613-19.
- Brown, J. H. and R. E. Good. 1984. Thermosonde and UHF radar measurements of  $C^2$  at Westford, Massachusetts- July 1981. AFGL-TR-84-0109. Hanscom AFB.
- Brown, J. H., R. E. Good, P. M. Bench, and G. Faucher. 1982. Sonde experiments for comparative measurements of optical turbulence. AFGL-TR-82-0079. Hanscom AFB.
- Champagne, F. H., C. A. Friehe, J. C. LaRue, and J. C. Wyngaard. 1977. Flux measurements, flux estimation techniques, and fine scale turbulence measurements in the unstable surface layer over land. J. Atmos. Sci. 34: 515-30.
- Dewan, E. W. 1980. Optical turbulence forecasting: A tutorial. AFGL-TR-80-0030. Hanscom AFB.
- Eaton, F. D., W. A. Peterson, J. R. Hines, and G. Fernandez. 1985. Isoplanatic angle direct measurements and associated atmospheric conditions. Applied Optics 24: 3264-73.
- Environmental Science Services Administration, National Aeronautics and Space Administration, and United States Air Force. 1966. U. S. Standard Atmosphere Supplements, 1966. Washington, D. C.: U. S. Government Printing Office.
- Fairall, C. W. and R. Markson. 1984. Aircraft measurements of atmospheric velocity and temperature microturbulence spectra. Dept. of Meteo. Tech. Report. Pennsylvania State University.
- Fairall, C. W. and R. Markson. 1985. Aircraft measurements of temperature and velocity microturbulence in the stably stratified free troposphere. Seventh Symposium on Turbulence and Diffusion. American Meteorological Society (12-5 November): 180-3.
- Fairall, C. W. and R. Markson. 1987. Mesoscale variations in surface stress, heat fluxes, and drag coefficient in the marginal ice zone during the 1983 marginal ice zone experiment. J. Geophys. Res. 92: 6921-32.

# REFERENCES

- Fairall, C. W. and G. E. Schacher. 1977. Frequency response of hot wires used for atmospheric turbulence measurements in the marine environment. Rev. Sci. Inst. 48: 12-7.
- Fairall, C. W. and D. W. Thomson. 1985. Some preliminary comments and conclusions on radar-performance-related parameters extracted from CAPTEX raob sounding measurements. Dept. of Meteorology Tech. Report. Pennsylvania State University.
- Fried D. L. and G. E. Mevers. 1974. Evaluation of  $r_o$  for propagation down through the atmosphere. Applied Optics 13: 2620-2.
- Gregg, M. C. 1987. Diapycnal mixing in the thermocline: A review. J. Geophys. Res. 92: 5249-86.
- Hecht, E. 1986. Optics. 2d ed. Reading: Addison-Wesley.
- Hill, R. J. and S. F. Clifford. 1978. Modified spectrum of atmospheric temperature fluctuations and its application to optical propagation. J. Opt. Soc. Am. 68: 892-9.
- Hinze, J. 1975. Turbulence. 2d ed. New York: McGraw-Hill.
- Iribarne, J. V. and W. L. Godson. 1981. Atmospheric thermodynamics. 2d ed. Dordrecht: D. Reidel.
- Kennedy, P. J. and M. A. Shapiro. 1980. Further encounters with clear air turbulence in research aircraft. J. Atmos. Sci. 37: 986-93.
- Loos, G. C. and C. B. Hogge 1979. Turbulence of the upper atmosphere and isoplanatism. Applied Optics 18: 2654-61.
- Nastrom, G. D., K. S. Gage, and B. B. Balsley. 1981. Variability of  $C_n^2$  at Poker Flat, Alaska, from mesosphere, stratosphere, troposphere (MST) Doppler radar observations. Proceedings of the SPIE 277: 10-5.
- Ochs, G. R., R. S. Lawrence, T. Wang and P. Zieske. 1976. Stellar-scintillation measurement of the vertical profile of refractive-index turbulence in the atmosphere. Proceedings of the SPIE 75: 48-53.

REFERENCES

- Ochs, G. R., T. Wang, and E. Merrem. 1977. Stellar scintillometer model II for measurement of refractive turbulence profiles. Tech. Memo. ERL WPL-25. National Atmospheric and Oceanic Administration.
- Ottersten, H. 1969. Atmospheric structure and radar backscattering in clear air. Radio Sci. 4: 1179-93.
- Panofsky, H. A. and J. A. Dutton. 1984. Atmospheric diffusion. New York: John Wiley and Sons.
- Stevens, K. B. 1985. Remote measurements of the atmospheric isoplanatic angle and determination of refractive turbulence profiles by direct inversion of the scintillation amplitude covariance function with Pikhonov regularization. Ph. D. diss., Naval Post-graduate School, Monterey.
- Strauch, R. G., A. S. Frisch, and B. L. Weber. 1986. Wind measurements in the upper troposphere with UHF and VHF radar. 23rd Conference on Radar Meteorology Preprints 1 (22-6 September): 48-51.
- Strohbehn, J. W., ed. 1978. Laser beam propagation in the atmosphere. Berlin: Springer-Verlag.
- Tatarskii, V. I. 1971. The effects of the turbulent atmosphere on wave propagation. Jerusalem: Israel Program for Scientific Translations.
- Wallace, J. M. and P. V. Hobbs. 1977. Atmospheric science an introductory survey. New York: Academic Press.
- Wesely, M. L. 1976. The combined effects of temperature and humidity fluctuations on refractive index. J. Appl. Meteo. 15: 43-9.
- VanZandt, T. E., J. L. Green, K. S. Gage, and W. L. Clark. 1978. Vertical profiles of refractivity turbulence structure constant: Comparison of observations by the Sunset Radar with a new theoretical model. Radio Science, 13: 819-29.
- VanZandt, T. E., K. S. Gage and J. M. Warnock. 1981. An improved model for the calculation of profiles of  $C_n^2$  and  $\epsilon$  in the free atmosphere from background profiles of wind, temperature and humidity. Twentieth Conference on Radar Meteorology Preprints. (30 November to 3 December): 129-35.

# DISTRIBUTION LIST

addresses	number of copies
RADC/OCSP ATTN: Donald M. Stebbins Griffiss AFB NY 13441-5700	10
Airborne Research Associates 46 Kendal Common Road Weston, MA 02193	5
RADC/DOVL Technical Library Griffiss AFB NY 13441-5700	1
Administrator Defense Technical Info Center DTIC-FDA Cameron Station Building 5 Alexandria VA 22304-6145	5
Strategic Defense Initiative Office Office of the Secretary of Defense Wash DC 20301-7100	2
AFIT/LDEE Building 640, Area B Wright-Patterson AFB OH 45433-6583	1
AUL/LSE Maxwell AFB AL 36112-5564	1
HQ Air Force SPACECOM/XPYS ATTN: Dr. William R. Matoush Peterson AFB CO 80914-5001	1

HQ Air Training Command  
ATC/TTOI  
Randolph AFB TX 78150-5001

1

Commanding Officer  
Naval Avionics Center  
Library  
D/765  
Indianapolis IN 46219-2189

1

Commanding Officer  
Naval Ocean Systems Center  
Technical Library  
Code 96428  
San Diego CA 92152-5000

1

Superintendent  
Naval Post Graduate School  
Code 1424  
Monterey CA 93943-5000

1

Commanding Officer  
Naval Research Laboratory  
Code 2627  
Washington DC 20375-5000

2

Commanding Officer  
US Army Missile Command  
Redstone Scientific Info Center  
AMSMI-RD-CS-R (Documents)  
Redstone Arsenal AL 35898-5241

2

Rand Corporation  
Technical Library  
ATTN: Ms. Doris Helfer  
PO Box 2138  
Santa Monica CA 90406-2138

1

ESD/XTP  
Hanscom AFB MA 01731-5000

1

the Optical Sciences Co  
Attn: Dr. David Fried  
P. O. Box 1329  
Placentia, CA 92670

1

SAIC 1  
Attn: Dr. Frederick Gebhardt  
1040 Waltham Street  
Lexington, MA 02173

W.J. Schafer Associates 1  
ATTN: Dr. Peter Ulrich  
1901 Fort Meyer Drive  
Arlington, VA 22209

WL/AR-1 1  
ATTN: Dr. C. B. Hogge  
Kirtland AFB, NM 87117-6008

North East Research Associates 1  
ATTN: Dr. Robert Meyers  
800 W. Cummings Park, Suite 4500  
Woburn, MA 01801

Farfield Inc. 1  
ATTN: Dr. James Wallace  
6 Thoreau Way  
Sudbury, MA 01776

Adaptive Optics Associates 1  
ATTN: Dr. Larry Schumtz  
54 Cambridge Park Drive  
Cambridge, MA 02140

Litton ITEK Optical Systems 1  
ATTN: Dr. Robert Aldrich  
10 Maguire Road  
Lexington, MA 02173

HQ AF Space Command/XPD 1  
ATTN: Col. R. Benedict  
Peterson AFB, CO 80914-5001

Hughes Research Laboratory 1  
ATTN: Dr. C. Giuliano  
3011 Malibu Canyon Road  
Malibu, CA 90265



Lockheed Missiles and Space Co. Document Management ATTN: Dr. R. Lytell 3251 Hanover Street Palo Alto, CA 94304	1
AVCO Research Laboratory ATTN: Dr. P. McCormick P.O. Box 261 Puunene, HI 96784	1
Thermal Electron Tech. ATTN: Dr. Robert Hunter 9555 Distribution Avenue San Diego, CA 92121	1
Naval Sea Systems Command PMS-405-200 ATTN: John Albertine Washington DC 20362-5101	1
M.I.T Lincoln Laboratory ATTN: Dr. C. Primmerman P.O. Box 73 Lexington, MA 02173	1
Lockheed Missiles and Space Co. Document Management L556 Mail Station c/51-40 B586 P.O. Box 3504 Sunnyvale, CA 94088-3504	1
SDIO-TDE Pentagon ATTN: LCDR J. Garner Washington, DC 20301-7100	1
RADC (OL-AB) c/o AVCO Research Labs ATTN: Maj. T. Zych P.O. Box 261 Puunene, Maui, HI 96784	1
AFWAL/AAWW-3 ATTN: Mr. George Vogel Wright-Patterson AFB, OH 45433-6543	1

Perkin-Elmer ATTN: Mr. Neufield GSO-MS-966 100 Wooster Heights Road Danbury, CT 06810	1
DARPA/DEO ATTN: Dr. Shen Shey 1400 Wilson Boulevard Arlington, VA 22209	1
WL/AR9A ATTN: Dr. Robert Fugate Kirtland AFB, NM 87117	1
Eastman Kodak Company ATTN: Mr. Stanley Refermat P.O. Box L Rochester, NY 14624	1
Optron Systems, Inc. ATTN: Dr. Cardinal Warde 31 Green St. Waltham, MA 02154	1
Naval Sea Systems Command Dept of the Navy ATTN: CDR F. Marcell PMS-405-200 Washington, DC 20362-5101	1
The BDM Corporation ATTN: Dr. Susan Carson 1801 Randolph Road, SE Albuquerque, NM 87106	1
MIT Lincoln Laboratory ATTN: Dan Hermann 244 Wood Street Lexington, MA 02173	1
SAIC ATTN: E. Alan Phillips Suite 310 1215 Jefferson Davis Highway Arlington, VA 22202	1

AVCO Research Laboratory 1  
ATTN: Dr Jack Daughtery  
2385 Revere Beach Parkway  
Everett, MA 02148

W.J Schafer Associates 1  
ATTN: Dr. Daniel Leslie  
1500 Wilson Blvd.  
Arlington, VA 22209

AVCO Research Laboratory 1  
ATTN: Dr. Robert Slater  
2385 Revere Beach Parkway  
Everett, MA 02148

W. J. Schafer Associates 1  
Suite 205  
2000 Randolph Road, SE  
Albuquerque, NM 87106

Aerospace Corporation 1  
ATTN: Dr. Robert Heidner  
P.O. Box 92957  
Los Angeles CA 90009

The Pennsylvania State University 1  
Dept of Meteorology  
ATTN: Dr. D. W. Thomson  
505 Walker Building  
University park, PA 16802

AFGL/OPA 1  
ATTN: R. Beland  
Hanscom AFB, MA 01731

AFGL/OPA 1  
ATTN: E. Murphy  
Hanscom AFB, MA 01731

Lawrence Livermore National Lab 1  
ATTN: Dr. Thomas Karr  
P.O. Box 5508  
Livermore, CA 94550

Ground Based Laser Project Office Ground Based Laser ATTN: Dr. Thomas Hall CSSD-H-F3 White Sands Missile Range, NM 88002	1
AVCO Research Laboratory ATTN: Steven Heising Suite 109 4410 E. Fountain Road Colorado Springs, CO 80916	1
The Jet Propulsion Laboratory ATTN: Dr. Aden Meinel 4800 Oak Grove Drive Pasadena, CA 91109-5000	1
SAIC ATTN: John Vasselli 199 Liberty Plaza Suite 200 Rome, NY 13440	1
Hughes Aircraft Corporation EDSG Bldg E-55 ATTN: Dr. Wilbur Brown P.O. Box 902 El Segundo, CA 90245	1
ERIM Advanced Concepts Division ATTN: Richard Paxman P.O. Box 8618 Ann Arbor, MI 48107	1
FTD/SDMSY ATTN: Capt. Felicia Ansty Wright-Patterson AFB, OH 45433-6508	2
Lockheed Missiles and Space Co. ATTN: Dr. Naresh Mehta GBFEL TIE BCS Program Atmospheric Propagation Group Palo Alto, CA 94304	1
Nonlinear Systems, Inc. ATTN: Dr. Vladimir Krapchev Suite 3121 222 Third St. Cambridge, MA 02142	1

JASONS  
ATTN: Dr. Patrick Diamond  
Meyer Hall 8-019  
University of California, San Diego  
La Jolla, Ca 92093

1

TRW  
ATTN: Dr. Charles Kilchine  
3300 Avenida Pico  
San Clemente, CA 92672

1

U. S. Army Lab. Command  
Atmospheric Sciences Lab  
ATT: Dr. Robert Rubio  
SLCAS-AS-D  
WSMR, NM 88002

1



## *MISSION of Rome Air Development Center*

*RADC plans and executes research, development, test and selected acquisition programs in support of Command, Control, Communications and Intelligence (C<sup>3</sup>I) activities. Technical and engineering support within areas of competence is provided to ESD Program Offices (POs) and other ESD elements to perform effective acquisition of C<sup>3</sup>I systems. The areas of technical competence include communications, command and control, battle management information processing, surveillance sensors, intelligence data collection and handling, solid state sciences, electromagnetics, and propagation, and electronic reliability/maintainability and compatibility.*